UNIVERSITÀ DELLA CALABRIA

Università della Calabria

Dottorato di Ricerca in "Scienze e Tecnologie Fisiche, Chimiche e dei Materiali"
in convenzione con il CNR

XXX ciclo

Tesi di dottorato

Solid-shell finite element and isogeometric models for nonlinear analysis and design of elastic shells using Newton, Koiter and Koiter-Newton solution strategies

S.S.D. Scienza delle costruzioni ICAR/08

Supervisore
Prof. Giovanni Garcea

Coordinatore
Prof. Vincenzo Carbone

Co-supervisore
Ing. Leonardo Leonetti

Dottorando
Ing. Domenico Magisano

Novembre 2017

To the loving memory of my father.

Contents

Sommario

L'obbiettivo di questo lavoro è quello di sviluppare un modello numerico adeguato per l'analisi e l'ottimizzazione di strutture in parete sottile, in particolare nel caso di materiali compositi fibro-rinforzati, tenendo conto delle nonlinearità geometriche del modello meccanico. Diversi aspetti del problema, per cui ancora oggi non esistono soluzioni affidabili ad efficienti, vengono affrontati: tecniche di discretizzazione, metodi di analisi e di ottimizzazione. Nel primo capitolo, dopo un breve richiamo a metodi di Riks e di Koiter, vengono discussi i vantaggi di un modello solido misto in tensione e spostamento in questo contesto di analisi e le ripercussioni sulle performance dei metodi di soluzione. Il secondo capitolo, dopo l'introduzione di un elemento finito solid-shell misto, riformula il metodo di Koiter, rendendolo uno strumento accurato ed efficiente per l'analisi di sensibilità alle imperfezioni. Quest'ultimo viene sfruttato nel terzo capitolo che propone una strategia di ottimizzazione di strutture in composito basata sull'analisi Monte Carlo che prende in considerazione la forma peggiore di imperfezione geometrica. Il quarto capitolo illustra un'implementazione efficiente del metodo Koiter-Newton, che sfrutta la predizione alla Koiter e l'efficienza della formulazione mista per ricostruire il percorso di equilibrio con un numero esiguo di iterazioni alla Newton. Nel quinto capitolo, i vantaggi della formulazione mista nel metodo di Newton vengono estesi ad elementi finiti basati su formulazione in spostamento attraverso la tecnica dei punti di integrazione misti. Nel sesto capitolo, il modello ad elementi finiti viene trasformato in un'analisi isogeometrica per ridurre il numero di variabili discrete sfruttando funzioni di forma ad alta continuità e la rappresentazione esatta della geometria. Questo modello è reso accurato ed efficiente attraverso integrazioni ridotte definite sulla patch e punti di integrazione misti. I vantaggi rispetto agli elementi finiti di ordine basso sono molto evidenti nei casi di instabilità di gusci curvi, come mostrato nel settimo capitolo che illustra un'analisi isogeometrica alla Koiter.

Abstract

This thesis aims at developing a reliable and efficient numerical framework for the analysis and the design of slender elastic shells, in particular when composite materials are adopted, taking account of the geometrically nonlinear behaviour. Different aspects of this challenging topic are tackled: discretisation techniques, numerical solution strategies and optimal design. The first chapter, after a short summary of the Riks and Koiter methods, discusses the important advantages of using a mixed (stress-displacement) solid model for analysing shell structures over traditional shell models and the implications of this on the performances of the solution strategies. The second chapter introduces a mixed solid-shell model and reformulates the Koiter method to obtain an effective tool for analysing imperfection sensitive structures. This approach is the starting point of the third chapter, which proposes a stochastic optimisation strategy for the layup of composite shells, able to take account of the worst geometrical imperfection. The fourth chapter extends the benefits of the mixed formulation in the Newton iterative scheme to any displacement-based finite element model by means of a novel strategy, called Mixed Integration Point. The fifth chapter illustrates an efficient implementation of the novel Koiter-Newton method, able to recover the equilibrium path of a structure accurately with a few Newton iterations, combining an accurate Koiter predictor with the reduced iterative effort due to a mixed formulation. The solid-shell discrete model is reformulated in the sixth chapter, following the isogeometric concept, by using NURBS functions to interpolate geometry and displacement field on the middle surface of the shell in order to take advantage of their high continuity and of the exact geometry description. The approach is made accurate and efficient in large deformation problems by combining the Mixed Integration Point strategy with a suitable patch-wise reduced integration. The resulting discrete model proves to be much more convenient than low order finite elements, especially in the analysis of curved shells undergoing buckling. This is shown in the seventh chapter, which proposes an efficient isogeometric Koiter analysis.

Introduction

Shell structures are employed as primary structural elements in a very wide range of applications, ranging from aerospace to civil engineering. Their success is mainly due to the high strength/weight ratio that is crucial for lightweight structures. In addition to isotropic metal materials, multi-layered composites are widely used. In this case, the structural performances can be tailored by a proper choice of the fibre orientation within each layer [1]. The use of such materials together with the structural optimisation, results in slender structures, whose failure is often dominated by buckling and/or excessive deformations which compromise the structural functionality. A reliable modelling of the problem is an essential tool for designers. This issue is commonly known as a geometrically nonlinear structural problem, that is a mathematical problem in which the nonlinearity is due to the relationship between strains and displacements/rotations. As a result, the structural behaviour of slender structures is described by means of a nonlinear system of partial differential equations, whose solution requires adequate numerical methods which take into account two different aspects: the discretisation technique, mandatory for general geometries, boundary conditions and material properties distribution, and the strategy for solving the nonlinear discrete equations. The standard approach to simulate the behaviour of this kind of structure consists in the use of the finite element method [2] to transform the continuum problem into a discrete one. The nonlinear discrete equations are then solved by using the static Riks approach based on the Newton iterative method, which provides the equilibrium path of the structure [3]. This strategy is well established and effective for assigned data, but it can be time consuming with current computers because of the number of discrete degrees of freedom required to approximate the differential equations over the domain and the iterative effort for solving the nonlinear discrete equations. This limitation makes the approach unsuitable in the design stage of shell structures, when a large number of analyses is generally required to identify optimal solutions, such as in the optimal stacking sequence in laminates. Moreover, as is well known, nonlinear problems can exhibit a strong sensitivity to even small deviations of the initial data. This is very common in buckling problems, where small imperfections, especially geometrical ones, can strongly affect the structural response [4, 5]. In this context, a different solution approach, named Koiter method, has also been developed over

the years[6]. It is based on a reduced order model, which approximates the finite element solution exploiting the Koiter's theory of elastic stability [7]. This kind of analysis is much more efficient than the Riks method for analysing an assigned structure, and provides a quick and accurate prediction of the initial post-buckling behaviour for a wide range of structural problems. Its most attractive feature is the theoretical possibility of including the effects of the imperfections directly in the reduced model of the perfect structure, built once and for all. The current formula to account for the imperfections, available in literature, can however lead to significant errors compared to the Riks reference solution [5] and to the Koiter solution with re-construction of the reduced order model. Recently, a novel strategy, named Koiter-Newton approach, has been proposed [8]. It is based on a predictor-corrector scheme, like the Riks one, where the Koiter method is used as an accurate predictor in order to reduce the number of corrector steps involving Newton iterations. Although this approach is more accurate than the Koiter method and more efficient than the Riks one, it can still be too time consuming for optimisation processes and imperfection sensitivity analyses, because some Newton iterations in all the variables of the finite element model are necessary.

Although there has been a great amount of research into this topic over the years, the state-of-the-art numerical tools do not give an effective answer for the needs of the engineers. This thesis aims at developing a reliable and efficient numerical framework for the analysis and the design of slender elastic shells, in particular when composite materials are adopted, taking account of the geometrically nonlinear behaviour. Different aspects of the topic are tackled: discretisation techniques, numerical solution strategies and optimal design.

The first chapter, after a brief summary of the Riks and Koiter methods, discusses the advantages of using a mixed (stress-displacement) solid model for analysing shell structures over traditional shell models. In the second chapter, a new strategy to account for geometrical imperfections in Koiter analysis is derived, which overcomes the inaccuracies of previous proposals. The main idea is to correct the reduced order model of the perfect structure taking the imperfections into account to make the Koiter method a reliable and efficient tool for analysing imperfection sensitive structures.

In the third chapter, the great efficiency and the improved accuracy of the Koiter method is used within a stochastic optimisation strategy for composite shells. The goal is to search for the best stacking sequence that maximises the structural performance, optimising the post-buckling behaviour. Its feasibility is due to the reduced order model built for each material setup, which allows a random scan of the optimisation parameters domain considering the worst geometrical imperfection in the evaluation of the structural response.

The study carried out in the first chapter explains how the advantages of the mixed formulation over the displacement-based one is due to the direct use of the stresses as independent variables in the solution algorithms. Starting from this consideration, the fourth chapter extends the benefits of the mixed formulation

to any displacement-based finite element model. The idea is to introduce stress variables in the solution process, even if the discrete approximation is governed by displacement variables only. To this purpose, a strategy, called Mixed Integration Points is proposed and implemented within the Newton iterative scheme.

The fifth chapter investigates the novel Koiter-Newton method and, in particular, an implementation of the algorithm based on the mixed solid-shell model. The goal is to recover the equilibrium path of a structure accurately with a few Newton iterations, combining an accurate Koiter predictor with the reduced iterative effort due to a mixed formulation.

Although the linear solid-shell finite element discretisation is robust and efficient, it may require a significant number of degrees of freedom for the analysis of curved shells and for approximating the buckling modes of compressed structures, usually characterised by highly continuous shapes. For this reason, the solid-shell discrete model is reformulated in the sixth chapter, following the isogeometric concept [9], exploiting NURBS functions to interpolate geometry and displacement field on the middle surface in order to take advantage of their high continuity and of the exact geometry description. The model is made efficient and accurate by combining the Mixed Integration Point strategy with a suitable patch-wise reduced integration. The isogeometric solid-shell model is used in the seventh chapter for constructing the reduced order model of the Koiter method in a very efficient way, because a very low number of discrete variables and integration points are needed.

Finally, the main results obtained in this thesis are summarised in the concluding chapter.

Chapter 1

Advantages of mixed solid models in geometrically nonlinear analysis

Abstract

This chapter deals with two main advantages in the analysis of slender elastic structures both achieved through the mixed (stress and displacement) format with respect to the more commonly used displacement one: i) the smaller error in the extrapolations usually employed in the solution strategies of nonlinear problems; ii) the lower polynomial dependence of the problem equations on the finite element degrees of freedom when solid finite elements are used. The smaller extrapolation error produces a lower number of iterations and larger step length in path-following analysis and a greater accuracy in Koiter asymptotic method. To focus on the origin of the phenomenon the two formats are derived for the same finite element interpolation. The reduced polynomial dependence improves the Koiter asymptotic strategy in terms of both computational efficiency, accuracy and simplicity.

1.1 Introduction

In recent years an increasing amount of research has aimed at developing new efficient solid finite elements [10] for the linear and nonlinear analysis of thin structures. This is due to some advantages of solid elements in comparison to classical shell elements. In particular in the elastic nonlinear analysis of slender structures they allow the use of the 3D continuum strain and stress measures employing translational degrees of freedom (DOFs) only [10, 11, 12, 13]. In this way it is possible to avoid the use of complicated and expensive rules for updating the rotations and, by using the Green-Lagrange strain measure, to coherently

describe the structural behaviour through a low order dependence on the displacement field without the need to employ complex, geometrically exact formulations, which are not always available or accurate [14, 15]. In this way solid elements allow a simpler expression of the strain energy and its variations with a gain in computational efficiency.

However, formulating robust solid-shell elements is more demanding than shell elements. To maintain an acceptable number of DOFs, the elements proposed are usually based on a low order displacement interpolation. Consequently they have the disadvantages of *interpolation lockings*: the shear and membrane locking also present in classical shell elements and trapezoidal and thickness locking, typical of low order solid-shell elements [16]. Interpolation lockings are usually rectified by means of Assumed Natural Strain, Enhanced Assumed Strain [17, 18, 19, 20] and mixed (stress-displacement) formulations [10, 13, 21, 22]. In this way solid-shell elements have now reached a high level of efficiency and accuracy and have also been used to model composites or laminated beams [19, 23, 21, 24] and shell structures in both the linear [17, 12] and nonlinear [20, 11, 10] range. Among the most effective and interesting proposals, there are the mixed solid-shell elements of Sze and coauthors [10, 21, 25, 26, 27, 28, 29, 24, 30, 31] which extend the initial PT18β hybrid element of Pian and Tong to thin shell.

When comparing mixed and displacement finite elements many authors (see for example [10] and [11]) observe that the mixed ones are more robust and allow larger steps in path-following geometrically nonlinear analyses. However the reasons for these better performances are, in our opinion, not clear, as they are often wrongly attributed to the properties of the finite element interpolation. One of the goals of this chapter is therefore to clarify the true reason and origin of this phenomenon, extending the results presented some years ago [32, 33] in the context of path-following and Koiter analyses of 2D framed structures.

Mixed and displacement descriptions, while completely equivalent at the continuum level, behave very differently when implemented in path-following and Koiter solution strategies even when they are based on the same finite element interpolations, that is when they are equivalent also at the discrete level. This is an important, even if frequently misunderstood, point in developing numerical algorithms and it has been discussed in [32, 33, 6] to which readers are referred for more details.

Since the solution strategies of a nonlinear problem usually involve linearisations, a *smooth enough* description of the problem that makes the extrapolation error as small as possible is crucial. Mixed and displacement descriptions are characterized by a different extrapolation errors and so they behave very differently when used within a numerical solution process. For shells or beams, in the presence of large displacements (rigid rotations) and high membrane/flexural stiffness ratios, the extrapolation with the displacement description is affected by a large error that causes: i) a very slow convergence rate in path-following analysis; ii) an unreliable estimate of the bifurcation point along an extrapolated fundamen-

tal path and then a low accuracy of the Koiter method based on an asymptotic expansion in this point. As will be shown, the mixed description is unaffected by this phenomenon named *extrapolation locking*. Note that it is a locking of the nonlinear problem when described in a displacement format and it not related to the FE interpolation. The term locking is used in analogy to the interpolation locking of the finite element, because it produces an overestimated extrapolated stiffness which gets worse with the slenderness of the structure. On the contrary the mixed format of the nonlinear problem is unaffected by the extrapolation locking and this ensures: in path-following analysis, a fast convergence of the Newton (Riks) iterative process; in asymptotic analysis, which uses extrapolations which are not corrected by an iterative process [34, 35], an accurate recovery of the equilibrium path.

In this chapter a mixed and a displacement description are derived for the same finite element, so obtaining two completely equivalent discrete problems, in order to show that their different behaviour is not due to the interpolation fields and that the extrapolation locking occurs for any displacement finite element. This allows us to thoroughly investigate this important phenomenon which has not been taken into account by the scientific community.

Another important advantage is related to the minimum strain energy dependence on the finite element (FE) discrete variables when solid elements based on the quadratic Green-Lagrange strain measure are employed: the fourth order dependence on displacement variables in the displacement formulation and the third order in stress and displacement variables in the mixed case. This has a significant effect on the efficiency, robustness and coherence of the asymptotic analysis when the mixed description is used. It allows, in fact, the zeroing of all the strain energy variations of an order greater than the third and, consequently, permits light numerical formulations and an improvement in accuracy. In this way it is possible to develop a new Koiter algorithm, which is more accurate and computationally efficient than that based on classical shell elements, well suited to the imperfection sensitivity analysis of slender structures.

Finally it is worth mentioning that the use of both displacement and stress variables increases the dimension of the problem, but generally the computational extra–cost, with respect to a displacement analysis, is very low. This is because the global operations involve displacement DOFs only by performing a static condensation of the stress variables defined at element level. This small computational extra-cost is largely compensated: in path-following analysis, by larger steps and fewer iterations with respect to the displacement case; in asymptotic analysis, by the zeroing of the computationally expensive fourth order strain energy variations. It will be also shown how the slow change of the Jacobian matrix when expressed in mixed variables allows, in path following analyses, an efficient use of the modified Newton method with a further significant reduction in the computational cost. To summarize the chapter deals with two important advantages, both achieved with the mixed format with respect to the commonly used displacement

one: i) the smaller error in the extrapolations usually employed in the solution of nonlinear problems; ii) the lower polynomial dependence of the problem equations on the FE DOFs when a solid finite element is used. The chapter is organized as follows: Section 2 briefly reviews asymptotic and path-following methods; Section 3 presents the mixed and displacement descriptions based on the solid finite element and the advantages of mixed solid elements in Koiter analysis; Section 4 describes why extrapolation locking phenomenon occurs for slender structures and its effect on the two solution algorithms adopted; Section 5 presents some numerical tests; finally, the conclusions are reported.

1.2 Numerical strategies in nonlinear FE analysis

This section briefly summarises the path following and asymptotic methods. A complete review of both the approaches can be found in [3, 36, 6, 35].

1.2.1 The discrete nonlinear equations

We consider a slender hyperelastic structure subject to conservative loads $p[\lambda]$ proportionally increasing with the amplifier factor λ. The equilibrium is expressed by the virtual work equation

$$\Phi[u]'\,\delta u - \lambda \hat{p}\,\delta u = 0 \quad , \quad u \in \mathcal{U}\ ,\ \delta u \in \mathcal{T} \tag{1.1}$$

where $u \in \mathcal{U}$ is the field of configuration variables, $\Phi[u]$ denotes the strain energy, $\mathcal{T}$ is the tangent space of $\mathcal{U}$ at u and a prime is used to express the Frechèt derivative with respect to u. $\mathcal{U}$ is assumed to be a linear manifold so that its tangent space $\mathcal{T}$ will be independent of u. When a mixed format is adopted the configuration variables u collect both displacement and stress fields. Eq.(1.1) can be rewritten, using a FE discretisation $u = \mathbf{N}_u\mathbf{u}$ as

$$\mathbf{r}[\mathbf{u},\,\lambda] \equiv \mathbf{s}[\mathbf{u}] - \lambda\,\hat{\mathbf{p}} = \mathbf{0}, \quad \text{with} \quad \begin{cases} \mathbf{s}^T\delta\mathbf{u} \equiv \Phi'[u]\delta u \\ \hat{\mathbf{p}}^T\delta\mathbf{u} \equiv \hat{p}\,\delta u \end{cases} \tag{1.2}$$

where $\mathbf{r} : \mathbb{R}^{N+1} \to \mathbb{R}^N$ is a nonlinear vectorial function of the vector $\mathbf{z} \equiv \{\mathbf{u}, \lambda\} \in \mathbb{R}^{N+1}$, collecting the configuration $\mathbf{u} \in \mathbb{R}^N$ and the load multiplier $\lambda \in \mathbb{R}$, $\mathbf{s}[\mathbf{u}]$ is the *response vector* and $\hat{\mathbf{p}}$ the *reference load vector*. Eq.(1.2) represents a system of N-equations and $N+1$ unknowns and defines the *equilibrium path* as a curve in $\mathbb{R}^{N+1}$ from a known initial configuration $\mathbf{u}_0$, corresponding to $\lambda = 0$. The tangent stiffness matrix is also defined as

$$\delta\mathbf{u}_2^T\mathbf{K}[\mathbf{u}]\delta\mathbf{u}_1 = \Phi''[u]\delta u_1\delta u_2 \ \ , \ \ \forall\,\delta\mathbf{u}_1, \delta\mathbf{u}_2 \tag{1.3}$$

where δu_i are generic variations of the configuration field u and $\delta\mathbf{u}_i$ the corresponding FE vectors.

1.2.2 Path–following analysis

The Riks approach [3] completes the equilibrium equations (1.2) with the additional constraint $g[\mathbf{u},\lambda]-\xi=0$ which defines a surface in $\mathbb{R}^{N+1}$. Assigning successive values to the control parameter $\xi=\xi^{(k)}$ the solution of the nonlinear system

$$\mathbf{R}[\xi]\equiv\begin{bmatrix}\mathbf{r}[\mathbf{u},\lambda]\\ g[\mathbf{u},\lambda]-\xi\end{bmatrix}=\mathbf{0} \tag{1.4}$$

defines a sequence of points (steps) $\mathbf{z}^{(k)}\equiv\{\mathbf{u}^{(k)},\,\lambda^{(k)}\}$ belonging to the equilibrium path. Starting from a known equilibrium point $\mathbf{z}_0\equiv\mathbf{z}^{(k)}$ the new one $\mathbf{z}^{(k+1)}$ is evaluated correcting a first *extrapolation* $\mathbf{z}_1=\{\mathbf{u}_1,\,\lambda_1\}$ by a sequences of estimates $\mathbf{z}_j$ (loops) by a Newton–Raphson iteration

$$\begin{cases}\tilde{\mathbf{J}}\dot{\mathbf{z}}=-\mathbf{R}_j\\ \mathbf{z}_{j+1}=\mathbf{z}_j+\dot{\mathbf{z}}\end{cases} \tag{1.5a}$$

where $\mathbf{R}_j\equiv\mathbf{R}[\mathbf{z}_j]$ and $\tilde{\mathbf{J}}$ is the Jacobian of the nonlinear system (1.4) at $\mathbf{z}_j$ or its suitable estimate. The simplest choice for $g[\mathbf{u},\lambda]$ is the linear constraint corresponding to the orthogonal hyperplane

$$\mathbf{n}_u^T(\mathbf{u}-\mathbf{u}_1)+n_\lambda\,(\lambda-\lambda_1)=\Delta\xi\quad\text{where}\quad\begin{cases}\mathbf{n}_u\equiv\mathbf{M}\,(\mathbf{u}_1-\mathbf{u}^{(k)})\\ \mathbf{n}_\lambda\equiv\mu\,(\lambda_1-\lambda^{(k)})\end{cases} \tag{1.5b}$$

$\mathbf{M}$ and μ being some suitable metric factors [32], $\Delta\xi$ an assigned increment of ξ and

$$\tilde{\mathbf{J}}\approx\left[\frac{\partial\mathbf{R}[\mathbf{z}]}{\partial\mathbf{z}}\right]_{\mathbf{z}_j}=\begin{bmatrix}\tilde{\mathbf{K}} & -\hat{\mathbf{p}}\\ \mathbf{n}_u^T & n_\lambda\end{bmatrix} \tag{1.5c}$$

The standard load controlled scheme is obtained assuming $g[\mathbf{u},\lambda]=\lambda$ (see [32] for further details) while keeping $\tilde{\mathbf{K}}=\mathbf{K}[\mathbf{u}_1]$ we have the modified Newton-Raphson scheme.

Convergence of the path–following scheme.

The convergence of the iterative process (1.5) has been widely discussed in [32] and can be expressed in the condition

$$\mathbf{R}_{j+1}=\left(\mathbf{I}-\mathbf{J}_s\tilde{\mathbf{J}}^{-1}\right)\mathbf{R}_j \tag{1.5d}$$

where $\mathbf{I}$ is the identity matrix and $\mathbf{J}_s\equiv\int_0^1\mathbf{J}[\mathbf{z}_j+t(\mathbf{z}_{j+1}-\mathbf{z}_j)]\;dt$ the secant Jacobian matrix. The iteration converges if in some norm we have $\left\|\mathbf{I}-\mathbf{J}_s\tilde{\mathbf{J}}^{-1}\right\|<1$ and it will be as fast as $\tilde{\mathbf{J}}$ is close to $\mathbf{J}_s$. Also note that the convergence condition for a load controlled scheme is obtained by replacing $\tilde{\mathbf{J}}$ and $\mathbf{J}_s$ with $\tilde{\mathbf{K}}$ and $\mathbf{K}_s$

respectively. For the displacement format in the case of positive definite $\tilde{\mathbf{K}}$ the convergence condition can be simplified as

$$0 < \mathbf{u}^T \mathbf{K}_s \mathbf{u} < 2\mathbf{u}^T \tilde{\mathbf{K}} \mathbf{u}, \quad \forall \mathbf{u} \tag{1.5e}$$

A convergence condition similar to Eq.(1.5e) but limited to the subspace of non-singular values of $\tilde{\mathbf{K}}$ holds also for the arc-lenght scheme [32] that, like for the load controlled case, is as faster as

$$\mathbf{u}^T \mathbf{K}_s \mathbf{u} \approx \mathbf{u}^T \tilde{\mathbf{K}} \mathbf{u}, \quad \forall \mathbf{u} \tag{1.5f}$$

and it converges in a single iteration when $\mathbf{K}_s = \tilde{\mathbf{K}}$ because of the linearity of Eq.(1.5b).

The arc-length scheme provides a simple way to overcome limit points because $\tilde{\mathbf{J}}$ is not singular even when $\tilde{\mathbf{K}}$ is singular. The convergence is, however, strongly affected by the variables chosen to describe the problem since a smoother representation of the equilibrium path makes it easy to fulfil the condition (1.5f) allowing large steps and few loops. In the following it will be shown that this desirable behaviour occurs in the case of a mixed description while the displacement one, for any FE model, is affected by an *extrapolation locking* that could produce a pathological reduction in the step size (increase in iterations) and in some cases a loss of convergence.

1.2.3 Koiter method

The Koiter asymptotic approach, derived as a finite element implementation [6, 35, 37, 38, 39, 40, 41, 42, 43, 44, 45] of the Koiter theory of elastic stability [46] provides an effective and reliable strategy for predicting the initial post-critical behaviour in both cases of limit or bifurcation points and makes the imperfection sensitivity analysis easy and affordable [5, 34]. The solution process is based on a third order Taylor expansion of Eq.(1.1), in terms of load factor λ and modal amplitudes ξ_i. The steps of the algorithm are

1. The *fundamental path* is obtained as a linear extrapolation

$$\mathbf{u}^f[\lambda] := \mathbf{u}_0 + \lambda \hat{\mathbf{u}} \tag{1.6a}$$

where the initial path tangent $\hat{\mathbf{u}}$ is a solution of the linear system. Letting $\hat{u} := \mathbf{N}_u \hat{\mathbf{u}}$

$$(\Phi''[u_0]\hat{u} - p)\delta u = 0, \ \forall \delta u \quad \Rightarrow \quad \mathbf{K}_0 \, \hat{\mathbf{u}} = \hat{\mathbf{p}} \ , \ \mathbf{K}_0 := \mathbf{K}[\mathbf{u}_0] \tag{1.6b}$$

2. A cluster of *buckling loads* λ_i, $i = 1 \cdots m$ and associated *buckling modes* $\dot{v}_i := \mathbf{N}_u \dot{\mathbf{v}}_i$, are obtained along the extrapolated $\mathbf{u}^f[\lambda]$ from the critical condition

$$\Phi''[u_f[\lambda]]\dot{v}_i \delta u \equiv \delta \mathbf{u}^T \mathbf{K}[\lambda] \dot{\mathbf{v}}_i = 0 \quad i = 1 \cdots m \quad \forall \delta \mathbf{u} \tag{1.6c}$$

Eq.(1.6c) defines the following nonlinear eigenvalue problem

$$\mathbf{K}[\lambda_i]\,\dot{\mathbf{v}}_i = \mathbf{0} \;\;,\;\; \mathbf{K}[\lambda] \equiv \mathbf{K}[\mathbf{u}_0 + \lambda\,\hat{\mathbf{u}}] \tag{1.6d}$$

that, in the multi-modal buckling case, is usually simplified by means of a linearisation near $(\mathbf{u}_b, \lambda_b)$ [37],

$$\Phi''[u_f[\lambda]]\dot{v}_i\delta u \approx (\Phi''_b + (\lambda - \lambda_b)\Phi'''_b\hat{u})\dot{v}_i\delta u \tag{1.6e}$$

where λ_b is a reference value for the cluster, the subscript "b" denotes quantities evaluated at $\mathbf{u}_b \equiv \mathbf{u}^f[\lambda_b]$ and, letting δ_{ij} the Kronecker symbol, the following normalization is used

$$\Phi'''_b\hat{u}\dot{v}_i\dot{v}_j = -\delta_{ij}. \tag{1.6f}$$

In the following, $\mathcal{V} := \{\dot{\mathbf{v}} = \sum_{i=1}^{m}\xi_i\dot{\mathbf{v}}_i\}$ will denote the subspace spanned by the buckling modes and $\mathcal{W} := \{w := \mathbf{N}_u\mathbf{w} : \Phi'''_b\hat{u}\dot{v}_i w = 0\,,\; i = 1\cdots m\}$ is its orthogonal complement.

3. The asymptotic approximation for the required path is defined by the expansion

$$\mathbf{u}[\lambda, \xi_k] := \lambda\hat{\mathbf{u}} + \sum_{i=1}^{m}\xi_i\dot{\mathbf{v}}_i + \frac{1}{2}\sum_{i,j=1}^{m}\xi_i\xi_j\mathbf{w}_{ij} + \frac{1}{2}\lambda^2\hat{\hat{\mathbf{w}}} \tag{1.6g}$$

where $\mathbf{w}_{ij}, \hat{\hat{\mathbf{w}}} \in \mathcal{W}$ are quadratic corrections introduced to satisfy the projection of the equilibrium equation (1.1) into $\mathcal{W}$ and obtained by the linear systems

$$\begin{array}{l}\delta\mathbf{w}^T(\mathbf{K}_b\mathbf{w}_{ij} + \mathbf{p}_{ij}) = 0 \\ \delta\mathbf{w}^T(\mathbf{K}_b\hat{\hat{\mathbf{w}}} + \hat{\hat{\mathbf{p}}}) = 0\end{array} \quad , \quad \forall\mathbf{w} \in \mathcal{W} \tag{1.6h}$$

where $\mathbf{K}_b \equiv \mathbf{K}[\lambda_b]$ and vectors $\mathbf{p}_{ij}$ and $\hat{\hat{\mathbf{p}}}$ are defined by the energy equivalence

$$\delta\mathbf{w}^T\mathbf{p}_{ij} = \Phi'''_b\dot{v}_j\dot{v}_j\,\delta w, \quad \delta\mathbf{w}^T\hat{\hat{\mathbf{p}}} = \Phi'''_b\hat{u}^2\,\delta w$$

4. The following energy terms are computed for $i, j, k = 1\cdots m$:

$$\begin{aligned}
\mathcal{A}_{ijk} &= \Phi'''_b\dot{v}_i\dot{v}_j\dot{v}_k \\
\mathcal{B}_{00ik} &= \Phi''''_b\hat{u}^2\dot{v}_i\dot{v}_k - \Phi''_b\hat{\hat{w}}w_{ik} \\
\mathcal{B}_{0ijk} &= \Phi''''_b\hat{u}\dot{v}_i\dot{v}_j\dot{v}_k \\
\mathcal{B}_{ijhk} &= \Phi''''_b\dot{v}_i\dot{v}_j\dot{v}_h\dot{v}_k - \Phi''_b(w_{ij}w_{hk} + w_{ih}w_{jk} + w_{ik}w_{jh}) \\
\mathcal{C}_{ik} &= \Phi''_b\hat{\hat{w}}w_{ik} \\
\mu_k[\lambda] &= \frac{1}{2}\lambda^2\Phi'''_b\hat{u}^2\dot{v}_k + \frac{1}{6}\lambda^2(\lambda_b - 3\lambda)\Phi''''_b\hat{u}^3\dot{v}_k
\end{aligned} \tag{1.6i}$$

5. The equilibrium path is obtained by projecting the equilibrium equation (1.1) into $\mathcal{V}$ and assuming a coherent Taylor expansion in λ and ξ_i

$$\mu_k[\lambda]+(\lambda_k-\lambda)\xi_k-\lambda_b(\lambda-\frac{\lambda_b}{2})\sum_{i=1}^{m}\xi_i\mathcal{C}_{ik}+\frac{1}{2}\sum_{i,j=1}^{m}\xi_i\xi_j\mathcal{A}_{ijk}+\frac{1}{2}(\lambda-\lambda_b)^2\sum_{i=1}^{m}\xi_i\mathcal{B}_{00ik}$$
$$+\frac{1}{2}(\lambda-\lambda_b)\sum_{i,j=1}^{m}\xi_i\xi_j\mathcal{B}_{0ijk}+\frac{1}{6}\sum_{i,j,h=1}^{m}\xi_i\xi_j\xi_h\mathcal{B}_{ijhk}=0,\quad k=1\cdots m \quad (1.6j)$$

The equations (1.6j) are an algebraic nonlinear system of m equations in the $m+1$ variables λ, $\xi_1\cdots\xi_m$, with known coefficients and solved using a path–following algorithm.

Remarks on Koiter analysis.

Asymptotic analysis uses fourth order variations of the strain energy in an extrapolated bifurcation point and requires fourth order accuracy to be guaranteed. In the past, much effort has been devoted to developing geometrically exact structural models [14, 34, 15]. These models however use 3D finite rotations and consequently they have complex and expensive strain energy variations. Also, being based on the fundamental path extrapolation, the accuracy of the method is very sensitive to the format used in the problem description. Both these problems are solved naturally when using a mixed solid element which, furthermore, improves the computational efficiency and accuracy as shown in the next sections.

1.3 The solid finite element

In this section, two equivalent descriptions, one in stresses and displacements called *mixed description* based on the Hellinger-Reissner functional and another, in displacement variables only, called *displacement description*, are derived for the mixed Pian and Tong finite element [2]. The use of the same interpolations makes it possible to directly compare the different formats maintaining the same discrete approximation. Obviously the displacement description is natural when displacement based finite elements are employed. The dramatic improvement in efficiency due to the joint use of a solid element and mixed description in Koiter analysis is also discussed.

1.3.1 Solid element equations in convective coordinates

We consider a solid finite element and denote with $\boldsymbol{\zeta}=\{\zeta^1,\zeta^2,\zeta^3\}$ the convective coordinates used to express the FE interpolation. The initial configuration, assumed as reference, is described by the position vector $\mathbf{X}[\boldsymbol{\zeta}]$ while $\mathbf{x}[\boldsymbol{\zeta}]$ represents the same position in the current configuration. They are related by the

transformation

$$\mathbf{x}[\boldsymbol{\zeta}] = \mathbf{X}[\boldsymbol{\zeta}] + \mathbf{d}[\boldsymbol{\zeta}] \tag{1.7}$$

where $\mathbf{d}[\boldsymbol{\zeta}]$ is the displacement field. The covariant (or convected) base vectors are obtained by partial derivatives of the position vectors with respect to the convective coordinates as $\mathbf{G}_i = \mathbf{X}_{,i}$ where the comma followed by i denotes differentiation with respect to ζ^i. The contravariant base vectors are defined by the orthonormality conditions $\mathbf{G}_i \cdot \mathbf{G}^j = \delta_i^j$ where δ_i^j is the Kronecker symbol and a dot denotes the scalar product. Adopting the convention of summing on repeated indexes the Green-Lagrange strain measure in covariant components becomes

$$\boldsymbol{\varepsilon} = \bar{\varepsilon}_{ij} \left(\mathbf{G}^i \otimes \mathbf{G}^j \right) \quad \text{with} \quad \bar{\varepsilon}_{ij} = \frac{1}{2} \left(\mathbf{X}_{,i} \cdot \mathbf{d}_{,j} + \mathbf{d}_{,i} \cdot \mathbf{X}_{,j} + \mathbf{d}_{,i} \cdot \mathbf{d}_{,j} \right) \tag{1.8}$$

The second Piola-Kirchoff stress tensor in contravariant components is

$$\boldsymbol{\sigma} = \bar{\sigma}^{ij} \left(\mathbf{G}_i \otimes \mathbf{G}_j \right) \tag{1.9}$$

Finally the constitutive law is assumed to be linear as $\boldsymbol{\sigma} = \mathbf{C}\boldsymbol{\varepsilon}$ with the elastic tensor $\mathbf{C}$ that, assuming an isotropic and homogeneous material, is expressed in the fixed global orthonormal reference frame $\{\mathbf{e}_1, \mathbf{e}_2, \mathbf{e}_3\}$. Both $\boldsymbol{\sigma}$ and $\boldsymbol{\varepsilon}$ can be expressed in the fixed system in terms of the so-called *physical components*. For the stress we have

$$\boldsymbol{\sigma} = \sigma^{ij} \mathbf{e}_i \otimes \mathbf{e}_j = \bar{\sigma}^{ij} \left(\mathbf{G}_i \otimes \mathbf{G}_j \right) \tag{1.10}$$

that exploiting the relation $\mathbf{G}_i \cdot \mathbf{G}^j = \delta_i^j$ furnish

$$\sigma^{rs} = \bar{\sigma}^{ij} t_i^r t_j^s \quad \text{with} \quad t_i^r = (\mathbf{e}^r \cdot \mathbf{G}_i) = \frac{\partial X^r}{\partial \zeta^i} \tag{1.11}$$

or in matrix format by collecting the components of t_i^r in the Jacobiam matrix $\mathbf{J}_e$ we obtain $\boldsymbol{\sigma} = \mathbf{J}_e \bar{\boldsymbol{\sigma}} \mathbf{J}_e^T$. By adopting as usual a Voigt notation, we can express stress and strain tensors in a vector form

$$\boldsymbol{\varepsilon} = \left[\varepsilon_{11}, \varepsilon_{22}, \varepsilon_{33}, 2\varepsilon_{23}, 2\varepsilon_{13}, 2\varepsilon_{12} \right]^T, \quad \boldsymbol{\sigma} = \left[\sigma_{11}, \sigma_{22}, \sigma_{33}, \sigma_{23}, \sigma_{13}, \sigma_{12} \right]^T \tag{1.12}$$

where the same symbol is used to denote both quantities in Voight or tensor notation and we have

$$\boldsymbol{\sigma} = \mathbf{T}_\sigma \bar{\boldsymbol{\sigma}}, \qquad \boldsymbol{\varepsilon} = \mathbf{T}_\sigma^{-T} \bar{\boldsymbol{\varepsilon}} \tag{1.13}$$

where $\mathbf{T}_\sigma$ is defined by Eq.(1.11).

1.3.2 The finite element interpolation

The position vector of a point inside the element and its displacement are interpolated, using a trilinear 8 nodes hexahedron, as

$$\mathbf{X}[\boldsymbol{\zeta}] = \mathbf{N}_d[\boldsymbol{\zeta}] \mathbf{X}_e \quad , \quad \mathbf{d}[\boldsymbol{\zeta}] = \mathbf{N}_d[\boldsymbol{\zeta}] \mathbf{d}_e \tag{1.14a}$$

where vectors $\mathbf{d}_e$ and $\mathbf{X}_e$ collect the element nodal displacements and coordinates and matrix $\mathbf{N}_d[\boldsymbol{\zeta}]$ the trilinear interpolation functions. The Green-Lagrange strain components are obtained from Eq.(1.8) as

$$\bar{\boldsymbol{\varepsilon}} = \left(\boldsymbol{\mathcal{L}}[\boldsymbol{\zeta}] + \frac{1}{2}\boldsymbol{\mathcal{Q}}[\boldsymbol{\zeta}, \mathbf{d}_e] \right) \mathbf{d}_e, \tag{1.14b}$$

where matrices $\boldsymbol{\mathcal{L}}$ and $\boldsymbol{\mathcal{Q}}$ are so defined

$$\boldsymbol{\mathcal{L}}[\boldsymbol{\zeta}] \equiv \begin{bmatrix} \mathbf{G}_1^T \mathbf{N}_{d,1} \\ \mathbf{G}_2^T \mathbf{N}_{d,2} \\ \mathbf{G}_3^T \mathbf{N}_{d,3} \\ \mathbf{G}_3^T \mathbf{N}_{d,2} + \mathbf{G}_2^T \mathbf{N}_{d,3} \\ \mathbf{G}_1^T \mathbf{N}_{d,3} + \mathbf{G}_3^T \mathbf{N}_{d,1} \\ \mathbf{G}_1^T \mathbf{N}_{d,2} + \mathbf{G}_2^T \mathbf{N}_{d,1} \end{bmatrix}, \quad \boldsymbol{\mathcal{Q}}[\boldsymbol{\zeta}, \mathbf{d}_e] \equiv \begin{bmatrix} \mathbf{d}_e^T \mathbf{N}_{d,1}^T \mathbf{N}_{d,1} \\ \mathbf{d}_e^T \mathbf{N}_{d,2}^T \mathbf{N}_{d,2} \\ \mathbf{d}_e^T \mathbf{N}_{d,3}^T \mathbf{N}_{d,3} \\ \mathbf{d}_e^T (\mathbf{N}_{d,3}^T \mathbf{N}_{d,2} + \mathbf{N}_{d,2}^T \mathbf{N}_{d,3}) \\ \mathbf{d}_e^T (\mathbf{N}_{d,1}^T \mathbf{N}_{d,3} + \mathbf{N}_{d,3}^T \mathbf{N}_{d,1}) \\ \mathbf{d}_e^T (\mathbf{N}_{d,1}^T \mathbf{N}_{d,2} + \mathbf{N}_{d,2}^T \mathbf{N}_{d,1}) \end{bmatrix} \tag{1.14c}$$

and, from now on, the dependence on $\boldsymbol{\zeta}$ is omitted to simplify the notation. Note that the Assumed Natural Strain techniques can be applied to Eq.(1.14) in order to improve the element performance for curved shells (see [10, 16]) simply changing the definition of matrices $\boldsymbol{\mathcal{L}}[\boldsymbol{\zeta}]$ and $\boldsymbol{\mathcal{Q}}[\boldsymbol{\zeta}, \mathbf{d}_e]$ without affecting the format of the equations.

For the contravariant stress components we use the "optimal" interpolation proposed by Pian and Tong [2, 21] defined as

$$\bar{\boldsymbol{\sigma}}[\boldsymbol{\zeta}] = \mathbf{N}_\sigma[\boldsymbol{\zeta}] \boldsymbol{\beta}_e \tag{1.14d}$$

where $\boldsymbol{\beta}_e$ collects the 18 stress parameters and the interpolation functions $\mathbf{N}_\sigma[\boldsymbol{\zeta}]$ are given in [2, 21]. The FE defined by Eqs (1.14) is called PT18β. Finally we use Eq.(1.13) to obtain the Cartesian components with $\mathbf{T}_\sigma$ and its inverse evaluated for $\boldsymbol{\zeta} = \mathbf{0}$.

1.3.3 The Mixed finite element strain energy

The strain energy is expressed as a sum of element contributions $\Phi[u] \equiv \sum_e \Phi_e[u]$. Making V_e the finite element volume and using the interpolations defined above, we obtain

$$\begin{aligned} \Phi_e[u] &\equiv \int_{\Omega_e} \left(\boldsymbol{\sigma}^T \boldsymbol{\varepsilon} - \frac{1}{2} \boldsymbol{\sigma}^T \mathbf{C}^{-1} \boldsymbol{\sigma} \right) dV_e \\ &= \boldsymbol{\beta}_e^T (\mathbf{L}_e + \frac{1}{2}\mathbf{Q}_e[\mathbf{d}_e]) \mathbf{d}_e - \frac{1}{2} \boldsymbol{\beta}_e^T \mathbf{H}_e \boldsymbol{\beta}_e \end{aligned} \quad \text{with} \quad \begin{cases} \mathbf{H}_e \equiv \displaystyle\int_{\Omega_e} \mathbf{N}_\sigma^T \mathbf{T}_\sigma^T \mathbf{C}^{-1} \mathbf{T}_\sigma \mathbf{N}_\sigma dV_e \\ \mathbf{L}_e \equiv \displaystyle\int_{\Omega_e} \mathbf{N}_\sigma^T \boldsymbol{\mathcal{L}}[\boldsymbol{\zeta}] dV_e \\ \mathbf{Q}_e \equiv \displaystyle\int_{\Omega_e} \mathbf{N}_\sigma^T \boldsymbol{\mathcal{Q}}[\boldsymbol{\zeta}, \mathbf{d}[\boldsymbol{\zeta}]] dV_e \end{cases} \tag{1.15}$$

where $dV_e = \det[\mathbf{J}_e[\mathbf{0}]]d\zeta_1 d\zeta_2 d\zeta_3$ and the integrals are evaluated with $2 \times 2 \times 2$ Gauss points. Note that exploiting the linear dependence of $\mathbf{Q}_e[\mathbf{d}_e]$ from $\mathbf{d}_e$ and its symmetry we have

$$\begin{aligned} &\mathbf{Q}_e[\mathbf{d}_{e1}]\mathbf{d}_{e2} = \mathbf{Q}_e[\mathbf{d}_{e2}]\mathbf{d}_{e1}, \quad \forall \mathbf{d}_{e1}, \mathbf{d}_{e2} \\ &\boldsymbol{\beta}_e^T \mathbf{Q}_e[\mathbf{d}_e]\mathbf{d}_e = \mathbf{d}_e^T \boldsymbol{\Gamma}_e[\boldsymbol{\beta}_e]\mathbf{d}_e \quad \text{with} \quad \boldsymbol{\Gamma}_e[\boldsymbol{\beta}_e] \equiv \sum_{i,j=1}^{3} \int_{\Omega_e} \bar{\sigma}^{ij} \mathbf{N}_{d,i}^T \mathbf{N}_{d,j} \; dV_e \end{aligned} \tag{1.16}$$

Strain energy variations of the PT18β element in mixed description.

Eq.(1.15) allows the expression of the strain energy as an algebraic nonlinear function of the element vector related to the vector $\mathbf{u}$, collecting all the parameters of the FE assemblage, through the relation

$$\mathbf{u}_e \equiv \begin{bmatrix} \boldsymbol{\beta}_e \\ \mathbf{d}_e \end{bmatrix} = \boldsymbol{\mathcal{A}}_e \mathbf{u} \tag{1.17}$$

where matrix $\boldsymbol{\mathcal{A}}_e$ contains the link between the elements. Furthermore we denote with $\delta\mathbf{u}_{ei} = \{\delta\boldsymbol{\beta}_{ei}, \delta\mathbf{d}_{ei}\}$ the element vector corresponding to the variation $\delta\mathbf{u}_i$.

The first variation of the strain energy (1.15) is then

$$\Phi'_e \delta u_1 = \begin{bmatrix} \delta\boldsymbol{\beta}_{e1} \\ \delta\mathbf{d}_{e1} \end{bmatrix}^T \begin{bmatrix} \mathbf{s}_{e\beta} \\ \mathbf{s}_{ed} \end{bmatrix} \quad \text{with} \quad \begin{cases} \mathbf{s}_{e\beta} \equiv (\mathbf{L}_e + \dfrac{1}{2}\mathbf{Q}_e[\mathbf{d}_e])\mathbf{d}_e - \mathbf{H}_e\boldsymbol{\beta}_e \\ \mathbf{s}_{ed} \equiv \mathbf{B}_e[\mathbf{d}_e]^T \boldsymbol{\beta}_e \end{cases} \tag{1.18a}$$

and $\mathbf{B}_e[\mathbf{d}_e] \equiv \mathbf{L}_e + \mathbf{Q}_e[\mathbf{d}_e]$.

In the same way and exploiting the first of (1.16) the second strain energy variation is

$$\begin{aligned} \Phi''_e \delta u_1 \delta u_2 &= \begin{bmatrix} \delta\boldsymbol{\beta}_{e1} \\ \delta\mathbf{d}_{e1} \end{bmatrix}^T \begin{bmatrix} -\mathbf{H}_e & \mathbf{B}_e[\mathbf{d}_e] \\ \mathbf{B}_e[\mathbf{d}_e]^T & \boldsymbol{\Gamma}_e[\boldsymbol{\beta}_e] \end{bmatrix} \begin{bmatrix} \delta\boldsymbol{\beta}_{e2} \\ \delta\mathbf{d}_{e2} \end{bmatrix} \\ &= \delta\mathbf{u}_{e1}^T (\mathbf{K}_{0e} + \mathbf{K}_{1e}[\mathbf{u}_e])\delta\mathbf{u}_{e2} \end{aligned} \tag{1.18b}$$

that provides the element tangent stiffness matrix $\mathbf{K}_{me}[\mathbf{u}_e] = \mathbf{K}_{0e} + \mathbf{K}_{1e}[\mathbf{u}_e]$ as a sum of the linear elastic contribution $\mathbf{K}_{0e}$ and the geometric matrix $\mathbf{K}_{1e}[\mathbf{u}_e]$ implicitly defined in Eq.(1.18b). Using a similar approach the third variation becomes

$$\begin{aligned} \Phi'''_e \delta u_1 \delta u_2 \delta u_3 &= \left\{ \delta\boldsymbol{\beta}_{e1}^T \mathbf{Q}[\delta\mathbf{d}_{e3}]\delta\mathbf{d}_{e2} + \delta\boldsymbol{\beta}_{e2}^T \mathbf{Q}[\delta\mathbf{d}_{e3}]\delta\mathbf{d}_{e1} + \delta\boldsymbol{\beta}_{e3}^T \mathbf{Q}[\delta\mathbf{d}_{e2}]\delta\mathbf{d}_{e1} \right\} \\ &= \begin{bmatrix} \delta\boldsymbol{\beta}_{e1} \\ \delta\mathbf{d}_{e1} \end{bmatrix}^T \begin{bmatrix} \mathbf{s}''_{e\beta}[\delta\mathbf{d}_{e2}, \delta\mathbf{d}_{e3}] \\ \mathbf{s}''_{e\beta}[\delta\mathbf{d}_{e2}, \delta\mathbf{d}_{e3}] \end{bmatrix} \end{aligned} \tag{1.18c}$$

where

$$\begin{cases} \mathbf{s}''_{e\beta}[\delta\mathbf{d}_{e2}, \delta\mathbf{d}_{e3}] \equiv \mathbf{Q}[\delta\mathbf{d}_{e3}]\delta\mathbf{d}_{e2} \\ \mathbf{s}''_{ed}[\delta\mathbf{d}_{e2}, \delta\mathbf{d}_{e3}] \equiv \mathbf{Q}[\delta\mathbf{d}_{e3}]^T\delta\boldsymbol{\beta}_{e2} + \mathbf{Q}[\delta\mathbf{d}_{e2}]^T\delta\boldsymbol{\beta}_{e3} \end{cases} \tag{1.18d}$$

Finally Eq.(1.17) allow the evaluation, for each element vector $\mathbf{y}_e$ and matrix $\mathbf{Y}_e$ the quantities of the whole assemblage

$$\mathbf{y} = \sum_e \boldsymbol{\mathcal{A}}_e^T \mathbf{y}_e, \quad \mathbf{Y} = \sum_e \boldsymbol{\mathcal{A}}_e^T \mathbf{Y}_e \boldsymbol{\mathcal{A}}_e. \tag{1.19}$$

In particular, from the assemblages of vector $\mathbf{s}''_e$ we obtain vectors $\mathbf{p}_{ij}$ defined in Eq.(1.6h). Obviously, scalar quantities are directly evaluated as sums of local element contributions.

1.3.4 The displacement description of the PT18β element

The element can also be described in a displacement format by requiring that the discrete form of the constitutive laws is "a priori" satisfied. As in the present FE model the stress variables are locally defined at the element level, we have

$$\boldsymbol{\beta}_e[\mathbf{d}_e] = \mathbf{H}_e^{-1}(\mathbf{L}_e + \frac{1}{2}\mathbf{Q}_e[\mathbf{d}_e])\mathbf{d}_e \tag{1.20}$$

where, to highlight that in the displacement format the stresses are not independent variables, the dependence from $\mathbf{d}_e$ is explicitly reported. Substituting Eq.(1.20) in Eq.(1.15) we obtain the *displacement description* of the element strain energy

$$\Phi_e = \frac{1}{2}\left\{\mathbf{d}_e^T(\mathbf{L}_e + \frac{1}{2}\mathbf{Q}_e[\mathbf{d}_e])^T\mathbf{H}_e^{-1}(\mathbf{L}_e + \frac{1}{2}\mathbf{Q}_e[\mathbf{d}_e])\mathbf{d}_e\right\} \tag{1.21}$$

that has a 4th order dependence on the displacement variables only.

Note how an expression similar to Eq.(1.21), is obtained by using any other displacement based element when the Green-Lagrange strain tensor is employed. In this chapter, the use the displacement description of the PT18β element is preferred in order to have exactly the same discrete approximation for both the descriptions. Note that the finite element is the same but the format of the system of equations changes. This allows us to focus on how the problem description affects its numerical solution in large deformation problems (see also [32, 33]) and then to show and explain the better performance of the use of a mixed description (and so mixed element).

Strain energy variations of the PT18β element in displacement description.

For the displacement description the configuration variables are the displacements only and $\delta\mathbf{u}_{ei} = \delta\mathbf{d}_{ei}$. The first variation of Eq.(1.21) becomes

$$\Phi'_e\delta u_1 = \delta\mathbf{d}_{e1}^T\mathbf{s}_e[\mathbf{d}_e] \quad \text{whit} \quad \mathbf{s}_e[\mathbf{d}_e] \equiv \mathbf{B}_e^T[\mathbf{d}_e]\boldsymbol{\beta}_e[\mathbf{d}_e] \tag{1.22a}$$

where $\boldsymbol{\beta}_e[\mathbf{d}_e]$ is defined in Eq.(1.20). In the same way the second strain energy variation is

$$\Phi''_e \delta u_1 \delta u_2 = \delta \mathbf{d}_{e1}^T \left\{ \mathbf{B}_e^T[\mathbf{d}_e] \mathbf{H}_e^{-1} \mathbf{B}_e[\mathbf{d}_e] + \boldsymbol{\Gamma}[\boldsymbol{\beta}_e[\mathbf{d}_e]] \right\} \delta \mathbf{d}_{e2} \tag{1.22b}$$

where the tangent stiffness matrix has a second order dependence on $\mathbf{d}_e$

$$\mathbf{K}_{de} = \mathbf{K}_{0e} + \mathbf{K}_{1e}[\mathbf{d}_e] + \mathbf{K}_{2e}[\mathbf{d}_e, \mathbf{d}_e]. \tag{1.22c}$$

The third variation of the strain energy becomes

$$\begin{aligned} \Phi''' \delta u_1 \delta u_2 \delta u_3 &= \left\{ \delta \boldsymbol{\beta}_{e1}^T[\mathbf{d}_e] \mathbf{Q}[\delta \mathbf{d}_{e3}] \delta \mathbf{d}_{e2} + \delta \boldsymbol{\beta}_{e2}^T[\mathbf{d}_e] \mathbf{Q}[\delta \mathbf{d}_{e3}] \delta \mathbf{d}_{e1} + \delta \boldsymbol{\beta}_{e3}^T[\mathbf{d}_e] \mathbf{Q}[\delta \mathbf{d}_{e2}] \delta \mathbf{d}_{e1} \right\} \\ &= \delta \mathbf{d}_{e1}^T \mathbf{s}''[\delta \mathbf{d}_{e2}, \delta \mathbf{d}_{e3}] \end{aligned} \tag{1.22d}$$

where

$$\mathbf{s}''[\delta \mathbf{d}_{e2}, \delta \mathbf{d}_{e3}] \equiv \mathbf{Q}[\delta \mathbf{d}_{e3}]^T \delta \boldsymbol{\beta}_{e2}^T[\mathbf{d}_e] + \mathbf{Q}[\delta \mathbf{d}_{e2}]^T \delta \boldsymbol{\beta}_{e3}^T[\mathbf{d}_e] + (\mathbf{L}_e + \mathbf{Q}_e[\mathbf{d}_e])^T \mathbf{H}_e^{-1} \mathbf{Q}[\delta \mathbf{d}_{e3}] \delta \mathbf{d}_{e2}$$

and the quantities $\delta \boldsymbol{\beta}_{ei}^T[\mathbf{d}_e] \equiv \mathbf{H}_e^{-1} \mathbf{B}_e[\mathbf{d}_e] \delta \mathbf{d}_{ei},\ i = 1..3$, that are the variation in the stresses obtained from the constitutive equation (1.20) with respect to the displacements, are introduced.

Finally it is worth noting that in this case the 4th variation of the strain energy is not zero and we have

$$\begin{aligned} \Phi'''' \delta u_1 \delta u_2 \delta u_3 \delta u_4 = \{ \quad & \delta \mathbf{d}_{e1}^T \mathbf{Q}^T[\delta \mathbf{d}_{e4}] \mathbf{H}_e^{-1} \mathbf{Q}[\delta \mathbf{d}_{e3}] \delta \mathbf{d}_{e2} \\ & + \delta \mathbf{d}_{e2}^T \mathbf{Q}^T[\delta \mathbf{d}_{e4}] \mathbf{H}_e^{-1} \mathbf{Q}[\delta \mathbf{d}_{e3}] \delta \mathbf{d}_{e1} \\ & + \delta \mathbf{d}_{e3}^T \mathbf{Q}^T[\delta \mathbf{d}_{e4}] \mathbf{H}_e^{-1} \mathbf{Q}[\delta \mathbf{d}_{e2}] \delta \mathbf{d}_{e1} \} \end{aligned} \tag{1.22e}$$

1.3.5 Advantages of mixed solid finite elements in path-following and asymptotic analysis of slender structures

FE models directly derived from the 3D continuum using the Green strain measure have a low order dependence on the strain energy from the discrete FE parameters: $3rd$ and $4th$ order for mixed and displacement respectively. On the contrary geometrically exact shell and beam models [14, 15] or those based on co-rotational approaches [34, 5, 47], explicitly make use of the rotation tensor and its highly nonlinear representation. This implies that the strain energy is infinitely differentiable with respect to its parameters and leads to very complex expressions for the energy variations with a high computational burden of path following and much more of asymptotic analyses. In this last case the high order strain energy variations become so complex that often "ad hoc" assumptions are required to make the solution process effective (see section 4.3 of [34]). The consequence is that the fewer global degrees of freedom that could be employed using a shell FE

model do not necessarily imply a lesser computational cost as it depends, from the others, on the cost of evaluation of the strain energy variations. On the contrary for solid finite elements the strain energy, in both displacement and mixed form, has the lowest polynomial dependence on the corresponding discrete parameters and in particular in the mixed format of Eq.(1.15) has just one order more than in the linear elastic case. It implies the zeroing of all the fourth order strain energy variations required by the Koiter analysis with important advantages in terms of both computations and coherence of the method.

Simplifications and improvements in Koiter analysis using mixed solid elements.

The low order polynomial dependence of the strain energy on the parameters produces a first important simplification and improvement in the evaluation of the bifurcation points. With the usual adopted linear extrapolation in λ of the fundamental path $\mathbf{u}_f[\lambda] = \lambda\hat{\mathbf{u}}$ it is convenient to expand the bifurcation condition in Eq.(1.6d) from the origin as

$$\Phi''[u_f[\lambda]]\dot{v}_i\delta u = (\Phi_0'' + \lambda\Phi_0'''\hat{u} + \frac{1}{2}\lambda^2\Phi_0''''\hat{u}^2)\dot{v}_i\delta u \tag{1.23}$$

Note how the Taylor expansion in Eq.(1.23) is exact, due to the zeroing of all the high order energy terms. In particular the mixed expression of the buckling condition is automatically linear due to the zeroing of the 4th variation

$$\mathbf{K}_m[\lambda] = \mathbf{K}_0 + \lambda\mathbf{K}_1[\hat{\mathbf{u}}] \tag{1.24}$$

where $\mathbf{K}_0$ and $\mathbf{K}_1$ are obtained from assemblages of the element matrices in Eq.(1.18b). For the displacement description the equivalent bifurcation problem assumes the following form ($\hat{\mathbf{u}} = \hat{\mathbf{d}}$)

$$\mathbf{K}_d[\lambda] = \mathbf{K}_0 + \lambda\mathbf{K}_1[\hat{\mathbf{d}}] + \frac{1}{2}\lambda^2\mathbf{K}_2[\hat{\mathbf{d}}, \hat{\mathbf{d}}] \tag{1.25}$$

where again $\mathbf{K}_0$, $\mathbf{K}_1$ and $\mathbf{K}_2$ are obtained as assemblages of the element matrices reported in (1.22b).

To have an "exact" buckling condition independently of the closeness of the buckling loads is particularly important in the asymptotic method. It makes great use of buckling modes and loads and so their accurate evaluation strongly affects the quality of the complete equilibrium path reconstruction. This is possible in the case of solid finite elements while, in the general, due to the linearization in Eq.(1.6e) the accuracy depends on the magnitude of $(\lambda_i - \lambda_b)$. Furthermore in employing a mixed description the bifurcation condition is exactly a simple linear eigenvalue problem which provides the m bifurcation loads and modes naturally orthogonalized according to Eq.(1.6f) without any other assumption apart from the linear extrapolation of the fundamental path.

Another great advantage is in the evaluation of all the fourth order coefficients in Eq.(1.6i) that, for mixed solid elements, requires only second variations for their evaluation since the usually very complex fourth order strain energy variations are zero. In particular the energy terms reduce to

$$\begin{aligned}
\mathcal{A}_{ijk} =& \Phi_b''' \dot{v}_i \dot{v}_j \dot{v}_k \\
\mathcal{B}_{00ik} =& -\Phi_b'' \hat{\hat{w}} w_{ik} = -\mathcal{C}_{ik} \\
\mathcal{B}_{0ijk} =& 0 \\
\mathcal{B}_{ijhk} =& -\Phi_b''(w_{ij} w_{hk} + w_{ih} w_{jk} + w_{ik} w_{jh}) \\
\mu_k[\lambda] =& \frac{1}{2}\lambda^2 \Phi_b''' \hat{u}^2 \dot{v}_k
\end{aligned} \tag{1.26}$$

Furthermore the matrices in the bifurcation condition (1.24) and the non-zero strain variations in (1.26) assume simpler and lower cost expressions compared to standard shell elements. This makes the implementation of the asymptotic method very easy and reduces the total cost of the solution process.

However the main advantage in using a mixed formulation is its capability to rectify an important but underhand locking effect, called in [32, 33] *extrapolation locking*. This is deeply discussed in the next section.

1.4 Extrapolation locking and its cure by a mixed format

In this section the better performances of the mixed description in geometrically nonlinear analysis, in terms of robustness, efficiency and, relative to Koiter formulation, also in terms of accuracy, are shown and explained. In this context the displacement description of the problem, whatever the FE and the structural model used, is affected by a pathological *extrapolation locking* phenomenon investigated for the first time for 2D frames in [32, 33].

The displacement format, equivalent to the mixed one in terms of the finite element interpolation, makes it possible to focus the phenomenon in a general context and to highlight its origin.

1.4.1 A simple test

To show the extrapolation locking phenomenon the simple test in Fig.1.1 is considered. It consists of a bar of unitary length constrained with a linear spring on an end. With strain and stress constant along the bar the mixed and displacement functionals are, respectively,

$$\begin{aligned}
\Pi_{HR}[N, u, w] &\equiv N\epsilon[u, w] - \frac{1}{2}\frac{N^2}{EA} + \frac{1}{2}k_w\, w^2 - \lambda(c\, w - u) \\
\Pi[u, w] &\equiv \frac{1}{2}(EA\epsilon[u, w]^2 + k_w\, w^2) - \lambda(c\, w - u)
\end{aligned} \tag{1.27}$$

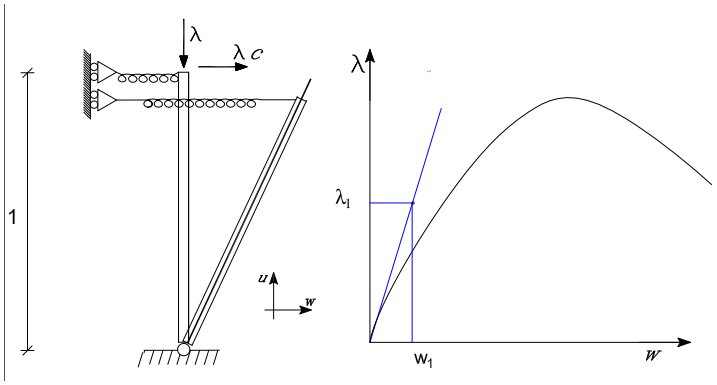

Figure 1.1: A simple test

where N is the axial force of the bar and the corresponding Green-Lagrange axial strain is

$$\epsilon[u,w] = u + \frac{1}{2}(u^2 + w^2)$$

The displacement stiffness matrix, evaluated as the Hessian of the displacement functional with respect to the displacement variables $\mathbf{d} = [u, w]$, becomes

$$\mathbf{K}_d[u,w] = \begin{bmatrix} N_d + EA(1+u)^2 & EA(1+u)\,w \\ EA(1+u)\,w & N_d + k_w + EAw^2 \end{bmatrix} \quad \text{with} \quad N_d = EA\varepsilon[u,w]$$

where N_d represent the axial force function of the displacement components. The mixed stiffness matrix, Hessian of the Hellinger-Reissner functional with respect to the mixed variables $\mathbf{u} = [N, \mathbf{d}]$, is

$$\mathbf{K}_m[N,u,w] = \begin{bmatrix} -\dfrac{1}{EA} & 1+u & w \\ 1+u & N & 0 \\ w & 0 & k_w + N \end{bmatrix}$$

where now N is directly a variable of the problem. Note that from the static condensation of N we obtain from $\mathbf{K}_m$ the same form of matrix $\mathbf{K}_d$ by replacing N_d by N. Starting from the equilibrium point with zero load and displacements we perform a linear extrapolation in λ of the linear elastic solution, $\mathbf{d}_1 = \{u_1, w_1\}$ for the displacement format and $\mathbf{u}_1 = \{N_1, \mathbf{d}_1\}$ for the mixed one, with

$$u_1 = -\frac{\lambda_1}{EA} \quad w_1 = \frac{c\lambda_1}{k_w}$$

the same for both the descriptions and $N_1 = -\lambda_1$ directly extrapolated unlike $N_d[u_1, w_1]$ that is function of the extrapolated displacements

$$N_d[u_1,w_1] = -\lambda_1 + \frac{\lambda_1^2}{2}\left(\frac{1}{EA} + \frac{c^2 EA}{k_w^2}\right).$$

For high values of EA/k_w^2 and also small c, the displacement approach predicts an axial tension instead of the correct axial compression and, as a consequences, a mistakenly overestimated stiffness, in direction w which consequently locks. The same phenomenon typically affects shell problems where the in-plane stiffness plays the role of EA and the flexural stiffness, usually much lower then the first one, the role of k_w. On the contrary extrapolation locking does not affect the mixed format as N_1 is expected to be a good estimate of the true axial force in the deformed configuration (small strain/large deformation hypothesis).

1.4.2 Generalization of the extrapolation problem in displacement format

The effects highlighted for the simple test are now generalized to the solid formulation. The use of a displacement description of a mixed finite element makes the origin of the extrapolation locking phenomenon evident. In order to compare the two formats, note that the stresses $\boldsymbol{\beta}[\mathbf{d}]$ in the displacement format are obtained, as a function of the displacements, from Eq.(1.20), while in the mixed format they are independent variables. Letting $\mathbf{z}_0$ be an equilibrium point we have for both the formats the same displacements and stresses. Performing an extrapolation, for example evaluating $\mathbf{z}_1$ along the linearisation in λ of the equilibrium path starting from $\mathbf{z}_0$, we obtain for the mixed format

$$\begin{bmatrix}\boldsymbol{\beta}_1\\ \mathbf{d}_1\end{bmatrix} = \begin{bmatrix}\boldsymbol{\beta}_0 + \Delta\lambda\hat{\boldsymbol{\beta}}\\ \mathbf{d}_0 + \Delta\lambda\hat{\mathbf{d}}\end{bmatrix} \quad \text{with} \quad \begin{bmatrix}-\mathbf{H} & \mathbf{B}[\mathbf{d}_0]\\ \mathbf{B}[\mathbf{d}_0]^T & \boldsymbol{\Gamma}[\boldsymbol{\beta}_0]\end{bmatrix}\begin{bmatrix}\hat{\boldsymbol{\beta}}\\ \hat{\mathbf{d}}\end{bmatrix} = \begin{bmatrix}\mathbf{0}\\ \hat{\mathbf{p}}\end{bmatrix}$$

so obtaining

$$\hat{\mathbf{d}} = \mathbf{K}_{c0}\mathbf{p} \quad \text{and} \quad \hat{\boldsymbol{\beta}} = \mathbf{H}^{-1}\mathbf{B}[\mathbf{d}_0]\hat{\mathbf{d}}$$

Since $\mathbf{K}_{c0} \equiv \boldsymbol{\Gamma}[\boldsymbol{\beta}_0] + \mathbf{B}[\mathbf{d}_0]^T\mathbf{H}^{-1}\mathbf{B}[\mathbf{d}_0]$ coincides with the stiffness matrix evaluated by the displacement format in the equilibrium point $\mathbf{z}_0$, $\hat{\mathbf{d}}$ is the same for both the formats.

In $\mathbf{z}_1$ we obtain the following stiffness matrices for the two descriptions

$$\mathbf{K}_m[\mathbf{d}_1, \boldsymbol{\beta}_1] = \begin{bmatrix}-\mathbf{H} & \mathbf{B}[\mathbf{d}_1]\\ \mathbf{B}[\mathbf{d}_1] & \boldsymbol{\Gamma}[\boldsymbol{\beta}_1]\end{bmatrix} \quad \mathbf{K}_d[\mathbf{d}_1] = \mathbf{B}[\mathbf{d}_1]^T\mathbf{H}^{-1}\mathbf{B}[\mathbf{d}_1] + \boldsymbol{\Gamma}[\boldsymbol{\beta}[\mathbf{d}_1]] \quad (1.28)$$

where now $\boldsymbol{\Gamma}[\boldsymbol{\beta}_1] \neq \boldsymbol{\Gamma}[\boldsymbol{\beta}[\mathbf{d}_1]]$ with $\boldsymbol{\beta}_1 \neq \boldsymbol{\beta}[\mathbf{d}_1]$. In the mixed case the stresses are directly extrapolated as $\boldsymbol{\beta}_1 = \boldsymbol{\beta}_0 + \Delta\lambda\mathbf{H}^{-1}\mathbf{B}[\mathbf{d}_0]\hat{\mathbf{d}}$ while for the displacement case they are evaluated, according to Eq.(1.20), as

$$\boldsymbol{\beta}_1[\mathbf{d}_1] = \boldsymbol{\beta}_0 + \mathbf{H}^{-1}(\Delta\lambda\mathbf{B}_0\hat{\mathbf{d}} + \frac{\Delta\lambda^2}{2}\mathbf{Q}[\hat{\mathbf{d}}]\hat{\mathbf{d}})$$

A wrong spurious term

$$\Delta\boldsymbol{\beta} = \Delta\lambda^2\frac{1}{2}\mathbf{H}^{-1}\mathbf{Q}[\hat{\mathbf{d}}]\hat{\mathbf{d}}$$

that is the stress produced by the quadratic part of the strain evaluated with a linear extrapolation of the displacement is present in the displacement extrapolation. This strain term has components even in the highest stiffness directions and so the estimated stresses are affected by a great error $\Delta\boldsymbol{\beta}$. The consequence is an overestimated tangent stiffness matrix for the displacement format. This is the same extrapolation locking as previously observed for the simple test. When, as is usual for slender structures, the condition number of $\mathbf{H}$ is high due to very different stiffness ratios (i.e. membrane/flexural) the phenomenon becomes very important and affects the displacement format in the solution strategies of the nonlinear problem. It produces difficulties in convergence in the path following scheme because the overestimated stiffness matrix in the current iteration is far from the secant one and could not fulfil the second part of the convergence condition (1.5e). Koiter analysis furnishes a wrong bifurcation point used by the method to approximate the equilibrium path. On the contrary the mixed extrapolation, directly linearises the stress and it is naturally free from the extrapolation locking.

Mixed vs displacement description in Koiter analysis using 3D solid elements

Recalling that the buckling condition is tested along an extrapolated path, in displacement variables it could be affected by extrapolation locking which produces an overestimated buckling load or loss of bifurcation. The proposed Koiter method uses an asymptotic expansion in an extrapolated point along the linearised fundamental path. For this reason the locking phenomenon previously described can strongly affect its accuracy [33, 15].

To avoid this error a linearized buckling analysis can be performed by zeroing the quadratic part of the strain depending on the extrapolated displacements $\mathbf{Q}_e[\hat{\mathbf{d}}_e] = \mathbf{0}$ (*frozen configuration* hypothesis). This eliminates the extrapolation locking as can be seen in Tab.1.1 where the buckling loads obtained with the displacement (D) and mixed (M) formats are compared with those of the frozen configuration (F) for the Euler beam of Fig.1.6. The comparisons are performed by changing both the aspect ratio $k = (t/\ell)^2$ and the imperfection load amplitude ϵ.

Table 1.1: Buckling analyses for the Euler beam/(exact value for the elastica)

k	$\epsilon = 0.01$	$\epsilon = 0.005$	$\epsilon = 0.001$	for all ϵ	
	D	D	D	F	M
10^4	failed	1.112	1.004	1.001	1.001
10^5	failed	failed	1.040	1.001	1.001
10^6	failed	failed	failed	1.001	1.001
10^7	failed	failed	failed	0.999	0.999

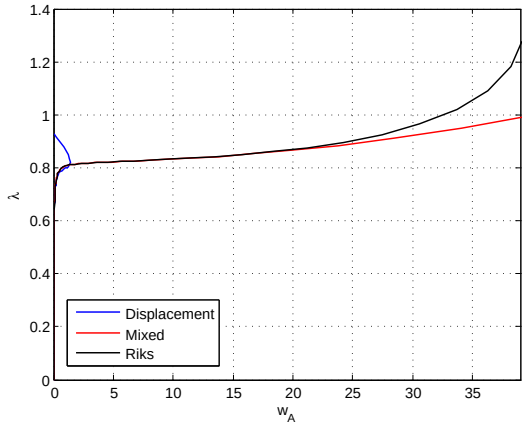

Figure 1.2: Equilibrium path for the Euler beam for $\epsilon = 0.001$ and $k = 10^4$

For this case, which has small pre-critical nonlinearities, it is worth noting that: i) the frozen configuration hypothesis rectifies the locking effect and furnishes accurate results; ii) the displacement description misses the bifurcation point, getting worse with the pre-critical nonlinearity due to the transversal force. Inaccuracy in the bifurcation points obviously leads to a completely wrong equilibrium path estimated by the asymptotic algorithm where, unlike the Riks method, the extrapolation error is not corrected by any iterative scheme. Finally it is important to note that also the energy terms in Eq.(1.6i) and then the estimated asymptotic equilibrium path in Eq.(1.6j) are very sensitive to the extrapolation locking and so, even when the bifurcation point is almost correctly evaluated, the post critical behaviour could be completely wrong when the displacement description is used. On the contrary the mixed description is unaffected by k (see Fig.1.2 and [33]) and the initial post critical path is recovered accurately .

The frozen configuration hypothesis could, however, lead to inaccuracy when the precritical displacements are not negligible, as in the shallow arc reported in Fig.1.3. In this case it is not capable of producing the correct bifurcation load and mode as reported in Tab.1.2 and consequently the energy terms also reported in Tab.1.2, used to estimate the equilibrium path. In Fig.1.4 the equilibrium path recovered by the Koiter mixed formulation is presented and compared with the frozen and the true path following solutions.

Mixed vs displacement description in path-following analysis

In the path-following scheme extrapolation locking occurs at each step and affects both the first extrapolation, used to evaluate the first estimate $\mathbf{z}_1$, and the corrector scheme in Eq.(1.5), which is based on a sequence of linearisations in the current estimates $\mathbf{z}_j$ of the solution. In this case extrapolation locking produces a strong deterioration in the convergence properties of the Newton (Riks) method.

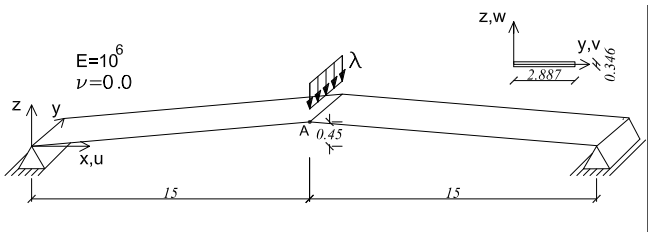

Figure 1.3: Geometry and material properties of the shallow arc

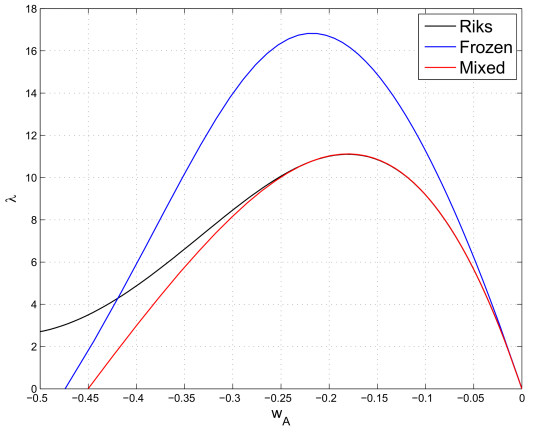

Figure 1.4: Equilibrium path for the shallow arc

Table 1.2: Shallow arc: comparison of relevant energy asymptotic quantities of Eq.(1.6j)

	M	F
λ_1	22.0202	30.6526
λ_2	30.6671	47.0652
$\mathcal{A}_{001}$	0.0196	0.0190
$\mathcal{A}_{111}$	47.9305	182.3644
$\mathcal{B}_{0011}$	-6.32 10^{-4}	0
$\mathcal{B}_{1111}$	8.2117	207.3178

It is useful to show how the two formats update the solution in an iterative Newton scheme. A load controlled case is considered to simplify the notation. The iteration in mixed format is

$$\begin{bmatrix} -\mathbf{H} & \mathbf{B}_j \\ \mathbf{B}_j^T & \mathbf{\Gamma}_j \end{bmatrix} \begin{bmatrix} \dot{\boldsymbol{\beta}} \\ \dot{\mathbf{d}} \end{bmatrix} = - \begin{bmatrix} \boldsymbol{\varepsilon}[\mathbf{d}_j] - \mathbf{H}\boldsymbol{\beta}_j \\ \mathbf{B}_j^T \boldsymbol{\beta}_j - \lambda \mathbf{p} \end{bmatrix} \quad \text{and} \quad \begin{bmatrix} \boldsymbol{\beta}_{j+1} \\ \mathbf{d}_{j+1} \end{bmatrix} = \begin{bmatrix} \boldsymbol{\beta}_j \\ \mathbf{d}_j \end{bmatrix} + \begin{bmatrix} \dot{\boldsymbol{\beta}} \\ \dot{\mathbf{d}} \end{bmatrix} \tag{1.29}$$

where $\mathbf{\Gamma}_j = \mathbf{\Gamma}[\boldsymbol{\beta}_j]$ and $\mathbf{B}_j \equiv \mathbf{B}[\mathbf{d}_j]$. Solving the mixed linear system in Eq.(1.29) we obtain

$$\begin{cases} \mathbf{d}_{j+1} = \mathbf{d}_j - \tilde{\mathbf{K}}_{dj}^{-1} \mathbf{r}_{dj} \\ \boldsymbol{\beta}_{j+1} = \mathbf{H}^{-1}(\boldsymbol{\varepsilon}[\mathbf{d}_j] + \mathbf{B}_j \dot{\mathbf{d}}) \end{cases} \quad \text{where} \quad \tilde{\mathbf{K}}_{dj} = \mathbf{B}_j^T \mathbf{H}^{-1} \mathbf{B}_j + \mathbf{\Gamma}_j \tag{1.30}$$

The same iteration in the displacement case is

$$\begin{cases} \mathbf{d}_{j+1} = \mathbf{d}_j - \mathbf{K}_j^{-1} \mathbf{r}_{dj} \\ \boldsymbol{\beta}[\mathbf{d}_{j+1}] = \mathbf{H}^{-1} \boldsymbol{\varepsilon}[\mathbf{d}_j + \dot{\mathbf{d}}] \end{cases} \quad \text{where} \quad \begin{aligned} \mathbf{K}_j &= \mathbf{B}_j^T \mathbf{H}^{-1} \mathbf{B}_j + \mathbf{\Gamma}[\boldsymbol{\beta}[\mathbf{d}_j]] \\ \boldsymbol{\varepsilon}[\mathbf{d}_{j+1}] &= \boldsymbol{\varepsilon}[\mathbf{d}_j] + \mathbf{B}_j \dot{\mathbf{d}} + \frac{1}{2} \mathbf{Q}[\dot{\mathbf{d}}] \dot{\mathbf{d}} \end{aligned} \tag{1.31}$$

where $\mathbf{r}_{dj} = \mathbf{B}_j^T \mathbf{H}^{-1} \boldsymbol{\varepsilon}[\mathbf{d}_j] - \lambda \mathbf{p}$ is the same for both the approaches and the stresses in the displacement iteration, functions of the displacements, are introduced for an easy comparison with the mixed format.

Eqs.(1.30) and (1.31) show that the only, but important, difference in the two formats consists in the way the stresses are obtained from the current linearisation. The spurious stress term

$$\Delta \boldsymbol{\beta} = \frac{1}{2} \mathbf{H}^{-1} \mathbf{Q}[\dot{\mathbf{d}}] \dot{\mathbf{d}}.$$

due to the extrapolation locking is present in the displacement iteration.

It is important to note that the displacement iterative scheme can be obtained from the mixed one by solving exactly, at each iteration, the constitutive equations. In this way the evolution of the displacement iterative process is forced to satisfy the constitutive constraint at each iteration and this, in general, leads to a deterioration in the convergence properties. On the contrary the mixed format performs a consistent linearisation of all the problem equations and allows the iterations to naturally evolve towards the solution.

The convergence of the Riks scheme is as fast as the iteration and secant stiffness matrix are near and then as $\mathbf{K}[\mathbf{u}]$ slowly changes with $\mathbf{u}$. The similarity of the stiffness matrices in two different points $\mathbf{K}_j \equiv \mathbf{K}[\mathbf{u}_j]$ and $\mathbf{K}_{j+1} \equiv \mathbf{K}[\mathbf{u}_{j+1}]$, according to Eq.(1.5f), is evaluated by the difference

$$\Delta k[\mathbf{u}] \equiv \mathbf{u}^T (\mathbf{K}_{j+1} - \mathbf{K}_j) \mathbf{u} \quad \forall \mathbf{u} : \mathbf{u}^T \mathbf{u} = 1 \tag{1.32}$$

In the displacement format, when the matrices are positive definite, it is easy to show Δk by means of a graphical interpretation

$$\Delta k_D = \mathbf{d}^T (\mathbf{K}_{dj+1} - \mathbf{K}_{dj}) \mathbf{d} = r_{j+1}^2[\mathbf{d}] - r_j^2[\mathbf{d}] \tag{1.33}$$

where $r_j[\mathbf{d}]$ and $r_{j+1}[\mathbf{d}]$ are the radii of the following ellipsoids

$$\mathcal{E}_k \equiv \{\mathbf{d} : \mathbf{d}^T \mathbf{K}_d[\mathbf{d}_k]^{-1}\mathbf{d} = 1\}, \quad k = j, j+1$$

When, as is usual for slender structures, the condition number of $\mathbf{H}$ and then of $\mathbf{K}_d$ is high due to very different stiffness ratios (i.e. membranal/flexural) the ellipsoids associated to $\mathbf{K}_d^{-1}$ are very stretched. In the small strain/large displacement hypothesis the ellipsoids are similar but slightly rotated. In this case even a small rotation produces a large Δk_d which increases with the condition number of $\mathbf{H}$ (see Fig.1.5). This is the reason for the pathological reduction in the step length, an increase in the total number of the iterations and, sometimes, the loss of convergence observed for the displacement description. In the mixed case we

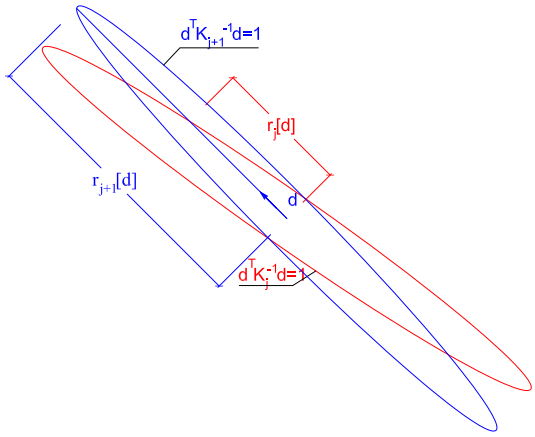

Figure 1.5: Graphical interpretation of Δk for the displacement description

have

$$\Delta k_M[\mathbf{u}] = \mathbf{d}^T \mathbf{\Gamma}[\boldsymbol{\beta}_{j+1} - \boldsymbol{\beta}_j]\mathbf{d} + 2\boldsymbol{\beta}^T \mathbf{Q}[\mathbf{d}_{j+1} - \mathbf{d}_j]\mathbf{d} \tag{1.34}$$

linearly dependent on the stress and displacement difference and unaffected by $\mathbf{H}$ and so by the extrapolation locking. Note that these deductions are general since for any structural model the strain energy can be expressed as a quadratic function of the stress variables through the Hellinger-Reissner functional and so the Hessian change is not influenced by $\mathbf{H}$ unlike the displacement case.

The occurrence of the locking is shown in the simple case of the Euler beam, for which the geometry and load conditions are reported in Fig.1.6.

In Tab.1.3 the number of steps and iterations (loops) to obtain the equilibrium path, directly related to the CPU time, are presented. The results of the mixed formulation, denoted by M, are unaffected by the coefficient $k = (t/\ell)^2$ while the displacement ones (D) pathologically depend on it.

Finally, in Fig.1.7, the minimum ρ_{min} and maximum ρ_{max} absolute value of the eigenvalues of the matrix $\mathbf{K}_{n+1}\mathbf{K}_n^{-1}$ is reported for both descriptions, where

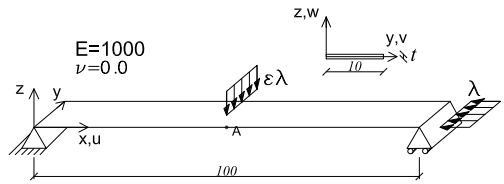

Figure 1.6: Eulero beam: analysis evolution for increasing k, mesh $1 \times 1 \times 40$

	Displacement				Mixed
k	10^4	10^5	10^6	10^7	(all k)
steps	38	43	67	failed	27
loops	133	166	328	failed	75

Table 1.3: Eulero beam: analysis evolution for increasing k, mesh $1 \times 1 \times 40$

$n+1$ and n denote two equilibrium points. The set of points in which the ρs are evaluated belongs on the equilibrium path obtained by the mixed description. It is important to observe how the mixed description ρ_{max} is independent of k and has almost the optimal value 1.0 while for the displacement description increases with the step length. Also note that if the second condition in Eq.(1.5e) is not fulfilled and this also heavily affects the convergence of the arc-length solution while the singular direction is filtered by the Riks constraint. We refer readers to [32, 33] for further details.

1.5 Numerical Results

In this section the effectiveness and reliability of both methods of analysis are tested in a series of benchmark problems. In particular for the path-following analysis the efficiency of the mixed description, which allows very large steps in comparison with the displacement one, is highlighted. For the Koiter formulation, the accuracy given by the mixed solid element is shown.

For all the tests only one element in the thickness is used while the same convergence conditions and arc-length parameters are adopted for mixed and displacement path-following analyses. The junctions are modelled with regular elements. The label Riks denotes the equilibrium paths obtained by the arc-length scheme (the same for both the descriptions), while labels Mixed and Frozen denote the asymptotic paths using the mixed description and the displacement one with the frozen configuration hypothesis.

1.5.1 Simply supported U-shape beam

The first test, with geometry and material reported in figure 1.8, consists in a simply supported compressed beam with a U-shape section. It presents a nonlinear

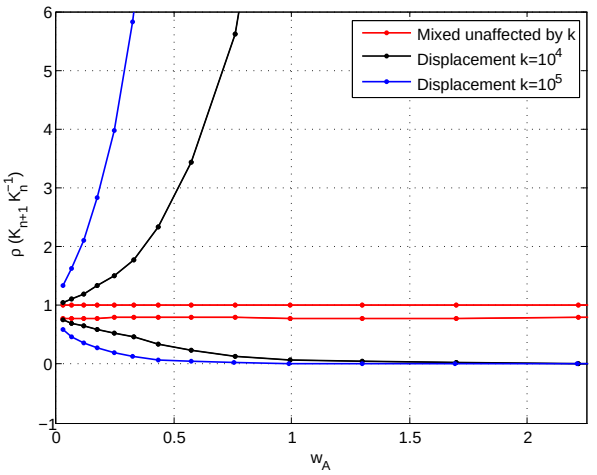

Figure 1.7: Minimum and maximum eigenvalues of matrix $\mathbf{K}_{n+1}\mathbf{K}_n^{-1}$ for the simple tests

pre-buckling behaviour due to two forces (torsional imperfections) at the mid-span and coupled instability. For this reason it is a good benchmark to test the accuracy of the asymptotic analysis. It was already studied in [48] using shell elements.

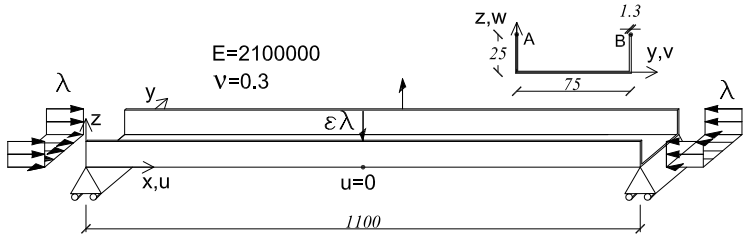

Figure 1.8: Channel section: geometry and loads.

The buckling values, obtained by using a mesh of $(8+8+18)\times 50$ elements are reported in Table 1.4 and compared with those computed using the displacement description with the frozen configuration hypothesis. The Koiter analysis uses the first four buckling modes plotted in Fig.1.9. It is possible to see how the first two modes are global, essentially flexural and torsional respectively, while the others are local modes.

The accuracy of the mixed asymptotic strategy in the evaluation of the limit load and of the initial post-critical behaviour is shown in Fig.1.10. It is also possible to observe the poor accuracy of the frozen configuration analysis in estimating both the limit load and equilibrium path. In Fig.1.11 the equilibrium path of Koiter method, in terms of the modal contributions ξ_k, is plotted. The

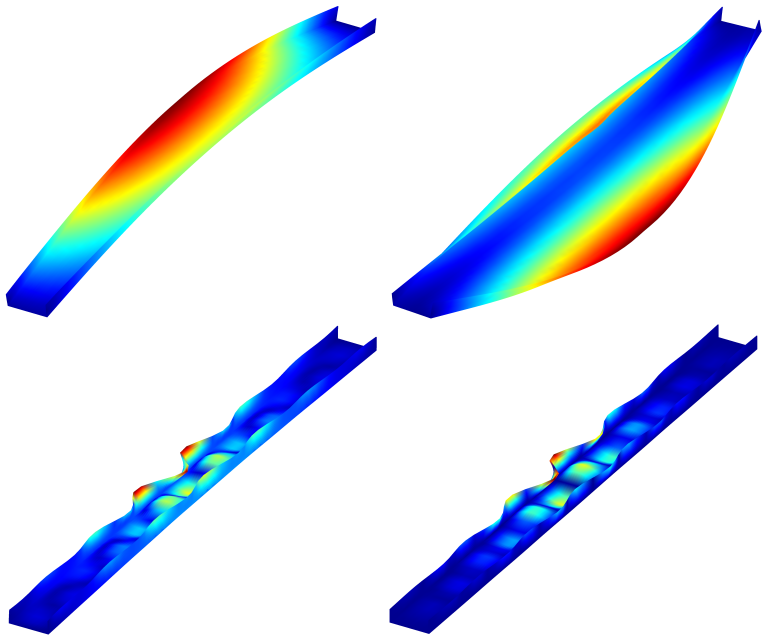

Figure 1.9: Channel section: Buckling modes

Table 1.4: Channel section: first 4 buckling loads.

	Mixed	Frozen
λ_1	1266.8	1291.5
λ_2	1828.1	1719.0
λ_3	3092.3	2949.7
λ_4	3114.7	2970.6

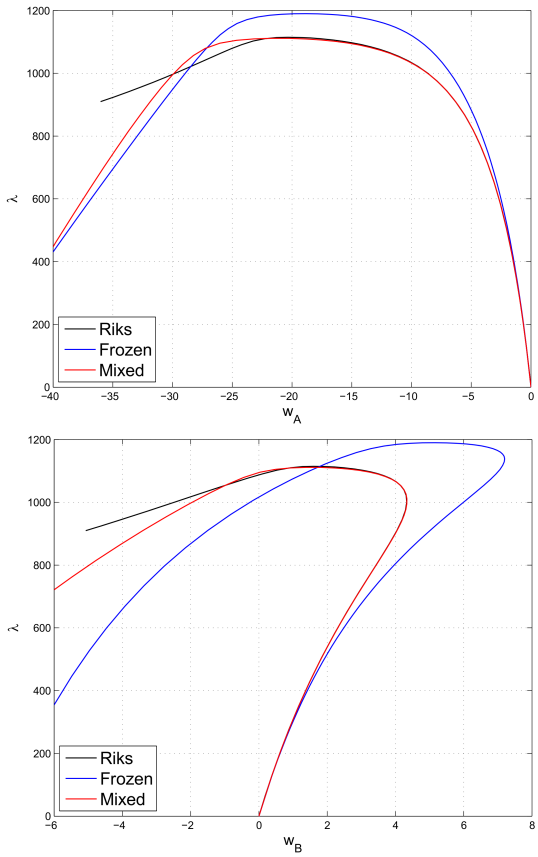

Figure 1.10: Channel section: Equilibrium paths $\lambda - w_A$, $\lambda - w_B$

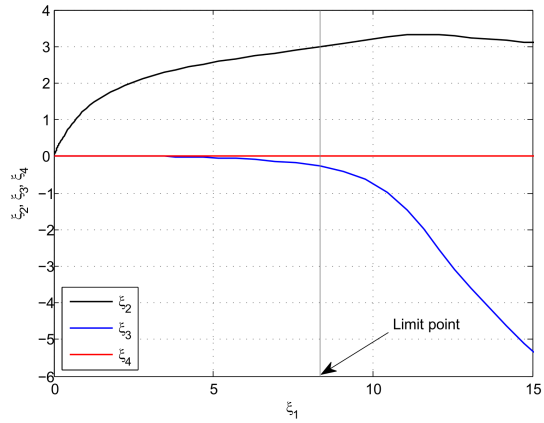

Figure 1.11: Channel section: Equilibrium paths in ξ_k space.

Table 1.5: Channel section: steps and iterations for path–following analysis.

	Mixed	Displacement	Mixed MN
steps	24	74	45
loops	73	175	233

strong effect of modal interaction between the third (local) mode and the first two flexural–torsional (global) modes is shown.

The results of the mixed asymptotic analysis are in good agreement with the path-following ones. In Tab.1.5 the steps and iterations of the mixed and displacement descriptions are compared. Obviously the equilibrium path is exactly the same but the better performances of the mixed description are evident even when a modified Newton-Raphson method (MN) is adopted.

1.5.2 A T beam

The second test regards the beam with data reported in Fig.1.12. It consists in a simply supported beam with a T shaped section loaded by a shear force acting at the mid-span and by a small imperfection ($\epsilon = 1/1000$) load as reported in the same figure. The pre-critical behaviour exhibits a strong nonlinearity and coupled buckling are also present in this case. A mesh of $(9 + 9 + 18) \times 100$ elements has been used.

Table 1.6: T section beam: first 4 buckling loads.

	Mixed	Frozen
λ_1	1092.1	936.8
λ_2	1869.1	1860.4
λ_3	1993.5	1989.6
λ_4	2258.9	2252.1

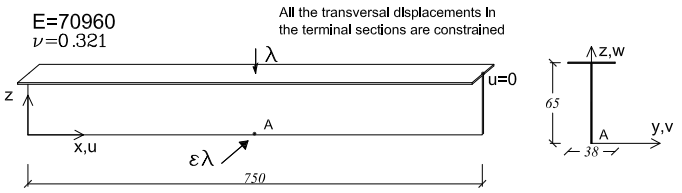

Figure 1.12: T section beam: geometry and loads

In Fig.1.13 the first 4 buckling modes, considered in the multimodal Koiter analysis, are plotted.

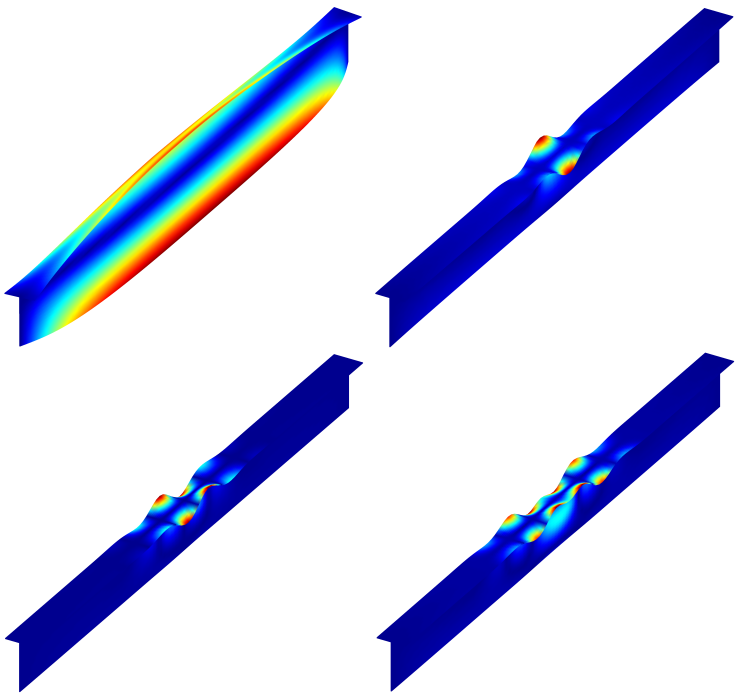

Figure 1.13: Channel section: First 4 Buckling modes

In Fig.1.14 the equilibrium paths recovered by using both asymptotic and path-following analysis are reported and compared. The solution is accurately recovered by the asymptotic strategy up to quite large displacements and the occurrence of a secondary bifurcation.

Also in this case (see Fig.1.15) the equilibrium path is plotted in terms of the modes amplitudes ξ_k showing a strong interaction among modes 1, 2 and 4.

In Tab.1.7 the steps and iterations of the mixed, using both full o modified Newton (MN) methods, and displacement descriptions are compared. This example highlights the excellent performances of the mixed description even more

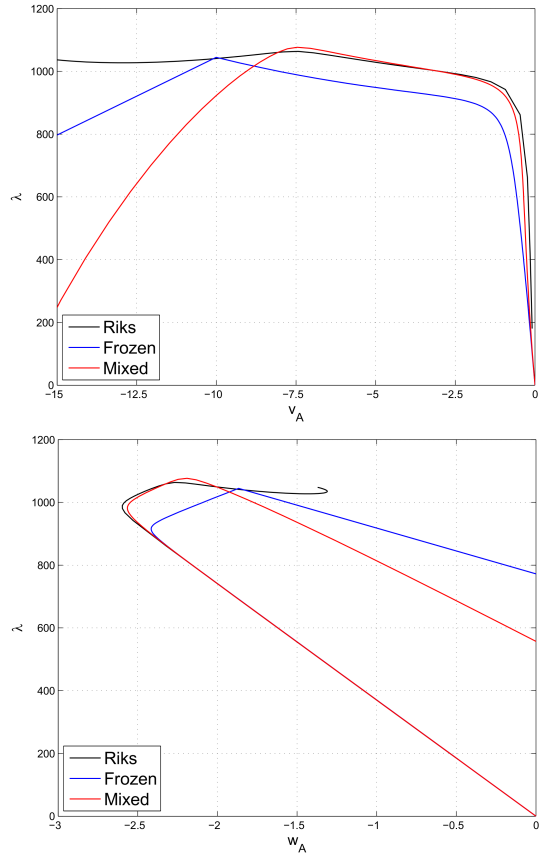

Figure 1.14: T section beam: Equilibrium paths $\lambda - w_A$, $\lambda - v_A$

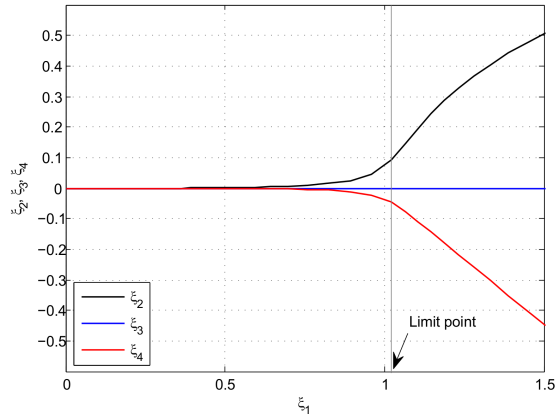

Figure 1.15: T section beam: Equilibrium paths in ξ_k space.

Table 1.7: T section beam: steps and iterations for path–following analysis.

	Mixed	Displacement	Mixed MN
steps	20	42	55
loops	60	169	252

than the previous test.

1.6 Summary

In this chapter, the better performances of the mixed format in the nonlinear analysis of slender structures have been shown and explained. To focus on the origin of this behaviour, which is independent of the finite element interpolation, a displacement description of a mixed solid finite element has been derived. In this way it has been possible to show how the displacement description, and so any displacement finite element, is affected by an underhand and neglected extrapolation locking phenomenon that produces slow or lack of convergence for the path–following analyses and inaccurate solutions for the Koiter method. The occurrence of the locking has been theoretically investigated and it has been indicated that it is due to the presence of directions with different stiffness as typically occurs for slender structures which are usually characterized by a high membrane/flexural stiffness ratio. These conclusions are general and hold for any nonlinear structural model and finite element. Many advantages of solid elements in geometrically nonlinear analysis are already known in literature. In this chapter, further important properties of mixed solid FE within the Koiter asymptotic formulation are shown. In fact, due to the simple 3rd order dependence of the strain energy on its FE parameters, all the higher order energy variations are null and so it is possible to have: i) an exact linear bifurcation analysis with improvements in its computational efficiency and accuracy for non near buckling loads; ii) simplification and greater accuracy in the evaluation of the energy variations required to recover the equilibrium path with a gain in terms of the computational cost; iii) a more simple and effective numerical method which is easy to include in FE packages. For these reasons, mixed solid models seems even more convenient and attractive with respect to standard shell ones in geometrically nonlinear analyses. Further details can be found in [49].

Chapter 2

Accurate and efficient a-posteriori account of geometrical imperfections in Koiter analysis using mixed solid-shell finite elements

Abstract

The Koiter method recovers the equilibrium path of an elastic structure using a reduced model, obtained by means of a quadratic asymptotic expansion of the finite element model. Its main feature is the possibility of efficiently performing sensitivity analysis by including a-posteriori the effects of the imperfections in the reduced nonlinear equations. The state-of-art treatment of geometrical imperfections is accurate only for small imperfection amplitudes and linear pre-critical behaviour. This chapter enlarges the validity of the method to a wider range of practical problems through a new approach, which accurately takes into account the imperfection without losing the benefits of the a-posteriori treatment. A mixed solid-shell finite element is used to build the discrete model. A large number of numerical tests, regarding nonlinear buckling problems, modal interaction, unstable post-critical and imperfection sensitive structures, validates the proposal.

2.1 Introduction

Thin-walled beams and shells are commonly used as primary components in structure engineering, due to their high specific strength and stiffness, which allow

weight and material economy. Their load-carrying capabilities are often determined by buckling, which often occurs for loads much lower than the failure loads of materials. The path-following strategy is the standard approach employed to analyze the nonlinear elastic behaviour of this kind of structure. Once the continuum problem has been discretised using the finite element (FE) method, the equilibrium path of the structure is traced step-by-step, solving a nonlinear system of equations, where the unknowns are the FE degrees of freedom (DOFs) and the load factor.

As a consequence of modal buckling interaction, shell-like structures may exhibit a very unstable post-buckling behaviour and may be highly sensitive to initial imperfections [50, 51, 52, 53, 54], especially to geometrical imperfections. In light of this an *imperfection sensitivity analysis* [6, 37, 5, 55] becomes mandatory. It consists in seeking the so called *worst (detrimental)* imperfection cases, which are the shapes of the geometrical imperfections associated with the minimum limit load (safety factor). The Monte Carlo simulation generally adopted to this end may require thousands of equilibrium path evaluations [56]. The use of composite structures, which require a layup optimization [4, 1], further complicates the design process.

Standard path-following approaches, aimed at recovering the equilibrium path for a single loading case and assigned imperfections, are not suitable for this purpose because of the high computational burden of the single run [57], and are unusable if no information about the worst imperfection shapes is available. For these reasons, the FE implementation of asymptotic methods [38, 58, 39, 40, 41, 42, 43, 44, 45, 35] based on Koiter's theory of elastic stability [7] has recently become [59, 49, 60, 61, 62, 8, 47, 63, 64, 65, 66] more and more attractive. The Koiter method consists of the construction of a reduced model, in which the FE model is replaced by its second order asymptotic expansion using the initial path tangent, m buckling modes and the corresponding second order modes, named quadratic correctives. In this way, once the reduced model is built, the equilibrium path of the structure can be obtained by solving the nonlinear reduced system of m equations in $m+1$ unknowns, which represent the modal amplitudes and the load factor. The coefficients of the reduced system are evaluated using strain energy variations up to the $4rd$ order. Shell structures can require a very large number of FE DOFs to avoid significant discretisation errors, while m is usually at most a few tens. Clearly the convenience of the method with respect to the standard path-following strategy is evident.

Since the first proposals [67, 6], the method has been continuously enhanced in terms of both accuracy and computational efficiency. In particular, a mixed (stress-displacement) formulation is required to avoid an *interpolation locking* phenomenon in the evaluation of the coefficients of the reduced system [6, 35, 68] and to make the asymptotic expansion accurate for a wider range, avoiding the *extrapolation locking* [33, 49] common in the displacement based approach and providing accurate results also for non-linear pre-critical behaviours. Geometrically exact

shells and beams [14, 15] or co-rotational approaches [34, 47] have been proposed to achieve structural model objectivity. Both the strategies make explicit use of the rotation tensor and its highly nonlinear representation. Alternatively in [59, 49], the method has been implemented exploiting the nonlinear Cauchy continuum based on a Green strain measure. In this way, adopting the mixed Hellinger-Reissner variational formulation, the strain energy has a $3rd$ order only polynomial dependence on the FE DOFs with the zeroing of all the fourth order strain energy variations. The resulting asymptotic formulation appears accurate, efficient and simple.

The effects of geometrical imperfections can be included in the Koiter analysis a-priori in the FE model, like it is mandatory for the standard path-following approach. In this way the modes used in the asymptotic expansion and the coefficient of the reduced system are recomputed for each imperfection. Although this procedure is cheaper than a path-following analysis, the re-construction of the reduced model involves a linearised buckling analysis and its computational cost can still prevent a Monte Carlo simulation. On the contrary the solution of the reduced system has a very low cost (usually fractions of seconds), negligible compared to the construction of the reduced model, because of the small value of m. Then the most attractive feature of the Koiter approach becomes apparent: the possibility of including a-posteriori the effects of the imperfections in the reduced model of the structure without imperfections, built once and for all, by simply adding some energy terms in the reduced system. In this way, a very fast imperfection sensitivity analysis, which can consider a very large number of imperfections in a reasonable computational time, is obtained, making possible a Monte Carlo simulation. Nevertheless, the state-of-the-art a-posteriori account of geometrical imperfections is based on the hypothesis of linear pre-critical behaviours and small imperfection amplitudes, that leads to additional terms in the reduced system which are just linear in the load factor. As a consequence, inaccuracies occur even for small pre-critical nonlinearities and significant imperfection amplitudes [5], considerably limiting the application of the method.

The goal of this chapter is to overcome these inaccuracies. A new accurate treatment of the geometrical imperfections is proposed. The asymptotic expansion of the perfect structure is corrected by adding a series of new modes, generated by the imperfection. In this way a more accurate formula for the additional imperfection terms in the reduced system is derived, which coherently takes into account the effects of the geometrical imperfection up to the $2nd$ order, without losing the advantages of the a-posteriori account. The chapter is organised as follows: Section 2 introduces a mixed solid-shell finite element model for composites; Section 3 recalls the current Koiter method for solid-shells elements; Section 4 derives the new Koiter algorithm for accurately taking into account geometrical imperfections; Section 5 presents some numerical tests and discusses the accuracy of the proposal; finally, the conclusions are reported.

2.2 The mixed solid-shell finite element

In this section, an implementation of the mixed solid-shell finite element proposed by Sze et al. in [21] is illustrated. It is an effective extension of the initial PT18β hybrid element of Pian and Tong [2] to composite shell structures. The element is presented in a Total Lagrangian formulation suitable for the Koiter strategy.

2.2.1 Kinematics in convective frame

We consider a solid finite element and denote with $\boldsymbol{\zeta} = \{\xi, \eta, \zeta\}$ the convective coordinates used to express the FE interpolation in natural coordinates. The initial configuration, assumed as reference, is described by the position vector $\mathbf{X}[\boldsymbol{\zeta}] \equiv \{X[\boldsymbol{\zeta}], Y[\boldsymbol{\zeta}], Z[\boldsymbol{\zeta}]\}$ while $\mathbf{x}[\boldsymbol{\zeta}]$ represents the same position in the current configuration. They are related by the transformation

$$\mathbf{x}[\boldsymbol{\zeta}] = \mathbf{X}[\boldsymbol{\zeta}] + \mathbf{d}[\boldsymbol{\zeta}] \tag{2.1}$$

where $\mathbf{d}[\boldsymbol{\zeta}]$ is the displacement field. Adopting the convention of summing on repeated indexes, the covariant Green-Lagrange strain measure components are

$$\bar{\varepsilon}_{ij} = \frac{1}{2}\left(\mathbf{X}_{,i}\cdot\mathbf{d}_{,j} + \mathbf{d}_{,i}\cdot\mathbf{X}_{,j} + \mathbf{d}_{,i}\cdot\mathbf{d}_{,j}\right) \quad \text{with} \quad i,j = \xi,\eta,\zeta \tag{2.2}$$

where a comma followed by k denotes the derivative with respect to k and $(\cdot)$ denotes the scalar product. The position vector of a point inside the element and its displacement are interpolated, using a trilinear 8 node hexahedron, as

$$\mathbf{X}[\boldsymbol{\zeta}] = \mathbf{N}_d[\boldsymbol{\zeta}]\mathbf{X}_e \quad , \quad \mathbf{d}[\boldsymbol{\zeta}] = \mathbf{N}_d[\boldsymbol{\zeta}]\mathbf{d}_e \tag{2.3}$$

where vectors $\mathbf{d}_e$ and $\mathbf{X}_e$ collect the element nodal displacements and coordinates and matrix $\mathbf{N}_d[\boldsymbol{\zeta}]$ the trilinear interpolation functions

$$\mathbf{N}_d[\boldsymbol{\zeta}] \equiv \left[\tfrac{1}{2}(1-\zeta)\mathbf{N}, \tfrac{1}{2}(1+\zeta)\mathbf{N}\right] \tag{2.4}$$

where $\mathbf{N} \equiv \begin{bmatrix} N_1, & N_2, & N_3, & N_4 \end{bmatrix}$ and

$$\begin{aligned} N_1 &= \frac{1}{4}(1-\xi)(1-\eta) \quad N_2 = \frac{1}{4}(1+\xi)(1-\eta) \\ N_3 &= \frac{1}{4}(1+\xi)(1+\eta) \quad N_4 = \frac{1}{4}(1-\xi)(1+\eta) \end{aligned} \tag{2.5}$$

Adopting a Voigt notation the Green-Lagrange covariant strain components in Eq.(2.2) are collected in vector $\bar{\boldsymbol{\varepsilon}} \equiv [\bar{\varepsilon}_{\xi\xi}, \bar{\varepsilon}_{\eta\eta}, 2\bar{\varepsilon}_{\xi\eta}, \bar{\varepsilon}_{\zeta\zeta}, 2\bar{\varepsilon}_{\eta\zeta}, 2\bar{\varepsilon}_{\xi\zeta}]^T$ that, exploiting Eq.(2.3), becomes

$$\bar{\boldsymbol{\varepsilon}} = \left(\boldsymbol{\mathcal{L}}[\boldsymbol{\zeta}] + \frac{1}{2}\boldsymbol{\mathcal{Q}}[\boldsymbol{\zeta}, \mathbf{d}_e]\right)\mathbf{d}_e, \tag{2.6}$$

where $\boldsymbol{\mathcal{L}}[\boldsymbol{\zeta}] \equiv \boldsymbol{\mathcal{Q}}[\boldsymbol{\zeta}, \mathbf{X}_e]$ and $\boldsymbol{\mathcal{Q}}$ is so defined

$$\boldsymbol{\mathcal{Q}}[\boldsymbol{\zeta}, \mathbf{d}_e] \equiv \begin{bmatrix} \mathbf{d}_e^T \mathbf{N}_{d,\xi}^T \mathbf{N}_{d,\xi} \\ \mathbf{d}_e^T \mathbf{N}_{d,\eta}^T \mathbf{N}_{d,\eta} \\ \mathbf{d}_e^T (\mathbf{N}_{d,\xi}^T \mathbf{N}_{d,\eta} + \mathbf{N}_{d,\eta}^T \mathbf{N}_{d,\xi}) \\ \mathbf{d}_e^T \mathbf{N}_{d,\zeta}^T \mathbf{N}_{d,\zeta} \\ \mathbf{d}_e^T (\mathbf{N}_{d,\zeta}^T \mathbf{N}_{d,\eta} + \mathbf{N}_{d,\eta}^T \mathbf{N}_{d,\zeta}) \\ \mathbf{d}_e^T (\mathbf{N}_{d,\xi}^T \mathbf{N}_{d,\zeta} + \mathbf{N}_{d,\zeta}^T \mathbf{N}_{d,\xi}) \end{bmatrix} \tag{2.7}$$

In order to circumvent shear and trapezoidal lockings, the natural transverse normal and shear strains are redefined by an *assumed natural strain* (ANS) formulation as

$$\begin{cases} \bar{\varepsilon}_{\zeta\zeta} = \bar{\varepsilon}_{\zeta\zeta}[-1,-1,0]N_1 + \bar{\varepsilon}_{\zeta\zeta}[-1,1,0]N_2 \\ \qquad + \bar{\varepsilon}_{\zeta\zeta}[1,1,0]N_3 + \bar{\varepsilon}_{\zeta\zeta}[1,-1,0]N_4 \\ \bar{\varepsilon}_{\xi\zeta} = \dfrac{1-\eta}{2}\bar{\varepsilon}_{\xi\zeta}[0,-1,0] + \dfrac{1+\eta}{2}\bar{\varepsilon}_{\xi\zeta}[0,1,0] \\ \bar{\varepsilon}_{\eta\zeta} = \dfrac{1-\xi}{2}\bar{\varepsilon}_{\eta\zeta}[-1,0,0] + \dfrac{1+\xi}{2}\bar{\varepsilon}_{\eta\zeta}[1,0,0] \end{cases} \tag{2.8}$$

assuming from now on that the Z-axis and the X-Y-plane are parallel to the ζ-axis and mid-surface of the shell respectively. The covariant strains can be linearised with respect to ζ in the following form

$$\bar{\boldsymbol{\varepsilon}} \approx \begin{bmatrix} \bar{\mathbf{e}}[\xi,\eta] + \zeta\, \bar{\boldsymbol{\chi}}[\xi,\eta] \\ \bar{\varepsilon}_{\zeta\zeta}[\xi,\eta] \\ \bar{\boldsymbol{\gamma}}[\xi,\eta] \end{bmatrix} \tag{2.9}$$

where

$$\bar{\mathbf{e}}[\xi,\eta] \equiv \begin{bmatrix} \bar{\varepsilon}_{\xi\xi} \\ \bar{\varepsilon}_{\eta\eta} \\ 2\bar{\varepsilon}_{\xi\eta} \end{bmatrix} \quad \bar{\boldsymbol{\chi}}[\xi,\eta] \equiv \begin{bmatrix} \bar{\varepsilon}_{\xi\xi,\zeta} \\ \bar{\varepsilon}_{\eta\eta,\zeta} \\ 2\bar{\varepsilon}_{\xi\eta,\zeta} \end{bmatrix} \quad \bar{\boldsymbol{\gamma}}[\xi,\eta] \equiv \begin{bmatrix} 2\bar{\varepsilon}_{\eta\zeta} \\ 2\bar{\varepsilon}_{\xi\zeta} \end{bmatrix}$$

The generalized covariant strains can be collected in vector $\bar{\boldsymbol{\rho}}[\zeta]$ as

$$\bar{\boldsymbol{\rho}}[\xi,\eta] \equiv \begin{bmatrix} \bar{\mathbf{e}} \\ \bar{\varepsilon}_{\zeta\zeta} \\ \bar{\boldsymbol{\chi}} \\ \bar{\boldsymbol{\gamma}} \end{bmatrix} = \left(\boldsymbol{\mathcal{L}}_\rho[\xi,\eta] + \frac{1}{2}\boldsymbol{\mathcal{Q}}_\rho[\xi,\eta,\mathbf{d}_e] \right) \mathbf{d}_e, \tag{2.10}$$

where matrix $\boldsymbol{\mathcal{L}}_\rho$ and $\boldsymbol{\mathcal{Q}}_\rho$ are automatically defined from (2.6) and (2.7) exploiting (2.8) and (2.9). The ith components of $\bar{\boldsymbol{\rho}}$ can be expressed in terms of matrix $\boldsymbol{\mathcal{Q}}_{\rho i}[\xi,\eta]$ as

$$\bar{\rho}_i = \mathbf{X}_e^T \boldsymbol{\mathcal{Q}}_{\rho i}[\xi,\eta]\mathbf{d}_e + \frac{1}{2}\mathbf{d}_e^T \boldsymbol{\mathcal{Q}}_{\rho i}[\xi,\eta]\mathbf{d}_e \tag{2.11}$$

Making the Jacobian matrix $\mathbf{J}$

$$\mathbf{J}[\xi,\eta] = \begin{bmatrix} \mathbf{X}_{,\xi} & \mathbf{X}_{,\eta} & \mathbf{X}_{,\zeta} \end{bmatrix} \tag{2.12}$$

constant with ζ (parallel to Z) and denoting with $\bar{\boldsymbol{\sigma}} \equiv [\bar{\sigma}_{\xi\xi}, \bar{\sigma}_{\eta\eta}, 2\bar{\sigma}_{\xi\eta}, \bar{\sigma}_{\zeta\zeta}, 2\bar{\sigma}_{\eta\zeta}, 2\bar{\sigma}_{\xi\zeta}]^T$ the vector collecting the contravariant stress components, it is possible to define, exploiting the stress-strain work, the quantities conjugate with $\bar{\boldsymbol{\rho}}$

$$\begin{aligned}\mathcal{W} &= \int_V \bar{\boldsymbol{\varepsilon}}^T \bar{\boldsymbol{\sigma}} dV \\ &= \int_\Omega \left(\bar{\boldsymbol{\mathcal{N}}}^T \bar{\mathbf{e}} + \bar{\boldsymbol{\mathcal{M}}}^T \bar{\boldsymbol{\chi}} + \bar{s}_{\zeta\zeta} \bar{\varepsilon}_{\zeta\zeta} + \bar{\boldsymbol{\mathcal{T}}}^T \bar{\boldsymbol{\gamma}} \right)\end{aligned}$$

where from now on $\int_\Omega (\cdots) = 2 \int_{-1}^{1} \int_{-1}^{1} (\cdots) \det(\mathbf{J}) d\xi d\eta$ and the stress resultants are defined

$$\begin{aligned}\bar{\boldsymbol{\mathcal{N}}} &\equiv \frac{1}{2} \int_{-1}^{1} \boldsymbol{\sigma}_p d\zeta \quad & \bar{\boldsymbol{\mathcal{M}}} &\equiv \frac{1}{2} \int_{-1}^{1} \zeta \boldsymbol{\sigma}_p d\zeta \\ \bar{s}_{\zeta\zeta} &\equiv \frac{1}{2} \int_{-1}^{1} \sigma_{\zeta\zeta} d\zeta \quad & \bar{\boldsymbol{\mathcal{T}}} &\equiv \frac{1}{2} \int_{-1}^{1} \boldsymbol{\tau} d\zeta\end{aligned} \tag{2.13}$$

with

$$\bar{\boldsymbol{\sigma}}_p = \begin{bmatrix} \bar{\sigma}_{\xi\xi} \\ \bar{\sigma}_{\eta\eta} \\ \bar{\sigma}_{\xi\eta} \end{bmatrix} \quad \bar{\boldsymbol{\tau}} = \begin{bmatrix} \bar{\sigma}_{\xi\zeta} \\ \bar{\sigma}_{\eta\zeta} \end{bmatrix}$$

The generalized contravariant stresses are collected in vector

$$\bar{\mathbf{t}} \equiv \left[\bar{\boldsymbol{\mathcal{N}}}, \bar{s}_{\zeta\zeta}, \bar{\boldsymbol{\mathcal{M}}}, \bar{\boldsymbol{\mathcal{T}}} \right]^T \tag{2.14}$$

so that the stress-strain work becomes

$$\mathcal{W} = \int_\Omega \bar{\mathbf{t}}[\xi, \eta]^T \bar{\boldsymbol{\rho}}[\xi, \eta]$$

2.2.2 Generalized stress interpolation

The generalized contravariant stresses are interpolated, as in [21]

$$\bar{\mathbf{t}}[\xi, \eta] = \mathbf{N}_\sigma[\xi, \eta] \boldsymbol{\beta}_e \quad \mathbf{N}_\sigma[\xi, \eta] = \begin{bmatrix} \mathbf{I}_9 & \mathbf{P}[\xi, \eta] \end{bmatrix} \tag{2.15}$$

where $\boldsymbol{\beta}_e$ collects the 18 stress parameters, $\mathbf{I}_9$ is a 9×9 identity matrix and $\mathbf{P}$ is

$$\mathbf{P}[\xi, \eta] = \begin{bmatrix} \eta & 0 & 0 & 0 & 0 & 0 & 0 & 0 & 0 \\ 0 & \xi & 0 & 0 & 0 & 0 & 0 & 0 & 0 \\ 0 & 0 & 0 & 0 & 0 & 0 & 0 & 0 & 0 \\ 0 & 0 & 0 & 0 & \xi & \eta & \xi\eta & 0 & 0 \\ 0 & 0 & \eta & 0 & 0 & 0 & 0 & 0 & 0 \\ 0 & 0 & 0 & \xi & 0 & 0 & 0 & 0 & 0 \\ 0 & 0 & 0 & 0 & 0 & 0 & 0 & 0 & 0 \\ 0 & 0 & 0 & 0 & 0 & 0 & 0 & \eta & 0 \\ 0 & 0 & 0 & 0 & 0 & 0 & 0 & 0 & \xi \end{bmatrix} \tag{2.16}$$

i.e. using an "optimal" interpolation similar to that proposed by Pian and Tong [2].

2.2.3 Transformation in physical coordinates

Finally the generalized Cartesian strain and stresses are obtained from the natural ones as

$$\begin{aligned} \mathbf{t} =& \mathbf{T}_\sigma \bar{\mathbf{t}} = \mathbf{T}[0,0]\bar{\mathbf{t}} \\ \boldsymbol{\rho} =& \mathbf{T}_\epsilon \bar{\boldsymbol{\rho}} = \mathbf{T}^{-T}[\xi,\eta]\bar{\boldsymbol{\rho}} \end{aligned} \quad \text{with} \quad \mathbf{T}[\xi,\eta] = \begin{bmatrix} \mathbf{T}_p & 0 & 0 & 0 \\ 0 & T_z & 0 & 0 \\ 0 & 0 & \mathbf{T}_p & 0 \\ 0 & 0 & 0 & \mathbf{T}_t \end{bmatrix} \tag{2.17}$$

where $T_z = J_{33}^2$ and

$$\begin{aligned} \mathbf{T}_p &= \begin{bmatrix} J_{11}^2 & J_{12}^2 & 2J_{11}J_{12} \\ J_{21}^2 & J_{22}^2 & 2J_{21}J_{22} \\ J_{21}J_{11} & J_{22}J_{12} & J_{22}J_{11} + J_{21}J_{12} \end{bmatrix} \\ \mathbf{T}_t &= \begin{bmatrix} J_{12}J_{33} + J_{13}J_{32} & J_{13}J_{31} + J_{11}J_{33} \\ J_{22}J_{33} + J_{23}J_{32} & J_{23}J_{31} + J_{21}J_{33} \end{bmatrix} \end{aligned} \tag{2.18}$$

Note that stresses are transformed with the matrix $\mathbf{T}$ evaluated in $\xi = 0, \eta = 0$ to preserve the constant stress state. More sophisticated transformations are possible [22].

2.2.4 Generalised laminate stiffness matrix

The procedure for the evaluation of the generalised laminate stiffness matrix is that proposed in [10] based on the analytic thickness integration. It consists in a homogenization technique aimed at employing just one element in the thickness direction even when the shell is composed of multiple layers.

In each layer an orthotropic elastic material is assumed with its properties given in a local reference system $\{\boldsymbol{i}_1, \boldsymbol{i}_2, \boldsymbol{i}_3\}$, with $\boldsymbol{i}_1$ the fibre direction defined by a rotation angle θ around $\boldsymbol{i}_3$ parallel to the Z axis. The material stiffness matrix in the Cartesian element reference system can be evaluated through a tensor rotation

$$\boldsymbol{\sigma} = \mathbf{C}\boldsymbol{\varepsilon} \quad \text{with} \quad \mathbf{C} = \mathbf{R}[\theta]^T \mathbf{C}' \mathbf{R}[\theta] = \begin{bmatrix} \mathbf{C}_p, & \mathbf{C}_{pz}, & \mathbf{0} \\ \mathbf{C}_{pz}^T, & C_z, & \mathbf{0} \\ \mathbf{0}, & \mathbf{0}, & \mathbf{C}_t \end{bmatrix} \tag{2.19}$$

where

$$\mathbf{C}' = \begin{bmatrix} \mathbf{C}'_p & \mathbf{C}'_{pz} & \mathbf{0} \\ (\mathbf{C}'_{pz})^T & C_z & \mathbf{0} \\ \mathbf{0} & \mathbf{0} & \mathbf{C}'_t \end{bmatrix} \tag{2.20}$$

with $C_z = C'_{3333}$ and

$$\mathbf{C}'_p \equiv \begin{bmatrix} C'_{1111} & C'_{1122} & 0 \\ C'_{1122} & C'_{2222} & 0 \\ 0 & 0 & C'_{1212} \end{bmatrix} \quad \mathbf{C}'_{pz} \equiv \begin{bmatrix} C'_{1113} \\ C'_{1122} \\ 0 \end{bmatrix}$$
$$\mathbf{C}'_t \equiv \begin{bmatrix} C'_{2323} & 0 \\ 0 & C'_{1313} \end{bmatrix}$$

The constitutive law of the multi-layered composite is obtained in terms of the kinematic assumptions for plane strain components $\boldsymbol{\varepsilon}_p$ and the shear ones $\boldsymbol{\gamma}$. In order to eliminate the thickness locking, following the approach proposed in [21], instead of a constant with Z thickness strain ε_{zz}, a constant stress σ_{zz} is assumed.

Starting from the inverse constitutive law of the generic lamina $\boldsymbol{\varepsilon} = \mathbf{C}^{-1}\boldsymbol{\sigma}$ that is, exploiting the decoupling of $\mathbf{C}_t$, as

$$\begin{bmatrix} \boldsymbol{\varepsilon}_p \\ \varepsilon_{zz} \end{bmatrix} = \begin{bmatrix} \mathbf{F}_{pp} & \mathbf{F}_{pz} \\ \mathbf{F}_{pz}^T & F_{zz} \end{bmatrix} \begin{bmatrix} \boldsymbol{\sigma}_p \\ \sigma_{zz} \end{bmatrix}$$

it is possible to evaluate σ_{zz} and $\boldsymbol{\varepsilon}_p$ as

$$\begin{aligned} \boldsymbol{\sigma}_p &= \mathbf{S}\boldsymbol{\varepsilon}_p + \mathbf{D}\sigma_{zz} \\ \varepsilon_{zz} &= -\mathbf{D}^T\boldsymbol{\varepsilon}_p + R\sigma_{zz} \end{aligned} \quad \text{with} \quad \begin{cases} R = F_{zz} + \mathbf{F}_{pz}^T\mathbf{D} \\ \mathbf{D} = -(\mathbf{F}_{pp})^{-1}\mathbf{F}_{pz} \\ \mathbf{S} = (\mathbf{F}_{pp})^{-1} \end{cases}$$

In terms of the quantities $\boldsymbol{\mathcal{N}}$ and $\boldsymbol{\mathcal{M}}$ defined in Eq.(2.13), we have

$$\begin{aligned} \begin{bmatrix} \boldsymbol{\mathcal{N}} \\ \varepsilon_{zz} \\ \boldsymbol{\mathcal{M}} \end{bmatrix} &= \frac{1}{2}\int_{-1}^{1} \begin{bmatrix} \mathbf{S} & \mathbf{D} \\ -\mathbf{D}^T & R \\ \zeta\mathbf{S} & \zeta\mathbf{D} \end{bmatrix} \begin{bmatrix} \mathbf{e} + \zeta\boldsymbol{\chi} \\ \sigma_{zz} \end{bmatrix} d\zeta \\ &= \frac{1}{2}\int_{-1}^{1} \begin{bmatrix} \mathbf{S} & \zeta\mathbf{S} & \mathbf{D} \\ -\mathbf{D} & -\zeta\mathbf{D} & R \\ \zeta\mathbf{S} & \zeta^2\mathbf{S} & \zeta\mathbf{D} \end{bmatrix} d\zeta \begin{bmatrix} \mathbf{e} \\ s_{zz} \\ \boldsymbol{\chi} \end{bmatrix} \end{aligned}$$

Letting

$$\begin{bmatrix} \mathbf{S}_0 & \mathbf{S}_1 & \mathbf{D}_0 \\ -\mathbf{D}_0 & \mathbf{D}_1 & R_0 \\ \mathbf{S}_1 & \mathbf{S}_2 & \mathbf{D}_1 \end{bmatrix} = \frac{1}{2}\int_{-1}^{1} \begin{bmatrix} \mathbf{S} & \zeta\mathbf{S} & \mathbf{D} \\ -\mathbf{D} & -\zeta\mathbf{D} & R \\ \zeta\mathbf{S} & \zeta^2\mathbf{S} & \zeta\mathbf{D} \end{bmatrix}$$

and recalling that the material properties change along ζ we have

$$\begin{bmatrix} \boldsymbol{\mathcal{N}} \\ \varepsilon_{zz} \\ \boldsymbol{\mathcal{M}} \end{bmatrix} = \begin{bmatrix} \mathbf{S}_0 & \mathbf{S}_1 & \mathbf{D}_0 \\ -\mathbf{D}_0 & \mathbf{D}_1 & R_0 \\ \mathbf{S}_1 & \mathbf{S}_2 & \mathbf{D}_1 \end{bmatrix} \begin{bmatrix} \mathbf{e} \\ s_{zz} \\ \boldsymbol{\chi} \end{bmatrix}$$

Now by expressing s_{zz} in terms of ε_{zz} and substituting it in the previous equation and performing the integration for the $\mathbf{C}_t$ part, we have the desired constitutive matrix equivalent to the laminate package

$$\mathbf{t}[\xi,\eta] = \mathbf{C}_\rho \boldsymbol{\rho}[\xi,\eta] \tag{2.21}$$

with

$$\mathbf{C}_\rho \equiv \begin{bmatrix} \mathbf{S}_0 + \mathbf{D}_0\mathbf{D}_0^T/R_0 & \mathbf{D}_0/R_0 & \mathbf{S}_1 + \mathbf{D}_0\mathbf{D}_0^T/R_0 & \mathbf{0} \\ \mathbf{D}_0^T/R_0 & 1/R_0 & \mathbf{D}_1^T/R_0 & \mathbf{0} \\ \mathbf{S}_1 + \mathbf{D}_1\mathbf{D}_0^T/R_0 & \mathbf{D}_1/R_0 & \mathbf{S}_2 + \mathbf{D}_1\mathbf{D}_1^T/R_0 & \mathbf{0} \\ \mathbf{0} & \mathbf{0} & \mathbf{0} & \mathbf{C}_{t0} \end{bmatrix}$$

2.2.5 On the computational cost of the solid-shell element

The mixed solid-shell element previously described is a solid element designed in order to employ just one element along the thickness direction. It is worth noting that it presents the same (minimal) displacement and stress parameters of others 4 node shell elements. In terms of DOFs, for example, it is equivalent to the shell element recently proposed in [64, 5] which has only 3 translations and 3 rotations for node and 18 stress parameters for element to assure an isostatic behaviour, i.e. the same number of kinematic and stress variables of the mixed solid-shell one. Since the stress parameters are locally defined, they can be eliminated by a static condensation at the element level with a very low computational extra-cost with respect to displacement based elements. In this way the stress DOFs are not involved in the global operations. Notwithstanding the minimal number of DOFs the convergence properties of the element are good, as reported in [28], where it is shown how it has a similar accuracy of other well-established shell elements.

2.3 Koiter method for mixed solid-shell FE models

In this section, the asymptotic approach described in [59] is recalled briefly. It is particularized for a strain energy which has a cubic polynomial dependence only from the configuration variables as occurs, for instance, for the nonlinear Cauchy continuum based on a Green strain measure, when a hybrid solid-shell FE model is employed. This allows the simplification of the asymptotic equations and focuses on the proposed treatment of the geometrical imperfections, which is, however, easily applicable to other finite elements and structural models. Further details on the Koiter method in general contexts can be found in [35, 34, 15].

2.3.1 The current implementation of the asymptotic algorithm

Consider a slender hyperelastic structure subject to conservative nominal loads $\hat{p}$ proportionally increasing with the amplifier factor λ. The equilibrium is expressed

by the virtual work equation

$$\Phi'[u]\,\delta u - \lambda \hat{p}\,\delta u = 0, \qquad u \in \mathcal{U}\ ,\ \delta u \in \mathcal{T} \tag{2.22}$$

where $u \in \mathcal{U}$ is the field of configuration variables which collects both displacement and stress fields, $\Phi[u]$ denotes the strain energy, $\mathcal{T}$ is the tangent space of $\mathcal{U}$ at u and a prime is used to express the Frechèt derivative with respect to u. It is assumed that $\mathcal{T}$ is independent of u.

Due to the assumed 3rd order polynomial dependence of $\Phi[u]$ on u, it can be exactly replaced with its 3rd order Taylor expansion from a given configuration $u = u_0$, that is

$$\Phi'[u]\delta u := \left(\Phi'_0 + \Phi''_0(u-u_0) + \frac{1}{2}\Phi'''(u-u_0)^2\right)\delta u, \quad \forall \delta u \in \mathcal{T}, \tag{2.23}$$

where a subscript denotes, from now on, the point in which the quantities are evaluated, i.e. $\Phi'_0 \equiv \Phi'[u_0]$ and so on, while the quantity Φ''' is constant with u.

Fundamental path.

The method starts with the evaluation of the *fundamental path* $u_f[\lambda]$ assumed as analytical in λ and approximated with its tangent in the (known) equilibrium configuration $(u_0, \lambda_0 = 0)$ as $u_f = u_0 + \lambda\hat{u}$. It is evaluated through a first order Taylor expansion in λ of Eq.(2.22), that is

$$\Phi''_0 \hat{u}\delta u - \hat{p}\delta u = 0, \quad \forall \delta u \in \mathcal{T}. \tag{2.24}$$

Buckling loads and modes.

With the adopted linear extrapolation in λ of the fundamental path, it is possible to evaluate the *bifurcation condition*, that is the singularity of the second strain energy variation, as

$$\Phi''[u_f[\lambda]]\dot{v}_i\delta u \equiv (\Phi''_0 + \lambda\Phi'''\hat{u})\dot{v}_i\delta u = 0\ \forall \delta u \in \mathcal{T} \tag{2.25}$$

where $\dot{v}_i$ and λ_i are the bifurcation modes and loads. Note that the expression in Eq.(2.25) is exact, due to the zeroing of all the higher order energy terms, and so the buckling condition is exactly a linear eigenvalue problem [49], which provides the m bifurcation loads and modes, orthogonalized according to

$$\Phi'''\hat{u}\dot{v}_i\dot{v}_k = -\delta_{ik} \tag{2.26}$$

with δ_{ik} the Kronecker symbol.

The reduced model of the perfect structure.

According to a Lyapunov-Schmidt decomposition [69], $\mathcal{U}$ is decomposed as a direct sum of the critical subspace $\mathcal{V}$ and its orthogonal complement $\mathcal{W}$, defined as

$$\mathcal{U} = \mathcal{V} \oplus \mathcal{W}, \qquad \begin{cases} \mathcal{V} = \{v : \ v = \sum_{i=1}^{m} \xi_i \dot{v}_i\} \\ \mathcal{W} = \{w : \ \Phi''' \hat{u} \dot{v}_i w = 0\} \end{cases} \tag{2.27}$$

where ξ_i, with $i = 1 \cdots m$ are the buckling mode amplitudes.

The space of admissible configurations, following a Galerkin approach, is limited to

$$u_d = u_f[\lambda] + v[\xi_i] + w[\lambda, \xi_i] \tag{2.28}$$

where the corrective term $w \in \mathcal{W}$ is assumed to be at least quadratic in λ and ξ_i and the compact notation $f[\xi_i]$ is used to denote the dependence of function f on all the ξ_i.

Using a Ritz-Galerkin approach the equilibrium equation is imposed assuming $\dot{v}_i$ and δw as test functions, and the configuration defined by u_d, that is

$$\begin{aligned} r_w[\lambda, \xi_i] \equiv & \{\Phi'[u_d] - \lambda \hat{p}\}\delta w = 0 \\ r_k[\lambda, \xi_i] \equiv & \{\Phi'[u_d] - \lambda \hat{p}\}\dot{v}_k = 0. \end{aligned} \tag{2.29}$$

From the condition $r_w[\lambda, \xi_i] = 0$ and using a Taylor expansion up to the 2th order in $\lambda, \xi_1, \cdots \xi_m$ we obtain the *quadratic correctives* (see [59])

$$w = \frac{1}{2}\lambda^2 \hat{\hat{w}} + \frac{1}{2}\sum_{ij} \xi_i \xi_j w_{ij} \quad \begin{cases} \Phi''_b \hat{\hat{w}} \delta w = -\Phi''' \hat{u}^2 \delta w \\ \Phi''_b w_{ij} \delta w = -\Phi''' \dot{v}_i \dot{v}_j \delta w \end{cases} \quad \forall \delta w \in \mathcal{W} \tag{2.30}$$

where the subscript b denotes quantities evaluated in $\lambda_b \hat{u}$ and λ_b is a suitable reference value of the bifurcation load (the first bifurcation load or a mean value of the bifurcation cluster).

From the condition $r_k[\lambda, \xi_i] = 0$ we obtain the reduced nonlinear system which defines the equilibrium path

$$\begin{aligned} r_k[\lambda, \xi_i] \equiv \mu_k[\lambda] + (\lambda_k - \lambda)\xi_k - \frac{1}{2}\lambda^2 \sum_{i=1}^{m} \xi_i \mathcal{C}_{ik} + \frac{1}{2}\sum_{i,j=1}^{m} \xi_i \xi_j \mathcal{A}_{ijk} \\ + \frac{1}{6}\sum_{i,j,h=1}^{m} \xi_i \xi_j \xi_h \mathcal{B}_{ijhk} = 0, \quad k = 1 \cdots m \end{aligned} \tag{2.31}$$

where

$$\begin{aligned} \mathcal{A}_{ijk} = & \Phi''' \dot{v}_i \dot{v}_j \dot{v}_k \\ \mathcal{C}_{ik} = & \Phi''_b \hat{\hat{w}} w_{ik} \\ \mathcal{B}_{ijhk} = & -\Phi''_b (w_{ij} w_{hk} + w_{ih} w_{jk} + w_{ik} w_{jh}) \\ \mu_k[\lambda] = & \frac{1}{2}\lambda^2 \Phi''' \hat{u}^2 \dot{v}_k. \end{aligned} \tag{2.32}$$

Eqs.(2.31) are an algebraic nonlinear system of m equations in the $m+1$ variables λ, $\xi_1 \cdots \xi_m$ that, due to the small size of the system, can be efficiently solved using specialized variants of the arc–length scheme. Second and third order variations of the strain energy are required for the evaluation of coefficients in Eq.(2.32).

Standard a-posteriori account of geometrical imperfections.

Small imperfections, expressed by an initial displacement $\tilde{u}$, can easily be considered in the asymptotic analysis. In the current proposal [6, 35] the following coefficients

$$\tilde{\mu}_k := \lambda \Phi''' \hat{u} \tilde{u} \dot{v}_k \tag{2.33}$$

are added to Eq.(2.31), that is

$$r_k + \tilde{\mu}_k = 0 \tag{2.34}$$

and the reduced model is corrected adding $\tilde{u}$ to the expression (2.28)

$$u_d = \tilde{u} + u_f[\lambda] + v[\xi_i] + w[\lambda, \xi_i]. \tag{2.35}$$

So, once the steps in Eqs.(2.24), (2.25), (2.30), (2.32) of the analysis have been performed, once and for all, small imperfections in the geometry can be taken into account by adding a few additional terms in the expression of r_k. The computational extra-cost is negligible since just the reduced nonlinear equations Eq.(2.31) have to be solved again for each new imperfection. In this way the method allows a low cost imperfection sensitivity analysis. In particular the reader is referred to [56] where the imperfection sensitivity analysis is performed by means of a Monte Carlo simulation showing how thousands of geometrical imperfections can be analysed in a few minutes in order to detect the worst imperfection shape.

However, comparisons with standard path-following analyses show that the accuracy of this approach is limited to small imperfection amplitudes and structures with an almost linear pre-critical behaviourr. The aim of this chapter is, then, to improve its accuracy, making the approach suitable for a wider range of practical problems.

2.3.2 FEM implementation of the asymptotic approach

Denoting with a bold symbol the discrete FEM counterpart of the continuum quantities, and referring to the solid-shell finite element model presented in [59], the construction of the reduced model of the *perfect structure* consists of the following steps.

1. The fundamental path defined by Eq.(2.24) becomes in FE format

$$\mathbf{u}^f[\lambda] = \mathbf{u}_0 + \lambda \hat{\mathbf{u}} \;\;,\;\; \mathbf{K}_0\, \hat{\mathbf{u}} = \hat{\mathbf{p}} \;\;,\;\; \mathbf{K}_0 \equiv \mathbf{K}[\mathbf{u}_0] \tag{2.36a}$$

and requires the solution of a linear system to evaluate the initial path tangent $\hat{\mathbf{u}}$.

2. The buckling modes and loads are obtained by the following eigenvalue problem

$$\mathbf{K}[\lambda]\dot{\mathbf{v}} \equiv (\mathbf{K}_0 + \lambda \mathbf{K}_1[\hat{\mathbf{u}}])\dot{\mathbf{v}} = \mathbf{0} \tag{2.36b}$$

where $\mathbf{K}_0$ and $\mathbf{K}_1$ are obtained from the following energy equivalence

$$\delta\mathbf{u}^T\mathbf{K}_0\delta\mathbf{u} := \Phi_0''\delta u^2 \qquad \delta\mathbf{u}^T\mathbf{K}_1\delta\mathbf{u} = \Phi_0'''\hat{u}\delta u^2.$$

3. The $m\times(m+1)/2$ quadratic correctives FE vectors $\mathbf{w}_{ij}, \hat{\hat{\mathbf{w}}} \in \mathcal{W}$ are obtained by the solution of the linear systems ($i = 1\dots m, j = i\dots m$)

$$\begin{aligned} \mathbf{K}_b\mathbf{w}_{ij} + \mathbf{p}_{ij} &= \mathbf{0} \\ \mathbf{K}_b\hat{\hat{\mathbf{w}}} + \mathbf{p}_{00} &= \mathbf{0} \end{aligned} \quad , \quad \forall \mathbf{w} \in \mathcal{W} \tag{2.36c}$$

in which $\mathbf{K}_b \equiv \mathbf{K}[\lambda_b]$, $\mathbf{p}_{ij}, \mathbf{p}_{00}$ are defined as a function of modes $\dot{\mathbf{v}}_i$ and $\hat{\mathbf{u}}$ by the energy equivalences

$$\begin{aligned} \delta\mathbf{w}^T\mathbf{p}_{ij} &= \Phi_b'''\dot{v}_j\dot{v}_j\delta w \\ \delta\mathbf{w}^T\mathbf{p}_{00} &= \Phi_b'''\hat{u}^2\delta w. \end{aligned}$$

Vectors $\mathbf{w}_{ij}$ are obtained by solving the following linear systems adopting a Lagrangian multiplier approach (see [37])

$$\begin{cases} \mathbf{K}_b\mathbf{w}_{ij} + \mathbf{p}_{ij} = \mathbf{0} \\ \mathbf{w}_{ij}^T\mathbf{K}_1\dot{\mathbf{v}}_k = 0, \qquad k = 1\cdots m. \end{cases} \tag{2.36d}$$

The solution of Eq.(2.36d) can be obtained adopting the iterative scheme proposed in [37] which uses the already decomposed matrix $\mathbf{K}_0$. The same approach is used to evaluate $\hat{\hat{\mathbf{w}}}$.

4. Evaluation of the coefficients in Eq.(2.32) of reduced equilibrium system in Eq.(2.31) as a sum of finite element contributions.

The evaluation of the equilibrium path, to be repeated for each imperfection, requires the following steps

1. evaluation of $\tilde{\mu}_k = \lambda\Phi'''\hat{u}\tilde{u}\dot{v}_k$;

2. solution of the reduced system in Eq.(2.34) and drawing of the equilibrium path according to Eq.(2.35).

2.4 Accurate account of geometrical imperfections

In this section the Koiter algorithm is reformulated in order to coherently consider the presence of geometrical imperfections, removing the hypothesis of linear pre-critical behaviour which leads to Eq.(2.33). In this way it is possible to overcome the inaccuracy in the limit load evaluation observed, for example, in Fig.19 of [5]. The imperfection sensitivity analysis can still be performed in the post-processing of the Koiter method, when the geometrical imperfections are expressed as a linear combination of known shapes like, as usual, the displacement shape of the buckling modes.

2.4.1 The strain energy and the equilibrium path of the structure with geometrical imperfection

Using a Hellinger-Reissner variational principle the mixed strain energy $\Phi[u]$ is expressed, as usual in a FE context, as a sum of element contributions

$$\Phi[u] = \sum_e \int_{\Omega_e} \left(\mathbf{t}^T \boldsymbol{\rho}[\mathbf{d}] - \frac{1}{2} \mathbf{t}^T \mathbf{C}_\rho^{-1} \mathbf{t} \right) d\Omega_e \tag{2.37}$$

$\boldsymbol{\rho}[\mathbf{d}]$ and $\mathbf{t}$ are the vectors collecting the generalized strains and stresses components for the given structural model, Ω_e is the finite element domain and $\mathbf{d}$ is the displacement field and $\mathbf{C}_\rho^{-1}$ the compliance matrix of the structural model.

The strain energy of the structure for an initial imperfection characterized by an assigned displacement $\tilde{\mathbf{d}}$ and zero stress is assumed as

$$\Phi_I[u] \equiv \sum_e \int_{\Omega_e} \left(\mathbf{t}^T (\boldsymbol{\rho}[\mathbf{d}] - \boldsymbol{\rho}[\tilde{\mathbf{d}}]) - \frac{1}{2} \mathbf{t}^T \mathbf{C}_\rho^{-1} \mathbf{t} \right) d\Omega_e. \tag{2.38}$$

Denoting with a symbol δ the variation of $\mathbf{d}$ and $\mathbf{t}$, the first variation of $\Phi_I[u]$ becomes

$$\begin{aligned} \Phi_I[u]' \delta u &= \sum_e \int_{\Omega_e} \left\{ \delta \mathbf{t}^T (\boldsymbol{\rho}[\mathbf{d}] - \boldsymbol{\rho}[\tilde{\mathbf{d}}] - \mathbf{C}_\rho^{-1} \mathbf{t}) - \mathbf{t}^T \boldsymbol{\rho}'[\mathbf{d}] \delta \mathbf{d} \right\} d\Omega_e \\ &= (\Phi[u]' - \Phi'[\tilde{u}]) \delta u \end{aligned} \tag{2.39}$$

that is the difference between the perfect and imperfect structure first order strain energy variation, being

$$\Phi'[\tilde{u}] \delta u := \sum_e \int_{\Omega_e} \delta \mathbf{t}^T \boldsymbol{\rho}[\tilde{\mathbf{d}}] d\Omega_e \tag{2.40}$$

the first variation of the perfect structure evaluated in $\tilde{u}$ (which has $\tilde{\mathbf{t}} = \mathbf{0}$).

The equilibrium path is obtained from the following condition

$$(\Phi[u]' - \Phi'[\tilde{u}] - \lambda p) \delta u = 0 \quad \forall \delta u \tag{2.41}$$

which in FE format becomes

$$\mathbf{s}[\mathbf{u}] - \tilde{\mathbf{p}} - \lambda\,\hat{\mathbf{p}} = \mathbf{0}. \tag{2.42}$$

In particular the internal force vector $\mathbf{s}[\mathbf{u}]$, the load vector $\hat{\mathbf{p}}$ and the imperfection vector $\tilde{\mathbf{p}}$ are defined by the energy equivalences

$$\mathbf{s}^T\delta\mathbf{u} \equiv \Phi'[u]\delta u \;\;,\;\; \hat{\mathbf{p}}^T\delta\mathbf{u} \equiv \hat{p}\,\delta u \;\;,\;\; \tilde{\mathbf{p}}^T\delta\mathbf{u} \equiv \Phi'[\tilde{u}]\delta u \;\;,\;\; \forall\,\delta\mathbf{u}. \tag{2.43}$$

Eq.(2.42) can be solved using standard path-following techniques [32, 70, 49] for an assigned imperfection $\tilde{u}$. Note that in the hybrid solid-shell FE model, the internal force vector of the imperfect structure is obtained by simply subtracting a constant vector $\tilde{\mathbf{p}}$, evaluated once and for all at the beginning of the analysis, to the internal forces vector $\mathbf{s}[\mathbf{u}]$ of the perfect structure.

2.4.2 The new reduced model with geometrical imperfection

The space of admissible configurations that will be used in the Lyapunov-Schmidt decomposition is obtained by adding an additional term which represents the initial imperfection, to the configuration field of the perfect structure in Eq.(2.28) that is

$$u_d[\lambda, \xi_i, \tilde{\xi}_i] = \tilde{u} + \lambda\hat{u} + v[\xi_i] + w[\xi_i, \tilde{\xi}_i, \lambda] \tag{2.44}$$

where the geometrical imperfection is assumed to be a linear combination of a known shape $\bar{u}_i$

$$\tilde{u} = \sum_{i=1}^{n} \tilde{\xi}_i \bar{u}_i. \tag{2.45}$$

The imperfection shapes $\bar{u}_i$ are generic and can be, for example, the displacement part of the buckling modes as well as measured geometrical imperfections. Note that, unlike the reduced model in Eq.(2.35), now the quadratic correctives $w[\xi_i, \tilde{\xi}_i, \lambda]$ depend on the geometrical imperfection amplitudes $\tilde{\xi}_i$.

From now on the 3th order dependence of the strain energy on the configuration variables u (see Eq.(2.23)) will be exploited in order to simplify the exposition.

The residual equation (2.41) is firstly expanded in Taylor series starting from $\tilde{u}$, so obtaining

$$\left(\Phi''[\tilde{u}](u_d - \tilde{u}) + \frac{1}{2}\Phi[\tilde{u}]'''(u_d - \tilde{u})^2 - \lambda\hat{p}\right)\delta u = 0.$$

The first term in previous equation is expanded again from the initial configuration of the perfect structure ($u_0 = 0, \lambda = 0$)

$$\Phi''[\tilde{u}](u_d - \tilde{u})\delta u = (\Phi_0'' + \Phi'''\tilde{u})(u_d - \tilde{u})\delta u$$

and, remembering that $\Phi_0''\hat{u}\delta u = p\delta u$

$$\left(\Phi_0''(v + w) + \frac{1}{2}\Phi'''(\lambda\hat{u} + v + w)^2 + \Phi'''\tilde{u}(\lambda\hat{u} + v + w)\right)\delta u = 0. \tag{2.46}$$

With a further Taylor expansion of $\Phi_0''(\cdot)$ starting from the $u_k = \lambda_k \hat{u}$ and letting $\Phi_k'' = \Phi''[u_k]$

$$\Phi_0''(v+w)\delta u = (\Phi_k''(v+w) - \lambda_k \Phi'''\hat{u}(v+w))\delta u$$

the Eq.(2.46) becomes

$$\left(\Phi_k''(v+w) + (\lambda - \lambda_k)\Phi'''\hat{u}(v+w) + \frac{1}{2}\lambda^2\Phi'''\hat{u}^2 + \frac{1}{2}\Phi'''(v+w)^2 + \Phi'''\tilde{u}(\lambda\hat{u} + v + w)\right)\delta u = 0. \tag{2.47}$$

It is worth mentioning again that Eq.(2.47) does not contain any truncation error. Furthermore note that the equilibrium condition for the structure with no imperfection is regained for $\tilde{u} = 0$.

Projection of the equilibrium equation in the space $\mathcal{W}$.

The corrective field $w \in \mathcal{W}$ is obtained by projecting Eq.(2.47) in direction δw, i.e. assuming $\delta u = \delta w$, and expanding it in Taylor series up to the second order in the asymptotic parameters $(\lambda, \xi_i, \tilde{\xi}_i)$. The term $\Phi_k''\dot{v}\delta w$, by exploiting the bifurcation $\Phi_i''\dot{v}_i\delta u = 0$ and the orthogonality $\Phi'''\hat{u}\dot{v}_i\delta w = 0$ conditions, becomes

$$\Phi_k''\dot{v}\delta w = \sum_{i=1}^{n} \xi_i \left\{\Phi_i''\dot{v}_i + (\lambda_k - \lambda_i)\Phi'''\hat{u}\dot{v}_i\right\}\delta w = 0$$

that allows the simplification of the residual equation as

$$\begin{aligned}\tilde{r}_w[\xi_i, \lambda, \tilde{\xi}] \equiv \Big\{ &\Phi''[\lambda\hat{u}]w + \frac{1}{2}\lambda^2\Phi'''\hat{u}^2 \\ &+\frac{1}{2}\Phi'''(v^2 + 2wv + w^2) + \Phi'''\tilde{u}(\lambda\hat{u} + v + w)\Big\}\delta w = 0\end{aligned} \tag{2.48}$$

with $\Phi''[\lambda\hat{u}]w = \Phi_k''w + (\lambda - \lambda_k)\Phi'''\hat{u}w$.

Assuming

$$\Phi''[\lambda\hat{u}]w \approx \Phi_b''w \quad \text{with} \quad \Phi_b'' \equiv \Phi''[\lambda_b\hat{u}]$$

with λ_b a suitable reference value of the bifurcation cluster and maintaining only the terms of the quadratic polynomial order in $\lambda, \xi_i, \tilde{\xi}_i$ the residual equation simplifies as

$$\tilde{r}_w[\lambda, \xi_i, \tilde{\xi}_i] \equiv \left\{\Phi_b''w + \frac{1}{2}\lambda^2\Phi'''\hat{u}^2 + \frac{1}{2}\Phi'''v^2 + \Phi'''\tilde{u}(\lambda\hat{u} + v)\right\}\delta w = 0. \tag{2.49}$$

Remembering the expression of $v[\xi_i]$, the quadratic correctives of the imperfect structure are sums of the correctives for zero imperfections of Eq.(2.30) and of the additional contribution due to the geometrical imperfection

$$w[\xi_i, \tilde{\xi}_i, \lambda] = \frac{1}{2}\lambda^2\hat{w} + \frac{1}{2}\sum_{i,j}\xi_i\xi_j\ddot{w}_{ij} + \tilde{w} \tag{2.50}$$

where

$$\tilde{w} = \lambda\tilde{\hat{w}} + \sum_i \xi_i \dot{\tilde{w}}_i \tag{2.51}$$

with

$$\tilde{\hat{w}} := \sum_j \tilde{\xi}_j \hat{\tilde{w}}_j, \quad \dot{\tilde{w}}_i := \sum_j \tilde{\xi}_j \dot{\tilde{w}}_{ij}. \tag{2.52}$$

The terms in Eq.(2.52) can be evaluated, once and for all in the perfect structure step of the Koiter analysis, being known the imperfection basis, as

$$\begin{cases} \Phi_b'' \hat{\tilde{w}}_i \delta w = -\Phi''' \hat{u} \bar{u}_i \delta w \\ \Phi_b'' \dot{\tilde{w}}_{ij} \delta w = -\Phi''' \dot{v}_i \bar{u}_j \delta w \end{cases} \quad \forall \delta w \in \mathcal{W}. \tag{2.53}$$

The new reduced equations with geometrical imperfection.

Exploiting the orthogonality condition $\Phi''' \hat{u} w \dot{v}_k = 0$ the kth equilibrium equation, obtained assuming $\delta u = \dot{v}_k$ in Eq.(2.47), becomes

$$\tilde{r}_k \equiv \left((\lambda - \lambda_k)\Phi''' \hat{u} v + \frac{1}{2}\lambda^2 \Phi''' \hat{u}^2 + \frac{1}{2}\Phi'''(v+w)^2 + \Phi''' \tilde{u}(\lambda\hat{u} + v + w) \right) \dot{v}_k = 0. \tag{2.54}$$

Substituting the expression of w and v previously obtained, using the mode normalization condition in Eq.(2.26) and maintaining terms in $\lambda, \xi_i, \tilde{\xi}_i$ until the 3rd polynomial order, the equilibrium equation becomes

$$\tilde{r}_k[\lambda, \xi_i] \equiv r_k[\lambda, \xi_i] + \tilde{\mu}_k[\lambda, \xi_i] = 0, \quad k = 1 \cdots m \tag{2.55}$$

with $r_k[\lambda, \xi_i] = 0$ the kth reduced equilibrium equation in Eq.(2.31) and the new imperfection factor $\tilde{\mu}_k$ defined as

$$\begin{aligned} \tilde{\mu}_k \equiv & \sum_i \xi_i \lambda \Phi''' v_i \hat{\tilde{w}} \dot{v}_k + \frac{1}{2}\sum_{ij} \xi_i \xi_j \left(\Phi''' v_i \dot{\tilde{w}}_j \dot{v}_k + \Phi''' v_j \dot{\tilde{w}}_i \dot{v}_k + \Phi''' \tilde{u} \ddot{w}_{ij} \dot{v}_k \right) \\ & + \lambda \Phi''' \tilde{u}(\hat{u} + \hat{\tilde{w}}) \dot{v}_k + \sum_i \xi_i \Phi''' \tilde{u}(\dot{v}_i + \dot{\tilde{w}}_i)\dot{v}_k + \frac{1}{2}\lambda^2 \Phi''' \tilde{u} \hat{\tilde{w}} \dot{v}_k. \end{aligned} \tag{2.56}$$

It is possible to observe that the only change, with respect to the standard reduced system in subsection 2.3.1 regards the imperfection coefficient $\tilde{\mu}_k$ which is now more complex than the one used in Eq.(2.32), which only maintains the linear contribution in λ

$$\tilde{\mu}_k = \lambda \Phi''' \hat{u} \tilde{u} \dot{v}_k$$

while the quadratic terms in λ and the terms in ξ are neglected, leading to inaccuracy as the pre-critical nonlinearity increases.

Furthermore, note that the proposed reduced model assumes the following final expression

$$u_d[\lambda, \xi_i, \tilde{\xi}_i] = \tilde{u} + \lambda(\hat{u} + \hat{\tilde{w}}) + \sum_i \xi_i (\dot{v}_i + \dot{\tilde{w}}_i) + \frac{1}{2}\sum_{ij} \xi_i \xi_j \ddot{w}_{ij} + \frac{1}{2}\lambda^2 \hat{\tilde{w}}. \tag{2.57}$$

The new correctives can be seen as a correction to the fundamental path tangent and the buckling modes of the perfect structures in order to take into account the geometrical imperfection.

2.4.3 FEM implementation of the proposed algorithm

The construction of the reduced model of the perfect structure presented in subsection 2.3.2 is completed by adding the evaluation of the new corrective after Eq.(2.36c)

$$\begin{cases} \mathbf{K}_b \dot{\tilde{\mathbf{w}}}_{ij} + \tilde{\mathbf{p}}_{ij} & = \mathbf{0} \\ \mathbf{K}_b \hat{\tilde{\mathbf{w}}}_i + \tilde{\mathbf{p}}_{0i} & = \mathbf{0} \end{cases} \quad , \quad \forall \mathbf{w} \in \mathcal{W} \tag{2.58}$$

where

$$\delta \mathbf{w}^T \tilde{\mathbf{p}}_{ij} = \Phi_b''' \bar{v}_j \dot{u}_j \delta w \quad \delta \mathbf{w}^T \tilde{\mathbf{p}}_{0i} = \Phi_b''' \hat{u} \bar{u}_i \delta w.$$

The imperfection coefficients $\tilde{\mu}_k$ are evaluated using the expression (2.56) instead of (2.33). Once the reduced nonlinear system (2.55) is solved, the equilibrium path is traced according to (2.57).

The computational cost of the Koiter method with the proposed a-posteriori account of the geometrical imperfections remains of the order of that required by a standard linearised buckling analysis, that is dominated by the factorization of the matrix $\mathbf{K}_0$. With respect to the standard approach, recalled in the previous section, it is necessary to evaluate the new $m \times m$ correctives $\dot{\tilde{\mathbf{w}}}_{ij}$, and m correctives $\hat{\tilde{\mathbf{w}}}_i$ by means of the linear problem in Eq.(2.58) and the corresponding third order strain energy variations in Eq.(2.56).

2.5 Numerical results

In this section some benchmarks are considered in order to test the accuracy of the proposed a-posteriori account of geometrical imperfection. A comparison with the different approaches is made. In particular, the numerical results report:

- the solution of the full FE model nonlinear equations (2.42), obtained using a standard path-following technique, denoted as *Riks* and considered the reference solution;

- the solution obtained through the Koiter method including the imperfection a-priori in the model by assuming $u_0 = \tilde{u}$ in subsection 2.3.1, which means that the reduced model is re-constructed for each imperfection while $\tilde{\mu}_k = 0$, denoted as K_0;

- the solution obtained through the Koiter method using the reduced model of the perfect structure, built once and for all, and taking into account the imperfection a-posteriori in the standard way recalled in 2.3.1, denoted as K_{lin};

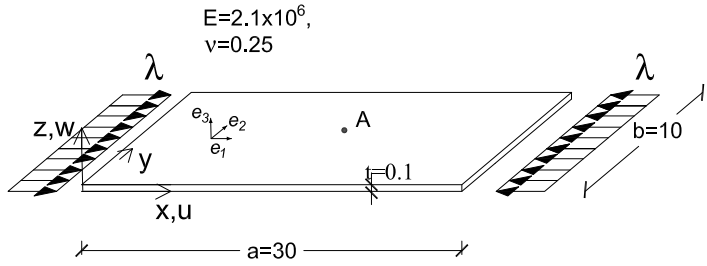

Figure 2.1: Simply supported plate: geometry, load and boundary conditions.

- the solution obtained through the Koiter method using the reduced model of the perfect structure, built once and for all, and taking into account the imperfection a-posteriori according to the new proposal described in 2.4.2, denoted as K_{quad}.

The geometrical imperfection is given as a linear combination of the displacement shapes of the buckling modes and its maximum displacement components, denoted as $\tilde{u}_{max}$.

2.5.1 Simply supported plate

The first example regards a simply supported and uniformly compressed plate whose geometry, load and boundary conditions are reported in Fig.2.1. The imperfection shape is proportional to the first buckling mode reported in the same figure.

Fig.2.2 shows the equilibrium paths obtained with the different methods. In this case the proposed K_{quad} approach provides results very similar to reference *Riks* ones, even for a large imperfection magnitude, while the standard K_{lin} approach gives a result which is completely wrong. In this case the energy terms associated with $\dot{\tilde{\mathbf{w}}}$ and $\hat{\tilde{\mathbf{w}}}$ are large also for small values of the imperfection amplitude due to the membrane hyperstaticity of the plate.

2.5.2 Cylindrical isotropic and laminated roofs

The structure, whose geometry and loads are pictured in Fig.2.3, is a semi-cylindrical roof loaded by a central force whose curved edges are free while the straight ones are hinged. Three material configuration are studied: the first one in an isotropic material characterized by $E = 3.10275$ and Poisson ratio $\nu = 0.3$, the second and the third ones are laminated materials characterized by two different layups, $[0°/90°/0°]$ and $[90°/0°/90°]$ respectively with respect to the $\mathbf{e}_1$-axis, whose properties are reported in Fig.2.3. The FE mesh consists of 18×8 elements.

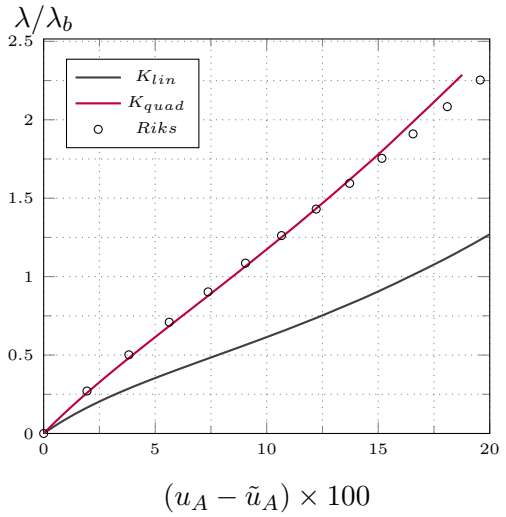

Figure 2.2: Simply supported plate: geometry and equilibrium paths for $\tilde{u}_{max} = t$

The imperfection shape is the displacement shape of the first buckling mode. In Figs.2.4, 2.5 and 2.6 the equilibrium paths and the limit loads for different values of the imperfection amplitude $\tilde{u}_{max}$ are reported. It is possible to observe how the proposed Koiter method with a-posteriori account K_{quad} furnishes accurate results for significant values of the imperfection amplitudes, very close to the a-priori account K_0 whose limit load always coincides with the *Riks* one. Since the pre-critical behaviour is nonlinear even for the structure without imperfections, the standard a-posteriori account K_{lin} fails also for very small imperfection amplitudes.

Finally, it is worth noting from Fig.2.7 how the buckling mode corrected with $\dot{\tilde{w}}_1$, according to Eq.(2.57), has a shape similar to those obtained considering the imperfection a-priori in the FE model.

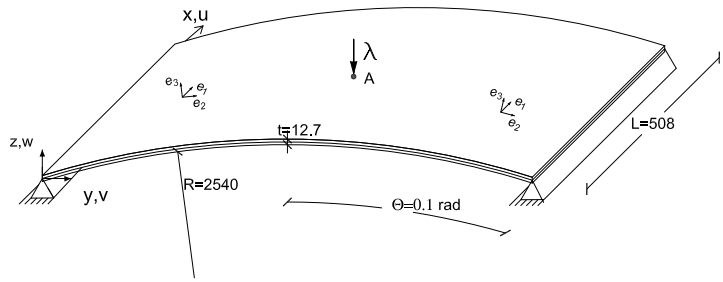

E_{11}	$E_{22} = E_{33}$	$\nu_{12} = \nu_{13}$	ν_{23}	$G_{12} = G_{13}$	G_{23}
3.3	1.1	0.25	0.25	0.66	0.44

Figure 2.3: Cylindrical roof subjected to a central pinching force with material properties of the ply.

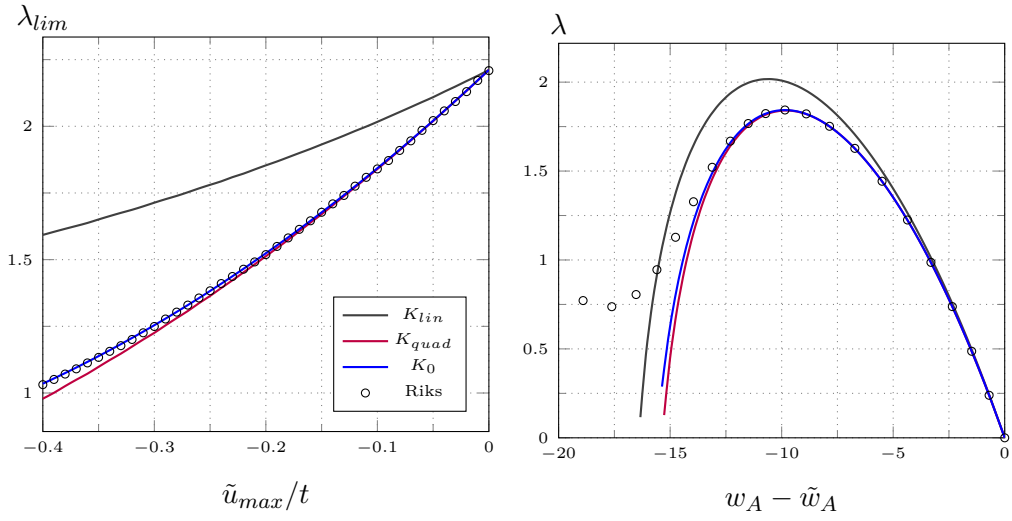

Figure 2.4: Cylindrical isotropic roof: limit load versus imperfection magnitude (left) and equilibrium paths for $\tilde{u}_{max} = 0.1t$ (right).

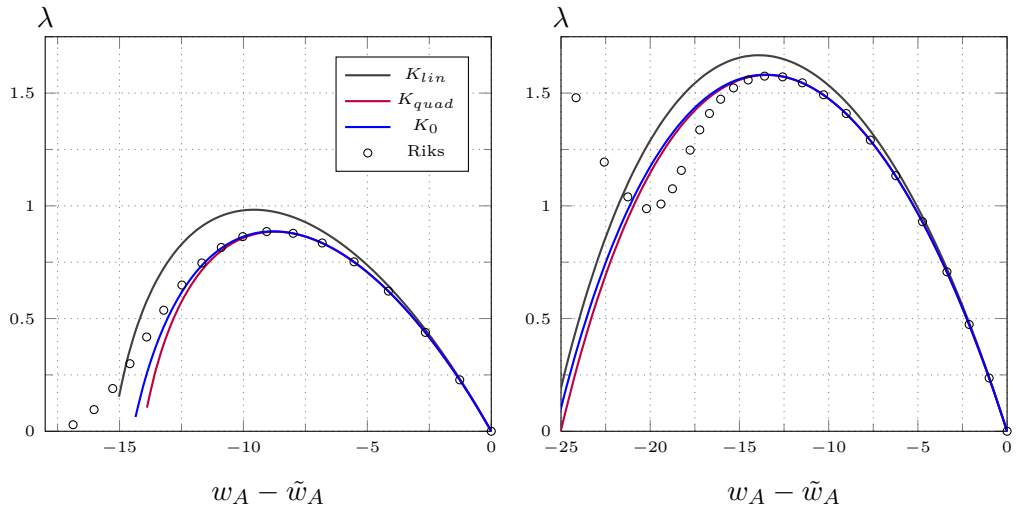

Figure 2.5: Cylindrical laminated roof: equilibrium paths for $u_{max} = 0.1t$ for layup [0/90/0] (left) and [90/0/90] (right).

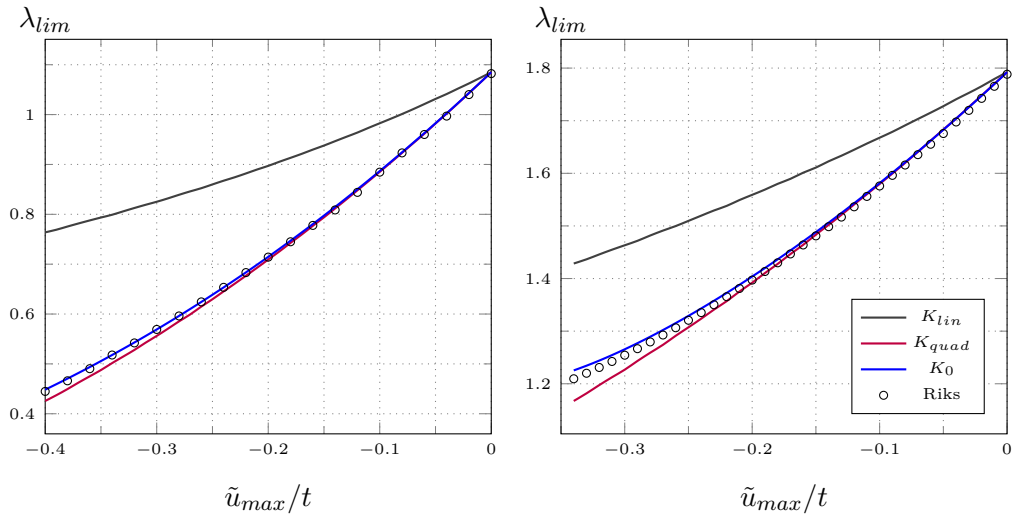

Figure 2.6: Cylindrical laminated roof: limit load vs imperfection magnitude for layup [0/90/0] (left) and [90/0/90] (right).

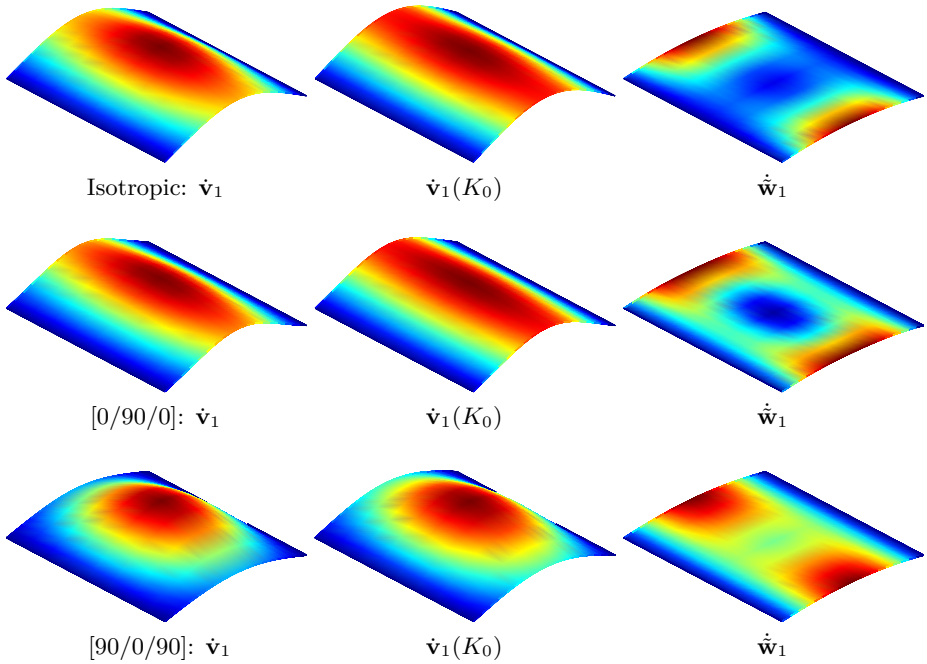

Figure 2.7: Cylindrical roof: bucking mode of the structure without imperfection, with $\tilde{u}_{max} = 0.2t$ and $\dot{\tilde{w}}_1$ for either isotropic, [0/90/0] and [90/0/90] cases.

2.5.3 Compressed simply supported channel section

A simply supported channel section, whose geometry and material properties are reported in Fig.2.8 is now analysed with 2 different shapes of the imperfection depicted in Fig.2.13: the first one is the displacement shape of the first buckling mode (flexural), the second one corresponds to the displacement shape of the 3rd buckling mode (local with 13 half-waves). The structure exhibits buckling mode interaction phenomena.

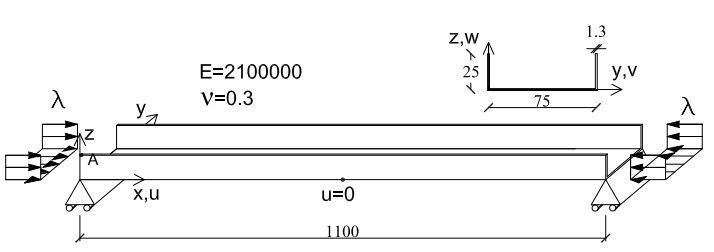

Figure 2.8: Compressed simply supported channel section with material properties.

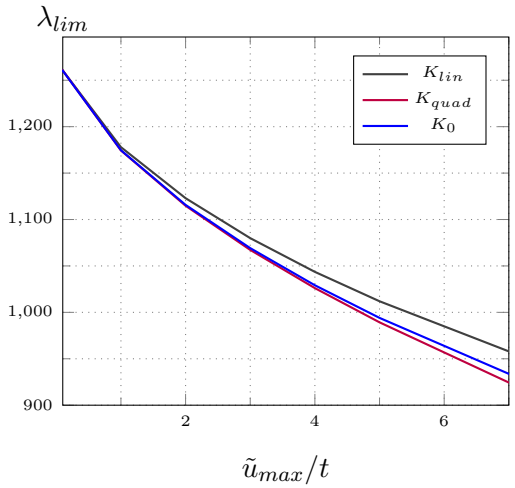

Figure 2.9: C-section: limit load versus imperfection magnitude for flexural imperfection.

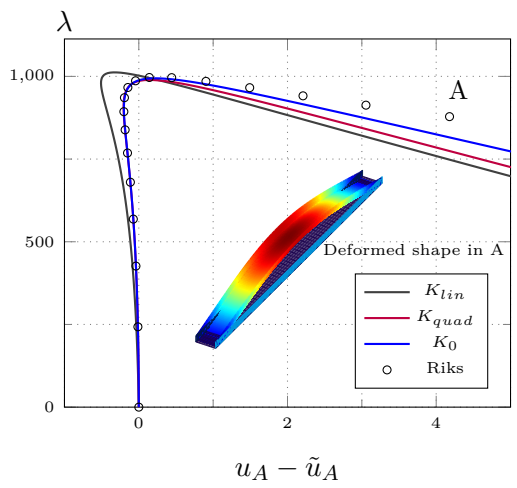

Figure 2.10: C-section: equilibrium paths for first buckling shape imperfection and $u_{max} = 5t$ (upwards).

In Fig.2.9 it is reported how the limit loads change with the amplitude of the first imperfection, while Fig.2.10 shows the equilibrium paths for $\tilde{u}_{max} = 5t$. In Fig.2.11 the buckling modes and correctives for K_0 and K_{quad} are reported. It can be observed how the buckling mode of the imperfect structure presents a shortening, while for the perfect structure presents a similar shape by summing

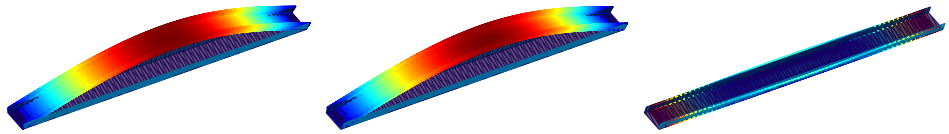

Figure 2.11: C-section: buckling mode of the structure without imperfection (left), with an imperfection in the direction of the first buckling mode of amplitude $\tilde{u}_{max} = 5t$ (centre) and the relative $\dot{\tilde{w}}_1$ (right, displacement factor 10).

its first buckling mode $\dot{v}_1$ and the corrective $\dot{\tilde{w}}_1$, according to Eq.(2.57). The good behaviour in the evaluation of the limit point of K_{quad} is evident while K_{lin} presents significant errors in the equilibrium path evaluation notwithstanding the fairly accurate value of the limit load.

In Fig.2.12 the equilibrium paths and the deformed shapes in two equilibrium points for the second imperfection, are presented. The corresponding mode shapes and how they change with the imperfection are reported in Fig.2.13. Also in this case the good behaviour of the proposal K_{quad}, compared to K_{lin}, is evident.

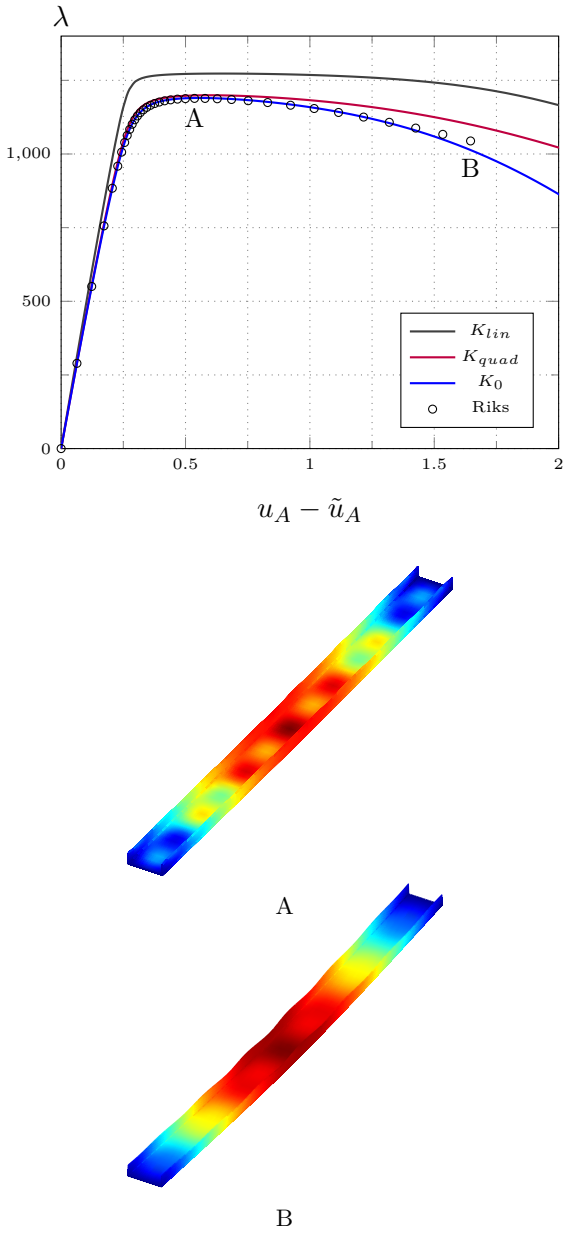

Figure 2.12: C-section: equilibrium paths and deformed configurations for third buckling shape imperfection and $\tilde{u}_{max} = -0.5t$. 12 modes have been considered in asymptotic analysis.

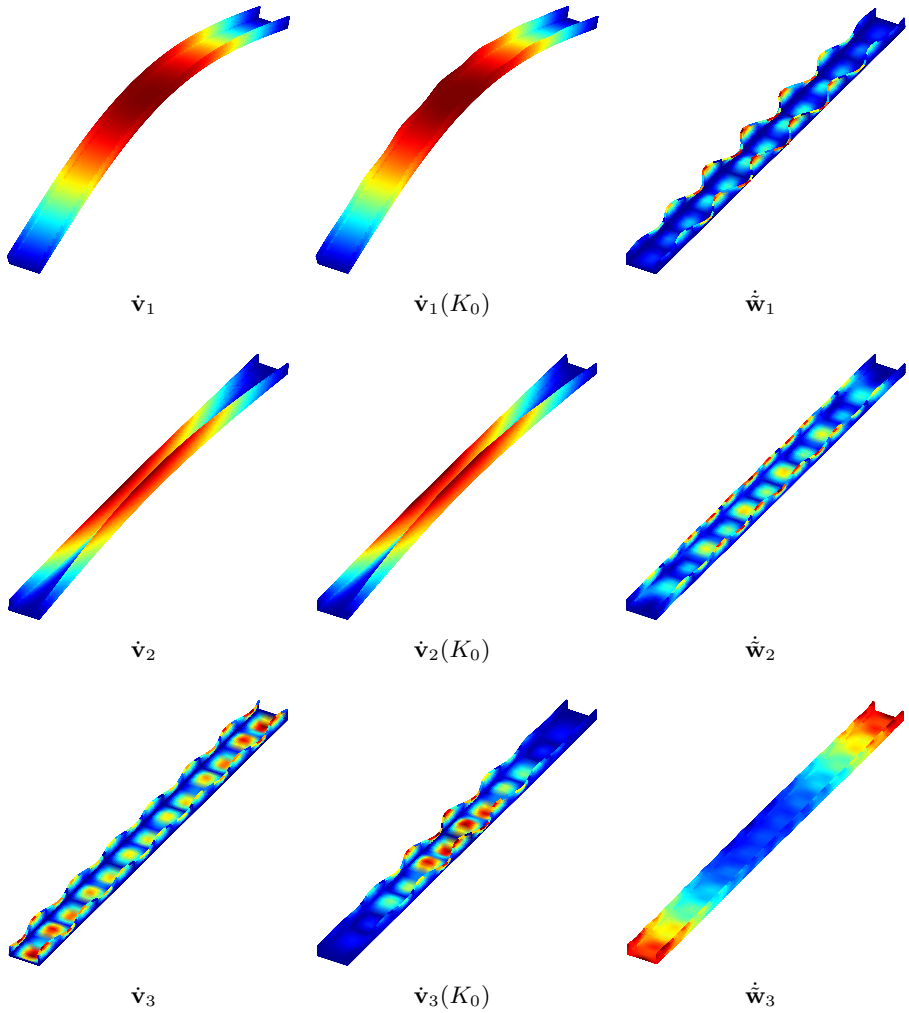

Figure 2.13: C-section: first, second and third buckling modes of the structure without imperfection, with $\tilde{u}_{max} = 0.5t$ in the direction of the third buckling mode and $\dot{\tilde{w}}$ (displacement factor 10).

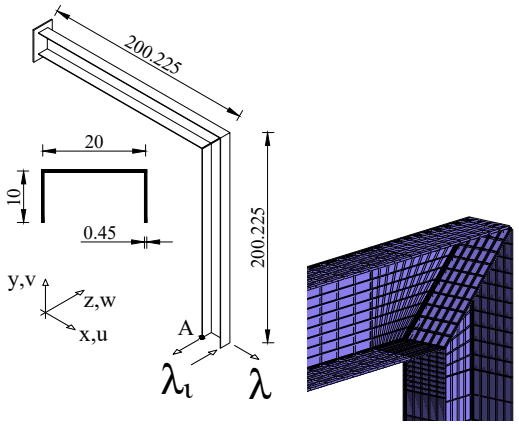

Figure 2.14: Frame: geometry and mesh grid detail.

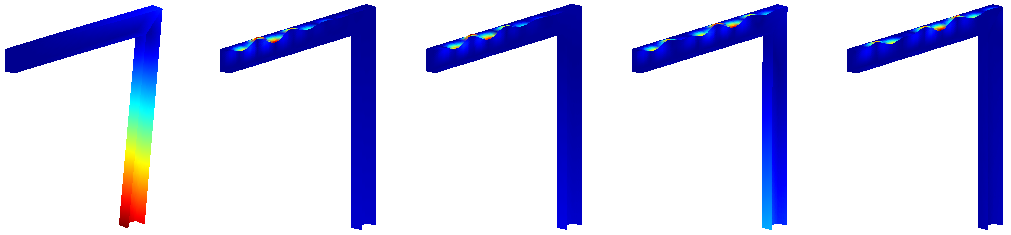

$\lambda_{b,1} = 0.570.$ $\lambda_{b,2} = 0.722.$ $\lambda_{b,3} = 0.726.$ $\lambda_{b,4} = 0.769.$ $\lambda_{b,5} = 0.774.$

Figure 2.15: Frame: First 5 buckling modes of the structure without geometrical imperfections.

2.5.4 Frame

The last test regards the frame reported in Fig.2.14. The first 5 buckling modes of the perfect structure are reported in Fig.2.15, while the limit load versus imperfection amplitude curve for a geometrical imperfection with the shape of the second buckling mode and the equilibrium path for $\tilde{u}_{max} = 0.4t$ are reported in Fig.2.16. In the same figure, the equilibrium path of the structure without imperfections is presented, in order to point out the strong imperfection sensitivity of the frame and the modal interaction phenomenon. Even in this last case the proposal K_{quad} provides very accurate results with a limit point which coincides with the a-priori account K_0 and *Riks* solution, while inaccuracies occur for K_{lin}.

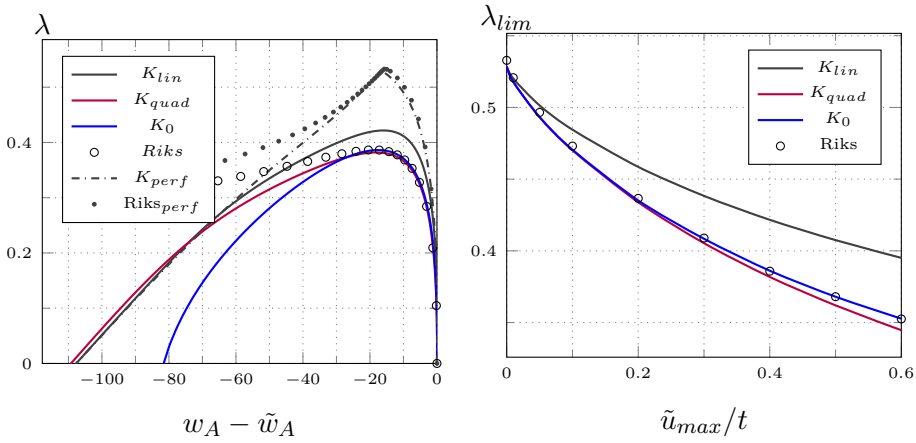

Figure 2.16: Frame: equilibrium paths for geometrical imperfection along the second buckling mode and $\tilde{u}_{max} = 0.4t$ (left) and magnitude imperfection sensitivity (right).

2.6 Summary

A new strategy to include, a-posteriori, geometrical imperfections in Koiter analysis was proposed in this chapter. The main idea is to correct the linear modes of the perfect structure reduced model using additional corrective modes, which take into account the imperfections. The reduced system of the imperfect structure is obtained starting from the system of the perfect structure by adding some terms, which coherently consider the geometrical imperfection up to the second order. In this way, the Koiter method with a-posteriori account of the imperfections becomes accurate even for pre-critical nonlinearities and significant imperfection amplitudes, making the approach suitable for a wide range of practical problems. A large number of numerical tests, regarding shell structures in both isotropic or laminated materials and also presenting multimodal buckling and pre-critical nonlinearities, validated the proposal. The limit load provided by the new a-posteriori account is very close to the path-following reference solution and to that provided by the Koiter method with the imperfection included a-priori in the model. Finally, this work confirmed that the Koiter method is definitely a suitable tool for analysing imperfection sensitive structures and showed that the a-posteriori account of the geometrical imperfections is not only a possibility, but also an accurate and efficient choice. Interested readers can find further details in [59, 71].

Chapter 3

Post-buckling optimisation strategy of imperfection sensitive composite shells using Koiter method and Monte Carlo simulation

Abstract

A numerical stochastic strategy for the optimisation of composite elastic shells undergoing buckling is presented. Its scope is to search for the best stacking sequence that maximises the collapse load optimising the post-buckling behaviour. Its feasibility is due to a reduced order model built for each material setup starting from a hybrid solid-shell finite element model exploiting a multimodal Koiter method. The approach has no limitations concerning geometry, boundary conditions and distribution of the elastic properties. The collapse load is evaluated using a Monte Carlo simulation able to detect the worst imperfection shape, including a-posteriori the imperfections in the reduced order model. For a limited number of parameters the proposal allows to analyse all the possible layups. In the general case, it makes use of a random scanning of the design parameters with different levels of adaptability.

3.1 Introduction

Thin-walled composite panels are common in a wide range of engineering applications nowadays, particularly in the aeronautic and aerospace context, where they are often employed as primary structural components. Due to the high

strength/weight ratio, the structural response is dominated by buckling and it turns out to be mainly influenced by two factors: the geometry and the elastic properties. While the former is often imposed by the structural functionality and only little changes are possible, the spatial distribution of the material properties, e.g fibre orientations, can be easily tailored in composite shells. As a consequence, an efficient optimisation process of the material is required to obtain the desired structural response, usually defined in terms of deflections and load-carrying capacity. Many manufacturing options are currently available for this purpose: multi-layered and variable thickness composites [72], variable angle tows (VATs) [73] and grid stiffeners [74].

Many optimisation strategies proposed in the literature use the linearised buckling load as the objective function of the design. In [75], a parametric study on rectangular composite plates points out how the buckling load changes with geometry, boundary conditions and stacking sequence, with the aim of providing guidelines for designers. An optimisation of the stacking sequence with respect to the buckling load is carried out in [76] for panels with T stiffeners, in [77, 78] for VAT plates and in [79] the optimisation focuses on stiffened laminated wing panels.

However, when optimised with respect to the linearised buckling load, structures often suffer from a phenomenon known as buckling mode interaction, which leads to an unstable post-critical behaviour [80]. These structures often exhibit a high sensitivity to imperfections, that is a deterioration of their bearing capacity due to geometrical, load and material deviations [5]. For this reason, a more reliable design, which takes account of the full geometrically nonlinear behaviour, has also been investigated over the years. In this framework, a collapse state is declared when the applied load exceeds the limit load, for the unstable cases, or because it produces deformations which compromise the usability, accounting for the stiffness reduction that typically characterises the post-buckling regime. Optimising the post-buckling behaviour in terms of collapse load is, however, a challenging task. In fact, a suitable mechanical model and its discrete approximation are required to describe the complexity of practical problems in terms of geometry, boundary conditions and structural behaviour accurately. This means that the structural response is generally described by a high number of discrete nonlinear equations, whose solution furnishes the equilibrium path. Furthermore, as the collapse load can be strongly influenced by small deviations of geometry, material properties and boundary conditions, the equilibrium path should be evaluated for a statistically significant number of imperfections in order to obtain a reliable estimate of the load safety factor.

The Riks arc-length strategy, based on the Newton method, is the standard tool for solving the discrete nonlinear equations and reconstructing the equilibrium path. Although this approach is effective for assigned data, it is not suitable for an optimisation process, which requires the evaluation of the equilibrium path for each change in the design variables, and for an imperfection sensitivity analysis

because the single run is too time consuming with current CPUs. For these reasons, when addressing this topic, researchers focused their attention on simplified approaches following, often simultaneously, two main strategies: i) reducing the number of discrete variables by using simplifying assumptions on the mechanical model and its discrete approximation; ii) using optimisation strategies based on a quick prediction of the post-critical behaviour by means of simplifying assumptions on nonlinear response. Different proposals are available in literature. In [81] the post-buckling behaviour of compressed rectangular plates is studied by a semi-analytical solution and the layer thicknesses are chosen as optimisation variables. The nonlinear response is described by a path-tracing finite element (FE) analysis in the optimisation algorithm proposed in [82]. It consists in optimising, with respect to the design variables, the collapse load evaluated by a nonlinear buckling problem. The algorithm is extended in [83, 84] in order to take account of geometrical imperfections and the worst imperfection case is included in the optimisation process. A study of the effect of the material degradation in the design of curved stiffened panels is presented in [85]. A Rayleigh–Ritz method which allows the effective treatment of simple geometries is employed in [86]. This model is used to minimize the maximum transverse displacement of stable VAT plates in the post-buckling regime. In [72] the same authors look for a "Buckle Free" solution, that is limiting the axial stiffness reduction after bifurcation. The optimisation of grid-stiffened structures with curved stiffeners in the critical and post-critical regime is addressed in [87, 74] by using a hybrid model and surrogate models. The hybrid framework presented allows dimple imperfections to be taken into account.

An interesting way of coherently performing an optimisation of slender structures is offered by strategies based on Koiter's theory of elastic stability [46]. They make use of an asymptotic expansion of the equilibrium equations which allows the description of the initial post-critical behaviour in terms of some variables related to the slope and curvature of the bifurcated branches [88]. These quantities can be optimised in order to obtain the desired structural response. A first attempt in using the Koiter method to perform a minimum weight optimisation of stiffened curved panels, discretised by means of the finite strip method, is proposed in [89]. The post-buckling regime is expressed in a semi-analytical form and depends on 4 variables only. More recently, in [88, 90], formulations based on simplified structural models and a single buckling mode are used to optimise the post-buckling behaviour of composite and VAT structures.

Despite the difficulties found in modelling the structural problem and predicting the nonlinear behaviour, another tricky issue is the solution of the optimisation problem. This is always expressed, indeed, as a nonlinear and non convex mathematical programming problem, whose solution is generally computationally expensive and extremely difficult because of the possible presence of multiple local minima. It represents, ultimately, the most penalising aspect of the analysis. Among the others, frequently employed solution strategies are the random search

methods [79], genetic algorithms [91] and gradient based techniques such as the method of moving asymptotes [92] and sequential linear programming [93].

In this work, we propose an optimisation strategy for composite shells which uses a reduced order model (ROM), obtained by the FE implementation of the multimodal Koiter method seen in the previous chapter, for the evaluations of the equilibrium path. In particular, the nonlinear equilibrium equations are written for a solid-shell FE discretisation and are projected in a suitable subspace, defined by an asymptotic expansion of the FE unknowns based on the initial path tangent, the first linearised buckling modes and second order modes, named quadratic correctives. In this way, it is possible to build a ROM in which the complexity of the structural problem, including complex geometries and behaviours, is preserved while the number of variables is drastically reduced to a few modal amplitudes, since a few buckling modes are usually necessary to estimate the initial post-buckling response. Complex material configurations can also be easily analysed as shown in recent applications to VAT panels [63]. Furthermore, the use of an efficient total Lagrangian solid-shell FE model based on a mixed (stress-displacement) description reduces the effort for the construction of the ROM and makes it possible to easily evaluate the interactions among buckling modes. In addition, the solid-shell FE allows an accurate modelling of complex geometrical local features like stiffeners. The accuracy of the ROM based on this asymptotic formulation has been extensively tested in the evaluation of the equilibrium path of shell structures [59, 49] obtaining results as accurate as those of path-following analyses. The solution of the optimisation problems is obtained by a stochastic simulation which can be collocated in the framework of the random search methods [94]. The goal is to maximise the collapse load by selecting an optimal stacking sequence of the multi-layered structure. The construction of the ROM, to be performed for each layup, is the most expensive part of the analysis but its cost is of the order of a linearised buckling analysis [49, 59, 5, 63]. The most interesting feature of this strategy is that the sensitivity to geometrical imperfections is easily included in the optimisation process. To this purpose, the collapse load is evaluated statistically by means of a Monte Carlo simulation aimed at detecting the worst imperfection shape. This requires the evaluation of the equilibrium path for thousands of randomly generated imperfection shapes in order to estimate the lowest collapse load for each layup. This kind of sensitivity analysis, that is generally very expensive, has conversely a negligible computational cost thanks to the possibility offered by the Koiter method of including a-posteriori, in the ROM of the perfect structure, the effects of the imperfections [71]. In this way, once the ROM of the perfect structure is available, the evaluation of equilibrium path for each imperfection only requires the solution of a small sized nonlinear system, usually of less than ten equations, carried out in fractions of second.

A stochastic strategy is employed to select random layups. It is a simple multi-stage process which evaluates the optimal solution as follows: i) an initial searching in the domain of all the possible layups is performed and the best solutions are

selected; ii) the optimal solution is obtained by searching in the neighbourhood of the best layups selected in i). For a limited number of the optimisation variables, it will also be shown how the efficiency of the Koiter method makes it possible to analyse all the possible layups by means of a uniform scanning. The effectiveness of the proposed strategy is tested on two structural optimisations regarding a curved panel and a stiffened curved panel in compression taking into account the worst imperfection shape.

3.2 Imperfection sensitivity analysis by Koiter method

Slender composite structures are sensitive to imperfections in many cases. This means that for an assigned set of data, the limit load value and the post-critical behaviour cannot be described properly without considering the effects of imperfections. Among all the possible deviations from the initial data those regarding the geometry are the most significant ones, as shown for instance in [95] for unstiffened cylinders. For this reason, this work focuses on these kind of imperfections considered as linear combinations of buckling modes. In this section, an imperfection sensitivity analysis based on the Koiter method [34] is presented for detecting the worst imperfections by means of a Monte Carlo approach. A solid-shell FE [10, 59] is used to make the method efficient and model the geometry, e.g. stiffeners, accurately.

A posteriori account of geometrical imperfections

Geometrical imperfections can easily be included in the analysis as shown in the previous chapter. They can be expressed as an initial displacement $\tilde{\mathbf{u}}$, assumed to be a linear combination of known shapes $\bar{\mathbf{u}}_i$,

$$\tilde{\mathbf{u}} = \sum_{i=1}^{n} \tilde{\xi}_i \bar{\mathbf{u}}_i. \tag{3.1}$$

In this work, the imperfection shapes $\bar{\mathbf{u}}_i$ are chosen as the displacement part of the buckling modes.

The method allows to take account of imperfections in the final stage by simply adding some additional imperfection terms $\tilde{\mu}_k$ to Eq.(2.31) that becomes

$$r_k + \tilde{\mu}_k = 0. \tag{3.2}$$

Over the years, two different approaches have been developed. The first one, as used in [34, 15, 37], modifies the ROM by simply adding the imperfection vector $\tilde{\mathbf{u}}$ to the ROM of perfect structure in Eq.(2.28)

$$\mathbf{u}_d[\lambda, \xi_i] = \tilde{\mathbf{u}} + \lambda \hat{\mathbf{u}} + \mathbf{v}[\xi_i] + \mathbf{w}[\xi_i, \lambda]. \tag{3.3}$$

This approach, labelled K_{lin}, proves to be extremely efficient but accurate only for small imperfection amplitudes and almost linear pre-critical behaviour. It is, in any case, a powerful tool to obtain information about the worst imperfection shapes because thousands of imperfections can be analysed in a few seconds.

The second strategy, named K_{quad}, has been recently proposed in [71] and updates the ROM as

$$\mathbf{u}_d[\lambda, \xi_i, \tilde{\xi}_i] = \tilde{\mathbf{u}} + \lambda(\hat{\mathbf{u}} + \tilde{\hat{\mathbf{w}}}) + \sum_i \xi_i(\dot{\mathbf{v}}_i + \dot{\tilde{\mathbf{w}}}_i) + \frac{1}{2}\sum_{ij} \xi_i \xi_j \ddot{\mathbf{w}}_{ij} + \frac{1}{2}\lambda^2 \hat{\tilde{\mathbf{w}}}. \tag{3.4}$$

considering new corrective modes generated by the imperfection, which can be seen as a correction to the initial path tangent and the buckling modes of the perfect structures. They can be evaluated as

$$\begin{cases} \mathbf{K}_b \dot{\tilde{\mathbf{w}}}_{ij} + \tilde{\mathbf{p}}_{ij} & = \mathbf{0} \\ \mathbf{K}_b \hat{\tilde{\mathbf{w}}}_i + \tilde{\mathbf{p}}_{0i} & = \mathbf{0} \end{cases}, \quad \forall \mathbf{w} \in \mathcal{W} \tag{3.5}$$

where

$$\tilde{\mathbf{p}}_{ij} = \mathbf{K}_1[\bar{\mathbf{v}}_i]\dot{\mathbf{u}}_j, \quad \tilde{\mathbf{p}}_{0i} = \mathbf{K}_1[\hat{\mathbf{u}}]\bar{\mathbf{u}}_i.$$

This approach is a little more expensive than the first one, but is more accurate in the case of nonlinear pre-critical path and increasing imperfection amplitudes. The projection of the FE equations (2.22) in directions $\dot{\mathbf{v}}_i$, $i = 1..m$ using the updated ROMs furnishes the imperfection effects on the ROM of the perfect structure in terms of the additional coefficients $\tilde{\mu}_k$ in Eq.(2.34).

The computational cost of the Koiter method with both a-posteriori accounts of the geometrical imperfections is of the order of that required by a standard linearised buckling analysis, that is dominated by the factorization of the matrix $\mathbf{K}_0$.

3.2.1 A Monte Carlo imperfection sensitivity analysis

The geometrical imperfections are expressed as in Eq.(2.45) where $\tilde{\xi}_i$ are uniformly random generated numbers that set the maximum imperfection shape to a fixed value

$$\max |\tilde{\mathbf{u}}| = \tilde{u}_{max}. \tag{3.6}$$

In this way it is possible to obtain a statistical sample of imperfections and to draw, for each of them, the equilibrium path. As is well known, we can have a stable post-critical behaviour, usually characterised by a reduction in the stiffness, or an unstable post-critical path with limit point. The collapse is reached because the applied load exceeds the limit load or because the stiffness reduction leads to deformations which compromise the usability. This means that the collapse load associated to $\tilde{\mathbf{u}}$ can be defined as the minimum between the limit load λ_{lim}, if it exists, and the load $\bar{\lambda}$ related to a fixed displacement of a control point

$$\lambda_c = \min_{\tilde{\mathbf{u}}} \Big\{ \lambda_{lim}(\tilde{\mathbf{u}}), \quad \bar{\lambda}(\tilde{\mathbf{u}}) \Big\}.$$

Because of its extreme nature, as shown in [56], the frequencies distribution of the limit load is best fitted by a type 1 extreme value distribution, also known as Gumbel max distribution. It defines the probability density function as

$$f(\lambda_c) = \sigma^{-1} \exp\left(\frac{\mu - \lambda_c}{\sigma}\right) \exp\left(-\exp\left(\frac{\mu - \lambda_c}{\sigma}\right)\right) \tag{3.7}$$

where μ and σ are the location parameter and scale parameter, respectively. It is also useful to define the cumulative distribution function as

$$F(\lambda_c) = \int_{-\infty}^{\lambda_c} f(x)dx \tag{3.8}$$

which represents the probability that a generic imperfection leads to a collapse load lower than λ_c. By inverting Eq.(3.8) it is possible to obtain the collapse load $\lambda_{c,x}$ which has the probability of x not being exceeded.

The number of imperfections to include in the sensitivity analysis is based on the convergence of the parameters μ and σ. In particular the number of imperfections starts from an initial value and is increased step by step until the parameters converge. The convergence criterion can be chosen as follows: the variation of μ and σ is limited to a tolerance value ϵ_π between two consecutive steps three times in a row, as expressed, for example for μ, as follows

$$\frac{\mu_j - \mu_i}{\mu_j} \leq \epsilon_\pi \quad \forall i = j-1, \cdots, j-3$$

where j denotes the current step.

3.3 Optimal layup design

In this section two simple optimisation approaches based on the proposed Koiter method are presented. Even if the proposed approaches are very simple they highlight how thousands of equilibrium path evaluations can be effectively performed. More refined stochastic algorithms [94] can also be adopted.

3.3.1 The optimisation algorithms

This section deals with the optimal design of imperfection sensitive shells. Although it focuses on seeking optimal layups for a fixed structural geometry, the procedure is general and can be easily adapted to geometry optimisation. In particular, the optimisation problem consists in searching for the solution which maximizes the collapse load λ_c, as defined in 3.2.1, that is

$$\begin{aligned} &\underset{\boldsymbol{\vartheta}}{\text{maximize}} \quad \lambda_c(\boldsymbol{\vartheta}) \\ &\text{subject to} \quad \vartheta_i \in \{0^\circ, 18^\circ, \ldots, 162^\circ, 180^\circ\} \end{aligned}$$

where ϑ_i is the fiber orientation of the ith layer and $\boldsymbol{\vartheta}$ is the vector collecting all ϑ_i. Depending on the way it is searched for in the optimization parameters domain, the procedure can be applied in two ways. The first one, named *Uniform scanning*, is the simplest and can be used when the optimisation involves a few parameters. The second one, called *Random scanning*, is more suitable when the number of parameters increases and it is based on a Monte Carlo like approach.

3.3.2 Uniform scanning

The approach is based on the simple idea of uniformly scanning the space of the possible layups. In this way, at the end of the process, the collapse load trend with the parameters is completely known and the actual optimal solution can be easily identified. Even if the number of analyses can be significantly high, the efficiency of the Koiter method makes them possible in a reasonable computational time when the space is defined by a few parameters. It is evident, indeed, that the number of analyses increases exponentially with the dimension of the sought parameter space.

The approach consists of two stages. During the first one the space is uniformly scanned and, for each lamination, an imperfection sensitivity analysis is performed to detect the collapse load. The K_{lin} approach to account a-posteriori for geometrical imperfection, as exposed in 3.2, is employed to identify the optimal solutions. The second stage is aimed at checking the best solutions found in stage 1 by repeating the imperfection sensitivity analysis with more restrictive tolerances on the μ and σ parameters, as defined in 3.2.1, and including their effect using the K_{quad} approach which proves to be more accurate. Finally, the structure with the best layup subjected to the worst imperfection shape is analysed by means of a path-following Riks analysis using the full FE model. The diagram in Fig.3.1 summarises the steps of the whole process.

3.3.3 Random scanning

The main problem of uniformly scanning the domain of the optimisation parameters is that the number of analyses can increase enormously and, although the Monte Carlo imperfection sensitivity analysis with the Koiter method is efficient, it can prevent the solution of the problem. The second approach proposed overcomes this problem by also using the Monte Carlo method to detect the best stacking sequence. There are three stages in this process. In the first one, the space of the optimisation parameters is sampled with a fixed number N_1 of uniformly generated random values and for each of them the imperfection sensitivity analysis furnishes the limit load and its fractile. Starting from the solutions of stage 1, the second stage better investigates some areas of the domain of interest, that is the areas near to the higher collapse loads. To this purpose, the Monte Carlo simulation at stage 2 (zooming stage) no longer uses uniform random num-

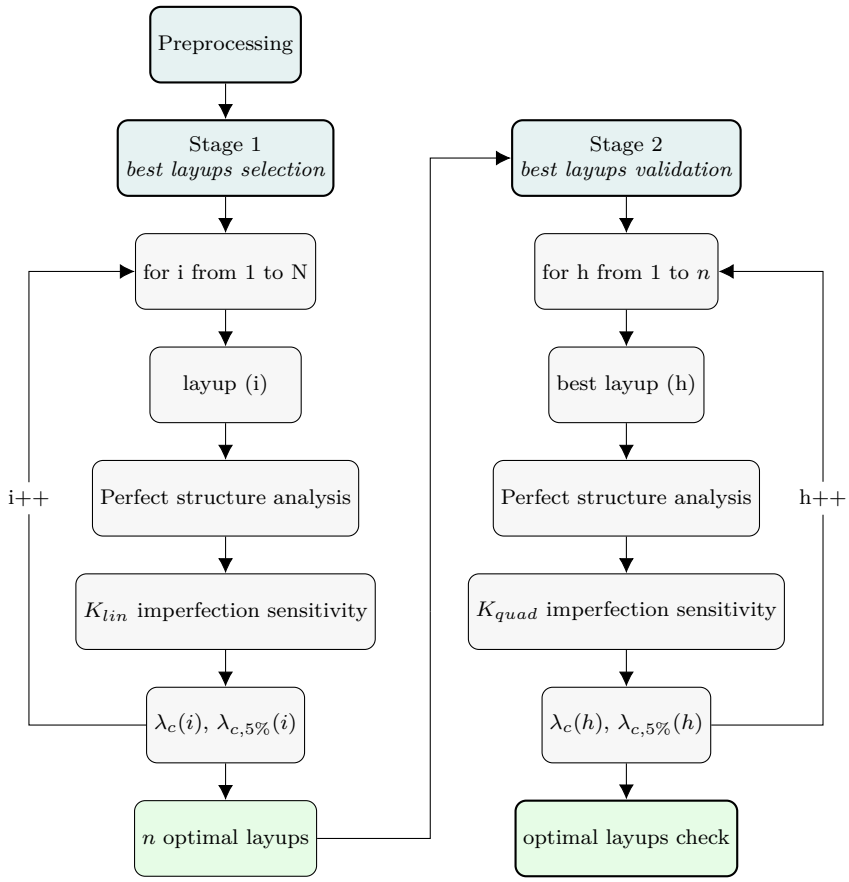

Figure 3.1: Diagram of the uniform scanning.

bers but a fixed number N_2 of random layups near to the laminations selected at the first stage. The population of layups of interest drastically reduces allowing an efficient estimate of the collapse load even for a large number of parameters. This strategy is particularly suitable for optimising the stacking sequence of imperfection sensitive slender structures because all the layer orientations can be chosen as independent optimisation parameters and their number is usually of the order of tens. In addition, the strategy can be adapted to the specific problem because subsequent zooming stages can be performed to investigate the areas of the domain that seem to be of particular interest from one stage to another until satisfactory results are obtained. After the zooming stage sequences a final stage is performed to validate the optimal results found; it is carried out using the K_{quad} formula to include imperfections effects and with a larger number of imperfection shapes. Lastly, the results are further tested with path following analyses on the selected laminations with the worst imperfection cases.

In Fig.3.2 the approach is summarised. It is written for the particular case of one zooming stage only. The continuum domain of the angles is discretised; its borders are denoted with ϑ_i and ϑ_f, while ϑ_p is the discretisation step. In the subsequent zooming stages the symbol δ is added to the domain borders to define the neighbourhood of the angles it is scanned in.

3.4 Numerical results

Two examples of stacking sequence optimisation based on the proposed strategy are presented in this section. The first one consists in searching for the optimal values of two lamination parameters of a curved panel in compression and, due to the relatively small complexity of the problem, the uniform scanning approach is employed. The second test regards the optimisation of a stacking sequence defined by eight parameters, that is the fibre orientation of each layer, and the random scanning approach is used because of the extremely large number of possible layups. The capability of the proposed approach for describing the overall structural behaviour as well as to find optimal solutions can be seen, highlighting the strong influence of the lamination on the collapse load. Concerning the sensitivity analysis for the detection of the worst imperfection shape, the results provided by the Koiter method with the two a-posteriori account of the imperfections (K_{lin} and K_{quad}) are compared with the full FE solution (labelled as $Riks$) obtained using the standard arc-length method.

3.4.1 Curved panel in compression

The test regards a curved cylindrical panel in compression. The geometry, the loads and the boundary conditions pictured in Fig.3.3 are related to the middle surface of the panel. The thickness of the shell is equal to $10\,mm$.

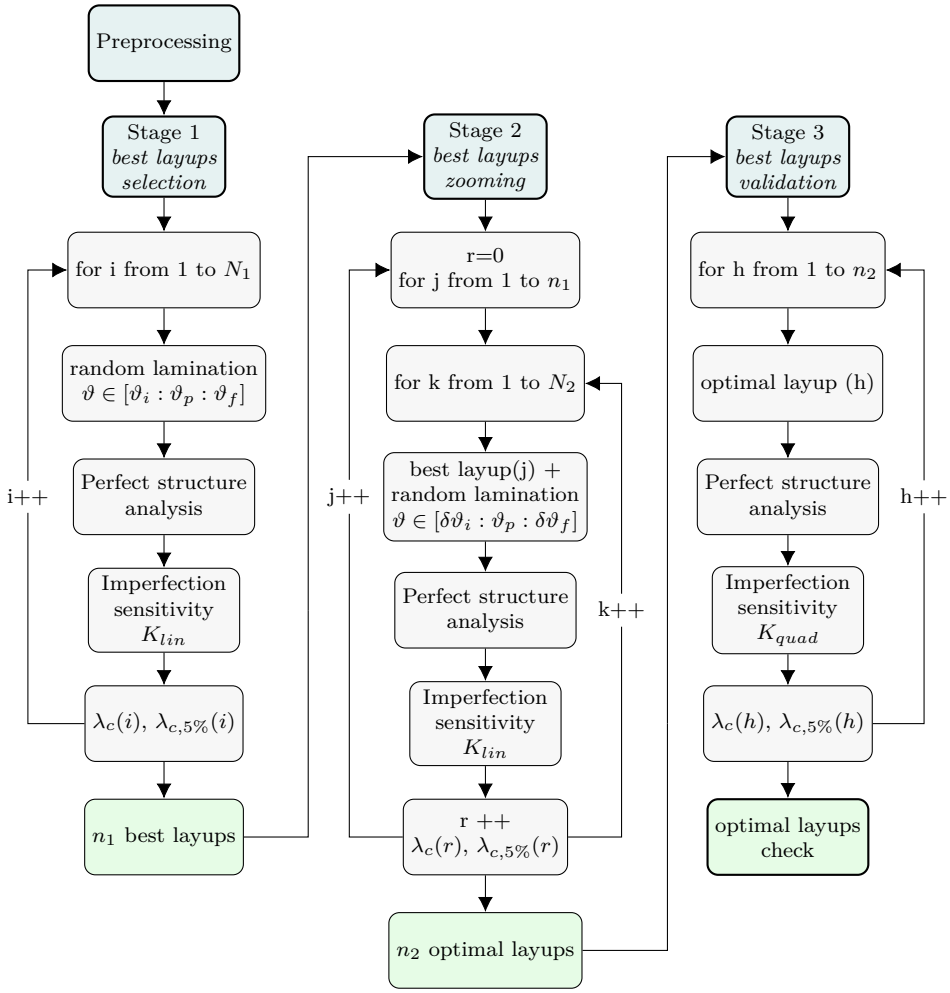

Figure 3.2: Diagram of the random scanning.

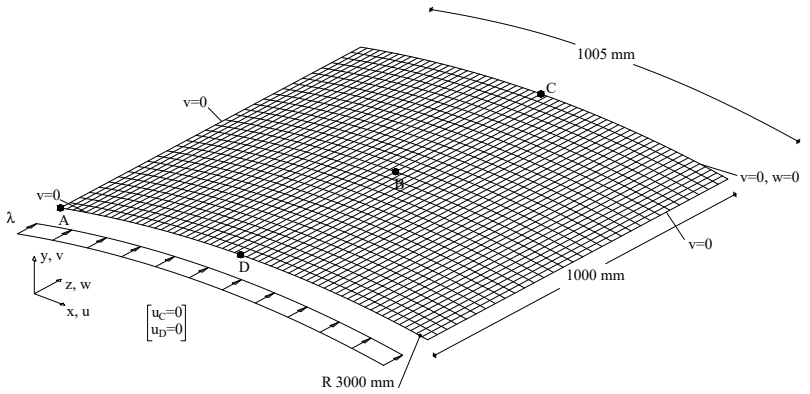

Figure 3.3: Curved panel: geometry and boundary conditions.

The properties of the material are $E_1 = 30.6\,GPa$, $E_2 = 8.7\,GPa$, $\nu_{12} = 0.29$, $G_{12} = 3.24\,GPa$, $G_{23} = 2.9\,GPa$. The panel is composed of six layers and the stacking sequence is $[\pm\vartheta_1, \pm\vartheta_2, \pm\vartheta_3]$, from inside-out and measured with respect to the 1-axis of the local reference system which is aligned with z. The structure is discretised by a mesh grid made of 60 solid-shell elements along the curved edges and 30 along the straight ones.

The optimisation problem consists in seeking the values of ϑ_1 and ϑ_3 which maximise the collapse load, while ϑ_2 is assumed constant and equal to 0°.

The imperfection sensitivity analysis is carried out assuming random geometrical imperfections following the Monte Carlo method; the imperfections are generated as a linear combination of the displacement part of the buckling modes and uniformly distributed random numbers represent the coefficients of the combination. The resulting imperfection shape is scaled in order to have a maximum component equal to 0.1 of the thickness.

The space of the sought angles is uniformly scanned from 0° to 180° every 18°. The details of the two stages of the analysis are summarised in Tab.3.1. The best 10 laminations detected in stage 1 are checked in stage 2. The same is done for the worst 10 laminations in order to show the great influence of the stacking sequence on the structural performances.

The number of significant buckling modes for the construction of the ROM generally changes with the lamination and cannot be imposed a-priori. In this respect, an adaptive criterion of selection is used. It consists in including the modes corresponding to critical loads that do not exceed 1.5 times the lowest one.

For the potential cases of stable post-critical behaviour, the deformation limit is reached when the displacement component w_A becomes greater than $2\,mm$.

Figure 3.4 shows, for stage 1, the trend of the first buckling load and of the collapse load in the angles domain. It can be observed that, as expected, the buckling load values are not directly linked to the collapse loads. It is worth noting

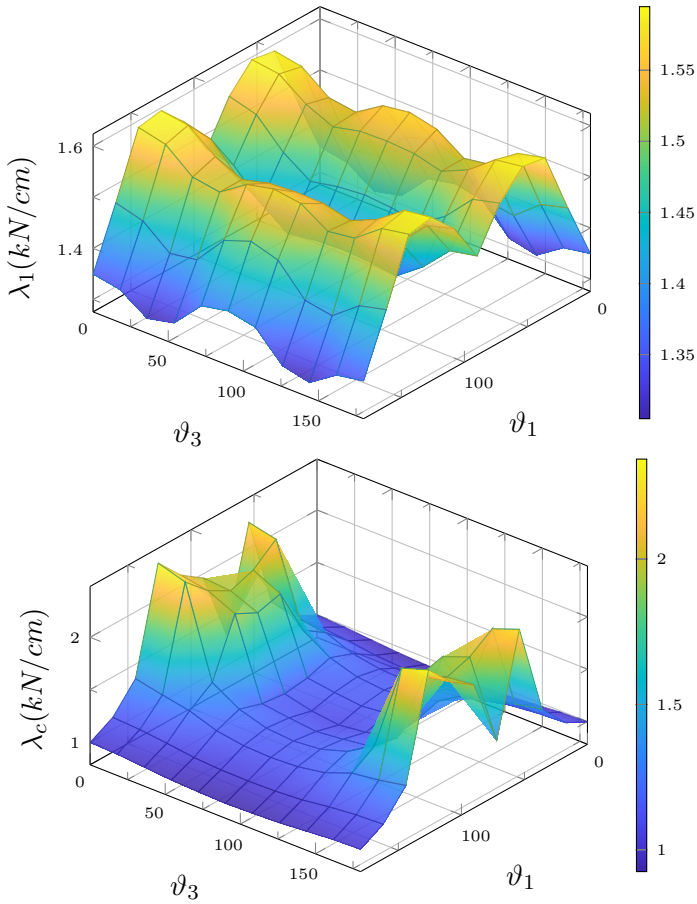

Figure 3.4: Curved panel: results of stage 1 in terms of first buckling load (left) and collapse load (right) trend with respect to the lamination angles.

		stage 1	stage 2
	laminations	100	20
	ϵ_π tolerance	3/100	3/1000
	method	K_{lin}	K_{quad}
imperfections	starting	200	200
	increment	100	100
	maximum	2000	10000

Table 3.1: Curved panel: parameters of the Monte Carlo simulation.

that the unstable cases are the most frequent (darkest areas) and produce a low collapse load coincident with the limit load, while the maximum values (lighter areas) of the collapse load correspond to stable cases where the deformation limit dominates. In Fig.3.5 the collapse load is normalised with respect to the first eigenvalue, showing that the former is much lower then the second one for the unstable cases and confirming that the linearised buckling load is not a reliable objective function for the optimization.

The best and the worst 10 cases, in terms of collapse load, are summarised in Tab.3.2 for both stages. It highlights that stage 2 gives smaller collapse loads than stage 1 and that the number of imperfections significantly increases between the two stages due to the more restrictive values for the distribution parameters σ and μ adopted. The analysis shows also that the best stacking sequences detected at stage 1 are also the optimal ones of the stage 2. Note also that, as expected, the worst and best cases are symmetric with respect to the fibre direction and this confirms the robustness of the proposal in terms of number of numerical experiments.

The extreme cases are analysed more deeply in the following. The stacking sequence $[0_4/\pm 90]$ furnishes the worst results in terms of collapse load. For this lamination, the equilibrium paths corresponding to the worst imperfection shape are reported in Fig.3.6 using the Koiter method, with both K_{lin} and K_{quad} approaches, and a path-following strategy. The solution found by K_{quad} is in accordance with the one of the path following analysis on the full FE model and, in particular, the collapse load is accurately predicted. Conversely, the cheaper approach K_{lin} gives a slightly higher value of the collapse load but is however able to capture the structural behaviour. The buckling modes and the quadratic correctives used in the Koiter analysis for building the ROM of the corresponding perfect structure are pictured in Fig.3.7 while Fig.3.8 and Fig.3.9 show the deformed configuration at collapse load and the worst imperfection shape, respectively.

To point out the influence of the number of buckling modes included in the ROM on the collapse load, an imperfection sensitivity analysis with 3 modes, that is the number used during the scan process, and 8 modes has been carried out

lamination	buckling loads			Stage 1			Stage 2		
	λ_1	λ_2	λ_3	λ_c	$\frac{\lambda_c}{\lambda_1}$	N_i	λ_c	$\frac{\lambda_c}{\lambda_1}$	N_i
$[\pm 126/0_4]$	1.595	1.986	-	2.344	1.470	500	2.354	1.476	2797
$[\pm 126/0_2/\pm 18]$	1.587	1.971	-	2.265	1.427	500	2.304	1.452	1599
$[\pm 126/0_2/\pm 162]$	1.587	1.975	-	2.260	1.424	499	2.294	1.445	1698
$[\pm 54/0_4]$	1.595	1.986	-	2.245	1.408	500	2.277	1.428	1699
$[\pm 54/0_2/\pm 18]$	1.587	1.975	-	2.187	1.377	500	2.228	1.404	1699
$[\pm 54/0_2/\pm 162]$	1.587	1.971	-	2.148	1.354	500	2.215	1.396	1298
$[\pm 108/0_4]$	1.548	1.993	-	2.107	1.361	500	2.172	1.403	2100
$[\pm 108/0_2/\pm 18]$	1.535	1.966	-	2.061	1.343	500	2.122	1.383	1597
$[\pm 108/0_2/\pm 162]$	1.533	1.969	-	2.060	1.343	600	2.127	1.387	1600
$[\pm 72/0_2/\pm 18]$	1.533	1.969	-	2.014	1.314	600	2.074	1.353	1500
$[0]_6$	1.350	1.978	-	0.996	0.738	352	0.970	0.719	1499
$[0_4/\pm 18]$	1.340	1.938	-	0.987	0.736	466	0.966	0.720	2974
$[0_4/\pm 162]$	1.340	1.938	-	0.987	0.736	585	0.966	0.720	2064
$[0_4/\pm 36]$	1.305	1.799	-	0.965	0.740	493	0.945	0.724	2385
$[0_4/\pm 144]$	1.305	1.799	-	0.965	0.740	493	0.945	0.724	1791
$[0_4/\pm 54]$	1.317	1.661	-	0.944	0.717	500	0.910	0.691	3391
$[0_4/\pm 126]$	1.317	1.661	-	0.944	0.717	800	0.910	0.691	4679
$[0_4/\pm 108]$	1.371	1.632	2.022	0.933	0.680	500	0.894	0.652	2498
$[0_4/\pm 72]$	1.371	1.632	2.022	0.933	0.680	700	0.893	0.652	2100
$[0_4/\pm 90]$	1.382	1.628	1.962	0.925	0.669	500	0.885	0.641	2499

Table 3.2: Curved panel: results of the best 10 and the worst 10 laminations. The loads are expressed in kN/cm.

for the case $[0_4/\pm 90]$. The minimum collapse load and its 5% fractile provided when increasing the imperfections has been monitored. The results are pictured in Fig.3.10. The collapse load from the two cases stabilises at the same value although when 3 modes are employed it converges for a smaller number of imperfections. On the contrary, as expected, the fractiles are quite different because, by enlarging the number of the modes, the space of the possible imperfections also increases without providing any further information about the worst imperfection, which is well represented by the first 3 modes.

Moreover, for a fixed number of modes, the frequency distribution converges quickly. This can be seen in Fig.3.10 where the fractile does not change significantly, or in Fig.3.11 and Tab.3.3 which show, for 8 modes, how the probability density function and the parameters of the distribution vary with the number of imperfections.

The other extreme lamination is $[\pm 126/0_4]$, characterised by a stable post critical behaviour and the highest collapse load. In Fig.3.13, the corresponding equilibrium paths traced by Koiter (ROM) and Riks (full FE model) analyses are reported showing a good agreement. The deformed configuration at the last evaluated equilibrium point is shown as well. The buckling modes and the corresponding corrective modes used to construct the ROM are pictured in Fig.3.14.

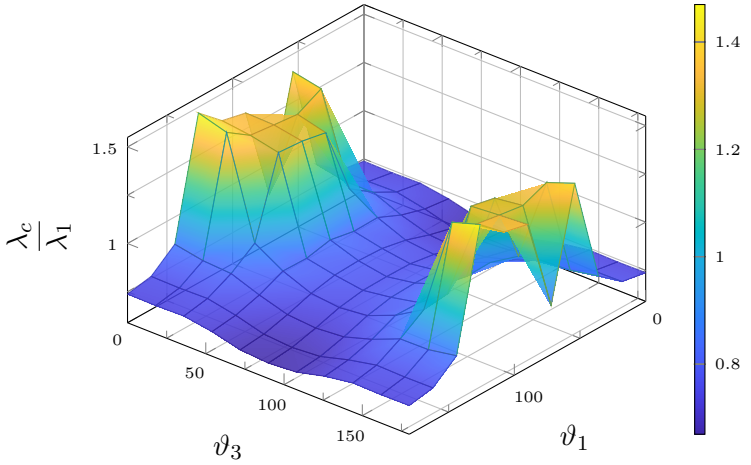

Figure 3.5: Curved panel: results of stage 1 in terms of collapse load normalised with respect to the first buckling load.

3.4.2 Stiffened panel

The second test regards a curved panel with "T" stiffeners in compression, like those commonly employed for aeronautical structures [79]. In Fig.3.15 an axonometric projection shows the geometry and the boundary conditions, while geometrical details of a section have been pictured in Fig.3.16. The v displacement of the lateral faces of the four panels is bounded and the deformation of only one curved edge is constrained, also along z. In the illustrations, it is possible to see the mesh grid details for the 3D solid-shell description of the structure. It is worth noting how the solid-shell finite element allows us to model, easily and accurately, the connection between the panel and the stiffeners, with no need for rigid links or offsets, in contrast to classical shell models. The curved faces and the stiffener ends are loaded by a uniform line load $\lambda = 1$.

The same material is employed for the skin and the stiffeners and it is characterised by $E_1 = 30.6\,GPa$, $E_2 = 8.7\,GPa$, $\nu_{12} = 0.3$, $G_{12} = 3.4\,GPa$, $G_{23} = 2.9\,GPa$, with respect to the local reference system which has the direction 1 aligned with the global direction z while the direction 3 is along the normal at the middle plane of the skin. The stiffener lamination is supposed to be constant and equal to 0°, while eight layers define the lamination of the skin labelled as $[\vartheta_1/\ldots/\vartheta_8]$ where every ϑ_i is a multiple of 18° and can vary from 0° to 180°. The purpose of the test is studying the variability of the post-critical behaviour when the lamination changes and seeking the laminations with the maximum collapse load. The solutions with minimum collapse load are searched as well, just to identify the range of variability of the structural performances. The collapse load for

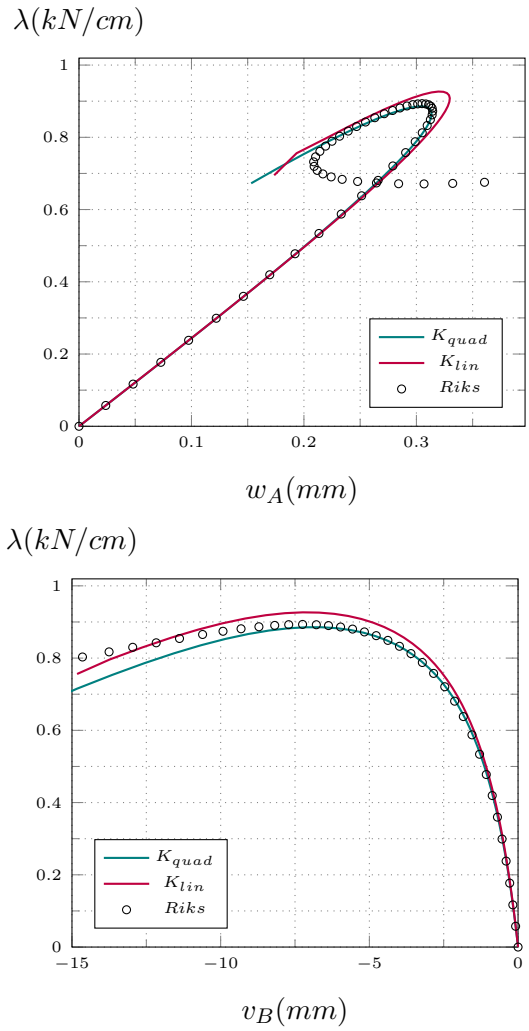

Figure 3.6: Curved panel: equilibrium path for the worst imperfection shape in stage 2, path following vs Koiter a-posteriori, lamination $[0_4/\pm 90]$.

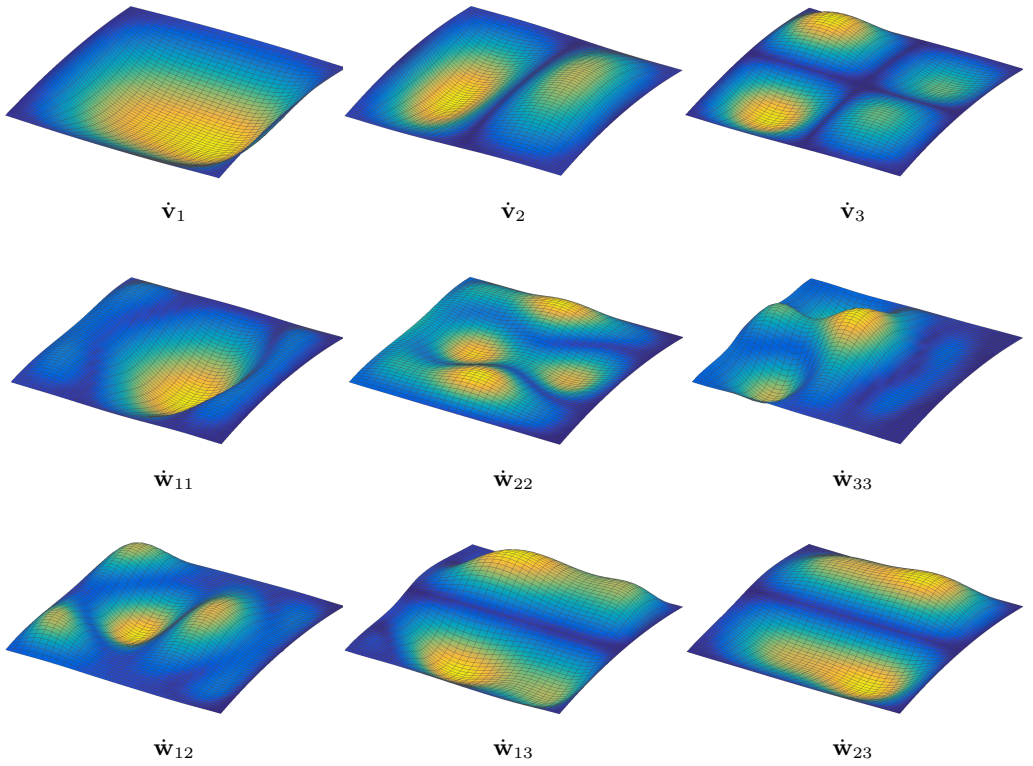

Figure 3.7: Curved panel: buckling modes and quadratic correctives, case $[0_4/\pm 90]$.

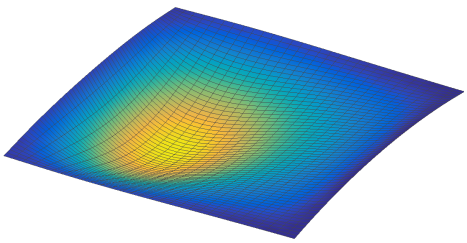

Figure 3.8: Curved panel: deformed shape at collapse point, case $[0_4/\pm 90]$.

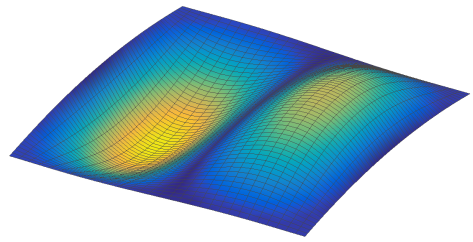

Figure 3.9: Curved panel: worst imperfection shape, lamination $[0_4/\pm 90]$.

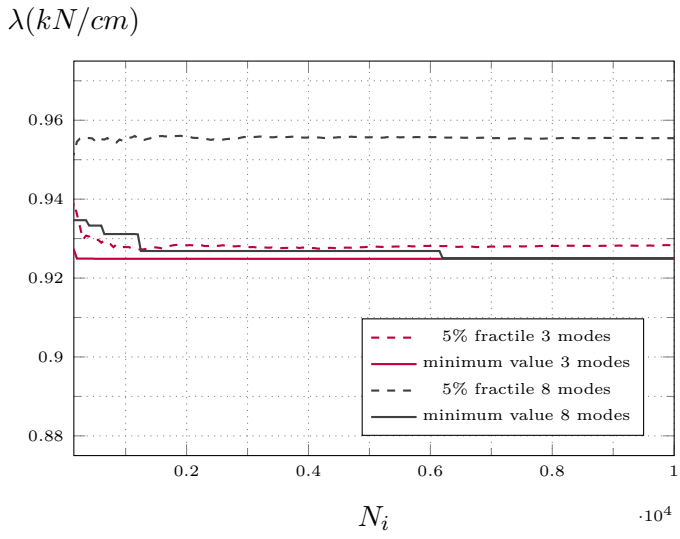

Figure 3.10: Curved panel: 5% fractile and minimum value of the collapse load versus number of imperfections for 3 and 8 modes, case $[0_4/\pm 90]$.

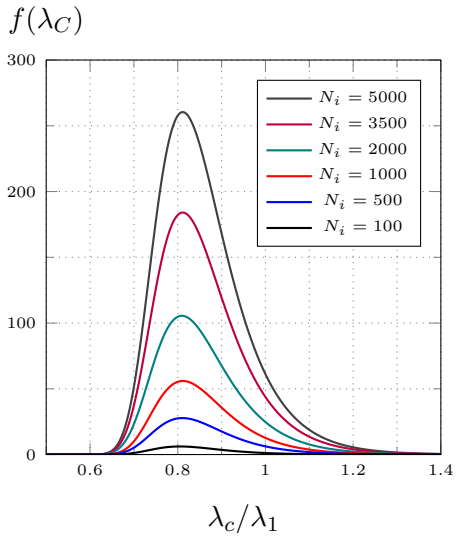

Figure 3.11: Curved panel: Gumbel max probability density function for different number of imperfections, lamination $[0]_6$, 8 modes.

N_i	μ	σ
100	-0.8049	0.0755
500	-0.8105	0.0788
1000	-0.8116	0.0786
2000	-0.8094	0.0809
3500	-0.8113	0.0806
5000	-0.8113	0.0801

Table 3.3: Curved panel: distribution parameters variation with the number of imperfections, lamination $[0]_6$.

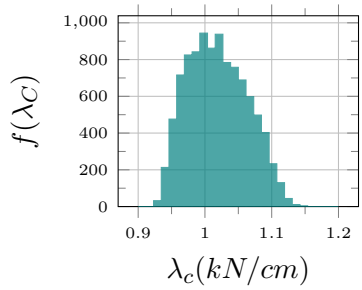

Figure 3.12: Curved panel: frequencies of the collapse load, lamination $[0_4/\pm 90]$, 8 buckling modes, 10000 imperfections.

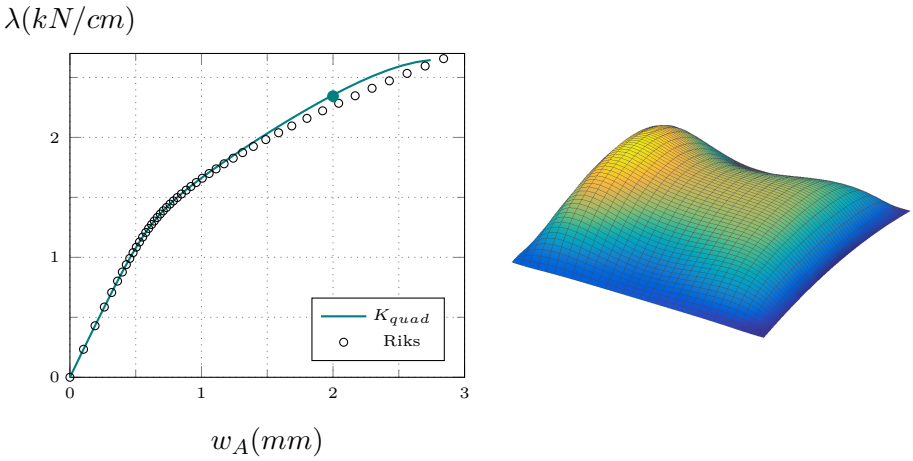

Figure 3.13: Curved panel: equilibrium path (left) and deformed shape at the last evaluated equilibrium point (right), lamination $[\pm 126/0_4]$.

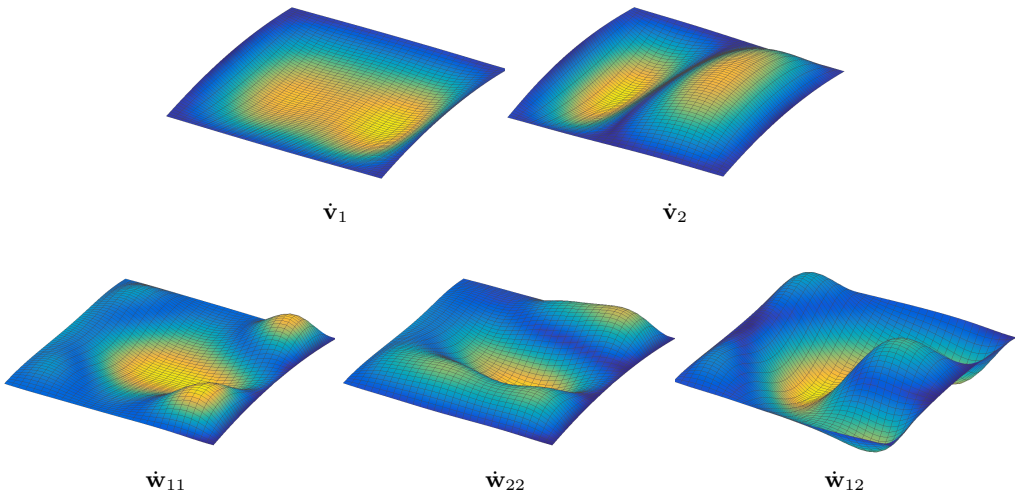

Figure 3.14: Curved panel: buckling modes and quadratic correctives for the case $[\pm 126/0_4]$.

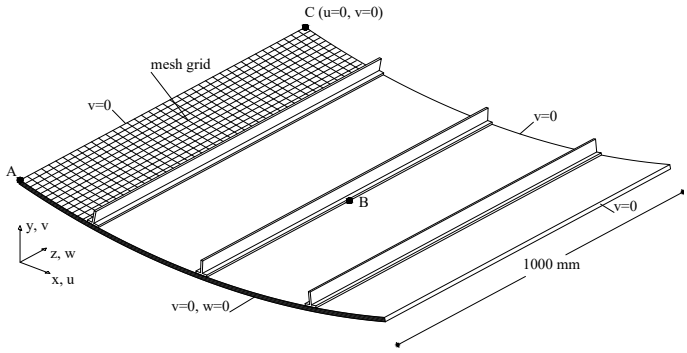

Figure 3.15: Stiffened panel: geometry and boundary conditions.

the stable configurations is the load producing the deformation limit $w_A = 4\,mm$. As in the first test, the buckling modes employed for the ROM of the Koiter analyses correspond to buckling loads which do not exceed 1.5 times the first one.

The parameters used to set up the three stages of the random scanning approach are reported in Tab.3.4. In the first stage, 2500 random uniformly generated laminations are analysed and the 10 best and the 10 worst laminations (in terms of collapse load), reported in Tab.3.5, are selected. In the second stage, for each of these configurations, a further 100 randomly generated laminations are considered with each layer angle that can vary between $-36°$ and $36°$ with an increment of $18°$ with respect to the likely optimal values identified by the first stage. Lastly, in stage 3 the best 10 and the worst 10 results obtained in stage 2, and labelled as indicated in Tab.3.6, are analysed using the accurate account of geometrical imperfections and a more restrictive tolerance for parameters μ and σ; a summary of the results is reported in Tab.3.7.

Even though the number of finite element parameters is quite significant, the code is not really time consuming. For instance, the average time taken by a prototype code for analysis each layup at stage 1 is 32.02 seconds (i7-6700HQ CPU 2.6Ghz, Matlab R2016a, single core) considering that the average number of imperfections per layup is 805.

		stage 1	stage 2	stage 3
	laminations	2500	2000	20
	tolerance	3/100	5/1000	3/1000
	method	K_{lin}	K_{lin}	K_{quad}
	starting	50	200	200
imperfections	increment	50	50	100
	maximum	2000	2000	10000

Table 3.4: Stiffened panel: parameters of the Monte Carlo simulation.

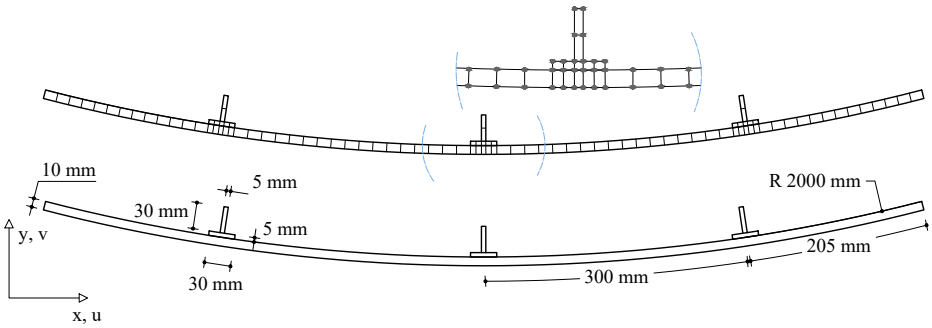

Figure 3.16: Stiffened panel: section geometry and mesh.

The curves in Fig.3.17 plot the collapse load, the two lowest buckling loads λ_1 and λ_2 and the ratio between the collapse load and the first eigenvalue as a function of a lamination index. This is an integer number which is assigned to each lamination after they are ordered in terms of decreasing collapse load. The laminations with the smallest index have a stable behaviour and collapse for reaching the deformation limit. The buckling loads in these cases are well separated from each other. The first buckling load is actually quite constant with the lamination though, when the second one gets closer to it, the collapse load, due to modal interaction phenomenon, drastically reduces. This behaviour is significantly more evident in Fig.3.18 where the results of stage 2 are reported. The best laminations in terms of collapse load are characterised by an evident distance between the first and the second linearised buckling load and exhibit a stable behaviour. Conversely, for the worst laminations, the second eigenvalue is very close to the first one and the modal interaction leads to a relevant unstable behaviour with an imperfection sensitive limit load. Some equilibrium paths are presented in Fig.3.19. The collapse loads predicted by the Koiter method are practically coincident with those provided by the Riks analysis with the full FE model. The buckling modes used in the ROM and some quadratic correctives are pictured in Fig.3.20 and in Fig.3.23 for the laminations L1 and L20 respectively. In addition, Fig.3.21 shows the worst imperfection shape detected in stage 2 for the lamination L20 and the corresponding deformed shape at the limit point is reported in Fig.3.22. The convergence of the Monte Carlo optimisation is shown in Fig.3.24, that is the trend of the maximum and the minimum collapse load for an increasing number of analysed laminations. In particular, a little over a thousand of layups has to be considered to obtain a converged value of the maximum collapse load. Lastly, Fig.3.25 indicates how the structural behaviour in terms of equilibrium path drastically changes with the stacking sequence and, in particular, how the post-critical behaviour varies from strongly unstable to stable, confirming again the great influence of a stacking sequence optimisation.

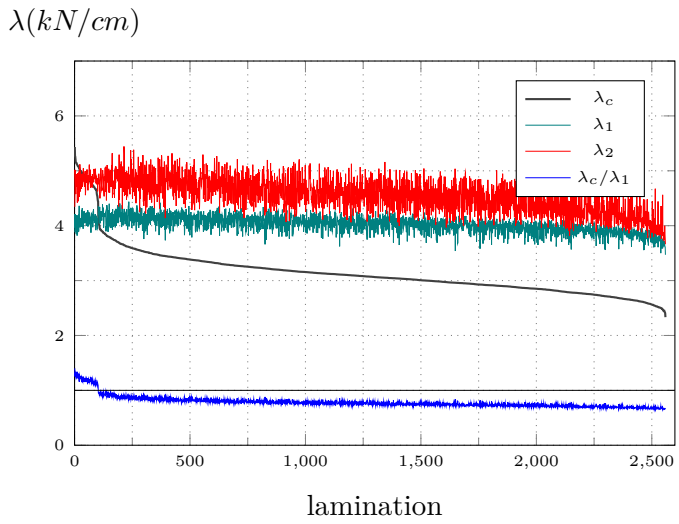

Figure 3.17: Stiffened panel: collapse load and buckling loads for the lamination in order of decreasing collapse load, stage 1.

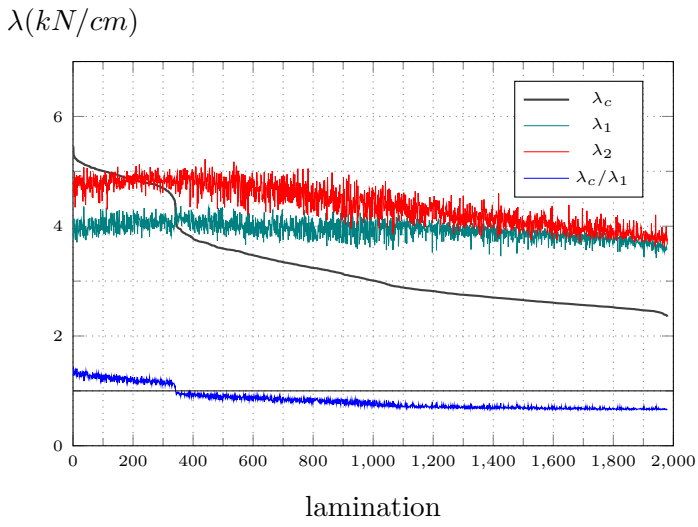

Figure 3.18: Stiffened panel: collapse load, fractile and buckling loads for the lamination in order of decreasing collapse load, stage 2.

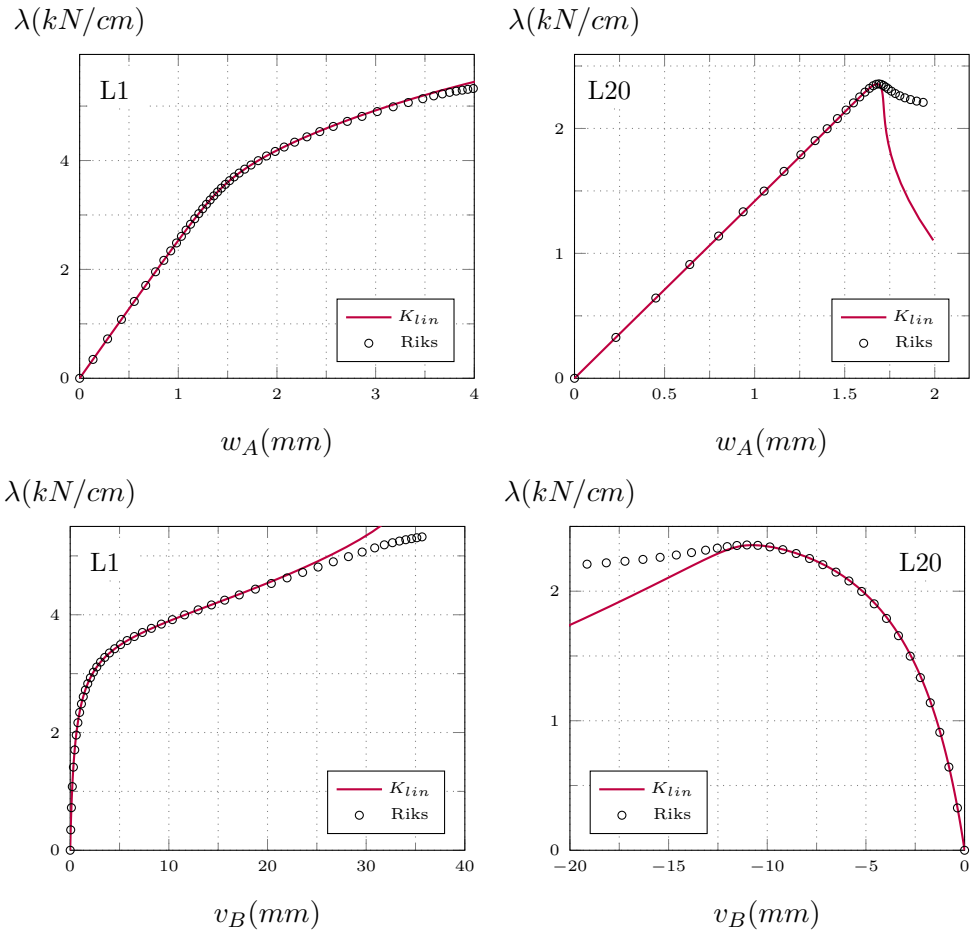

Figure 3.19: Stiffened panel: equilibrium paths for the worst imperfection shape and laminations L1 and L20, path following vs Koiter.

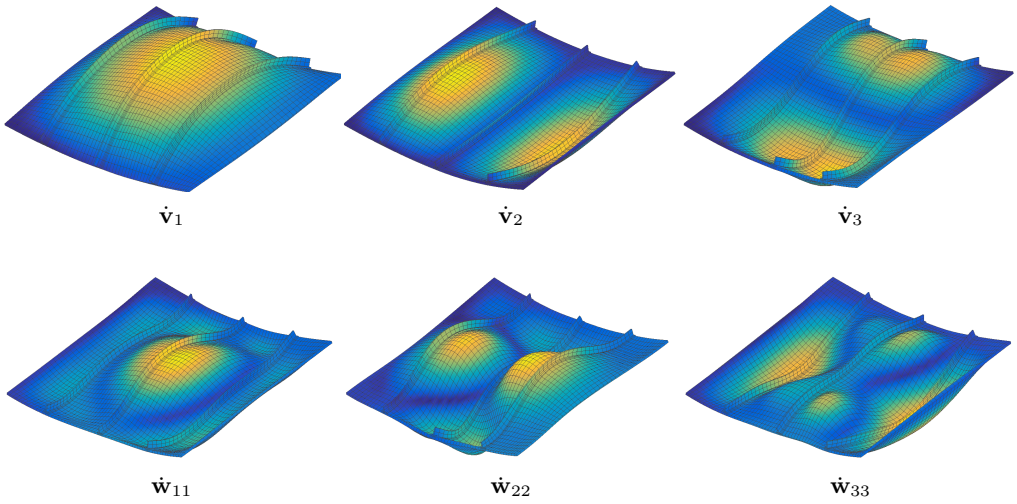

Figure 3.20: Stiffened panel: buckling modes and quadratic correctives, case L1.

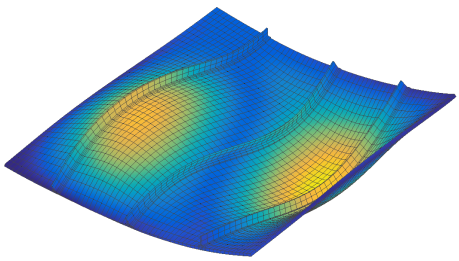

Figure 3.21: Stiffened panel: worst imperfection shape, L20.

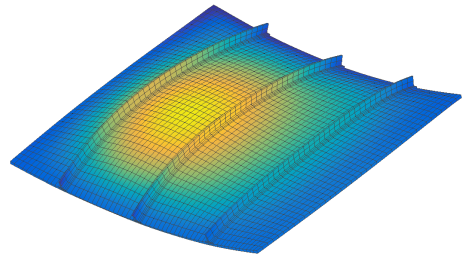

Figure 3.22: Stiffened panel: deformed shape at collapse point, L20.

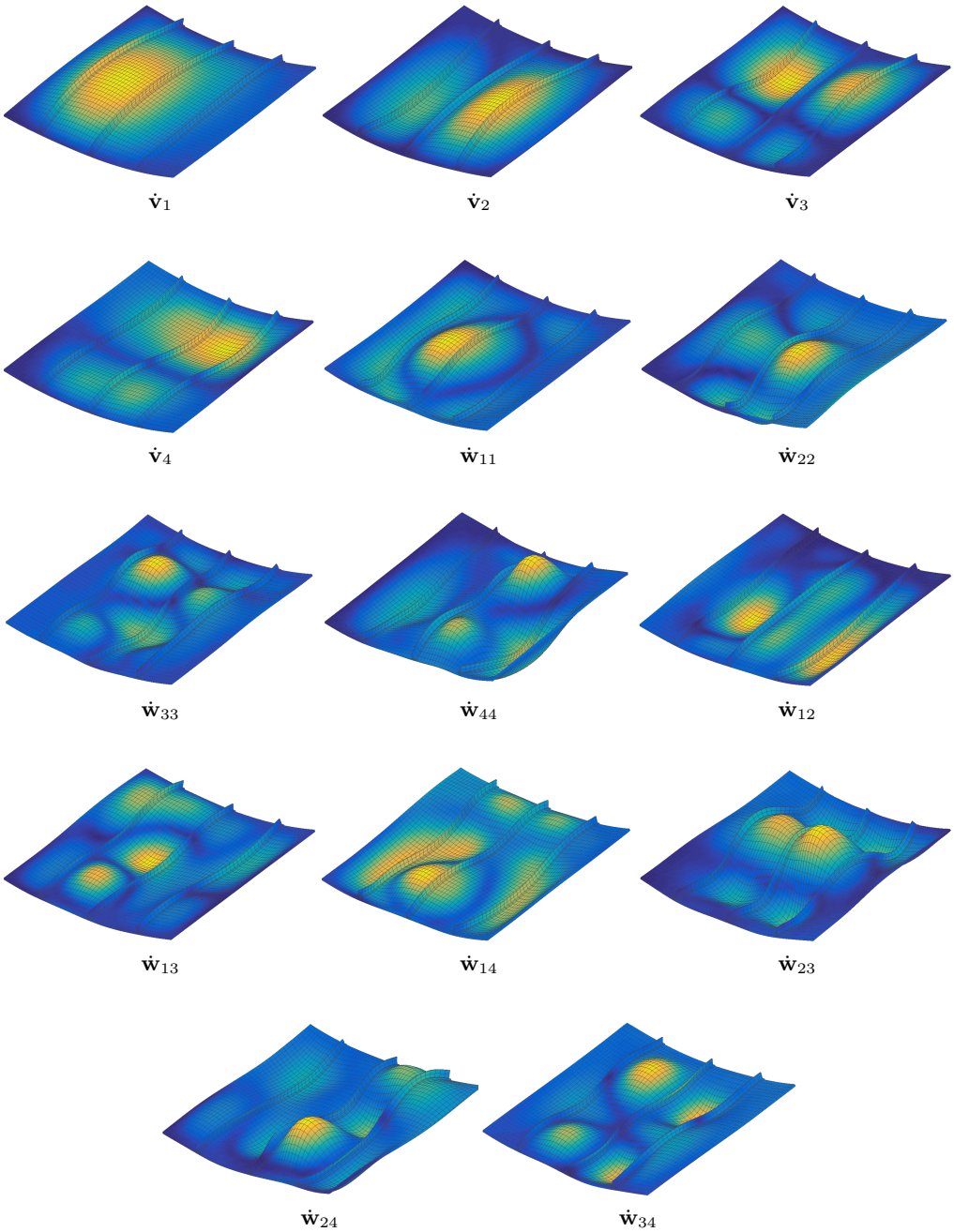

Figure 3.23: Stiffened panel: buckling modes and quadratic correctives, case L20.

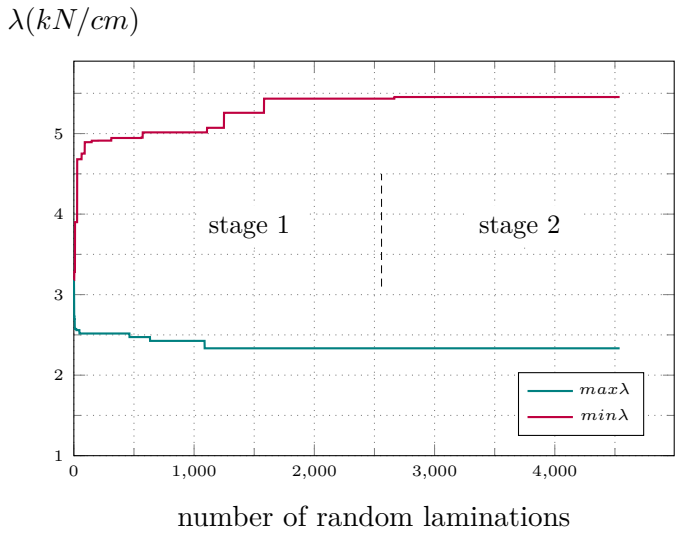

Figure 3.24: Stiffened panel: maximum and minimum collapse loads when the laminations increase.

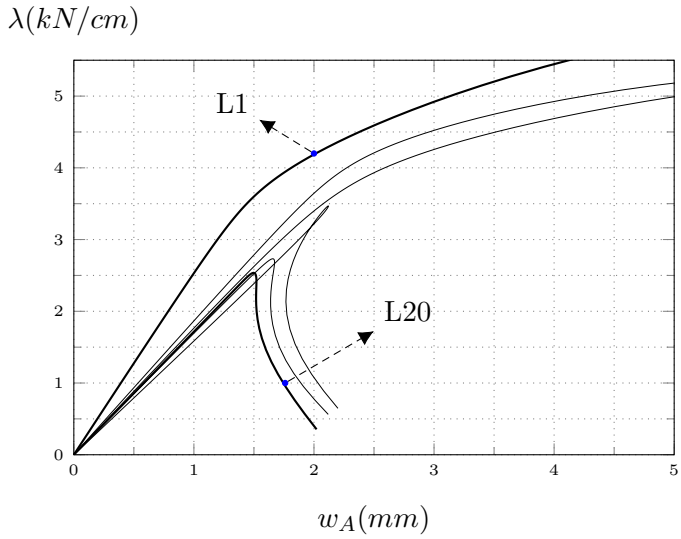

Figure 3.25: Stiffened panel: equilibrium paths for some laminations at stage 2.

lamination	λ_1	λ_2	λ_c	$\lambda_{c,5}$	λ_c/λ_1	N_i
[18/36/162/72/0/0/0/0]	3.8805	4.3430	5.4337	-	1.4003	350
[108/36/72/162/0/72/0/162]	4.2127	5.0184	5.2665	-	1.2501	350
[108/36/162/144/18/0/162/0]	3.9662	4.8839	5.2580	-	1.3257	200
[126/126/0/144/162/0/18/0]	3.8521	4.7065	5.1439	-	1.3354	350
[90/108/0/18/18/0/162/0]	3.8604	4.7119	5.0942	-	1.3196	550
[54/54/18/0/54/0/162/0]	3.8930	4.7015	5.0641	-	1.3008	300
[72/126/72/72/0/108/0/0]	4.3619	4.9789	5.0532	-	1.1585	350
[36/54/108/18/36/0/0/162]	4.0863	4.7736	4.9990	-	1.2234	400
[72/126/36/18/144/18/0/0]	4.0992	4.9873	4.9985	-	1.2194	300
[54/72/0/72/36/0/0/0]	3.9844	4.6742	4.9831	-	1.2506	250
[162/144/162/144/144/72/108/90]	3.6837	3.7316	2.4582	2.4614	0.6673	300
[162/0/18/90/90/126/126/108]	3.6686	3.7659	2.4519	2.4539	0.6683	250
[0/0/126/72/72/126/72/108]	3.7314	3.7613	2.4511	2.4534	0.6569	300
[18/18/108/108/36/126/54/54]	3.6627	3.8805	2.4505	2.4525	0.6690	300
[18/18/144/108/126/108/90/126]	3.6901	3.7830	2.4503	2.4525	0.6640	400
[162/162/54/108/126/72/90/108]	3.6955	3.8094	2.4295	2.4316	0.6574	400
[0/126/108/108/126/90/126/90]	3.6464	3.9985	2.4255	2.4286	0.6652	250
[18/162/54/54/108/108/108/126]	3.6160	3.8386	2.4211	2.4234	0.6696	300
[0/18/144/108/54/54/90/72]	3.6131	3.7729	2.4016	2.4048	0.6647	450
[18/18/0/36/54/72/54/72]	3.4698	3.6626	2.3334	2.3359	0.6725	250

Table 3.5: Stiffened panel: results of the best 10 and the worst 10 laminations, stage 1. The loads are expressed in kN/cm.

3.5 Summary

A strategy completely based on stochastic simulations for optimising the stacking sequence of slender composite shells undergoing buckling was presented in this chapter. The objective function is the collapse load, evaluated by taking into account the initial post-buckling behaviour. The main idea consists in the use of random numerical experiments for detecting both the best layup and the worst shape of the geometrical imperfection. A solid-shell finite element model was adopted to describe the structural problem accurately with no limitation on geometry, material configuration and boundary conditions. Generally, the discrete problem is governed by a significant number of degrees of freedom, which makes the Monte Carlo optimisation prohibitive. For this reason, the FE unknowns were replaced, for each random layup by a reduced order model built, according to the multimodal Koiter method, starting from the initial path tangent and a few buckling modes associated to the first eigenvalues of a linearised buckling analysis. The ROM, governed by a few modal amplitudes, made it possible, for each material configuration, to quickly predict the initial post-buckling path of the perfect structure with a high accuracy in both stable and limit point situations, including the modal interaction phenomenon. Moreover, the safest collapse load of each stacking sequence, corresponding to the worst imperfection shape,

label	lamination
L1	[108/18/162/162/0/18/180/0]
L2	[72/0/162/144/0/0/198/0]
L3	[108/18/72/198/18/72/0/180]
L4	[126/0/162/108/18/0/180/18]
L5	[108/54/144/180/18/0/180/18]
L6	[108/162/36/0/108/0/0/18]
L7	[0/72/162/36/18/0/18/0]
L8	[90/18/180/162/18/18/162/0]
L9	[72/18/126/18/0/0/36/180]
L10	[108/54/180/144/0/18/180/18]
L11	[0/126/126/126/126/90/108/126]
L12	[0/0/108/90/108/126/108/90]
L13	[198/180/72/72/90/54/72/72]
L14	[162/162/72/72/108/90/126/126]
L15	[162/162/72/90/90/90/108/126]
L16	[18/108/126/108/108/108/90/108]
L17	[180/18/54/54/72/90/108/72]
L18	[0/162/126/126/90/108/90/72]
L19	[198/198/36/108/126/90/72/72]
L20	[180/0/54/72/72/90/90/72]

Table 3.6: Stiffened panel: labels of the best 10 and the worst 10 laminations, stage 2.

was estimated by means of a Monte Carlo imperfection sensitivity analysis, that is the evaluation of the equilibrium path for thousands of imperfections. This part, that is usually quite time consuming, was made really inexpensive by including the effects of the imperfections directly in the ROM of the perfect structure. The number of imperfections to consider was controlled by checking the convergence of the parameters of the Gumbel-max distribution, which represents the probability density function of the collapse load well.

Two examples of layup optimisation regarding curved multi-layered panels, with and without stiffeners, were reported. In the first one, the stacking sequence was expressed in terms of two parameters. In this case, the great efficiency of the Koiter method made it possible to uniformly scan the entire population of stacking sequences. In the second one, the fibre orientation of each of the eight layers was chosen as an independent parameter. The complexity of the problem was handled by means of the more general random search and it was shown that a converged value of the maximum collapse load is obtained with a thousand random layups. The numerical results confirm the importance of correct design of the stacking sequence, which should take account of the post-critical behaviour to maximise the collapse load. The optimisation led to a drastic change in structural behaviour, which ranges from unstable and sensitive to imperfections to stable without imperfection sensitivity. The examples showed that, on the contrary,

	buckling loads				Stage 2			Stage 3		
	λ_1	λ_2	λ_3	λ_4	λ_c	$\frac{\lambda_c}{\lambda_1}$	i	λ_c	$\frac{\lambda_c}{\lambda_1}$	N_i
L1	3.771	4.663	5.610	-	5.450	1.442	850	5.463	1.449	1200
L2	3.801	4.605	5.645	-	5.302	1.395	1100	5.314	1.398	2200
L3	4.140	4.823	5.975	-	5.289	1.276	600	5.300	1.280	2500
L4	3.876	4.534	5.713	-	5.277	1.361	900	5.286	1.364	2100
L5	4.016	4.982	5.786	-	5.260	1.310	600	5.250	1.307	2200
L6	4.025	4.762	5.826	-	5.254	1.306	950	5.260	1.307	1700
L7	3.785	4.344	5.644	-	5.238	1.384	700	5.244	1.386	3600
L8	3.752	4.615	5.573	-	5.236	1.396	800	5.242	1.397	1600
L9	3.956	4.781	5.713	-	5.229	1.322	950	5.238	1.324	800
L10	3.971	4.891	5.720	-	5.227	1.316	950	5.240	1.320	1400
L11	3.587	3.864	5.110	5.305	2.389	0.666	750	2.381	0.664	2300
L12	3.550	3.809	5.000	5.111	2.387	0.672	800	2.380	0.670	2598
L13	3.562	3.835	5.111	5.131	2.387	0.670	1000	2.380	0.668	2200
L14	3.618	3.752	5.238	5.341	2.382	0.658	750	2.374	0.656	1800
L15	3.618	3.765	5.195	5.343	2.381	0.658	1100	2.373	0.656	1400
L16	3.563	3.992	5.184	5.220	2.378	0.667	500	2.373	0.666	2300
L17	3.621	3.757	5.116	5.255	2.380	0.657	700	2.369	0.654	1400
L18	3.585	3.744	5.058	5.269	2.373	0.662	650	2.364	0.659	1900
L19	3.579	3.774	5.153	5.289	2.371	0.662	750	2.362	0.660	1600
L20	3.579	3.663	4.967	5.140	2.353	0.658	900	2.345	0.655	1500

Table 3.7: Stiffened panel: stage 2 and stage 3 results. The loads are expressed in kN/cm.

the smallest linearised buckling load cannot be used as objective function for the optimisation as it can generally be quite different from the collapse load, especially in the case of modal interaction. This is evident in the second test proposed where the first buckling load is practically constant with the lamination while the collapse load changes significantly. Further details can be found in [96].

Chapter 4

How to improve efficiency and robustness of the Newton method in displacement-based finite element analysis

Abstract

This chapter shows how to significantly improve the robustness and the efficiency of the Newton method in geometrically nonlinear structural problems discretised via displacement-based finite elements. The strategy is based on the relaxation of the constitutive equations at each integration point. This leads to an improved iterative scheme which requires a very low number of iterations to converge and can withstand very large steps in step-by-step analyses. The computational cost of each iteration is the same as the original Newton method. The impressive performances of the proposal are shown by many numerical tests. In geometrically nonlinear analysis, the proposed strategy, called MIP Newton, seems worthy to replace the standard Newton method in any finite element code based on displacement formulations. Its implementation in existing codes is very easy.

4.1 Introduction

Slender structures are usually characterized by large displacements and rotations but small strains. This situation is commonly known as geometrically nonlinear problem, because leads to a mathematical problem in which the nonlinearities are due to geometric effects, that is the nonlinear relationship between the strains and the displacements/rotations. Many practical problems can be framed in this context. Some examples are metal and composite structures, often character-

ized by buckling phenomena and strong imperfection sensitivity, drape simulation problems and deployable structures characterized by very large displacements.

The standard approach to simulate the behaviour of this kind of structures consists of the use of the finite element (FE) method, in order to transform the continuum problem into a discrete one. The nonlinear discrete equations, completed with an arc-length constraint defining the step size, are solved step-by-step by using the Newton iterative method, in order to evaluate the equilibrium path of the structure.

Although this strategy is well established, it can be plagued by its high computational cost, due to two different limitations: i) the number of FE degrees of freedom (DOFs) used to approximate the differential equations; ii) the number of iterations required to obtain an equilibrium point and then to trace the desired equilibrium path, once the continuum problem has been discretized. In this work attention is focused only on the second aspect and, to avoid any misunderstandings, the word "convergence", used throughout this chapter, refers only to the iterative method, which provides the solution of the nonlinear discrete problem.

Most of the existing FE codes are based on displacement formulations, i.e. the kinematic field is interpolated and the discrete kinematic DOFs represent the unknowns of the nonlinear equations. Other kinds of formulations are possible, like for instance the mixed (stress-displacement) one, also known as hybrid-stress, in which both the stress and the displacement fields are interpolated. When comparing mixed and displacement finite elements many authors observe that the mixed ones are more robust and allow larger steps in path-following geometrically nonlinear analyses [10, 11]. This fact was investigated for the first time some years ago in [32], when it was shown that the robustness and the efficiency (in terms of number of iterations) of the Newton iterative scheme are penalized in displacement formulations because of a phenomenon that was called "extrapolation locking". This is not a locking of the FE discretisation, but of the iterative scheme usually found in beam/shell problems, when the axial/membrane stiffness is much higher than the flexural one. In these cases the iteration matrix evaluated in the current estimates of the equilibrium point can be far from the optimal one, in terms of the convergence condition of the Newton method. The number of iterations required to evaluate the equilibrium path, quickly grows as the stiffness ratios of the structure increase while, at the same time, the step size required to avoid loss of convergence drastically decreases. This phenomenon, that is typical of FE displacement formulation, does not affect mixed FE formulations, which are free from "extrapolation locking" [33, 48]. In recent years many other researchers have experienced the better behaviour of the mixed FE models in geometrically non–linear analyses. In [10] a displacement and a mixed (hybrid-stress) solid-shell FE are developed which, if converged, yield close predictions. However, the authors conclude that the mixed element converges more readily and can withstand larger load increments than the displacement one in all the examined problems. In the ABAQUS manual (29.3.3-9), it is reported that hybrid beam elements are provided

in order to make the convergence of the iterative method faster, when the beam's rotations are large. The first chapter investigated the fast convergence and the high robustness of mixed FE models, providing a clear explanation of the origin of the phenomenon in a general context. It was shown that the evolution of the displacement iterative process is forced to satisfy the constitutive equations at each iteration and this constraint leads to a deterioration in the convergence properties. On the contrary in mixed FE models the stress DOFs are independent variables, directly extrapolated and corrected, which only at convergence satisfy the discrete constitutive equations. The mixed iterative scheme is then free to naturally evolve to the solution while the displacement iterative scheme is constrained to follow an assigned evolution in which the constitutive equations must be satisfied. Thus, the ready convergence of the Newton method for mixed FEs is not linked to the FE interpolation, but due to the different "format" of the iterations. Mixed elements have a higher computational cost in constructing their element stiffness matrix and internal force vector with respect to displacement FEs, because of the stress extra-variables usually condensed at element level, but their use in geometrically nonlinear problems is justified by their readier convergence.

The question posed in this work is *"is it possible to use a mixed iterative scheme without introducing a mixed FE interpolation?"*. A positive answer to this question would have important implications since a great part of the existing code is based on well-established displacement FE interpolations. In this chapter it will be shown that this is possible and a mixed format of the Newton method for geometrically nonlinear structural problems discretised via displacement-based finite elements is presented. The strategy is inspired by the more efficient iterative scheme for mixed FE models. The idea consists of the relaxation of the constitutive equations at each integration point. In this way, the stiffness matrix of a displacement-based FE maintains its original form. The only difference is that the stresses at each integration point, used for the matrix evaluation, are directly extrapolated and corrected, i.e. used as independent variables. This leads to a "better" iteration matrix, which allows a very low number of iterations and very large steps (increments) in step-by-step analyses. With respect to mixed FEs no stress interpolations are present, so avoiding any additional cost in the evaluation of the stiffness matrix. Furthermore the final equilibrium path is the same as the original displacement formulation since the constitutive law is recovered exactly at convergence.

The method, that named MIP (Mixed Integration Point) Newton, converges much faster than the standard Newton method, as shown by many numerical tests with different structural models and FEs. The gain in terms of number of iterations required is impressive as well as the very large steps that the MIP Newton can withstand without loss of convergence. The computational cost of a MIP iteration is the same as a standard one. Furthermore, the iteration matrix evaluated with the MIP strategy is so "good" that the modified version of the method (MIP modified Newton), which computes and decomposes the iteration

matrix at the first estimate of each equilibrium point, can be conveniently adopted. From the implementation point of view, a few changes to the standard approaches are required, without upsetting the existing FE codes and then its inclusion is straightforward. In geometrically nonlinear analysis, the proposed strategy is so robust, efficient and simple that it seems destined to replace the standard Newton method in any finite element code based on displacement formulations.

The chapter is organized as follows: Section 2 presents a short overview of the the equations of a general displacement-based finite element, in order to introduce the notation; Section 3 derives the new MIP Newton in both the full and modified version; Section 4 presents the two structural models and their FE interpolations used in the numerical tests together with some implementation details required to make the numerical tests reproducible; Section 5 presents a series of numerical tests and discusses the improvements in terms of robustness and efficiency of the proposal; finally, the conclusions are reported.

4.2 Path-following analysis via displacement FEs

4.2.1 The discrete nonlinear equations

We consider a slender hyperelastic structure subject to conservative loads $p[\lambda]$ proportionally increasing with the amplifier factor λ. The equilibrium is expressed by the virtual work equation

$$\Phi[u]'\,\delta u - \lambda p\,\delta u = 0 \quad , \quad u \in \mathcal{U}\ ,\ \delta u \in \mathcal{T} \tag{4.1}$$

where $u \in \mathcal{U}$ is the field of configuration variables, $\Phi[u]$ denotes the strain energy, $\mathcal{T}$ is the tangent space of $\mathcal{U}$ at u and a prime is used to express the Fréchet derivative with respect to u. We assume that $\mathcal{U}$ will be a linear manifold so that its tangent space $\mathcal{T}$ will be independent of u. In displacement formulation u is the displacement field, while when a mixed formulation is adopted u collects both displacement and stress fields. Eq.(4.1) can be rewritten, using a FE discretisation $u = \mathbf{N}_u\mathbf{u}$ as

$$\mathbf{r}[\mathbf{u},\,\lambda] \equiv \mathbf{s}[\mathbf{u}] - \lambda\,\mathbf{p} = \mathbf{0}, \quad \text{with} \quad \begin{cases} \mathbf{s}^T\delta\mathbf{u} \equiv \Phi'[u]\delta u \\ \mathbf{p}^T\delta\mathbf{u} \equiv p\,\delta u \end{cases} \tag{4.2}$$

where $\mathbf{r} : \mathbb{R}^{N+1} \to \mathbb{R}^N$ is a nonlinear vectorial function of the vector $\mathbf{z} \equiv \{\mathbf{u}, \lambda\} \in \mathbb{R}^{N+1}$, collecting the configuration $\mathbf{u} \in \mathbb{R}^N$ and the load multiplier $\lambda \in \mathbb{R}$, $\mathbf{s}[\mathbf{u}]$ is the *internal force vector* and $\mathbf{p}$ the *reference load vector*. Eq.(4.2) represents a system of N-equations and $N+1$ unknowns and its solutions define the *equilibrium paths* as curves in $\mathbb{R}^{N+1}$ from a known initial configuration $\mathbf{u}_0$, corresponding to $\lambda = 0$. The tangent stiffness matrix is also defined as

$$\delta\mathbf{u}_2^T\mathbf{K}[\mathbf{u}]\delta\mathbf{u}_1 = \Phi''[u]\delta u_1\delta u_2 \ \ , \ \ \forall\,\delta\mathbf{u}_1, \delta\mathbf{u}_2 \tag{4.3}$$

where δu_i are generic variations of the configuration field u and $\delta \mathbf{u}_i$ the corresponding FE vectors.

4.2.2 Displacement-based FE

In displacement-based FE formulations only the displacement field is interpolated in the domain and, thus,

$$\mathbf{u}[\boldsymbol{\zeta}] = \mathbf{N}_d[\boldsymbol{\zeta}]\mathbf{d}_e \tag{4.4}$$

where $\mathbf{d}_e$ are the element discrete DOFs, linked to the global ones $\mathbf{d}$ by the relation $\mathbf{d}_e = \mathbf{A}_e\mathbf{d}$ and $\boldsymbol{\zeta}$ are the coordinates used to express the FE interpolation. The dependence on the coordinates will be omitted in the following in order to simplify the notation. The strain energy can be expressed as a sum of element contributions $\Phi[u] \equiv \sum_e \Phi_e[u]$, where, letting V_e the finite element domain and $\mathbf{C}$ the constitutive matrix,

$$\Phi_e[u] \equiv \int_{V_e} \left(\frac{1}{2}\boldsymbol{\varepsilon}^T\mathbf{C}\boldsymbol{\varepsilon}\right) dV_e \tag{4.5}$$

and the strains or generalized strains $\boldsymbol{\varepsilon} = \mathcal{D}[\mathbf{u}]\mathbf{u}$, introducing the interpolation in (4.4), assume the general form

$$\boldsymbol{\varepsilon} = \mathbf{B}[\mathbf{d}_e]\mathbf{d}_e, \tag{4.6}$$

with the differential operator $\mathcal{D}$ and its discrete counterpart $\mathbf{B}$, in general, nonlinear in $\mathbf{u}$ and $\mathbf{d}_e$ respectively. The first variation of the strain measure can be written as

$$\delta\boldsymbol{\varepsilon} = \mathbf{Q}[\mathbf{d}_e]\delta\mathbf{d}_e$$

and, then, the first variation of the strain energy is

$$\Phi_e[u]'\delta u \equiv \int_{V_e} \left(\delta\boldsymbol{\varepsilon}^T\mathbf{C}\boldsymbol{\varepsilon}\right) dV_e = \int_{V_e} \left(\delta\mathbf{d}_e^T\mathbf{Q}[\mathbf{d}_e]^T\mathbf{C}\mathbf{B}[\mathbf{d}_e]\mathbf{d}_e\right) dV_e = \delta\mathbf{d}_e^T\mathbf{s}_e[\mathbf{d}_e] \tag{4.7}$$

where $\mathbf{s}_e[\mathbf{d}_e]$ is the element internal force vector. The second variation of the strain measure is

$$\delta\dot{\boldsymbol{\varepsilon}} = \boldsymbol{\mathcal{Q}}[\mathbf{d}_e, \dot{\mathbf{d}}_e]\delta\mathbf{d}_e = \boldsymbol{\mathcal{Q}}[\mathbf{d}_e, \delta\mathbf{d}_e]\dot{\mathbf{d}}_e$$

and its kth component is written as

$$\delta\dot{\varepsilon}_k = \dot{\mathbf{d}}_e^T\boldsymbol{\Psi}_k[\mathbf{d}_e]\delta\mathbf{d}_e$$

As $\boldsymbol{\sigma} = \mathbf{C}\boldsymbol{\varepsilon}$, the following expression holds

$$\boldsymbol{\sigma}^T\delta\dot{\boldsymbol{\varepsilon}} \equiv \sum_k \sigma_k\delta\dot{\varepsilon}_k = \dot{\mathbf{d}}_e^T\boldsymbol{\mathcal{G}}[\boldsymbol{\sigma}, \mathbf{d}_e]\delta\mathbf{d}_e$$

with

$$\boldsymbol{\mathcal{G}}[\boldsymbol{\sigma}[\mathbf{d}_e], \mathbf{d}_e] = \sum_k \sigma_k[\mathbf{d}_e]\boldsymbol{\Psi}_k[\mathbf{d}_e]\mathbf{d}_e \tag{4.8}$$

The second variation of the strain energy is

$$\Phi''_e[u]\delta u\dot{u} \equiv \int_{V_e} \left(\delta\boldsymbol{\varepsilon}^T\mathbf{C}\dot{\boldsymbol{\varepsilon}} + \delta\dot{\boldsymbol{\varepsilon}}^T\mathbf{C}\boldsymbol{\varepsilon}\right) dV_e = \delta\mathbf{d}_e^T\mathbf{K}_e[\mathbf{d}_e]\dot{\mathbf{d}}_e \tag{4.9}$$

with the element tangent stiffness matrix defined as

$$\mathbf{K}_e[\mathbf{d}_e] \equiv \int_{V_e} \left(\mathbf{Q}[\mathbf{d}_e]^T\mathbf{C}\mathbf{Q}[\mathbf{d}_e] + \boldsymbol{\mathcal{G}}[\boldsymbol{\sigma}[\mathbf{d}_e], \mathbf{d}_e]\right) dV_e \tag{4.10}$$

Numerical integration

The evaluation of the internal force vector and the tangent stiffness matrix, starting from the strain energy expression, requires integrations over the FE domain. The standard technique, usually employed to perform the integrations, is the Gauss quadrature, which allows the evaluation of the strain energy as

$$\Phi_e[\mathbf{d}_e] \equiv \sum_g^n \left(\frac{1}{2}\boldsymbol{\varepsilon}_g[\mathbf{d}_e]^T\mathbf{C}_g\boldsymbol{\varepsilon}_g[\mathbf{d}_e]\right) w_g \tag{4.11}$$

where subscript g denotes quantities evaluated in the integration point $\boldsymbol{\zeta}_g$ and w_g is the corresponding weight. If the coordinates $\boldsymbol{\zeta}$ in Eq.(4.4) are not the physical ones, w_g includes the determinant of the Jacobian matrix of the coordinate transformation, evaluated in the Gauss point. The internal force vector becomes

$$\mathbf{s}_e[\mathbf{d}_e] = \sum_g^n \left(\mathbf{Q}_g[\mathbf{d}_e]^T\mathbf{C}_g\boldsymbol{\varepsilon}_g[\mathbf{d}_e]\right) w_g \tag{4.12}$$

while the tangent stiffness matrix is

$$\mathbf{K}_e[\boldsymbol{\sigma}_g[\mathbf{d}_e], \mathbf{d}_e] = \sum_g^n \left(\mathbf{Q}_g[\mathbf{d}_e]^T\mathbf{C}_g\mathbf{Q}_g[\mathbf{d}_e] + \boldsymbol{\mathcal{G}}_g[\boldsymbol{\sigma}_g[\mathbf{d}_e], \mathbf{d}_e]\right) w_g \tag{4.13}$$

where $\mathbf{K}_e[\mathbf{d}_e]$ is written as $\mathbf{K}_e[\boldsymbol{\sigma}_g[\mathbf{d}_e], \mathbf{d}_e]$ as a reminder of the way it is computed.

Remarks

It is important to note that $\mathbf{K}_e$ in Eq.(4.10) contains the term $\boldsymbol{\mathcal{G}}[\boldsymbol{\sigma}[\mathbf{d}_e], \mathbf{d}_e]$, that depends on the stress evaluated using the current displacements $\mathbf{d}_e$. The true stresses, in large displacement and small strain problems, slowly change along the equilibrium path. Unfortunately, during an iterative process, $\mathbf{d}_e$ is just a current estimate and then, $\boldsymbol{\sigma}[\mathbf{d}_e] = \mathbf{C}\boldsymbol{\varepsilon}[\mathbf{d}_e]$, that is a nonlinear function of $\mathbf{d}_e$, can be very different from the stresses of the near equilibrium points. This "bad"

stress estimate gets worse when the structure presents directions with very different stiffness ratios and undergoes finite rotations, because $\boldsymbol{\varepsilon}[\mathbf{d}_e]$, during the iterations, can have non realistic components especially in the stiffest direction. This phenomenon leads to a slow convergence and an easy loss in convergence of the Newton method. Conversely, mixed FE formulations are not affected by this phenomenon because the stresses are directly extrapolated and corrected. This difference in the iterative scheme is the reason why mixed FEs allow a faster convergence of the Newton method in path-following analyses and can withstand large step sizes (increments).

4.3 Newton method with mixed integration points

The comments made in the preceding remarks lead to the following question: *"is it possible to exploit the advantages of the mixed iterative scheme for displacement-based FE models without changing the FE interpolation?"* This section gives an effective answer, proposing a Newton method based on the relaxation of constitutive equations at the level of the integration points during the iterative process. The approach, called MIP (Mixed Integration Point) Newton, allows a significant improvement in the performances of the method, without affecting the discrete approximation of the FE and without upsetting the existing FE codes. In fact the proposed strategy consists of a few changes to the standard iterative method, which are simple implementation details, but the benefits in geometrically nonlinear analysis are impressive, as will be shown in the numerical tests.

4.3.1 The MIP full Newton

The fundamental idea of the MIP Newton iterative scheme is to relax the constitutive equations at the level of each integration point. This is made by writing the total energy in a pseudo mixed form on the element

$$\Pi_e[\mathbf{u}_e] \equiv \Phi_e[\mathbf{u}_e] - \mathbf{d}_e^T \mathbf{p}_e \quad \text{with} \quad \mathbf{u}_e = \begin{bmatrix} \boldsymbol{\sigma}_1 \\ \vdots \\ \boldsymbol{\sigma}_n \\ \mathbf{d}_e \end{bmatrix} \tag{4.14}$$

where $\mathbf{p}_e$ is the element counterpart of the load vector $\mathbf{p}$ and the "mixed" strain energy $\Phi_e[\mathbf{u}_e]$ is obtained by rewriting Eq.(4.11) in a pseudo Helling-Reissner form as

$$\Phi_e[\mathbf{u}_e] \equiv \sum_{g=1}^{n} \left(\boldsymbol{\sigma}_g^T \boldsymbol{\varepsilon}_g[\mathbf{d}_e] - \frac{1}{2} \boldsymbol{\sigma}_g^T \mathbf{C}_g^{-1} \boldsymbol{\sigma}_g \right) w_g \tag{4.15}$$

in which the stresses at each integration point $\boldsymbol{\sigma}_g$ are now independent variables. The first variation of (4.15) is

$$\Phi'_e \delta u = \sum_{g=1}^{n} \begin{bmatrix} \delta\boldsymbol{\sigma}_g \\ \delta\mathbf{d}_e \end{bmatrix}^T \begin{bmatrix} \mathbf{s}_{g\sigma} \\ \mathbf{s}_{gd} \end{bmatrix} w_g \tag{4.16}$$

with

$$\begin{cases} \mathbf{s}_{g\sigma} \equiv \boldsymbol{\varepsilon}_g[\mathbf{d}_e] - \mathbf{C}^{-1}\boldsymbol{\sigma}_g \\ \mathbf{s}_{gd} \equiv \mathbf{Q}_g[\mathbf{d}_e]^T \boldsymbol{\sigma}_g \end{cases} \tag{4.17}$$

We can note that

- the stationarity of (4.14) with respect to $\boldsymbol{\sigma}_g$ leads to the constitutive equations $\boldsymbol{\sigma}_g = \mathbf{C}_g \boldsymbol{\varepsilon}_g[\mathbf{d}_e]$ and, thus, the FE remains based on a displacement formulation because the stresses satisfy the constitutive law along the equilibrium path exactly.

- the stresses at the integration points are independent variables and, thus, they are not forced to satisfy the constitutive law during the iterations but, the constitutive equations are solved together with the equilibrium equations and are satisfied only when convergence is obtained.

The second variation of (4.14) is

$$\Phi''_e \delta u \dot{u} = \sum_{g=1}^{n} \begin{bmatrix} \delta\boldsymbol{\sigma}_g \\ \delta\mathbf{d}_e \end{bmatrix}^T \begin{bmatrix} -\mathbf{C}_g^{-1} & \mathbf{Q}_g \\ \mathbf{Q}_g^T & \boldsymbol{\mathcal{G}}_g \end{bmatrix} \begin{bmatrix} \dot{\boldsymbol{\sigma}}_g \\ \dot{\mathbf{d}}_e \end{bmatrix} w_g \tag{4.18}$$

where $\boldsymbol{\mathcal{G}}_g \equiv \boldsymbol{\mathcal{G}}_e[\boldsymbol{\sigma}_g, \mathbf{d}_e]$ is the matrix $\boldsymbol{\mathcal{G}}_e$ evaluated in the integration point g, that is now a function of the displacement DOFs and of the independent stresses $\boldsymbol{\sigma}_g$. The Newton iteration, at the element level, becomes

$$\begin{bmatrix} -\mathbf{C}_1^{-1} w_1 & & & \mathbf{Q}_1 w_1 \\ & \ddots & & \vdots \\ & & -\mathbf{C}_n^{-1} w_n & \mathbf{Q}_n w_n \\ \mathbf{Q}_1^T w_1 & \dots & \mathbf{Q}_n^T w_n & \sum_g^n \boldsymbol{\mathcal{G}}_g w_g \end{bmatrix}^j \begin{bmatrix} \dot{\boldsymbol{\sigma}}_1 \\ \vdots \\ \dot{\boldsymbol{\sigma}}_n \\ \dot{\mathbf{d}}_e \end{bmatrix} = (\lambda^j + \dot{\lambda}) \begin{bmatrix} \mathbf{0} \\ \vdots \\ \mathbf{0} \\ \mathbf{p}_e \end{bmatrix} - \begin{bmatrix} \mathbf{s}_{1\sigma} w_1 \\ \vdots \\ \mathbf{s}_{n\sigma} w_n \\ \sum_g^n \left(\mathbf{Q}_g^T \boldsymbol{\sigma}_g w_g \right) \end{bmatrix}^j \tag{4.19}$$

where the superscript on matrices denotes that they are evaluated during the iterative process in the current estimate $\mathbf{u}_e^j$.

By performing a static condensation of the stresses $\dot{\boldsymbol{\sigma}}_g$, locally defined at the level of the integration point, we obtain

$$\dot{\boldsymbol{\sigma}}_g = \mathbf{C}_g \mathbf{Q}_g^j \dot{\mathbf{d}}_e + \mathbf{C}_g \mathbf{s}_{g\sigma}^j = \mathbf{C}_g \mathbf{Q}_g^j \dot{\mathbf{d}}_e + \mathbf{C}_g \boldsymbol{\varepsilon}_g^j - \boldsymbol{\sigma}_g^j \tag{4.20}$$

and letting $\mathbf{r}_{ce}[\mathbf{d}_e^j] = \mathbf{s}_{ce}[\mathbf{d}_e^j] - \lambda^j \mathbf{p}_e$

$$\mathbf{K}_e[\mathbf{u}_e^j]\dot{\mathbf{d}}_e = -\mathbf{r}_{ce}[\mathbf{d}_e^j] + \dot{\lambda}\mathbf{p}_e \tag{4.21}$$

with

$$\mathbf{K}_e[\boldsymbol{\sigma}_g^j, \mathbf{d}_e^j] = \sum_{g=1}^{n} \left(\mathbf{Q}_g[\mathbf{d}_e^j]^T \mathbf{C}_g \mathbf{Q}_g[\mathbf{d}_e^j] + \boldsymbol{\mathcal{G}}_g[\boldsymbol{\sigma}_g^j, \mathbf{d}_e^j] \right) w_g \tag{4.22}$$

the condensed tangent stiffness matrix, that has the same form as the classical displacement based one (4.13). However, this time it also depends on the independent stresses at the integration points, which are now directly extrapolated and corrected during the iterations.

Conversely, we can note that the condensed internal forces $\mathbf{s}_{ce}[\mathbf{d}_e^j]$

$$\mathbf{s}_{ce}[\mathbf{d}_e^j] = \sum_{g}^{n} \left(\mathbf{Q}_g^{jT} \mathbf{C}_g \boldsymbol{\varepsilon}_g^j \right) w_g$$

coincides exactly with the internal forces of the displacement-based formulation in Eq.(4.12). This iterative scheme is then very close to the standard Newton one for displacement-based FE models as it is highlighted in Tab. 4.1. The main difference consists of the different value of the stresses at the integration points used for the evaluation of the tangent stiffness matrix. In the Newton method the stresses $\boldsymbol{\sigma}_g$ are functions of the displacements and are forced to satisfy the constitutive law at each iteration. Conversely, in the MIP Newton $\boldsymbol{\sigma}_g$ are independent variables and so, are directly extrapolated and corrected and only at convergence satisfy the constitutive law. Clearly, the equilibrium path recovered is the same as the standard displacement approach, but the proposed method requires a much lower number of iterations, under equal convergence criteria, and can withstand larger step sizes (increments). The improved performances are mainly due to the "better" iteration matrix that is possible when the stresses, which slowly change along the equilibrium path, are chosen as independent variables of the iterative scheme. Furthermore, it is possible to note, looking at Tab.4.1, that the computational cost of a MIP iteration is practically the same as a standard one.

4.3.2 The MIP modified Newton

The modified Newton method evaluates and decomposes the iteration matrix in the first extrapolation (predictor) of each step. If the matrix is a good approximation of the secant one the method can converge in a reasonable number of iterations. Unfortunately, in geometrically nonlinear analysis, displacement-based FEs usually prevent the use of the modified scheme. In fact, already failure easily occurs for the full Newton and is assured for the modified method unless a very small step size and a very large number of iterations are used.
This is not the case with the previously proposed MIP Newton scheme. In fact, the

	Newton	MIP Newton
Predictor	$\mathbf{d}^1 = \mathbf{d}_{(k)} + \Delta\mathbf{d}$ $\lambda^1 = \lambda_{(k)} + \Delta\lambda$ $\boldsymbol{\sigma}_g[\mathbf{d}^1] = \mathbf{C}_g\boldsymbol{\varepsilon}_g[\mathbf{d}^1]$	$\mathbf{d}^1 = \mathbf{d}_{(k)} + \Delta\mathbf{d}$ $\lambda^1 = \lambda_{(k)} + \Delta\lambda$ $\boldsymbol{\sigma}_g^1 = \boldsymbol{\sigma}_{g(k)} + \Delta\boldsymbol{\sigma}_g$
Iteration matrix	$\mathbf{K}[\boldsymbol{\sigma}_g[\mathbf{d}^j], \mathbf{d}^j]$	$\mathbf{K}[\boldsymbol{\sigma}_g^j, \mathbf{d}^j]$
Residual vector	$\mathbf{s}[\mathbf{d}^j] - \lambda^j\mathbf{p}$	$\mathbf{s}[\mathbf{d}^j] - \lambda^j\mathbf{p}$
New estimate	$\mathbf{d}^{j+1} = \mathbf{d}^j + \dot{\mathbf{d}}$ $\lambda^{j+1} = \lambda^j + \dot{\lambda}$ $\boldsymbol{\sigma}_g^{j+1} = \mathbf{C}_g\boldsymbol{\varepsilon}_g[\mathbf{d}^{j+1}]$	$\mathbf{d}^{j+1} = \mathbf{d}^j + \dot{\mathbf{d}}$ $\lambda^{j+1} = \lambda^j + \dot{\lambda}$ $\boldsymbol{\sigma}_g^{j+1} = \boldsymbol{\sigma}_g^{j+1} + \dot{\boldsymbol{\sigma}}$

Table 4.1: Schematic description of the principal point of the algorithms: the differences between the standard Newton and the MIP Newton are marked in red.

stiffness matrix, evaluated using the direct extrapolation of the stresses from the previous step, is already a good estimation of the secant matrix and, furthermore, the MIP tangent matrix slightly changes during the iterative process. The matrix so evaluated in the first prediction is then suitable for use in all the iterations over the step, as required in the modified version of the method (MIP modified Newton). Clearly, the number of iterations required by MIP modified Newton is usually larger than that required by the MIP full Newton, but the direct extrapolation of the stress assures robustness and efficiency. The few extra-iterations are compensated by the need to calculate and decompose the iteration matrix just once in each step.

The Newton iteration can be written as

$$\begin{bmatrix} -\mathbf{C}_1^{-1}w_1 & & & \mathbf{Q}_1 w_1 \\ & \ddots & & \vdots \\ & & -\mathbf{C}_n^{-1}w_n & \mathbf{Q}_n w_n \\ \mathbf{Q}_1^T w_1 & \dots & \mathbf{Q}_n^T w_n & \sum_g^n \boldsymbol{\mathcal{G}}_g w_g \end{bmatrix}^1 \begin{bmatrix} \dot{\boldsymbol{\sigma}}_1 \\ \vdots \\ \dot{\boldsymbol{\sigma}}_n \\ \dot{\mathbf{d}}_e \end{bmatrix} = (\lambda^j + \dot{\lambda}) \begin{bmatrix} \mathbf{0} \\ \vdots \\ \mathbf{0} \\ \mathbf{p}_e \end{bmatrix} - \begin{bmatrix} \mathbf{s}_{1\sigma} w_1 \\ \vdots \\ \mathbf{s}_{n\sigma} w_n \\ \sum_g^n \left(\mathbf{Q}_g^T \boldsymbol{\sigma}_g w_g \right) \end{bmatrix}^j \tag{4.23}$$

where the superscript 1 denotes quantities evaluated in the first prediction of the new equilibrium point. By performing a static condensation of the stresses $\boldsymbol{\sigma}_g$, locally defined at the level of each integration point, we obtain

$$\dot{\boldsymbol{\sigma}}_g = \mathbf{C}_g\mathbf{Q}_g[\mathbf{d}_e^1]\dot{\mathbf{d}}_e + \mathbf{C}_g\mathbf{s}_{g\sigma}^j = \mathbf{C}_g\mathbf{Q}_g[\mathbf{d}_e^1]\dot{\mathbf{d}}_e + \mathbf{C}_g\boldsymbol{\varepsilon}_g^j - \boldsymbol{\sigma}_g^j \tag{4.24}$$

and letting $\mathbf{r}_{ce}[\mathbf{d}_e^j] = \mathbf{s}_{ce}[\mathbf{d}_e^j] - \lambda^j \mathbf{p}_e$

$$\mathbf{K}_e[\mathbf{u}_e^1]\dot{\mathbf{d}}_e = -\mathbf{r}_{ce}[\mathbf{d}_e^j] + \dot{\lambda}\mathbf{p}_e \tag{4.25}$$

where

$$\mathbf{K}[\mathbf{u}_e^j] = \sum_{g=1}^{n} \left(\mathbf{Q}_g[\mathbf{d}_e^1]^T \mathbf{C}_g \mathbf{Q}_g[\mathbf{d}_e^1] + \boldsymbol{\mathcal{G}}_g[\boldsymbol{\sigma}_g^1, \mathbf{d}_e^1] \right) w_g \tag{4.26}$$

is the iteration matrix, constant during the iterations of the single step. In the MIP modified Newton scheme we have to note that, with respect to the MIP full method, the condensed internal force vector

$$\mathbf{s}_{ce}[\mathbf{d}_e^j] = \sum_{g}^{n} \left(\mathbf{Q}_g[\mathbf{d}_e^j]^T \boldsymbol{\sigma}_g^j + \mathbf{Q}_g[\mathbf{d}_e^1]^T (\mathbf{C}_g \boldsymbol{\varepsilon}_g^j - \boldsymbol{\sigma}_g^j) \right) w_g \neq \mathbf{s}_e[\mathbf{d}_e^j]$$

does not coincide with that of the displacement-based scheme, because of the use of a constant iteration matrix. However, this is just a further implementation detail with a very low extra-cost, largely compensated by the constant iteration matrix.
Note that, even in this case, the stresses, at convergence but not during the iterative process, satisfy the constitutive law exactly and so the method provides the same equilibrium path as the standard displacement-based approach. However, note that the estimated iteration matrix in the modified MIP Newton is so "good" that usually the number of iterations required is even less than that required by the standard full Newton for displacement-based FE models.

4.3.3 MIP full Newton vs MIP modified Newton

Recall that, for the modified scheme, when the number of DOFs is large, the computational cost over the single step is dominated by the stiffness matrix decomposition, performed only once at the beginning of the step. The MIP modified Newton represents then an attractive alternative, if it is able to converge in a similar number of iterations to that of the MIP full Newton, which assembles and decomposes the matrix at each iteration. In fact, in this situation, an entire step of the modified version has a cost comparable with a single iteration of the full one. As shown in the numerical tests, the iterations required by the MIP modified Newton tends towards that required by the MIP full Newton, when the step size gets smaller. In many cases, the equilibrium path of the structure requires a step size small enough for an accurate description of the curve, even if the iterative method is able to converge using larger steps. In this case, the modified version is clearly the most effective choice. Conversely, when the curve can be described with a small number of points or when a single equilibrium configuration is sought, the MIP full Newton is recommended because of its ability to withstand very large steps without any loss in convergence. The Numerical Results section adds further comments on these aspects.

4.3.4 MIP strategy vs mixed formulation

The MIP approach previously presented is derived by rewriting Eq.(4.11) in a pseudo mixed form. The word "pseudo" is used because the standard procedure of prescribing interpolation functions for the stress components is replaced here by assigning a value to those variables directly at the integration points. From the stationarity of (4.14) we simply obtain a different writing of the standard residual equation for displacement formulations, where the constitutive equations of each integration point now appear explicitly. Note that, by "a priori" satisfying these constitutive equations, we regain the usual displacement approach. Conversely, the MIP strategy solves the constitutive equations and the equilibrium equations simultaneously during the iterations, so obtaining a mixed iteration scheme. The MIP strategy is then, simply, an algebraic manipulation of the nonlinear equations, which leads to an improved iterative method for displacement-based finite element models. Furthermore, since no shape function for the stress field is adopted, the extra-cost in constructing the tangent stiffness matrix, typical of mixed formulations [2, 10], is avoided. The stiffness matrix retains its original form, apart from the different values of $\boldsymbol{\sigma}_g$ during the iterations.

4.4 Implementation details

The impressively better performances of the proposed iterative strategy with respect to the standard Newton method hold for any structural model, displacement–based finite element and implementation choice of the Newton method and of the arc-length constraint. However, in this section, some details about all these aspects are provided, in order to make the numerical tests presented in the next section reproducible. In particular the structural models considered are chosen to be as simple and general as possible: i) 2D frames, based on the Reissner geometrically exact strain measure; ii) 3D shells, based on a solid-shell FE model and the Green-Lagrange strain measure. A Total Lagrangian formulation is chosen for both the models, even if other formulations can be easily employed.

4.4.1 Implementation details of the Newton scheme

- Predictor
  Starting from a known equilibrium point $\mathbf{z}_k$ the first predictor $\mathbf{z}_k^1$ of the new equilibrium point $\mathbf{z}_{k+1}$ is evaluated as

$$\mathbf{z}_1 = \mathbf{z}_k + \alpha(\mathbf{z}_k - \mathbf{z}_{k-1})$$

  where α defines the step size. For the first equilibrium point it is particularized as

$$\mathbf{z}_1 = \Delta\lambda_0 \begin{bmatrix} 1 \\ \hat{\mathbf{u}} \end{bmatrix}$$

being $\hat{\mathbf{u}}$ the linear elastic solution for the reference load $\mathbf{p}$.

- Arc-length parameters
  The arc-length constraint is defined by the metric factors $\mathbf{M}$ and μ. The metric matrix $\mathbf{M}$ is assumed to be a diagonal matrix with $M_{ii} = 1$ if the ith variable is a displacement, $M_{ii} = \ell^2$ if the ith variable is a rotation, ℓ being a characteristic length of the structures. The factor μ is selected as

$$\mu = \mu_0^2 \hat{\mathbf{d}}^T \mathbf{M} \hat{\mathbf{d}}$$

  where the factor μ_0, chosen to be equal to 10^{-2}, takes into account that for stability problems the initial tangent can be much larger than the average one.

- The adaptive step size
  The factor α which defines the step size is evaluated in an adaptive way in terms of the iterations required in the last step N_k and the desired number of iterations per step N_d, chosen as equal to 4, as

$$\alpha = 1 - \frac{0.5(N_k - N_d)}{N_k + N_d}$$

  The values of α are constrained by the condition $\alpha \in [0.5, 2]$.

- Convergence criteria
  Convergence is accepted if

$$(\dot{\mathbf{d}}^j)^T \mathbf{M} \dot{\mathbf{d}}^j < \text{Toll}^2 (\Delta\lambda_0^2 \hat{\mathbf{d}}^T \mathbf{M} \hat{\mathbf{d}})$$

  that is if the norm of the correction to the displacement solution is smaller than a desired tolerance $\text{Toll} = 10^{-4}$ compared to the initial solution increment. If the convergence condition is not satisfied after 20 iterations or if the error fails to decrease after two consecutive iterations, the iterations are abandoned and α is halved.

- The load-controlled analysis
  A load-controlled analysis can be performed by redefining the arc-length constraint as

$$\lambda = \lambda_{k+1}$$

  and setting $\alpha = 1$. The process is declared failed if the preceding convergence condition is not satisfied after 20 iterations.

4.4.2 The 2D beam element

The 2D beam model is based on the objective Reissner–Antman strain measure

$$\boldsymbol{\varepsilon} = \begin{bmatrix} \epsilon \\ \gamma \\ \chi \end{bmatrix} \quad \text{with} \quad \begin{cases} \epsilon = (1 + u_{,s}) \cos\varphi + w_{,s} \sin\varphi - 1 \\ \gamma = -(1 + u_{,s}) \sin\varphi + w_{,s} \cos\varphi \\ \chi = \varphi_{,s} \end{cases} \tag{4.27}$$

where u, w, φ are, respectively, the axial displacement, the transversal displacement and the rotation, functions of the abscissa along the beam axis s. The constitutive matrix is

$$\mathbf{C} = \begin{bmatrix} EA & 0 & 0 \\ 0 & GAr & 0 \\ 0 & 0 & EJ \end{bmatrix} \tag{4.28}$$

where E is the Young modulus, G is the shear modulus, A is the cross-section area, r is the shear correction factor and J is the cross-section moment of inertia. The finite element is assumed to be straight and the FE interpolation is very simple and consists of a 3 node quadratic Lagrangian interpolation for u, w, φ. The nodes are located at the ends and at the midspan of the element.

The interpolation of u, w, φ is introduced in Eq.(4.27) so obtaining the operator $\mathbf{B}$ in Eq.(4.6).

Two Gauss integration points are used to evaluate the internal force vector and the stiffness matrix.

4.4.3 The solid-shell element

For the shell structures a solid-shell element is used. However, the MIP method can also easily be used for standard shell elements.
The solid-shell element is based on the interpolation described in [10]. It is presented here in the case of a Green-Lagrange strain measure and in a Total Lagrangian description. Denoting with $\boldsymbol{\zeta} = \{\xi, \eta, \zeta\}$ the convective coordinates used to express the FE interpolation, the current configuration is described by the reference position vector $\mathbf{X}[\boldsymbol{\zeta}] \equiv \{X[\boldsymbol{\zeta}], Y[\boldsymbol{\zeta}], Z[\boldsymbol{\zeta}]\}$ and by the displacement field $\mathbf{d}[\boldsymbol{\zeta}]$. Adopting the convention of summing on repeated indexes, the covariant Green-Lagrange strain measure components are

$$\bar{E}_{ij} = \frac{1}{2} (\mathbf{X}_{,i} \cdot \mathbf{d}_{,j} + \mathbf{d}_{,i} \cdot \mathbf{X}_{,j} + \mathbf{d}_{,i} \cdot \mathbf{d}_{,j}) \quad \text{with} \quad i, j = \xi, \eta, \zeta \tag{4.29}$$

where a comma followed by k denotes the derivative with respect to k and $(\cdot)$ denotes the scalar product. The position vector of a point inside the element and its displacement are interpolated, using a trilinear 8 node hexahedron, as

$$\mathbf{X}[\boldsymbol{\zeta}] = \mathbf{N}_d[\boldsymbol{\zeta}] \mathbf{X}_e \quad , \quad \mathbf{d}[\boldsymbol{\zeta}] = \mathbf{N}_d[\boldsymbol{\zeta}] \mathbf{d}_e \tag{4.30}$$

where vectors $\mathbf{d}_e$ and $\mathbf{X}_e$ collect the element nodal displacements and coordinates and matrix $\mathbf{N}_d[\boldsymbol{\zeta}]$ the trilinear interpolation functions. Adopting a Voigt notation the Green-Lagrange covariant strain components in Eq.(4.29) are collected in vector $\bar{\mathbf{E}} \equiv [\bar{E}_{\xi\xi}, \bar{E}_{\eta\eta}, 2\bar{E}_{\xi\eta}, \bar{E}_{\zeta\zeta}, 2\bar{E}_{\eta\zeta}, 2\bar{E}_{\xi\zeta}]^T$ that, exploiting Eq.(4.30), becomes

$$\bar{\mathbf{E}} = \left(\boldsymbol{\mathcal{L}}[\boldsymbol{\zeta}] + \frac{1}{2}\boldsymbol{\mathcal{Q}}[\boldsymbol{\zeta}, \mathbf{d}_e] \right) \mathbf{d}_e, \tag{4.31}$$

In order to circumvent shear and trapezoidal lockings, the natural transverse normal strain $\bar{E}_{\zeta\zeta}$ and the shear strains $\bar{E}_{\xi\zeta}, \bar{E}_{\eta\zeta}$ are redefined by the *assumed natural strain* (ANS) technique [20, 13], assuming from now on that the Z-axis and the X-Y-plane are parallel to the ζ-axis and mid-surface of the shell respectively. To enhance the in-plane bending response of the element, the in-plane shear strain $\bar{E}_{\xi\eta}$ is substituted by its counterpart evaluated in $\xi = \eta = 0$, as a selective reduced integration (SRI). The covariant strains can be linearized with respect to ζ in the following form

$$\bar{\mathbf{E}} \approx \begin{bmatrix} \bar{\mathbf{e}}[\xi, \eta] + \zeta\, \bar{\boldsymbol{\chi}}[\xi, \eta] \\ \bar{E}_{\zeta\zeta}[\xi, \eta] \\ \bar{\boldsymbol{\gamma}}[\xi, \eta] \end{bmatrix} \tag{4.32}$$

where

$$\bar{\mathbf{e}}[\xi, \eta] \equiv \begin{bmatrix} \bar{E}_{\xi\xi} \\ \bar{E}_{\eta\eta} \\ 2\bar{E}_{\xi\eta} \end{bmatrix} \quad \bar{\boldsymbol{\chi}}[\xi, \eta] \equiv \begin{bmatrix} \bar{E}_{\xi\xi,\zeta} \\ \bar{E}_{\eta\eta,\zeta} \\ 2\bar{E}_{\xi\eta,\zeta} \end{bmatrix} \quad \bar{\boldsymbol{\gamma}}[\xi, \eta] \equiv \begin{bmatrix} 2\bar{E}_{\eta\zeta} \\ 2\bar{E}_{\xi\zeta} \end{bmatrix}$$

The generalized covariant strains can be collected in vector $\bar{\boldsymbol{\varepsilon}}$ as

$$\bar{\boldsymbol{\varepsilon}}[\xi, \eta] \equiv \begin{bmatrix} \bar{\mathbf{e}} \\ \bar{E}_{\zeta\zeta} \\ \bar{\boldsymbol{\chi}} \\ \bar{\boldsymbol{\gamma}} \end{bmatrix} = \left(\boldsymbol{\mathcal{L}}_\rho[\xi, \eta] + \frac{1}{2}\boldsymbol{\mathcal{Q}}_\rho[\xi, \eta, \mathbf{d}_e] \right) \mathbf{d}_e, \tag{4.33}$$

where matrix $\boldsymbol{\mathcal{L}}_\rho$ and $\boldsymbol{\mathcal{Q}}_\rho$ are automatically defined from Eq.(4.31) exploiting ASN, SRI and Eq.(4.32), so obtaining the operator $\mathbf{B}$ in Eq.(4.6).

Finally the generalized Cartesian strains are obtained from the natural ones as

$$\boldsymbol{\varepsilon} = \mathbf{T}\bar{\boldsymbol{\varepsilon}} \quad \text{with} \quad \mathbf{T}[\xi, \eta] = \begin{bmatrix} \mathbf{T}_p & 0 & 0 & 0 \\ 0 & T_z & 0 & 0 \\ 0 & 0 & \mathbf{T}_p & 0 \\ 0 & 0 & 0 & \mathbf{T}_t \end{bmatrix} \tag{4.34}$$

where, letting $\mathbf{J}$ the element Jacobian matrix, $T_z = 1/J_{33}^2$ and

$$\begin{aligned} \mathbf{T}_p &= \begin{bmatrix} J_{11}^2 & J_{12}^2 & 2J_{11}J_{12} \\ J_{21}^2 & J_{22}^2 & 2J_{21}J_{22} \\ J_{21}J_{11} & J_{22}J_{12} & J_{22}J_{11} + J_{21}J_{12} \end{bmatrix}^{-T} \\ \mathbf{T}_t &= \begin{bmatrix} J_{12}J_{33} + J_{13}J_{32} & J_{13}J_{31} + J_{11}J_{33} \\ J_{22}J_{33} + J_{23}J_{32} & J_{23}J_{31} + J_{21}J_{33} \end{bmatrix}^{-T} \end{aligned} \tag{4.35}$$

The generalized constitutive matrix $\mathbf{C}$ is evaluated starting from the constitutive law $\mathbf{S} = \mathbb{C}\mathbf{E}$, $\mathbf{S}$ being the second Piola-Kirchhoff stress tensor, performing an analytic pre-integration of $\mathbb{C}$ along the thickness direction and assuming a constant with Z stress S_{zz} instead of a constant thickness strain E_{zz}, in order to eliminate the thickness locking, following the approach proposed in [21].

A 2×2 grid of integration points on the middle plane of the shell is used to evaluate the internal force vector and the stiffness matrix.

The same format of the equations holds for other displacement based solid-shell elements [12].

4.5 Numerical tests

In this section some benchmarks concerning 2D framed structures and 3D shells are presented and discussed. The goal is to test and show the better performances of the proposed MIP approach with respect to the standard Newton method in terms of i) total number of iterations required to trace the equilibrium path or to obtain the deformed configuration for an assigned load, ii) the step size (or load increment) that the method can withstand without loss in convergence. For all the methods the convergence criteria and the analysis parameters are the same and are those reported in the previous section. Furthermore, remember that all the methods, when converged, provide the same equilibrium path and deformed configurations.

In the comparisons of the different methods reported in the following, the term "Newton" denotes the standard full Newton method, "MIP Newton" denotes the full Newton based on the MIP approach and "MIP M. Newton" denotes the modified Newton based on the MIP approach.

4.5.1 2D frame tests

The first tests are performed with a 2D beam model, based on the Antman strain measure and a quadratic Lagrangian FE interpolation for the displacements and the rotation. Two Gauss integration points are used. These simple numerical examples are presented because they are very easy to reproduce.

Clamped-Hinged arc

The first test is the clamped-hinged arc, already studied in many papers, for which the geometry, the loads and the material properties are reported in figure 4.1. A mesh of 36 finite elements has been used. The characteristic length used in the metric matrix to homogenize rotations and displacements is assumed as $\ell = R$.

The arc-length method with adaptive step size is adopted and the initial value of the load increment used is $\Delta\lambda_0 = 0.04$. The structure has been analyzed for different values of $k = AR^2/J$ to highlight the pathological dependence on

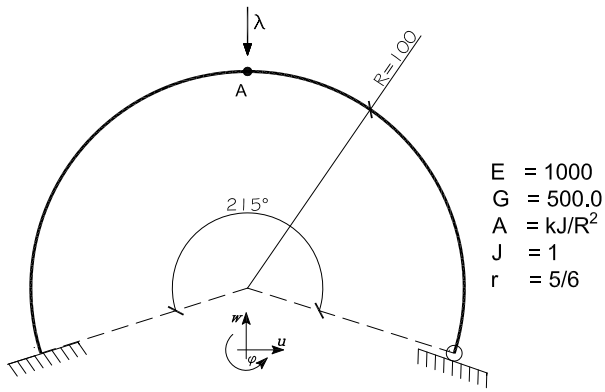

Figure 4.1: Clamped-hinged arc: geometry

	Newton		MIP Newton		MIP M. Newton	
k	steps	iters	steps	iters	steps	iters
10^5	126	512	45	149	66	256
10^6	208	889	45	149	66	256
10^7	425	1744	45	149	66	256

Table 4.2: Clamped-hinged arc: total number of steps and iterations for the evaluation of the equilibrium path.

this value of the robustness and performance of the path-following analysis. In Tab.4.2 the total number of steps and iterations required for the evaluation of the equilibrium path until a vertical displacement $w_A = -180$ is reported. We can observe that, even if the equilibrium path does not change for the considered values of k, the number of steps and total iterations required by the standard Newton drastically increases with k. Conversely, the performances of the MIP Newton, in both the full and the modified version are independent of k. In particular the MIP modified Newton, which requires only a matrix assemblage and factorization for each step, looks very convenient.

Finally in Fig.4.2 the equilibrium path and the evolution of the deformed configurations are presented.

Rigidly jointed truss

The second simple test consists of the rigidly jointed truss already studied in [32], for which the geometry, the loads and the material properties are reported in figure 4.3.

Six FEs for each beam have been used, while the initial load increment used in the arc-length strategy with adaptive step size is $\Delta\lambda_0 = 0.03$. The characteristic length used in the metric matrix to homogenize rotations and displacements is

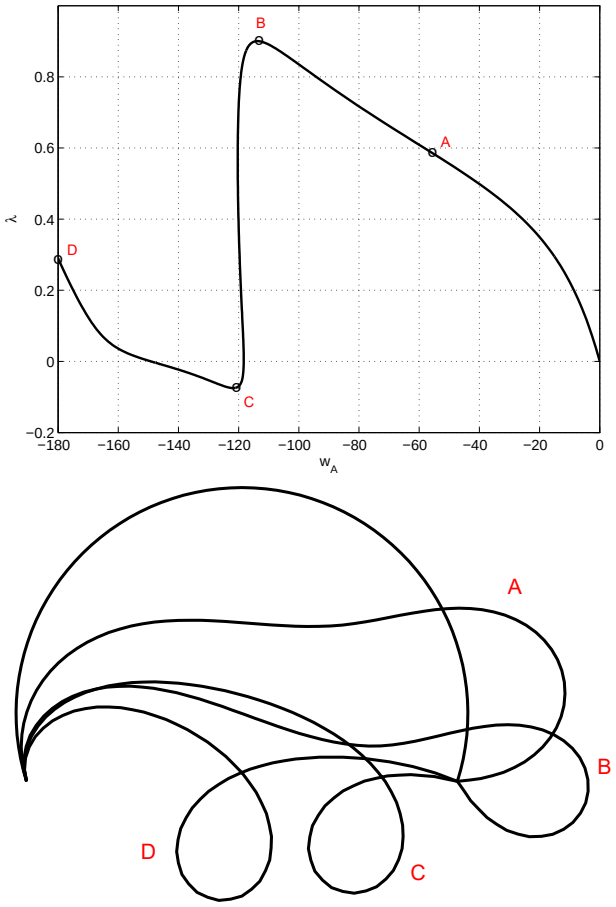

Figure 4.2: Clamped-hinged arc: equilibrium path and deformed configuration evolution

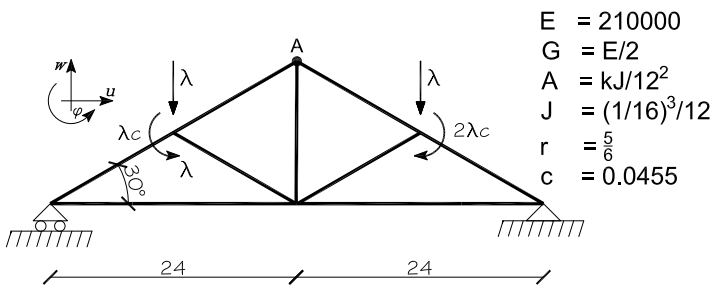

Figure 4.3: Rigidly jointed truss: geometry

	Newton		MIP Newton		MIP M. Newton	
k	steps	iters	steps	iters	steps	iters
10^5	121	426	74	221	74	221
10^6	176	651	74	221	74	221
10^7	253	965	74	221	74	221

Table 4.3: Rigidly jointed truss: total number of steps and iterations for the evaluation of the equilibrium path.

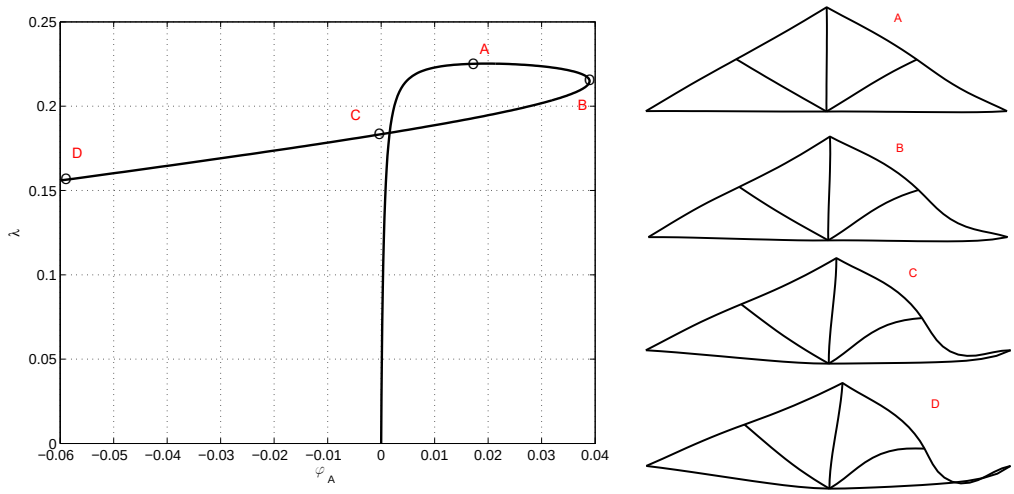

Figure 4.4: Rigidly jointed truss: equilibrium path and deformed configuration evolution

assumed as $\ell = H$, with H the truss height. Also in this case the structure has been analyzed for different values of $k = AH^2/J$ to highlight the effect of this value on the overall performance. In Tab.4.3 the total number of steps and iterations required for the evaluation of the equilibrium path until a rotation $\varphi_A = -0.06$ is reported. Even in this case, the equilibrium path does not change for the considered values of k and we can observe the increasing number of steps and iterations required by the standard Newton. On the contrary, the MIP Newton, in both the full and the modified approach, is independent of k with the MIP modified Newton which, in this case, requires the same steps and loops as the MIP full one with a gain in computation.

Finally in Fig.4.4 the equilibrium path and the evolution of the deformed configurations are presented.

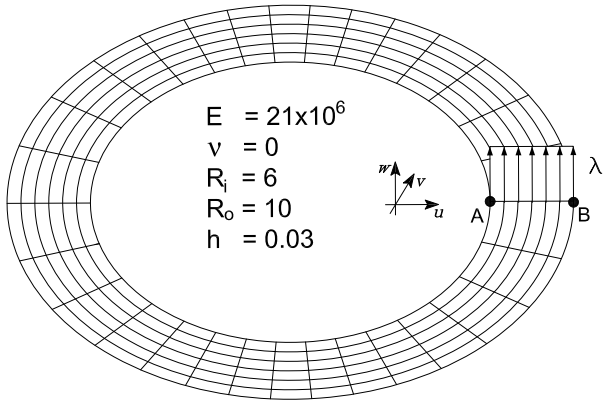

Figure 4.5: Slit annular plate: geometry

	Newton	MIP Newton	MIP M. Newton
Nsteps	iters	iters	iters
1	fails	9	fails
5	fails	20	fails
10	fails	32	44
20	175	54	58

Table 4.4: Slit annular plate: total number of iterations for the evaluation of the equilibrium path vs the number of load subdivisions.

4.5.2 Shell structures

A series of popular benchmarks regarding shell structures in finite deformations are tested using the solid-shell element recalled in the previous section.

4.5.3 Slit annular plate under line force

The first test is the slit annular plate described in Fig.4.5 and already analysed by many authors [10]. A mesh of 30×6 solid-shell FEs has been used.

In Fig.4.6 the equilibrium path and the last deformed configuration are presented.

To highlight the robustness of the proposed MIP Newton, the equilibrium path has been reconstructed using a load-controlled scheme. The maximum load value of 1 has been subdivided in *Nsteps* equal load increments. The total number of iterations required to evaluate the equilibrium path are reported in Tab.4.4.

The standard Newton fails to converge with the first 3 load subdivisions, while for the finest one it converges but the number of iterations required is very high. Conversely, the MIP Newton is able to evaluate the equilibrium point corresponding to $\lambda = 1$ with just a single load increment and only 9 iterations. When the number of load steps *Nsteps* increases, the number of iterations per

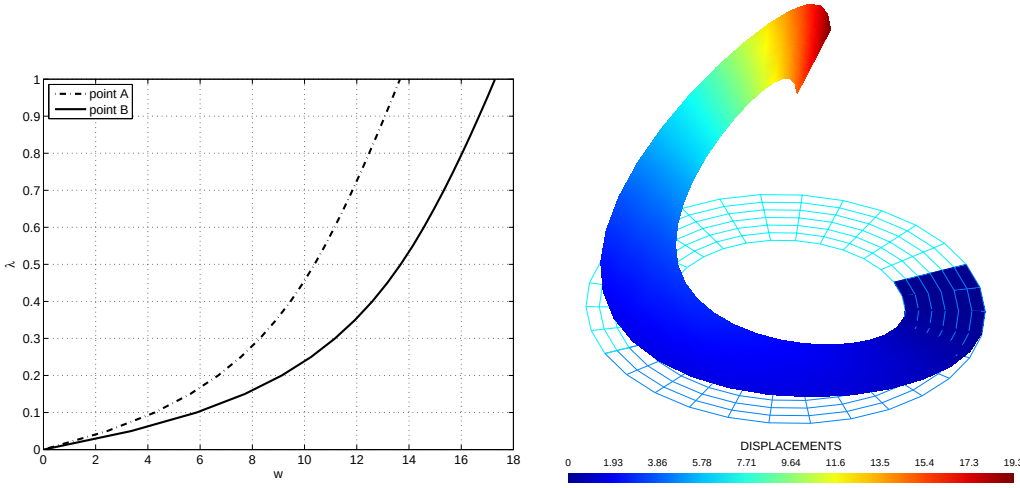

Figure 4.6: Slit annular plate: equilibrium path and deformed configuration at the last evaluated equilibrium point

step gets smaller, but the total number of iterations increases. However, even for the smallest step size the MIP Newton is more than three times more efficient than the standard Newton. Finally, the modified MIP Newton converges for reasonable values of the step size and with a number of iterations comparable with the full MIP Newton and much lower than that required by the standard full Newton.

4.5.4 Thin-walled cantilever beam

Finally a test regarding a thin-walled cantilever beam with U cross section is considered. Geometry, loads and material properties are reported in Fig.4.7. The FE mesh consists of 2880 solid-shell FEs, obtained via 32 equal subdivisions on the cross section and 90 subdivisions along the beam axis. As shown in [47] the structure is characterized by complex buckling mode interaction phenomena.

An arc-length technique with adaptive step size is used and the initial load increment is $\Delta\lambda_0 = 3$. Fig.4.8 depicts the equilibrium path and the deformed configuration at the limit and the final equilibrium point corresponding to a vertical displacement $w_A = -1$. The mode interaction is evident looking at the deformed shapes and produces the unstable post-critical behavior.

As for all the other tests, the MIP Newton, in both the full or the modified version, performs better with respect to the standard method as shown in Tab.4.5. In particular the full standard Newton requires a total number of iterations 3 times larger than the MIP full Newton and almost twice the MIP modified Newton.

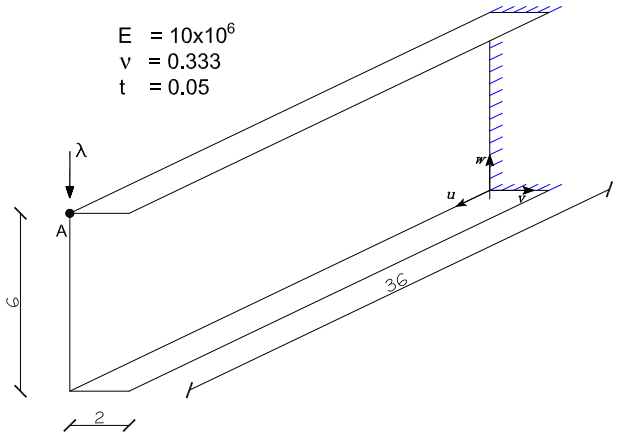

Figure 4.7: Thin walled cantilever beam: geometry

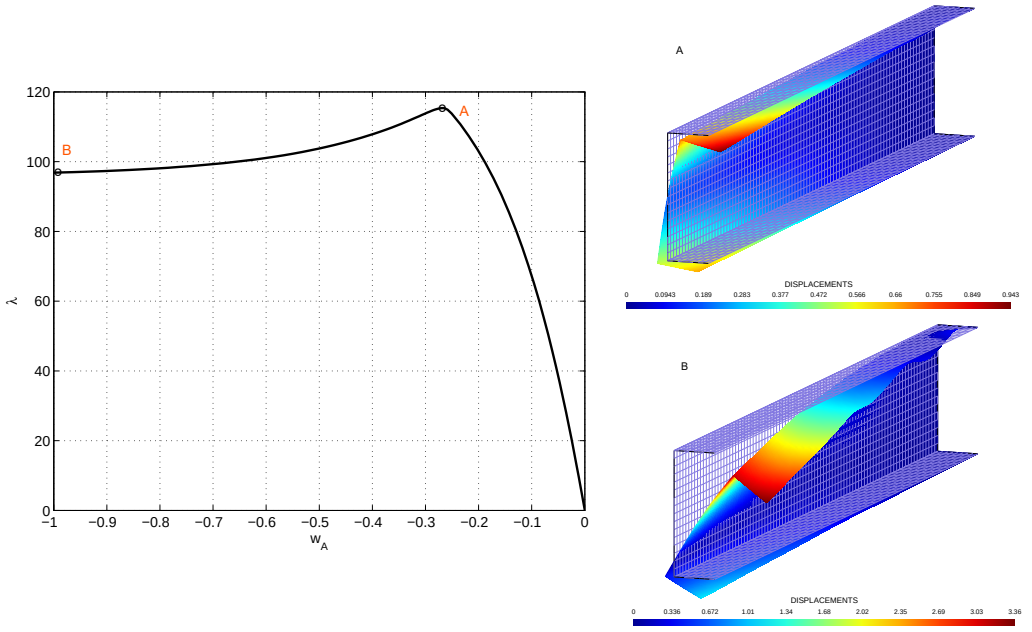

Figure 4.8: Cantilever beam: equilibrium path and deformed configuration at the last evaluated equilibrium point

	steps	iterations
Newton	82	301
MIP Newton	36	106
MIP M. Newton	55	175

Table 4.5: Thin-walled cantilever beam: total number of steps and iterations for the evaluation of the equilibrium path.

4.6 Summary

In geometrically nonlinear structural problems discretised via displacement-based finite elements, the standard Newton method easily diverges unless a small step size is used. Even if it converges, often a large number of iterations are required. A new strategy, called MIP Newton, is proposed to improve the robustness and the efficiency of the iterative method in step-by-step geometrically nonlinear analyses performed with displacement FE formulations. The approach proposed in this work is inspired by some previous studies regarding the advantages in the mixed (stress-displacement) formulation in geometrically nonlinear problems. In particular, in the first chapter it was shown how the convergence of the Newton method in displacement formulations is penalized by the constitutive constraint, i.e. at each iteration the method is forced to satisfy the constitutive law.

The main idea of the MIP strategy, proposed here, consists in the relaxation of the constitutive law at the level of each integration point. In this way, the stresses at the integration points become independent variables in the iterative process and, thus, they are directly extrapolated and corrected. The stresses are, then, no longer forced to satisfy the constitutive equations at each iteration, but the constitutive law is recovered exactly at convergence. The discrete approximation of the finite element remains, thus, exactly the same, but the performances of the MIP Newton are impressive. As shown in many numerical tests, it allows us to solve geometrically nonlinear problems with a very low number of steps and total iterations, in step-by-step analysis, with respect to the standard Newton method. The advantages in terms of computational time are clear, considering that the cost of a MIP iteration is the same as a standard one. Moreover, the MIP Newton can withstand very large step sizes (increments) without loss of convergence, which are impossible using the standard Newton. The iteration matrix evaluated with the MIP strategy is so "good" that the modified version of the method, which computes and decomposes the iteration matrix at the first estimate of each equilibrium point, can also be conveniently adopted.

The inclusion of the MIP Newton in existing finite element codes is simple and only requires the modification of a few implementation details in the standard method. The proposed iterative strategy is so robust, efficient and simple that, in geometrically nonlinear analysis, it seems worthy to replace the standard Newton method in any finite element code based on displacement formulations. Further details are reported in [70].

Future works will focus on the application of the MIP Newton in isogeometric analysis [9], where it is expected to have the same impact experienced in FE analysis. The proposal can be extended to other solution strategies such as the Koiter-Newton method [62, 8]. Efficient drape simulations are also expected.

Chapter 5

Mixed solid-shell concept within the novel Koiter-Newton approach

Abstract

The Koiter-Newton method had recently demonstrated a superior performance for nonlinear analyses of structures, compared to traditional path-following strategies. The method follows a predictor-corrector scheme to trace the entire equilibrium path. During a predictor step a reduced order model is constructed based on Koiter's asymptotic post-buckling theory which is followed by Newton iterations in the corrector phase to regain the equilibrium of forces. During a predictor step, the approach constructs a reduced order model based on Koiter's asymptotic post-buckling theory and combines its solution with a number of Newton iterations in a corrector phase to regain the equilibrium of forces. In this chapter, a robust mixed solid-shell implementation is presented to further enhance the efficiency of stability analyses in various aspects. It is shown that a Hellinger-Reissner variational formulation facilitates the reduced order model construction omitting an expensive evaluation of the inherent fourth order derivatives of the strain energy. Extremely large step sizes with a reasonable out-of-balance residual can be obtained with substantial impact on the total number of steps needed to trace the complete equilibrium path. More importantly, the numerical effort of the corrector phase involving Newton iterations of the full order model is drastically reduced to a few iterations per step thus revealing the true strength of the proposed formulation. Some problems from engineering are analysed and the results are compared to the conventional approach in order to highlight the gain in numerical efficiency for stability problems.

5.1 Introduction

Classical path-following strategies as used in the numerical analysis of buckling phenomena of thin-walled structures operate on a linearised form of the nonlinear governing equations of the deforming structure. A predictor step followed by an iterative corrector phase is commonly used to trace the entire load-displacement equilibrium path in a step-by-step manner [3]. The linearised equations allow for linear predictor steps only, tangential to the equilibrium path, which results in a substantial number of steps required to capture the full nonlinear structural response. Furthermore, the detection of bifurcations along the equilibrium path may easily fail using linear predictors unless a very small step size is adopted. Over the years, a number of asymptotic methods based on Koiter's post-buckling theory [7] have been developed to provide a failsafe analysis method at significantly reduced costs [38, 39, 41, 44, 68]. The Koiter method involves the construction of a reduced order model which is based on a second order asymptotic expansion using the path tangent and a few buckling modes. The method reduces the large number of equations needed to model accurately the elastic buckling behaviour of shells to a few nonlinear equations representing the modal amplitudes and the load factor of the deformed structure [59].

Recently, a novel Koiter-Newton approach has demonstrated successfully a reliable and accurate prediction of the buckling phenomena of thin-walled structures [8, 62]. The main idea of this approach is the use of Koiter's method as a non-linear predictor within the framework of a path-following strategy. The asymptotic characteristics of the proposed predictor step allows for significantly larger step sizes at reduced out-of-balance residual forces, the latter having a positive effect on the overall effort of the corrector phase. The method allows to trace the entire equilibrium path and to handle reliably snap-back and snap-through phenomena. In an extended version, the method provides a bifurcation indicator based on the constructed reduced order model which enables to trace the corresponding bifurcation branches. The method has proven to be a robust and computationally efficient solution approach though the corrector phase cannot fully profit from the reduced order model and requires a number of Newton iterations for each step, each iteration involving the solution of a linear system on the full model. In the past, it has been observed in several studies that mixed (stress and displacement) finite elements show superior properties compared to pure displacement-based elements in the context of a standard Newton approach for nonlinear analyses [10, 11]. In general, the mixed formulation allows for larger step sizes and requires less iterations to regain equilibrium. The first chapter observed the beneficial convergence properties of mixed model formulations in a general context. The study shows that the evolution of the iterative displacement process is forced to satisfy the constitutive equations in each iteration and this constraint leads to a drop of the convergence rate. In contrast, the stress components in the mixed model are introduced as independent variables which only

satisfy the discrete constitutive equations at convergence.

This chapter combines the superiority of mixed elements in terms of convergence properties with the efficiency of the reduced order principles of the Koiter-Newton approach. The direct prediction and correction of the stresses is exploited to minimize the number of Newton iterations in the corrector phase of each step. The Koiter predictor involves the construction of a *reduced order model* which requires derivatives of the strain energy up to the fourth order. Geometrically exact shell models [15] or co-rotational approaches [34, 47] are suited formulations to achieve structural model objectivity. Both strategies make use of finite rotations which make the evaluation of the strain energy and its derivatives highly complicated and expensive. In [62] simplified kinematics were proposed to streamline the construction of the reduced order model at the price of reducing its range of applicability.

The Koiter-Newton method is implemented for a nonlinear Cauchy continuum based on a Green-Lagrange strain measure and a solid-shell element interpolation. In this way, the construction of the reduced order model remains simple and favourable, maintaining a geometric exact strain measure. Furthermore, the adopted Hellinger-Reissner variational principle, in which the strain energy has only a third order polynomial dependence on the degrees of freedom leads to the zeroing all fourth order strain energy variations. Thus, the construction of the reduced order model is simpler and faster [59]. A mixed solid-shell element is introduced in the framework of the Koiter-Newton method and the algebraic quantities needed for the context of the reduced order modelling are derived. The proposed model is tested with a number of numerical tests, critically assessing its performance, its strengths and potential limitations. All numerical studies compare the proposed mixed model with the conventional displacement-based model, both showing a significant improvement compared with the classical path-following method.

The chapter is organized as follows: Section 2 briefly recalls the Koiter-Newton method and provides the governing equations for the construction of the reduced order model. In Section 3, the first, second and third algebraic quantities of the reduced model are derived for the mixed solid-shell element. Some numerical tests for verification and validation of the proposed and implemented model is presented in Section 4. Finally, the main findings are summarised.

5.2 Review of the Koiter–Newton approach

In the following, the principles and properties of the Koiter-Newton approach are briefly recalled. The method is capable to trace automatically the entire equilibrium path of a structure in a step by step manner. Each step involves the construction of a reduced order model at a known equilibrium state. The construction is based on Koiter's asymptotic theory on initial post-buckling stability

[7] and used as a predictor within a path-following analysis. In a corrector phase following each Koiter prediction, a Newton iteration is used to reduce the residual error to a pre-defined equilibrium level.

5.2.1 Construction of the reduced order model

The nonlinear behaviour of an elastic body is analysed, considering its state of equilibrium. Following a *Principle of Virtual Work*-formulation, the N governing nonlinear equations of the discretised structure result in a set of algebraic equations:

$$\mathbf{R}[\mathbf{u},\lambda] \;=\; \lambda\,\mathbf{f}^{ext} - \mathbf{f}^{int}[\mathbf{u}] \;=\; \mathbf{0} \tag{5.1}$$

where $\mathbf{R}$ is the residual force vector, $\mathbf{f}^{ext}$ represents the external load vector and λ is the load factor. The internal elastic forces $\mathbf{f}^{int}$ are dependent on the vector of primal unknowns $\mathbf{u}$:

$$\mathbf{f}^{int} \;=\; \frac{\partial U[\mathbf{u}]}{\partial \mathbf{u}} \tag{5.2}$$

where $U[\mathbf{u}]$ is the strain energy of the structure.

In the Koiter-Newton approach, a reduced order model is established to approximate the equilibrium equations in the neighbourhood of a known equilibrium state $[\mathbf{u}_0,\lambda_0]$ which is referred to in the following as *nominal configuration*. Furthermore, an unknown configuration near the nominal configuration is denoted with $[\mathbf{u},\lambda]$ where:

$$\mathbf{u} \;=\; \mathbf{u}_0 + \Delta\mathbf{u}\,. \tag{5.3}$$

Here, the concatenation of unknowns $\mathbf{u}_0$ and $\Delta\mathbf{u}$, Eq.(5.3), is assumed to be an addition. Considering beams and shells which take into account finite rotations, the concatenation will depend on the parametrization of the rotations.

The nonlinear equilibrium (5.1) is approximated with a truncated Taylor series expansion up to the third order with respect to $\mathbf{u}$ of the nominal configuration. The expansion terms follow from differentiation of the strain energy U up to the fourth order with respect to the unknown primal vector $\mathbf{u}$ according to (5.1) and (5.2). The equilibrium modifies to:

$$\mathcal{L}[\Delta\mathbf{u}] + \mathcal{Q}[\Delta\mathbf{u},\Delta\mathbf{u}] + \mathcal{C}[\Delta\mathbf{u},\Delta\mathbf{u},\Delta\mathbf{u}] + O[\|\Delta\mathbf{u}\|^4] \;=\; \Delta\lambda\mathbf{f}_{ex} \tag{5.4}$$

where $\mathcal{L}$ is a linear form, $\mathcal{Q}$ is quadratic form and $\mathcal{C}$ is cubic. Regarding a conservative system, there exists a direct correspondence between the forms of order p in Eq.(5.4) and a symmetric p-dimensional tensor, applicable to every component of the vector equation. Correspondingly, the linear, quadratic and cubic form of (5.4) can be expressed in terms of a two-dimensional, three-dimensional and four-dimensional tensor, respectively. Furthermore, the relations $\Delta\lambda = \lambda - \lambda_0$

and $\mathbf{f}[\mathbf{u}_0] = \lambda_0 \mathbf{f}_{ext}$ holds.

The Koiter-Newton method is used in the context of elastic shell buckling analyses considering structures with branching equilibrium paths and turning points. It is convenient to consider perturbation loads which excite neighbouring states of equilibrium to allow the system to change from the primary to a secondary equilibrium path. An appropriate selection of perturbation loads is discussed in detail in [8]. Taking into account these loads, the third order form of the equilibrium equations (5.4) may be extended to consider multiple loading of the form:

$$\mathcal{L}[\Delta\mathbf{u}] + \mathcal{Q}[\Delta\mathbf{u}, \Delta\mathbf{u}] + \mathcal{C}[\Delta\mathbf{u}, \Delta\mathbf{u}, \Delta\mathbf{u}] + O[\|\Delta\mathbf{u}\|^4] \quad = \quad \mathbf{F}\boldsymbol{\phi} \tag{5.5}$$

where the α-th column of $\mathbf{F}$ is formed by the a perturbation load vector $\mathbf{f}_\alpha$ and where the vector $\boldsymbol{\phi}$ represents the load amplitudes. The first column of $\mathbf{F}$ is chosen to be the external load vector $\mathbf{f}_{ext}$ with a corresponding first amplitude entry $\boldsymbol{\phi}_1 = \Delta\lambda$. Further columns of $\mathbf{F}$ are formed by sub-loads:

$$\mathbf{f}_\alpha \quad = \quad \mathbf{K}_\sigma \mathbf{v}_\alpha \qquad \alpha = 2, \ldots, m+1 \tag{5.6}$$

where m is a number of closely spaced buckling modes $\mathbf{v}_\alpha$ and $\mathbf{K}_\sigma$ is the geometric stiffness matrix of a linearised buckling problem [8].

The equilibrium (5.5) forms a $m+1$ dimensional hyper-surface for which the solution $\mathbf{u}$ is approximated by a series expansion. To this end, the equilibrium surface is parametrised in terms of generalised displacements $\boldsymbol{\xi} = \{\xi_1, \cdots, \xi_{m+1}\}$, and the displacement $\mathbf{u}$ is expanded to the third order with respect to ξ_i:

$$\Delta\mathbf{u} \quad = \quad \mathbf{u}_\alpha\, \xi_\alpha + \mathbf{u}_{\alpha\beta}\, \xi_\alpha\xi_\beta + \mathbf{u}_{\alpha\beta\gamma}\, \xi_\alpha\xi_\beta\xi_\gamma + O[\|\boldsymbol{\xi}\|^4] \tag{5.7}$$

where $\{\alpha, \beta, \gamma\} = 1, 2, \ldots, 1+m$, and the *Einstein* summation convention is applied. The first order displacements $\mathbf{u}_\alpha$ define the tangent plane to the equilibrium surface at the approximation point. Additional first order displacements are generated by considering the additional imperfection loads of Eq.(5.6). The second order displacements $\mathbf{u}_{\alpha\beta}$ and third order displacements $\mathbf{u}_{\alpha\beta\gamma}$ describe the interactions among first and second order displacement fields, respectively.

The equilibrium surface may be parametrised with an infinite number of choices for $\boldsymbol{\xi}$. Here, the parametrisation is chosen work-conjugate to the load amplitudes which results in the following orthogonality constraints:

$$\mathbf{f}_\alpha^T \mathbf{u}_\beta \quad = \quad \delta_{\alpha\beta} \tag{5.8}$$

$$\mathbf{f}_\alpha^T \mathbf{u}_{\beta\gamma} \quad = \quad 0 \tag{5.9}$$

$$\mathbf{f}_\alpha^T \mathbf{u}_{\beta\gamma\delta} \quad = \quad 0 \tag{5.10}$$

where $\delta_{\alpha\beta}$ is the Kronecker delta. Similarly, the load amplitudes $\boldsymbol{\phi}$ are approximated by a series expansion to ensure consistency in the governing equations:

$$\boldsymbol{\phi} \quad = \quad \overline{\mathcal{L}}[\boldsymbol{\xi}] + \overline{\mathcal{Q}}[\boldsymbol{\xi}, \boldsymbol{\xi}] + \overline{\mathcal{C}}[\boldsymbol{\xi}, \boldsymbol{\xi}, \boldsymbol{\xi}] + O[\|\boldsymbol{\xi}\|^4] \tag{5.11}$$

with $\overline{\mathcal{L}}$, $\overline{\mathcal{Q}}$ and $\overline{\mathcal{C}}$ being still to be determined, linear, quadratic and cubic forms. Using (5.7) and (5.11) in the equilibrium (5.5) and equating the coefficients of the various powers of $\boldsymbol{\xi}$ to zero results in the following three linear relations:

$$\begin{aligned} \overline{\mathcal{L}}[\mathbf{u}_\alpha] &= \mathbf{F}\,\bar{\mathbf{l}}_\alpha && (5.12)\\ \overline{\mathcal{L}}[\mathbf{u}_{\alpha\beta}] + \overline{\mathcal{Q}}[\mathbf{u}_\alpha, \mathbf{u}_\beta] &= \mathbf{F}\,\bar{\mathbf{u}}_{\alpha\beta} && (5.13)\\ \overline{\mathcal{L}}[\mathbf{u}_{\alpha\beta\gamma}] + \tfrac{2}{3}\left[\overline{\mathcal{Q}}[\mathbf{u}_{\alpha\beta}, \mathbf{u}_\gamma] + \overline{\mathcal{Q}}[\mathbf{u}_{\beta\gamma}, \mathbf{u}_\alpha] + \overline{\mathcal{Q}}[\mathbf{u}_{\gamma\alpha}, \mathbf{u}_\beta]\right] &+ \\ +\overline{\mathcal{C}}[\mathbf{u}_\alpha, \mathbf{u}_\beta, \mathbf{u}_\gamma] &= \mathbf{F}\,\bar{\mathbf{c}}_{\alpha\beta\gamma} && (5.14) \end{aligned}$$

where $\bar{\mathbf{l}}_\alpha$, $\bar{\mathbf{u}}_{\alpha\beta}$ and $\bar{\mathbf{c}}_{\alpha\beta\gamma}$ represent each column vectors of the multi-dimensional tensors according to the linear, quadratic and cubic forms $\overline{\mathcal{L}}$, $\overline{\mathcal{Q}}$ and $\overline{\mathcal{C}}$, respectively. Consideration of the orthogonality constraints (5.8)-(5.10) allows to express equations (5.12)-(5.14) in terms of two augmented systems of linear equations:

$$\begin{bmatrix} \mathbf{K} & -\mathbf{F} \\ -\mathbf{F}^T & \mathbf{0} \end{bmatrix} \begin{bmatrix} \mathbf{u}_\alpha \\ \bar{\mathbf{l}}_\alpha \end{bmatrix} = \begin{bmatrix} \mathbf{0} \\ -\mathbf{e}_\alpha \end{bmatrix} \qquad (5.15)$$

$$\begin{bmatrix} \mathbf{K} & -\mathbf{F} \\ -\mathbf{F}^T & \mathbf{0} \end{bmatrix} \begin{bmatrix} \mathbf{u}_{\alpha\beta} \\ \bar{\mathbf{u}}_{\alpha\beta} \end{bmatrix} = \begin{bmatrix} -\mathcal{Q}[\mathbf{u}_\alpha, \mathbf{u}_\beta] \\ \mathbf{0} \end{bmatrix} \qquad (5.16)$$

and the relation:

$$\bar{c}_{\alpha\beta\gamma\delta} = \mathcal{C}[\mathbf{u}_\alpha, \mathbf{u}_\beta, \mathbf{u}_\gamma, \mathbf{u}_\delta] - \tfrac{2}{3}[\mathbf{u}_{\alpha\beta}^T \mathcal{L}[\mathbf{u}_{\delta\gamma}] + \mathbf{u}_{\beta\gamma}^T \mathcal{L}[\mathbf{u}_{\delta\alpha}] + \mathbf{u}_{\gamma\alpha}^T \mathcal{L}[\mathbf{u}_{\delta\beta}]] \quad (5.17)$$

in which $\mathbf{K}$ is the $[N \times N]$-dimensional tangent stiffness matrix at the nominal configuration, i.e. the tensor representation of the linear form $\mathcal{L}$, where the $[N \times [m+1]]$-dimensional matrix $\mathbf{F}$ follows from the perturbation loads, Eq.(5.5), and $\mathbf{e}_\alpha$ denotes the the α-th unit vector with coefficient $e_\alpha = 1$. The load vector $\mathcal{Q}[\mathbf{u}_\alpha, \mathbf{u}_\beta]$ is assembled from the solution of (5.15) with coefficients $[Q_{i\alpha\beta}\, u_\alpha\, u_\beta]$.

The solution of the augmented systems of equations for $m+1$ load vectors provides the first and second order solutions needed to construct the reduced order model. In the following, a concise summary of the construction of the reduced order model and the global equilibrium solution is given. A detailed summary revealing the relations between the higher order forms of (5.5) and (5.11) and the derived systems of equations can be found in [8]:

- the tensor coefficients of the linear form $\overline{\mathcal{L}}$ are obtained from pre-multiplication of (5.12) with the first order solution $\mathbf{u}_\beta$ and using the orthogonality condition (5.8):

$$\bar{l}_{\alpha\beta} = \mathbf{e}_\beta^T \mathbf{l}_\alpha = \mathbf{u}_\beta^T\, \mathcal{L}[\mathbf{u}_\alpha] \qquad (5.18)$$

- the tensor coefficients of the quadratic form $\overline{\mathcal{Q}}$ are obtained from pre-multiplication of (5.13) with the first order solution $\mathbf{u}_\gamma$ and using the orthogonality condition (5.9):

$$\bar{q}_{\gamma\alpha\beta} = \mathbf{e}_\gamma^T \mathbf{u}_{\alpha\beta} = \mathbf{u}_\gamma^T\, \mathcal{Q}[\mathbf{u}_\alpha, \mathbf{u}_\beta] \qquad (5.19)$$

- the tensor coefficients of the cubic form $\overline{\mathcal{C}}$ are obtained from pre-multiplication of (5.14) with the first order solution $\mathbf{u}_\delta$ and using the orthogonality condition (5.10). Assuming a conservative system, the tensor of the corresponding cubic form is symmetric with coefficients:

$$\begin{aligned} \overline{c}_{\alpha\beta\gamma\delta} &= \mathcal{C}[\mathbf{u}_\alpha, \mathbf{u}_\beta, \mathbf{u}_\gamma, \mathbf{u}_\delta] + \\ &- \tfrac{2}{3}[\mathbf{u}_{\alpha\beta}^T \mathcal{L}[\mathbf{u}_{\delta\gamma}] + \mathbf{u}_{\beta\gamma}^T \mathcal{L}[\mathbf{u}_{\delta\alpha}] + \mathbf{u}_{\gamma\alpha}^T \mathcal{L}[\mathbf{u}_{\delta\beta}]]. \end{aligned} \tag{5.20}$$

  where $\mathcal{C}[\mathbf{u}_\alpha, \mathbf{u}_\beta, \mathbf{u}_\gamma, \mathbf{u}_\delta] = \mathbf{u}_\delta^T \mathcal{C}[\mathbf{u}_\alpha, \mathbf{u}_\beta, \mathbf{u}_\gamma]$ depends on the first order displacement solution only.

- with the equations (5.18)-(5.20), the following reduced order model of dimension $[m+1]$ can be established for the solution of the unknown generalized displacements $\boldsymbol{\xi}$:

$$\overline{\mathcal{L}}[\boldsymbol{\xi}] + \overline{\mathcal{Q}}[\boldsymbol{\xi}, \boldsymbol{\xi}] + \overline{\mathcal{C}}[\boldsymbol{\xi}, \boldsymbol{\xi}, \boldsymbol{\xi}] = \boldsymbol{\phi} = \Delta\lambda\, \mathbf{e}_1 \tag{5.21}$$

  where $\Delta\lambda$ is chosen to be the load parameter of the external load $\mathbf{f}_{ext}$ to determine the response to the actual loading and $\mathbf{e}_1$ is the first unit vector. Equation (5.21) is conveniently solved using an arc-length method [3] and its solution sets the generalized displacements $\boldsymbol{\xi}$ into a nonlinear relation to the actual load increment $\Delta\lambda$, which is mapped to the solution space of the total problem invoking the displacement expansion:

$$\mathbf{u} = \mathbf{u}_0 + \mathbf{u}_\alpha\, \xi_\alpha + \mathbf{u}_{\alpha\beta}\, \xi_\alpha \xi_\beta \tag{5.22}$$

  and the actual load factor $\lambda = \lambda_0 + \Delta\lambda$.

5.2.2 Koiter-Newton path-following analysis

The reduced order model of the previous sub-section is based on Koiter's asymptotic expansion theory and constructed at a known configuration along the nonlinear equilibrium path. The model solution, Eq.(5.22), is used as a computationally efficient predictor in a step-by-step path-tracing analysis. Compared to a linearised predictor scheme based on a Newton-type method the pre-eminence of the Koiter predictor becomes evident due to its asymptotic solution properties towards the equilibrium path which allows for significantly larger step sizes at reduced out-of-balance forces. The latter is driven to zero using a few Newton correction steps of the full system. The step size of the reduced order model is controlled by the following criteria:

$$\frac{\|\mathbf{R}\|}{\lambda \|\mathbf{f}_{ex}\|} \geq \epsilon \tag{5.23}$$

where the value of ϵ is a user defined measure for an appropriate step size. The applied convergence criterion for the Newton correction in this work was chosen

to be:

$$\frac{\|\mathbf{R}\|}{\lambda\|\mathbf{f}_{ex}\|} \leq 10^{-4}. \tag{5.24}$$

Following the work of *Riks* [3], a constraint hyperplane is adopted in order to avoid a possible loss of convergence near limit loads. Details of the Newton iteration with the Riks constraint can be found in [70].

The construction of the reduced order model is dominated by the factorization of the governing system of equations of the augmented problem (5.15) and (5.16), respectively. It is important to note that both systems of equations of dimension $[N + m + 1]$ have an identical system matrix, hence factorization is needed only once. The number m of perturbation loads is typically small $[< 10]$ since only modes which are closely spaced to the nominal configuration are considered. If buckling is fully absent only the external load vector becomes significant and the reduced order model degenerates to a model size of *one*. The computational effort of the correction phase requires p Newton iterations at each step using the full order model of equations to ensure sufficient stability of the scheme. The Koiter-Newton method, a part from the greater computational efficiency, compared to traditional path-following analyses allows, in case of multiple paths, to easily consider branch switching techniques. For example, as shown in [97], the method can be equipped with a bifurcation indicator based on the constructed reduced order model which enables to trace the corresponding bifurcation branches.

5.3 Solid-shell concept and mixed formulation

In the following, the contributions of a solid-shell element formulation to the global quantities of the algorithm are derived. The element type is an eight-node hybrid stress element proposed by *Sze* [10] and presented here using a Green-Lagrange strain measure. The main equation are reported in the second chapter. A pure displacement-based formulation and a mixed formulation are considered.

5.3.1 Displacement-based solid-shell element

Displacement-element contributions to the third order form governing equations

The third order form equilibrium of the Koiter-Newton method as previously presented is expressed in terms of a linear, quadratic and cubic form which are obtained in the following by differentiating the strain energy with respect to the global degrees of freedom, cf Eq.(5.2).

Notation: The quantities derived in the following refer to an element formulation if not stated differently. A corresponding element indicating index notation is

skipped for the sake of a better readability.

The strain energy contribution of the shell element and corresponding derivatives are:

$$U = \int_{\Omega^0} \frac{1}{2}\,\boldsymbol{\varepsilon}^T \mathbf{C}\,\boldsymbol{\varepsilon} \tag{5.25}$$

$$\frac{\partial U}{\partial \mathbf{q}} = \int_{\Omega^0} \tilde{\mathbf{B}}[\mathbf{q}]^T \boldsymbol{\sigma}[\mathbf{q}] \;=\; \mathbf{f}^{int}[\mathbf{q}] \tag{5.26}$$

$$\frac{\partial^2 U}{\partial \mathbf{q}^2} = \int_{\Omega^0} \tilde{\mathbf{B}}[\mathbf{q}]^T \mathbf{C}\;\tilde{\mathbf{B}}[\mathbf{q}] + \int_{\Omega^0} \sum_i \sigma_i[\mathbf{q}]\,\boldsymbol{\Gamma}_i \;=\; \mathbf{K}[\mathbf{q}] \tag{5.27}$$

where $\tilde{\mathbf{B}}[\mathbf{q}] = \mathbf{B}_L + \mathbf{B}_Q[\mathbf{q}]$, $\mathbf{K}$ is the element tangent stiffness matrix, cf Eq.(5.15), $\mathbf{f}^{int}$ represent the internal elastic element forces and

$$\boldsymbol{\sigma}[\mathbf{q}] = \quad \mathbf{C}\,\mathbf{B}[\mathbf{q}]\;\mathbf{q} \tag{5.28}$$

are the generalized second Piola-Kirchhoff stresses. The matrices $\boldsymbol{\Gamma}_i$ account for the geometric element stiffness and are defined as:

$$\boldsymbol{\Gamma}_i = \frac{\partial^2 \varepsilon_i}{\partial \mathbf{q}^2}\,. \tag{5.29}$$

Furthermore, the following discrete operators are introduced to express the quadratic and cubic form of the equilibrium in a compact notation:

$$\boldsymbol{\sigma}[\mathbf{q}_\alpha, \mathbf{q}_\beta] = \mathbf{C}\,\tilde{\mathbf{B}}[\mathbf{q}_\alpha]\,\mathbf{q}_\beta \tag{5.30}$$

$$\boldsymbol{\sigma}_L[\mathbf{q}] = \mathbf{C}\,\mathbf{B}_L\mathbf{q} \tag{5.31}$$

$$\boldsymbol{\varepsilon}_Q[\mathbf{q}_\alpha, \mathbf{q}_\beta] = \mathbf{B}_Q[\mathbf{q}_\alpha]\,\mathbf{q}_\beta \tag{5.32}$$

$$\boldsymbol{\sigma}_Q[\mathbf{q}_\alpha, \mathbf{q}_\beta] = \mathbf{C}\,\boldsymbol{\varepsilon}_Q[\mathbf{q}_\alpha, \mathbf{q}_\beta]. \tag{5.33}$$

Using (5.28)-(5.33), the following forms are derived:

Linear form The linear form is expressed in terms of the tangent properties at the known reference point with displacements $\mathbf{q}_0$:

$$\mathcal{L}[\mathbf{q}_\alpha] = \mathbf{K}[\mathbf{q}_0]\,\mathbf{q}_\alpha\,. \tag{5.34}$$

Quadratic form The quadratic form depends linearly on the known displacement state of the reference point and mixed quadratically on the first order displacements $\mathbf{q}_\alpha$ and $\mathbf{q}_\beta$, respectively,

$$\begin{aligned}\mathcal{Q}[\mathbf{q}_\alpha, \mathbf{q}_\beta] &= \int_{\Omega^0} \mathbf{B}_Q[\mathbf{q}_\alpha]^T \boldsymbol{\sigma}[\mathbf{q}_0, \mathbf{q}_\beta] + \mathbf{B}_Q[\mathbf{q}_\beta]^T \boldsymbol{\sigma}[\mathbf{q}_0, \mathbf{q}_\alpha] \\ &\qquad + \tilde{\mathbf{B}}[\mathbf{q}_0]^T \boldsymbol{\sigma}_Q[\mathbf{q}_\alpha, \mathbf{q}_\beta] \\ &= \mathbf{Q}[\mathbf{q}_\alpha]\mathbf{q}_\beta\end{aligned} \tag{5.35}$$

with

$$\mathbf{Q}[\mathbf{q}_\alpha] = \int_{\Omega^0} \mathbf{B}_Q[\mathbf{q}_\alpha]^T \mathbf{C}\, \tilde{\mathbf{B}}[\mathbf{q}_0] + \tilde{\mathbf{B}}[\mathbf{q}_0]^T \mathbf{C}\, \mathbf{B}_Q[\mathbf{q}_\alpha] + \sum_i \sigma_i[\mathbf{q}_0, \mathbf{q}_\alpha]\boldsymbol{\Gamma}_i \quad (5.36)$$

Cubic form Finally, the cubic form follows as:

$$\mathcal{C}[\mathbf{q}_\alpha, \mathbf{q}_\beta, \mathbf{q}_\gamma, \mathbf{q}_\delta] = \int_{\Omega^0} \{\boldsymbol{\sigma}_Q[\mathbf{q}_\alpha, \mathbf{q}_\beta]^T \boldsymbol{\varepsilon}_Q[\mathbf{q}_\gamma, \mathbf{q}_\delta] + \boldsymbol{\sigma}_Q[\mathbf{q}_\alpha, \mathbf{q}_\gamma]^T \boldsymbol{\varepsilon}_Q[\mathbf{q}_\beta, \mathbf{q}_\delta] + \boldsymbol{\sigma}_Q[\mathbf{q}_\alpha, \mathbf{q}_\delta]^T \boldsymbol{\varepsilon}_Q[\mathbf{q}_\gamma, \mathbf{q}_\beta]\} \quad (5.37)$$

Denoting the path tangent in $[\lambda_0, \mathbf{q}_0]$ with $\mathbf{q}_\lambda$, the geometrical stiffness matrix of the element is:

$$\mathbf{K}_\sigma = \int_\Omega \sum_i \sigma_{Li}[\mathbf{q}_\lambda]\boldsymbol{\Gamma}_i \quad (5.38)$$

where terms related to $\mathbf{B}_Q[\mathbf{q}_\lambda]$ in $\mathbf{Q}[\mathbf{q}_\lambda]$ are neglected as usual in displacement-based linearised buckling analysis, so obtaining a robust eigenvalue analysis as discussed in [33].

It is worth to note the following unique features of the derived model with impact to the solution properties:

- the model is purely displacement-based using displacement degrees of freedom only
- the strain energy has a 4^{th} order dependence on the displacement degrees of freedom and its derivatives are very simple because of the absence of finite rotations
- the Green-Lagrange strain measure is geometrically exact for a solid model
- the expanded nonlinear equilibrium, Eq.(5.4), is exact with any truncation error .

5.3.2 Mixed solid-shell element

Following the principle of *Hellinger-Reissner* [2] the strain energy expression can be rewritten in mixed form as:

$$U_M[\mathbf{u}] = \int_{\Omega^0} \boldsymbol{\sigma}^T \boldsymbol{\varepsilon} - \frac{1}{2}\boldsymbol{\sigma}^T \mathbf{C}^{-1} \boldsymbol{\sigma} \quad (5.39)$$

where the subscript M indicates the mixed formulation.

Here, it is important to note that the independent interpolation of the stresses allows to reduce the order of the polynomial dependence of the strain energy on the discrete degrees of freedom, resulting in $\boldsymbol{\sigma}$ being linear in $\boldsymbol{\beta}$ and $\boldsymbol{\varepsilon}$ being quadratic in $\mathbf{q}$.

Mixed element contributions to the third order form governing equations

The mixed internal force vector of the element is

$$\mathbf{s}_M[\mathbf{u}] = \begin{bmatrix} \mathbf{s}_\beta \\ \mathbf{s}_q \end{bmatrix} \tag{5.40}$$

with

$$\mathbf{s}_\beta = \int_{\Omega^0} \mathbf{N}_\sigma^T \left[\boldsymbol{\varepsilon}[\mathbf{q}] - \mathbf{C}^{-1} \boldsymbol{\sigma}[\boldsymbol{\beta}] \right] \tag{5.41}$$

$$\mathbf{s}_q = \int_{\Omega^0} \tilde{\mathbf{B}}[\mathbf{q}]^T \boldsymbol{\sigma}[\boldsymbol{\beta}] \tag{5.42}$$

and the mixed element stiffness matrix is:

$$\mathbf{K}_M[\mathbf{u}] = \begin{bmatrix} \mathbf{K}_{\beta\beta} & \mathbf{K}_{\beta q}[\mathbf{q}] \\ \mathbf{K}_{\beta d}[\mathbf{q}]^T & \mathbf{K}_{qq}[\boldsymbol{\beta}] \end{bmatrix} \tag{5.43}$$

with

$$\mathbf{K}_{\beta\beta} = -\int_{\Omega^0} \mathbf{N}_\sigma^T \, \mathbf{C}^{-1} \, \mathbf{N}_\sigma \tag{5.44}$$

$$\mathbf{K}_{\beta q}[\mathbf{q}] = \int_{\Omega^0} \mathbf{N}_\sigma^T \, \tilde{\mathbf{B}}[\mathbf{q}] \tag{5.45}$$

$$\mathbf{K}_{qq}[\boldsymbol{\beta}] = \int_{\Omega^0} \sum_i \sigma_i[\boldsymbol{\beta}] \, \boldsymbol{\Gamma}_i \tag{5.46}$$

which are evaluated as the gradient and the Hessian of the strain energy, respectively.

The linear, quadratic and cubic form of the Koiter-Newton equilibrium equations follow in analogy to the displacement formulation of 5.3.1:

$$\mathcal{L}_M[\mathbf{u}_\alpha] = \mathbf{K}_M[\mathbf{u}_0] \, \mathbf{u}_\alpha \tag{5.47}$$

$$\mathcal{Q}_M[\mathbf{u}_\alpha, \mathbf{u}_\beta] = \begin{bmatrix} \mathcal{Q}_\beta[\mathbf{q}_\alpha, \mathbf{q}_\beta] \\ \mathcal{Q}_q[\mathbf{u}_\alpha, \mathbf{u}_\beta] \end{bmatrix} \tag{5.48}$$

with

$$\mathcal{Q}_\beta[\mathbf{u}_\alpha, \mathbf{u}_\beta] = \int_{\Omega^0} \mathbf{N}_\sigma^T \, \boldsymbol{\varepsilon}_Q[\mathbf{q}_\alpha \, \mathbf{q}_\beta] \tag{5.49}$$

$$\mathcal{Q}_q[\mathbf{u}_\alpha, \mathbf{u}_\beta] = \int_{\Omega^0} \mathbf{B}_Q[\mathbf{q}_\alpha]^T \, \boldsymbol{\sigma}[\boldsymbol{\beta}_\beta] + \mathbf{B}_Q[\mathbf{q}_\beta]^T \boldsymbol{\sigma}[\boldsymbol{\beta}_\alpha] \tag{5.50}$$

The geometric stiffness matrix of the element is evaluated as

$$\mathbf{K}_\sigma[\boldsymbol{\beta}_\lambda] = \begin{bmatrix} \mathbf{0} & \mathbf{0} \\ \mathbf{0} & \mathbf{K}_{\sigma qq}[\boldsymbol{\beta}_\lambda] \end{bmatrix} \tag{5.51}$$

with

$$\mathbf{K}_{\sigma qq}[\boldsymbol{\beta}_\lambda] \;=\; \int_{\Omega^0} \sum_i \sigma_i[\boldsymbol{\beta}_\lambda]\boldsymbol{\Gamma}_i \,. \tag{5.52}$$

Finally, we note that the cubic form simplifies with:

$$\mathcal{C}_M[\mathbf{u}_\alpha, \mathbf{u}_\beta, \mathbf{u}_\gamma, \mathbf{u}_\delta] \;=\; 0 \tag{5.53}$$

which is a consequence of the introduced stress variables. The vanishing of the cubic form has a great impact on computational efficiency especially when the dimension of the reduced order model increases. This is a unique feature of the mixed solid-shell model combined with the Green- Lagrange strain measure. The variables are independent and condensed out on element level before assembly.

5.4 Numerical tests

In this section, various numerical tests with regard to buckling of thin-walled structures are considered to study the performances of the mixed solid-shell element within the framework of the Koiter-Newton method. In particular, the numerical performances in terms of convergence measures compared to the pure displacement-based formulation as introduced in [8] are assessed. The focus of these tests is primarily on the reduction of the number of Newton iterations at each step in comparison to the original approach, which require the consideration of the full order model thus dominating the numerical complexity of the analysis. A comparison of the Koiter-Newton method with traditional path-following methods revealing the method's ability to carry out a full nonlinear analysis with considerably fewer load steps has been carefully documented in [62, 97] and therefore is not considered here though this strength of the method is also an immanent property of the modified version proposed in this contribution.

The chosen examples include a benchmark test of a U-shape thin-walled beam under compression to verify the overall concept and a modified thin-walled beam structure from engineering. The equilibrium paths of both structures show a distinct nonlinear behaviour but a minor affinity to global buckling. With a thin cylinder structure we demonstrate the method's ability to trace reliably snap-back behaviour. Finally, we have selected a thin-walled frame structure to reveal the reliability of the method in presence of bifurcation after a strong nonlinear pre-critical behaviour.

In the Koiter-Newton method the equilibrium path is reconstructed evaluating just a few true equilibrium points. The solution between two consecutive points can be recovered exploiting the asymptotic reduced-order model predictor. Weak discontinuities in path in terms of kinks or a sudden change of the path tangent are identified as bifurcation points and reported accordingly.

5.4.1 U-shape cantilever beam

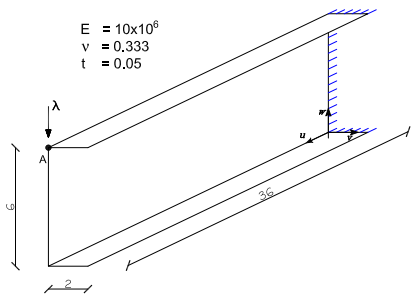

Figure 5.1: U-shape cantilever beam: model properties.

The U-shaped cantilever beam considered here is a standard benchmark problem to verify the nonlinear properties of the method, including local buckling phenomena [70]. Nevertheless, the problem is a severe test case for the Koiter-Newton approach due to a distinct nonlinear pre-critical behaviour which must be represented in the reduced order model by the degree of freedom associated with the external load. The geometry, the material properties and boundary conditions are depicted in Fig.5.1. The cantilever beam is subjected to an end shear force.

The analysis result in terms of solution steps along the equilibrium path is shown in Fig.5.2. The path was fully traced within 5 Koiter-Newton steps. The first 4 buckling modes, together with the external load, ended in a reduced order model of dimension 5. Both, the mixed and the displacement-based version show virtually identical results. In addition to the result of the non-linear analysis, we report in the figures depicting the load-displacement equilibrium path the buckling load of the linearised problem which is used to construct the first reduced order model at the reference configuration.

The asymptotic character of the Koiter-Newton predictor followed closely the nonlinear equilibrium path. Still, an average number of 5 Newton iterations in the corrector phase of each step were necessary for the displacement-based solution to recover equilibrium at a sufficient accuracy level. In Tab.5.1 we can compare the corrector effort of the two approaches, the solution-based and the mixed model. The results clearly reveal a superiority of mixed model which needed on average less than 3 Newton iterations in the corrector phase of each step to provide equilibrium of equivalent accuracy. Recalling the dominance of the corrector phase in the complexity analysis of the Koiter-Newton method and keeping in mind that the construction of the reduced order model is computationally cheaper for the mixed model avoiding the evaluation of the third order form, this improvement is quite encouraging with regard to larger problems.

In Fig.5.3 and Fig.5.4, the first and the second mode used to construct the reduced order model at the reference configuration and at the equilibrium point 3, respectively, are depicted. The distinct non-linear pre-critical path entails

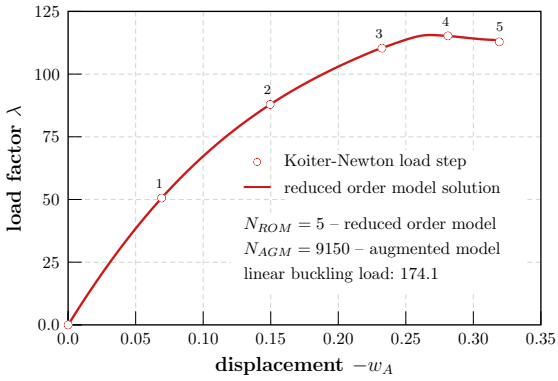

Figure 5.2: U-shape cantilever beam: equilibrium path with Koiter-Newton steps.

	displacement	mixed
step 1	3	2
step 2	5	3
step 3	4	3
step 4	5	2
step 5	8	4
total	25	14

Table 5.1: U-shape beam: number of Newton iterations in the corrector phase of each step.

essential changes of the relevant modes along the equilibrium path which requires a repeated construction of the reduced order model to capture reliably the limit point and any post-critial behaviour. This is confirmed, regarding the deformed configuration at the equilibrium point 4, which is well represented by the modes of the reduced order model, evaluated at 3.

5.4.2 Lipped channel column

Next, we consider a lipped channel column modelled as thin-walled structure under pressure load. The geometry, material properties and loads are shown in Fig.5.6. The cross-sectional in-plane displacements were constrained at both ends. The model is a perfect representative of structures with global-local buckling interaction leading to a high imperfection sensitivity.

The structure was analysed with 4 different amplitudes of the imperfection load

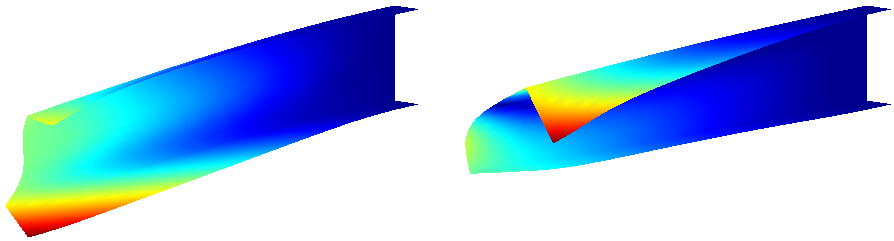

Figure 5.3: U-shape cantilever beam: first mode (left) and second mode (right) of the *reduced order model* constructed at the reference configuration.

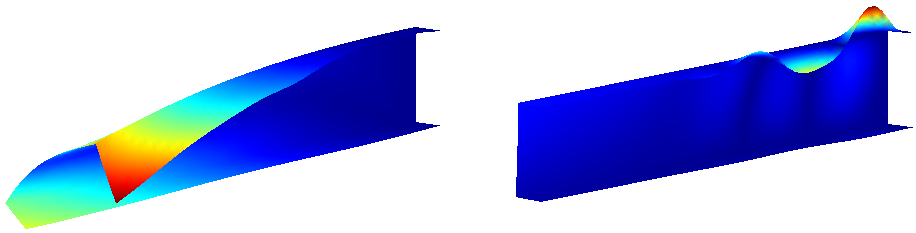

Figure 5.4: U-shape cantilever beam: first mode (left) and second mode (right) of the *reduced order model* constructed at 3.

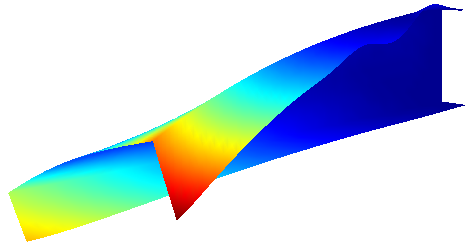

Figure 5.5: U-shape cantilever beam: deformed configuration (scale factor 10) at 4.

to study the column's sensitivity properties. The analysis results for the different imperfection loads are depicted in Fig.5.7 in which P denotes the cross-section perimeter, showing highly varying limit loads. The corresponding reduced order model of each analysis was constructed from 4 buckling modes adopting 3 Koiter-Newton steps to trace the complete equilibrium path. In Tab.5.2, the number of Newton iterations in the corrector phase of each step for the mixed and the displacement-based approach is reported. Again a reduction of the computational effort of more than 30% was observed. Compared to the results of 5.4.1 the gain in computational efficiency using the mixed model has slightly dropped but still

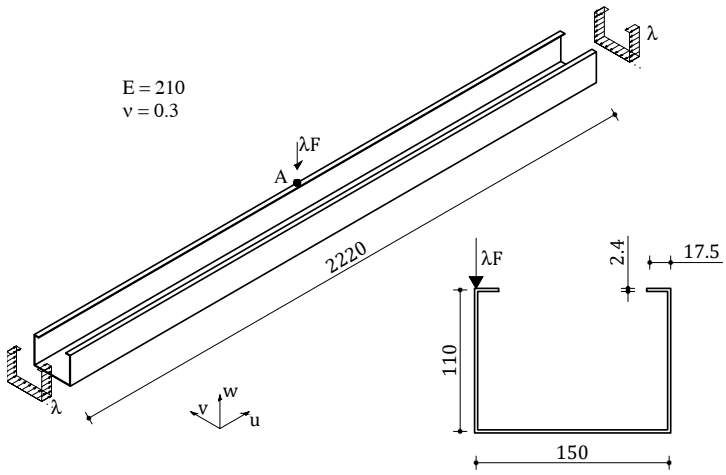

Figure 5.6: Lipped channel column: model properties.

is very clearly visible and indicates a superior performance.

	displacement	mixed
step 1	3	2
step 2	3	2
step 3	3	2
total	9	6

Table 5.2: Lipped channel column: number of Newton iterations in the corrector phase of each step.

The evolution of the deformed configuration along the equilibrium path is depicted in Fig. 5.8. A combination of torsional and local buckling is clearly visible.

5.4.3 Laminate composite cylinder subjected to axial compression

Cylinder buckling is a severe numerical test case for nonlinear solution methods since a pronounced snap-back behavior must be reliably captured with strongly degrading algebraic properties of the governing system of equations. Nevertheless, a steadily growing tendency to use laminate composite cylindrical structures as primary structures in aerospace engineering and other lightweight engineering disciplines emphasizes the importance of a highly reliable, accurate and compu-

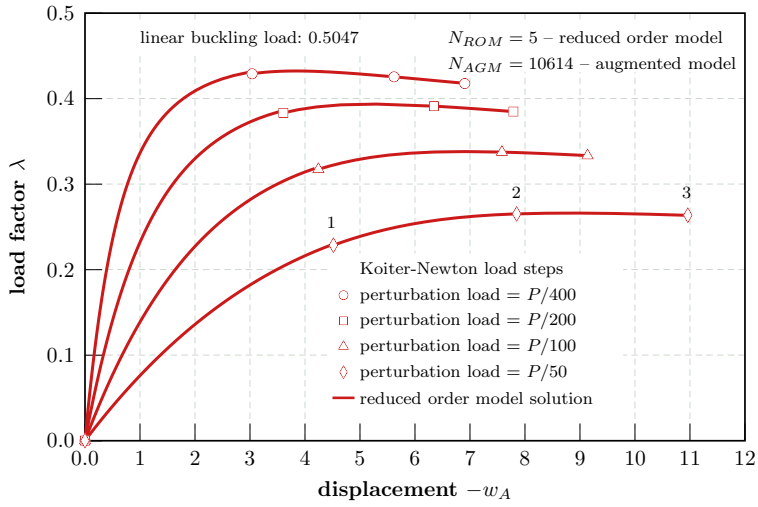

Figure 5.7: Lipped channel column: equilibrium paths for different perturbation loads.

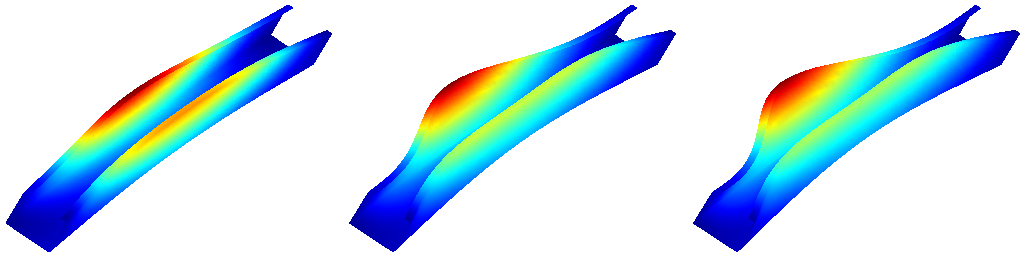

Figure 5.8: Lipped channel column: deformed configurations (scale factor 10) at 1, 2 and 3.

tationally efficient prognosis of stability properties.

The cylinder considered in the following and labelled Z33 and was manufactured and tested by DLR (German Aerospace Center) and is commonly used as validation model for numerical developments in the context of laminate composite shell design [56, 98]. The laminate stacking sequence is ${}_{in}[0/0/19/-19/37/-37/45/-45/51/-51]_{out}$ with the angles measured from the cylinder axis with respect to the outward normal. The cylinder has a height of 510, a radius of $R = 250$ and a wall-thickness of $t = 1.25$, cf Fig. 5.9. The ply properties are $E_1 = 123.6$, $E_2 = E_3 = 8.7$, $\nu_{12} = 0.32$, $\nu_{13} = \nu_{23} = 0$, $G_{12} = G_{13} = G_{23} = 5.7$.

The cylinder model is clamped at the bottom face and has a pinned support in radial direction at the top. A uniformly distributed load along the top rim was

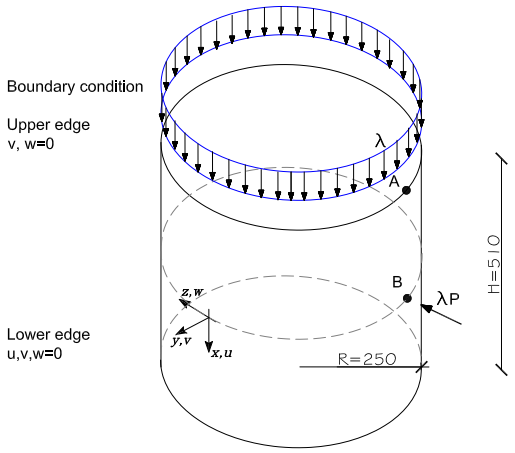

Figure 5.9: Laminate composite cylinder: model properties.

applied in axial direction. A geometric imperfection was introduced by a single perturbation load halfway up the cylinder axis. The end-shortening result was measured at a single node of the cylinder's top rim, labelled as displacement u_A.

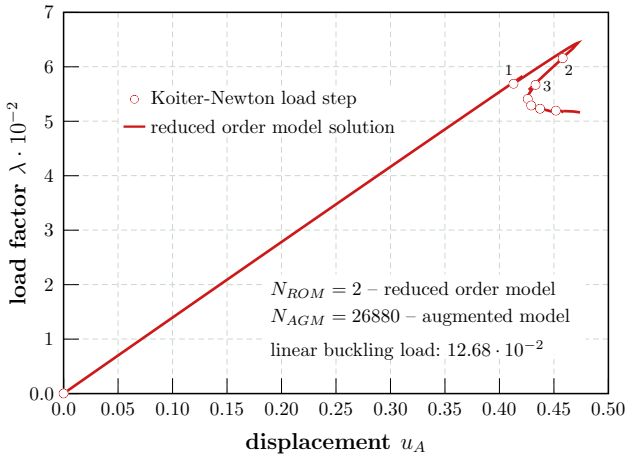

Figure 5.10: Laminate composite cylinder: equilibrium path.

The complete equilibrium path was traced with 7 Koiter-Newton steps, cf Fig.5.10. As common for compressed cylinders, the elastic response is characterized by an almost linear pre-critical path, followed by a bifurcation and snap-back behaviour. The cylinder problem demonstrates the ability of the nonlinear Koiter predictor to capture accurately the bifurcation point, which is a potential failure mode for standard arc-length techniques with linear predictor, unless a very small step size is used.

The constructed reduced order model used only a single buckling mode in

addition to the path tangent. The first and the second mode used to construct the reduced order model at the undeformed configuration and at the equilibrium point 1, respectively, are depicted in Fig.5.11 and Fig.5.12. From Fig.5.13 it can be seen that the modes change along the equilibrium path due to the applied imperfection load. As a consequence, a repeated reconstruction of the reduced order model was required to capture accurately the bifurcation and the post-critical deformation.

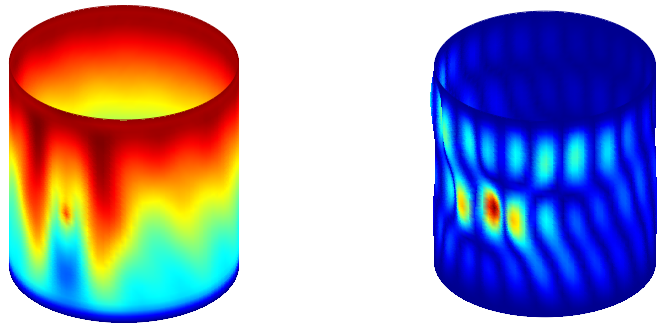

Figure 5.11: Laminate composite cylinder: first and second modes of the *reduced order model* at the reference configuration.

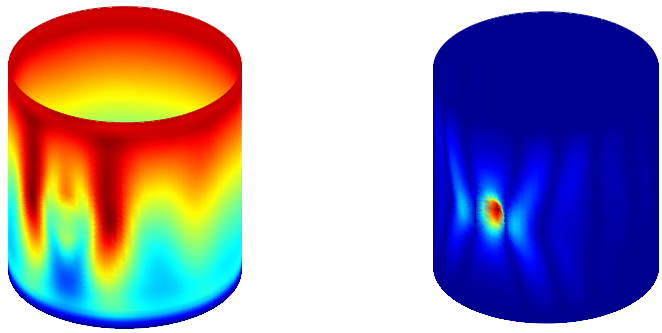

Figure 5.12: Laminate composite cylinder: first and second mode of the *reduced order model* at 1.

Finally, the number of Newton iterations in the corrector phase of each step are reported in Tab.5.3. Interestingly, the gain of computational efficiency using the mixed approach is very moderate compared to the pure displacement formulation which can be mainly attributed to an already extremely good performance of the the displacement-based Koiter-Newton model which is more than four times less compared to standard Newton-based method.

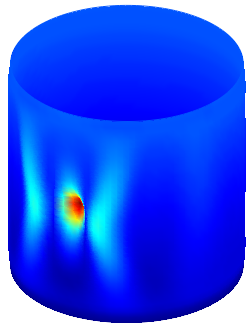

Figure 5.13: Laminate composite cylinder: deformed configuration (scale factor 25) at 2

	displacement	mixed
step 1	3	2
step 2	2	2
step 3	2	2
step 4	2	2
step 5	2	2
step 6	2	2
step 7	3	2
total	16	14

Table 5.3: Laminate composite cylinder: number of Newton iterations in the corrector phase of each step.

5.4.4 Thin-walled frame

Finally, a thin-walled frame structure, which undergoes a distinct nonlinear deformation with a bifurcation in the equilibrium path, is analysed. The geometry and boundary conditions are illustrated in Fig.5.14. The material properties are $E = 3.10275$ and $\nu = 0.3$.

The equilibrium path is depicted in Fig.5.15 which is characterised by the bifurcation along a nonlinear pre-critical path due to a local buckling near the clamped section. This can be seen from the evolution of the deformed configuration shown in Fig. 5.16.

The Koiter-Newton analysis was carried out with 4 steps using a reduced order model which was constructed on the basis of the first 6 buckling modes. Again, the proposed mixed formulation shows a significant improvement in terms of total number Newton iterations which reduced by more than 40% compared to

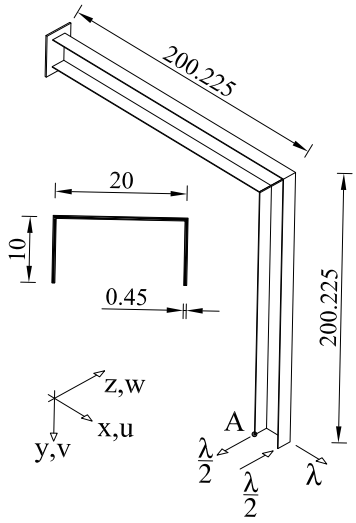

Figure 5.14: Thin-walled frame: model properties.

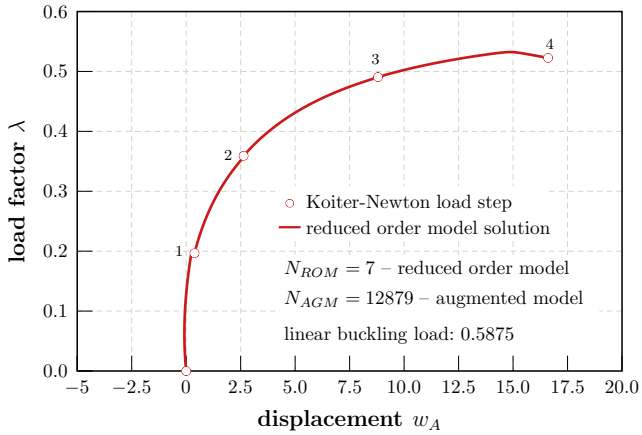

Figure 5.15: Thin-walled frame: equilibrium path.

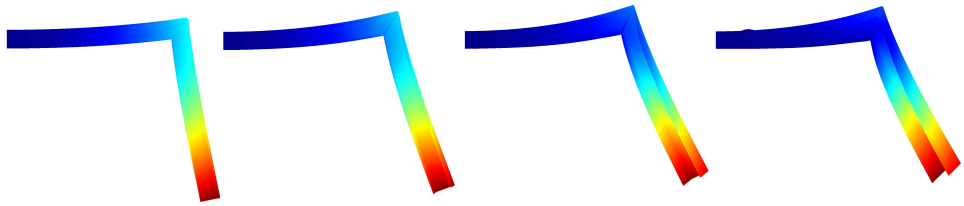

Figure 5.16: Thin-walled frame: evolution of the deformed configuration (scale factor 15).

the conventional model, cf Tab.5.4.

	displacement	mixed
step 1	4	2
step 2	3	2
step 3	4	2
step 4	3	2
total	14	8

Table 5.4: Thin-walled frame: number of iterations required.

5.5 Summary

This chapter explored the performance properties of a mixed model formulation in the framework of the recently introduced Koiter-Newton method, which is a reduced order model approach for geometric nonlinear analyses with an emphasis on buckling failure of thin-walled structures. In this context, a solid shell model was formulated following the Hellinger-Reissner variational principle which proved to be highly beneficial towards the computational efficiency of the analysis. The Koiter-Newton method is a step-by-step equilibrium path tracing approach which exploits the asymptotic expansion properties of Koiter's post-buckling theory in the predictor phase while mapping the solution space to a reduced order model. The construction of the reduced order model is based on the expansion of the elastic inner forces at a known state of equilibrium using the path tangent and a few closely spaced linear buckling modes, thus exciting bifurcating branches of the equilibrium path. In the mixed element formulation additional unknown stress degrees of freedom were introduced. The variables are independent of adjacent elements and thus can be eliminated on system level by an element-wise static condensation. The third order form vanishes in the mixed formulation thus simplifying and economizing the expensive contribution to the construction of the reduced order model. In general, the expansion applies derivatives of the strain energy up to the fourth order which requires the evaluation of linear, quadratic and cubic forms during the construction of the reduced order model. Using a mixed model, as favoured in this work, the cubic form vanishes due to independently behaving degrees of freedom representing the unknown stress resultants on element level with beneficial consequences in terms of a simplified formulation for the reduced order model and computational efficiency.

The proposed formulation was tested with several numerical tests and compared to the conventional Koiter-Newton method which, in a number of studies [8], has already proven a superior performance compared to classical path-tracing

technologies. The asymptotic Koiter predictor towards the equilibrium path allows for significantly increased step sizes such that the full path often can be traced within a few steps, revealing all neuralgic points along the path, including limit and branching points. Furthermore, a snap-back and snap-through behaviour as common in the analysis of thin shells and slender structures is reliably captured and makes the approach a robust technology for stability analyses. The real strength of the proposed formulation was revealed with the corrector phase in each step which uses Newton iterations on the full system to drive the force residual below the chosen accuracy level and therefore represents numerically the most expensive part of the analysis. We have observed that the novel approach can significantly reduce the number of iterations, partly by more than 50% and even in presence of bifurcation and for very large step sizes of problems which showed highly nonlinear deformation properties in the pre-critical range. In all tested cases an average number of *two* Newton iterations was observed to regain equilibrium .

The proposed Koiter-Newton approach is an essential extension of the conventional approach towards a reliable and robust nonlinear analysis tool for thin-walled structures, in particular when buckling is the dominant physical phenomenon. The mixed model formulation should be extended in future work to more sophisticated discretisation techniques, which exploit higher order approximation properties and will be able to further enhance the analysis quality in terms of accuracy and continuity of the elastic buckling response. Interested readers can find further details in [99].

Chapter 6

An isogeometric solid-shell model for large deformation analysis of elastic shells

Abstract

In this chapter, an isogeometric solid-shell model for geometrically nonlinear analyses is proposed. It is based on a linear interpolation through the thickness and a NURBS interpolation on the middle surface of the shell for both the geometry and the displacement field. The Green-Lagrange strains are linearised along the thickness direction and a modified generalized constitutive matrix is adopted to easily eliminate thickness locking without introducing any additional unknowns and to model multi-layered composite shells. Reduced integration schemes, which take into account the high continuity of the shape functions, are investigated to avoid interpolation locking and to increase the computational efficiency. The relaxation of the constitutive equations at each integration point is adopted in the iterative scheme in order to reconstruct the equilibrium path using large steps and a low number of iterations, even for very slender structures. This strategy makes it possible to minimize the number of stiffness matrix evaluations and decompositions and it turns out to be particularly convenient in isogeometric analyses.

6.1 Introduction

In recent years an increasing amount of research has aimed at developing new efficient solid-shell finite elements (FEs)[10, 11, 19, 12, 13] for nonlinear analysis of thin structures. This is due to the advantages of these kinds of elements in comparison to classical shell ones. In particular, they allow the use of 3D continuum strain measures employing translational degrees of freedom only, so avoiding complex and expensive rules for updating the rotations. Solid-shell elements are

often based on a linear displacement interpolation in order to achieve computational efficiency and then exhibit shear locking, also present in traditional shell elements, and trapezoidal and thickness locking, typical of solid elements [16]. These kinds of locking are usually sanitized by means of Assumed Natural Strain (ANS), Enhanced Assumed Strain (EAS) [17, 20] and mixed (hybrid) formulations [10, 21, 22]. Solid-shells have been used to model composites or laminated beams [19, 21, 24] and shell structures in both the linear [17, 12, 28] and nonlinear [20, 11, 10] range. Among the most effective and interesting proposals are the mixed solid-shell elements of Sze and co-authors [10] which extend the initial PT18β hybrid element of Pian and Tong [2] to thin shells and eliminate thickness locking by means of a modified generalized constitutive matrix. This approach makes it possible, as opposed to EAS, to avoid the introduction of additional degrees of freedom (DOFs) and to obtain good predictions for multi-layered composites. Although there is the effective elimination of the interpolation locking, low order solid-shell elements exhibit a poor behaviour when analysing curved geometries. High order Lagrangian interpolations, on the other hand, have been little used due to the high number of DOFs and computational cost for the integration and assembly of the quantities [30].

The isogeometric analysis (IGA) [9, 100] represents a good alternative to high order Lagrangian FEs. The main reason for its success is, in our opinion, the way it makes it possible to elevate the order of the shape functions while practically maintaining the same number of DOFs of linear Lagrangian interpolations. Another notable feature is that the high order continuity of the shape functions allows the total number of integration points to be reduced significantly as shown in [101, 102] compensating for the computational cost of the assembly of the discrete operators. Finally, the geometry is reproduced exactly, regardless of the mesh adopted and a simple link between CAD and structural analysis is available.

These considerations make IGA very attractive, particularly in geometrically nonlinear analysis where a highly continuous solution is often expected. However, there are some difficulties associated with IGA with respect to traditional finite elements. The use of very high order shape functions eliminates interpolation locking but, at the same time, increases the computational effort for the integration and the assembly of the discrete quantities and for the solution of the discrete problem because of the decrease in the stiffness matrix sparsity. For these reasons C^1 and C^2 NURBS interpolations are often preferred, even if they are not immune to locking phenomena. Due to the inter-element continuity of the interpolation, element-wise reduced integrations and strategies, like ANS [103], only alleviate, but do not eliminate locking, and so are not effective for very thin shells. For the same reason, mixed formulations with stress shape functions defined at element level are not able to prevent locking. Conversely, mixed formulations with continuous stress shape functions have been successfully proposed [104, 105]. However, in this way the total number of DOFs increases with respect to the initial displacement formulation and the static condensation of the stress variables, usually

employed in FE analysis and performed at the element level, can be carried out only at patch level and as a result is not convenient because it produces a full condensed stiffness matrix. An interesting alternative is the use of displacement formulations with patch-wise reduced integration rules [101]. These have been shown to alleviate and, in some cases, eliminate interpolation locking in linear elastic problems [102] employing a low number of integration points and so significantly improve the computational efficiency. This strategy seems more attractive than the mixed formulation, since it preserves the stiffness matrix sparsity without introducing additional unknowns and allows a more efficient integration.

However, when comparing mixed and displacement formulations in path-following geometrically nonlinear analyses, many authors observed that the mixed ones can withstand much larger step sizes (increments) with a reduced number of iterations to obtain an equilibrium point and then the equilibrium path. The reason for this is explained in [49, 32] where it is shown that the performances of the Newton method drastically deteriorate in displacement formulations when the slenderness of the structure increases. Conversely, the Newton method in mixed formulations is unaffected by this phenomenon, which depends only on the format of the iterative scheme adopted (mixed or purely displacement based) and also holds when a mixed and a displacement formulation provide the same discrete accuracy. To eliminate this inconvenience in displacement-based finite elements the Mixed Integration Point (MIP) strategy has been recently proposed in [70]. It consists of the relaxation of the constitutive equations at each integration point during the Newton iterative process.

This chapter proposes an isogeometric solid-shell formulation for geometrically nonlinear analyses of homogeneous and composite multi-layered shells, which uses a linear through-the-thickness interpolation of geometry and displacements. The nonlinear model is based on a Total-Lagrangian formulation adopting the Green-Lagrange strain measure. A linearisation of the strains and a pre-integration along the thickness direction allow the definition of a modified generalized constitutive matrix, which effectively eliminates thickness locking without introducing any additional through-the-thickness DOF [106] and leads to accurate predictions for composites. The displacement field and the geometry are rewritten in terms of semi-sum and semi-difference of the top and bottom surface quantities. The model so obtained allows a bidimensional description and interpolation of the geometry and displacements using 2D NURBS of generic order and continuity. Each control point is equipped with six DOFs but, in contrast to traditional shell models, no rotational DOF is employed. Shear and membrane locking, which already occur in linear elastic problems for low order NURBS [107], are even heavier in the nonlinear range when large displacements occur. Different patch-wise reduced integration rules [101, 102], previously proposed for linear analyses, are investigated in large deformation problems with the aim of eliminating interpolation locking and increasing the computational efficiency in the proposed solid-shell model when C^1 and C^2 NURBS are adopted.

The displacement-based solid-shell formulation so obtained seems able to provide accurate solutions, practically unaffected by locking, without the need of a mixed formulation and the corresponding, previously discussed, drawbacks. However, it is still plagued, like any displacement formulation, by the slow convergence rate and the lack of robustness of the Newton method when analyzing slender structures. The MIP strategy, which has been shown to avoid this inconvenience in the FE context [70], is extended to the proposed IGA framework with the aim of reducing the iterative effort and making it independent of the slenderness of the structure. Since the computational cost of evaluating and decomposing the stiffness matrix represents, in IGA, a significant part of the total cost of the analysis, the main goal is to exploit the high robustness of the MIP approach in order to minimize these operations by means of a modified Newton scheme, which is usually prevented by the displacement formulations in large deformation problems.

The chapter is organized as follows: section 2 presents the isogeometric solid-shell model for composite shells; in section 3 patch-wise reduced integrations are investigated for the elimination of the interpolation locking in the nonlinear range and the MIP iterative strategy is illustrated; numerical tests are carried out in section 4 to both validate the accuracy of the proposed isogeometric model and highlight the benefits in using MIP in the IGA context; finally the conclusions are reported.

6.2 The isogeometric solid-shell model

In this section the isogeometric solid-shell model for the geometrically nonlinear analysis of composite shells is presented. Starting from the FE model proposed in [10], a solid-shell model with a NURBS interpolation of generic order on the middle surface of the shell is derived. A Total Lagrangian formulation, based on a Green-Lagrange strain measure, is adopted.

6.2.1 NURBS basics

A B-Spline curve is represented as

$$\mathbf{u}[\xi] = \sum_{i=1}^{n} N_i^p[\xi]\mathbf{P}_i = \mathbf{N}[\xi]\mathbf{P} \tag{6.1}$$

where $\mathbf{P}_i$, $i = 1 \cdots n$ are control points and $N_i^p(\xi)$ are the set of B-Spline basis functions, which are piecewise polynomial functions of order p. The latter are defined by a set of non-decreasing real numbers $\Xi = [\xi_1, \xi_2, ..., \xi_{n+p+1}]$ known as knot vector. More details on the B-Spline parametrization can be found in [108]. B-spline basis functions are calculated recursively by using the formula

$$N_i^p[\xi] = \frac{\xi - \xi_i}{\xi_{i+p} - \xi_i} N_i^{p-1}[\xi] + \frac{\xi_{i+p+1} - \xi}{\xi_{i+p+1} - \xi_{i+1}} N_{i+1}^{p-1}[\xi]$$

for $p \geq 1$ and starting from piecewise constant functions ($p = 0$) defined as

$$N_i^0[\xi] = \begin{cases} 1, & \text{if} \quad \xi_i \leq \xi \leq \xi_{i+1} \\ 0, & \text{otherwise.} \end{cases}$$

B-Spline basis functions have attractive properties: they satisfy the partition of unity that makes them suitable for discretisation methods, have a compact support and are non-zero and non-negative within the knot interval $[\xi_i, \xi_{i+p+1}]$. The regularity r between two parametric or physical elements is described by the multiplicity of the associated knot in Ξ. The regularity is given by $r = p - s$ where p and s are the order used for the basis functions and the multiplicity of the knot ξ_i respectively.

Since B-splines are polynomial functions they are not able to represent circular arcs and conic sections exactly. For this reason NURBS extend the B-spline concept in order to represent these objects exactly. NURBS are obtained by a projective transformation of B-splines extending Eq.(6.1) by using

$$R_i^p[\xi] = \frac{N_i^p[\xi] w_i}{\sum_i^n N_i^p[\xi] w_i} \tag{6.2}$$

as shape functions. It is worth noting that all properties of B-Splines are maintained and, in particular, B-Splines are retrieved when all the weights are equal.

By applying the tensor product, the NURBS surface is constructed in a similar way to Eq.(6.1) as

$$\mathbf{u}[\xi, \eta] = \sum_{i=1}^{n} \sum_{j=1}^{m} R_i^p[\xi] M_j^q[\eta] \mathbf{P}_{ij} = \mathbf{N}[\xi, \eta] \mathbf{P} \tag{6.3}$$

where $\Xi = [\xi_1, \xi_2 ... \xi_{n+p+1}]$ and $\mathcal{H} = [\eta_1, \eta_2 ... \eta_{m+q+1}]$ are two knot vectors, R_i^p and M_j^q are the one-dimensional basis functions over these knot vectors and $\mathbf{P}_{ij}$ defines a set of $n \times m$ control points. The tensor product of the knot vectors Ξ and $\mathcal{H}$ defines a mesh of quadrilateral "isogeometric elements".

Weights, as well as control points of the initial geometry, are provided by the CAD model while suitable algorithms exist for the refinement required to approximate the unknown solution [108, 9]. The geometry is always represented exactly regardless of the mesh adopted.

6.2.2 Shell kinematics

A Total Lagrangian formulation is used to identify material points of the current configuration in terms of their position vector $\mathbf{X}(\xi, \eta, \zeta)$ in the reference configuration and the displacement state $\mathbf{d}(\xi, \eta, \zeta)$, cf Fig.6.1

$$\mathbf{x}(\xi, \eta, \zeta) = \mathbf{X}(\xi, \eta, \zeta) + \mathbf{d}(\xi, \eta, \zeta) \tag{6.4}$$

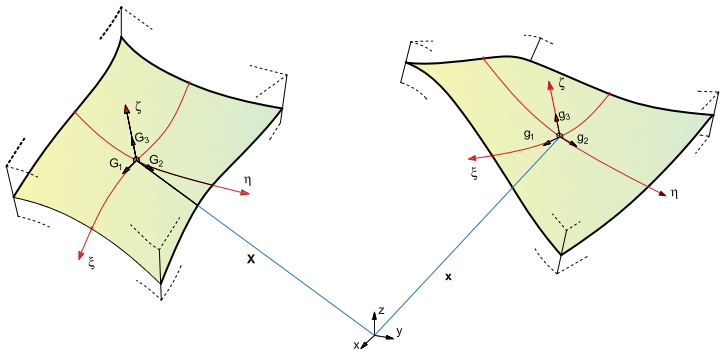

Figure 6.1: Undeformed and deformed shell geometry.

where $\boldsymbol{\zeta} = [\xi, \eta, \zeta]$ denote convective curvilinear shell coordinates with (ξ, η) representing in-plane coordinates and ζ being the shell thickness coordinate. The covariant basis vectors in the undeformed and deformed configuration are obtained from the corresponding partial derivatives of the position vectors $\mathbf{X}$ and $\mathbf{x}$, respectively

$$\mathbf{G}_i = \mathbf{X}_{,i}\,, \qquad \mathbf{g}_i = \mathbf{x}_{,i} = \mathbf{G}_i + \mathbf{d}_{,i} \qquad \text{with} \;\; i = 1, 2, 3\,, \tag{6.5}$$

where $()_{,i}$ denotes the partial derivative with respect to ith components of $\boldsymbol{\zeta}$. The contravariant basis vectors follow from the dual basis condition: $\mathbf{g}_i \cdot \mathbf{g}^j = \mathbf{G}_i \cdot \mathbf{G}^j = \delta_i^j$ and the metric coefficients are $g_{ij} = \boldsymbol{g}_i \cdot \boldsymbol{g}_j$ and $G_{ij} = \mathbf{G}_i \cdot \mathbf{G}_j$ with $(i, j = 1, 2, 3)$. The motion of material points from the initial reference configuration to the current configuration is described by the deformation map $\mathbf{F} : \mathbf{x} \to \mathbf{X}$

$$\mathbf{F} = \frac{\partial \mathbf{x}}{\partial \mathbf{X}} = \mathbf{g}_i \otimes \mathbf{G}^i. \tag{6.6}$$

and Einstein convention of summing on repeated indexes is adopted from now on. Using the deformation gradient in Eq.(6.6) and the metric tensor coefficients g_{ij} and G_{ij}, the Green-Lagrange strain tensor can be expressed as

$$\mathbf{E} = \frac{1}{2}(\mathbf{F}^T\,\mathbf{F} - \mathbf{I}) = \bar{E}_{ij}\,\mathbf{G}^i \otimes \mathbf{G}^j \tag{6.7}$$

with

$$\bar{E}_{ij} = \frac{1}{2}\left(\mathbf{X}_{,i} \cdot \mathbf{d}_{,j} + \mathbf{d}_{,i} \cdot \mathbf{X}_{,j} + \mathbf{d}_{,i} \cdot \mathbf{d}_{,j}\right) \quad \text{with} \quad i, j = 1, 2, 3 \tag{6.8}$$

where $(\cdot)$ means scalar product.

Assuming a linear through-the-thickness interpolation the position vector is expressed as

$$\mathbf{X} = \mathbf{X}_0[\xi, \eta] + \zeta \mathbf{X}_n[\xi, \eta] \tag{6.9}$$

where

$$\mathbf{X}_0 = \frac{1}{2}\left(\mathbf{X}[\xi,\eta,1] + \mathbf{X}[\xi,\eta,-1]\right), \quad \mathbf{X}_n = \frac{1}{2}\left(\mathbf{X}[\xi,\eta,1] - \mathbf{X}[\xi,\eta,-1]\right)$$

with $\zeta = 1$ and $\zeta = -1$ identifying the top and the bottom surface of the shell respectively.

Similarly, the displacement field $\mathbf{d} = \mathbf{d}_0[\xi,\eta] + \zeta\mathbf{d}_n[\xi,\eta]$ is described as a combination of the displacements

$$\mathbf{d}_0 = \frac{1}{2}\left(\mathbf{d}[\xi,\eta,1] + \mathbf{d}[\xi,\eta,-1]\right), \quad \mathbf{d}_n = \frac{1}{2}\left(\mathbf{d}[\xi,\eta,1] - \mathbf{d}[\xi,\eta,-1]\right).$$

The same convective coordinates $\boldsymbol{\zeta}$ are used for expressing the interpolation of the discrete model.

6.2.3 The isogeometric solid-shell element

The kinematics of the solid-shell model derived in 6.2.2 allows a 2D description of the shell. Following the isogeometric concept, geometry and displacement field are interpolated, over the element, as follows

$$\mathbf{X}[\boldsymbol{\zeta}] = \mathbf{N}_d[\boldsymbol{\zeta}]\mathbf{X}_e, \quad \mathbf{d}[\boldsymbol{\zeta}] = \mathbf{N}_d[\boldsymbol{\zeta}]\mathbf{d}_e \tag{6.10}$$

where $\mathbf{d}_e = [\mathbf{d}_{0e}, \mathbf{d}_{ne}]$ and $\mathbf{X}_e = [\mathbf{X}_{0e}, \mathbf{X}_{ne}]$ collect the element control points for displacement and geometry. The matrix $\mathbf{N}_d[\boldsymbol{\zeta}]$ collects the interpolation functions

$$\mathbf{N}_d[\boldsymbol{\zeta}] \equiv \Big[\mathbf{N}[\xi,\eta], \zeta\mathbf{N}[\xi,\eta]\Big] \tag{6.11}$$

where $\zeta \in [-1,+1]$ and $\mathbf{N}[\xi,\eta]$ are bivariate NURBS (6.3), functions of the middle surface coordinates only.

Adopting a Voigt notation, the Green-Lagrange covariant strain components in Eq.(6.8) are collected in vector $\bar{\mathbf{E}} = [\bar{E}_{\xi\xi}, \bar{E}_{\eta\eta}, 2\bar{E}_{\xi\eta}, \bar{E}_{\zeta\zeta}, 2\bar{E}_{\eta\zeta}, 2\bar{E}_{\xi\zeta}]^T$, that, exploiting Eq.(6.10), becomes

$$\bar{\mathbf{E}} = \left(\boldsymbol{\mathcal{L}}[\boldsymbol{\zeta}] + \frac{1}{2}\boldsymbol{\mathcal{Q}}[\boldsymbol{\zeta}, \mathbf{d}_e]\right)\mathbf{d}_e, \tag{6.12}$$

where $\boldsymbol{\mathcal{L}}[\boldsymbol{\zeta}] \equiv \boldsymbol{\mathcal{Q}}[\boldsymbol{\zeta}, \mathbf{X}_e]$ and $\boldsymbol{\mathcal{Q}}$ is so defined

$$\boldsymbol{\mathcal{Q}}[\boldsymbol{\zeta}, \mathbf{d}_e] \equiv \begin{bmatrix} \mathbf{d}_e^T\mathbf{N}_{d,\xi}^T\mathbf{N}_{d,\xi} \\ \mathbf{d}_e^T\mathbf{N}_{d,\eta}^T\mathbf{N}_{d,\eta} \\ \mathbf{d}_e^T(\mathbf{N}_{d,\xi}^T\mathbf{N}_{d,\eta} + \mathbf{N}_{d,\eta}^T\mathbf{N}_{d,\xi}) \\ \mathbf{d}_e^T\mathbf{N}_{d,\zeta}^T\mathbf{N}_{d,\zeta} \\ \mathbf{d}_e^T(\mathbf{N}_{d,\zeta}^T\mathbf{N}_{d,\eta} + \mathbf{N}_{d,\eta}^T\mathbf{N}_{d,\zeta}) \\ \mathbf{d}_e^T(\mathbf{N}_{d,\xi}^T\mathbf{N}_{d,\zeta} + \mathbf{N}_{d,\zeta}^T\mathbf{N}_{d,\xi}) \end{bmatrix}. \tag{6.13}$$

The covariant strains are conveniently linearised with respect to ζ

$$\bar{\mathbf{E}} \approx \begin{bmatrix} \bar{\mathbf{e}}[\xi,\eta] + \zeta\ \bar{\boldsymbol{\chi}}[\xi,\eta] \\ \bar{E}_{\zeta\zeta}[\xi,\eta] \\ \bar{\boldsymbol{\gamma}}[\xi,\eta] \end{bmatrix} \tag{6.14}$$

where

$$\bar{\mathbf{e}}[\xi,\eta] \equiv \begin{bmatrix} \bar{E}_{\xi\xi}[\xi,\eta,0] \\ \bar{E}_{\eta\eta}[\xi,\eta,0] \\ 2\bar{E}_{\xi\eta}[\xi,\eta,0] \end{bmatrix} \quad \bar{\boldsymbol{\chi}}[\xi,\eta] \equiv \begin{bmatrix} \bar{E}_{\xi\xi,\zeta}\,[\xi,\eta,0] \\ \bar{E}_{\eta\eta,\zeta}\,[\xi,\eta,0] \\ 2\bar{E}_{\xi\eta,\zeta}\,[\xi,\eta,0] \end{bmatrix} \quad \bar{\boldsymbol{\gamma}}[\xi,\eta] \equiv \begin{bmatrix} 2\bar{E}_{\eta\zeta}[\xi,\eta,0] \\ 2\bar{E}_{\xi\zeta}[\xi,\eta,0] \end{bmatrix}$$

are collected in the vector of generalized covariant strains $\bar{\boldsymbol{\varepsilon}}[\xi,\eta] \equiv \left[\bar{\mathbf{e}}, \bar{E}_{\zeta\zeta}, \bar{\boldsymbol{\chi}}, \bar{\boldsymbol{\gamma}}\right]^T$. In order to simplify the notation, the dependence of the quantities on ξ, η will be omitted from now on, when clear.

The generalized stress components, once the kinematic model is assumed, are automatically given by assuring the invariance of the internal work. By collecting the contravariant stress components $\bar{\mathbf{S}} \equiv [\bar{S}_{\xi\xi}, \bar{S}_{\eta\eta}, \bar{S}_{\xi\eta}, \bar{S}_{\zeta\zeta}, \bar{S}_{\eta\zeta}, \bar{S}_{\xi\zeta}]^T$, the work conjugate variables with $\bar{\boldsymbol{\varepsilon}}$ are obtained by

$$\begin{aligned} \mathcal{W} &= \int_V \bar{\mathbf{S}}^T \bar{\mathbf{E}} dV = \int_\Omega \left(\bar{\boldsymbol{\mathcal{N}}}^T \bar{\mathbf{e}} + \bar{\boldsymbol{\mathcal{M}}}^T \bar{\boldsymbol{\chi}} + \bar{s}_{\zeta\zeta} \bar{E}_{\zeta\zeta} + \bar{\boldsymbol{\mathcal{T}}}^T \bar{\boldsymbol{\gamma}} \right) \\ &= \int_\Omega \bar{\boldsymbol{\sigma}}^T \bar{\boldsymbol{\varepsilon}} d\Omega \end{aligned} \tag{6.15}$$

where, from now on, $\int_\Omega (...)\, d\Omega = 2 \int_{\xi_i}^{\xi_{i+1}} \int_{\eta_i}^{\eta_{i+1}} (...)\, det(\mathbf{J}[\xi,\eta,0]) d\xi d\eta$ and $\mathbf{J}$ denotes the Jacobian matrix $\mathbf{J}[\xi,\eta,\zeta] = [\mathbf{G}_1,\ \mathbf{G}_2,\ \mathbf{G}_3]^T$.

The generalized contravariant stresses $\bar{\boldsymbol{\sigma}} \equiv \left[\bar{\boldsymbol{\mathcal{N}}}, \bar{s}_{\zeta\zeta}, \bar{\boldsymbol{\mathcal{M}}}, \bar{\boldsymbol{\mathcal{T}}}\right]^T$ in Eq.(6.15) are then

$$\begin{aligned} \bar{\boldsymbol{\mathcal{N}}} &\equiv \frac{1}{2} \int_{-1}^{1} \bar{\boldsymbol{\sigma}}_p d\zeta \quad & \bar{\boldsymbol{\mathcal{M}}} &\equiv \frac{1}{2} \int_{-1}^{1} \zeta \bar{\boldsymbol{\sigma}}_p d\zeta \\ \bar{s}_{\zeta\zeta} &\equiv \frac{1}{2} \int_{-1}^{1} \bar{S}_{\zeta\zeta} d\zeta \quad & \bar{\boldsymbol{\mathcal{T}}} &\equiv \frac{1}{2} \int_{-1}^{1} \bar{\boldsymbol{\tau}} d\zeta \end{aligned} \tag{6.16}$$

with

$$\bar{\boldsymbol{\sigma}}_p = \begin{bmatrix} \bar{S}_{\xi\xi} \\ \bar{S}_{\eta\eta} \\ \bar{S}_{\xi\eta} \end{bmatrix} \quad \bar{\boldsymbol{\tau}} = \begin{bmatrix} \bar{S}_{\xi\zeta} \\ \bar{S}_{\eta\zeta} \end{bmatrix}.$$

6.2.4 The mapping between the parametric and the physical domains

The relation between the contravariant stresses and covariant strains in tensor notation and the corresponding Cartesian ones is

$$\mathbf{E} = \mathbf{J}^{-1} \bar{\mathbf{E}} \mathbf{J}^{-T} \quad \text{and} \quad \mathbf{S} = \mathbf{J}^T \bar{\mathbf{S}} \mathbf{J}, \tag{6.17}$$

that in Voigt notation can be written as

$$\mathbf{E} = \mathbf{T}_E \bar{\mathbf{E}} \quad \text{and} \quad \mathbf{S} = \mathbf{T}_S \bar{\mathbf{S}} \tag{6.18}$$

with $\mathbf{T}_S = \mathbf{T}_E^{-T}$.

From (6.9) $\mathbf{J} = \mathbf{J}_0[\xi,\eta] + \zeta \mathbf{J}_n[\xi,\eta]$ and its inverse can be linearized with respect to ζ as

$$\mathbf{J}^{-1}[\xi,\eta] = \mathbf{J}_0^{-1}[\xi,\eta] + \zeta \mathbf{J}_n^{-1}[\xi,\eta] \tag{6.19}$$

where it is possible to obtain $\mathbf{J}_n^{-1}$ by satisfying up to the first order in ζ the equation $\mathbf{J}\mathbf{J}^{-1} = \mathbf{I}$, that implies

$$\mathbf{J}_n^{-1} = \mathbf{J}_0^{-1}\mathbf{J}_n\mathbf{J}_0^{-1}.$$

Substituting Eq.(6.19) in Eq.(6.18) and maintaining only the linear terms in ζ we obtain the linearized expression of $\mathbf{T}_E = \mathbf{T}_{E0} + \zeta \mathbf{T}_{En}$. In particular letting

$$\mathbf{T}_{E0} = \begin{bmatrix} \mathbf{T}^0_{ee} & \mathbf{T}^0_{e\zeta} & \mathbf{T}^0_{e\gamma} \\ \mathbf{T}^0_{\zeta e} & T^0_{\zeta\zeta} & \mathbf{T}^0_{\zeta\gamma} \\ \mathbf{T}^0_{\gamma e} & \mathbf{T}^0_{\gamma\zeta} & \mathbf{T}^0_{\gamma\gamma} \end{bmatrix}, \qquad \mathbf{T}_{En} = \begin{bmatrix} \mathbf{T}^n_{ee} & \mathbf{T}^n_{e\zeta} & \mathbf{T}^n_{e\gamma} \\ \mathbf{T}^n_{\zeta e} & T^n_{\zeta\zeta} & \mathbf{T}^n_{\zeta\gamma} \\ \mathbf{T}^n_{\gamma e} & \mathbf{T}^n_{\gamma\zeta} & \mathbf{T}^n_{\gamma\gamma} \end{bmatrix}$$

we have, maintaining the linear terms in ζ only,

$$\mathbf{E} = \mathbf{T}_E \bar{\mathbf{E}} \approx \begin{bmatrix} \mathbf{e} + \zeta \boldsymbol{\chi} \\ E_{\zeta\zeta} \\ \boldsymbol{\gamma} \end{bmatrix}. \tag{6.20}$$

Equation (6.20) can be expressed in terms of the generalized strains as

$$\boldsymbol{\varepsilon} = \mathbf{T}_\epsilon \bar{\boldsymbol{\varepsilon}} \tag{6.21}$$

where $\boldsymbol{\varepsilon} = [\mathbf{e}, E_{\zeta\zeta}, \boldsymbol{\chi}, \boldsymbol{\gamma}]^T$ and

$$\mathbf{T}_\epsilon = \begin{bmatrix} \mathbf{T}^0_{ee} & \mathbf{T}^0_{e\zeta} & \mathbf{0}_{3\times 3} & \mathbf{T}^0_{e\gamma} \\ \mathbf{T}^0_{\zeta e} & T^0_{\zeta\zeta} & \mathbf{0}_{1\times 3} & \mathbf{T}^0_{\zeta\gamma} \\ \mathbf{T}^n_{ee} & \mathbf{T}^n_{e\zeta} & \mathbf{T}^0_{ee} & \mathbf{T}^n_{e\gamma} \\ \mathbf{T}^0_{\gamma e} & \mathbf{T}^0_{\gamma\zeta} & \mathbf{0}_{2\times 3} & \mathbf{T}^0_{\gamma\gamma} \end{bmatrix}.$$

Combining Eqs.(6.12), (6.14) and (6.21) it is possible to obtain the Cartesian generalized strain-displacement relationship

$$\boldsymbol{\varepsilon} = \left(\mathbf{L} + \frac{1}{2}\mathbf{Q}[\mathbf{d}_e] \right) \mathbf{d}_e. \tag{6.22}$$

6.2.5 Modified generalized constitutive matrix

Multi-layered composites can be modeled using layer-wise interpolations [109, 110] which provide accurate interlaminar stress reconstructions or homogenization techniques usually more efficient and suitable for predicting global behaviors accurately.

When a linear through-the-thickness interpolation is adopted, a generalized constitutive law of the multi-layered composite can be obtained following [10, 59]. It consists of a homogenization technique which imposes a constant with ζ stress $S_{\zeta\zeta}$ in order to eliminate thickness locking and obtain an accurate prediction of stresses and displacements. The material law of the generic lamina, assumed to be orthotropic elastic, can be conveniently expressed in a suitable reference system $\{\mathbf{e}_1, \mathbf{e}_2, \mathbf{e}_3\}$ according to the fibre direction as

$$\hat{\mathbf{S}} = \hat{\mathbf{C}}\hat{\mathbf{E}} \quad \text{with} \quad \hat{\mathbf{C}} = \begin{bmatrix} \hat{\mathbf{C}}_{pp} & \hat{\mathbf{C}}_{p\zeta} & \mathbf{0} \\ \hat{\mathbf{C}}_{p\zeta}^T & \hat{C}_{\zeta\zeta} & \mathbf{0} \\ \mathbf{0} & \mathbf{0} & \hat{\mathbf{C}}_t \end{bmatrix} \tag{6.23}$$

which furnishes, exploiting the decoupling of the transverse shear components, the inverse law as

$$\begin{bmatrix} \hat{\mathbf{E}}_p \\ \hat{E}_{\zeta\zeta} \end{bmatrix} = \begin{bmatrix} \hat{\mathbf{F}}_{pp} & \hat{\mathbf{F}}_{p\zeta} \\ \hat{\mathbf{F}}_{p\zeta}^T & \hat{F}_{\zeta\zeta} \end{bmatrix} \begin{bmatrix} \hat{\mathbf{S}}_p \\ \hat{S}_{\zeta\zeta} \end{bmatrix} \tag{6.24}$$

where symbol ($\hat{}$) denotes Cartesian components expressed with respect to $\{\mathbf{e}_1, \mathbf{e}_2, \mathbf{e}_3\}$ with $\mathbf{e}_3$ aligned to ζ and $\hat{\mathbf{E}}_p = \hat{\mathbf{e}} + \zeta\, \hat{\boldsymbol{\chi}}$. Eq.(6.24) can be rewritten as

$$\begin{aligned} \hat{\mathbf{S}}_p &= \mathbf{S}\hat{\mathbf{E}}_p + \mathbf{D}\hat{S}_{\zeta\zeta} \\ \hat{E}_{\zeta\zeta} &= -\mathbf{D}^T\hat{\mathbf{E}}_p + R\hat{S}_{\zeta\zeta} \end{aligned} \quad \text{with} \quad \begin{cases} R = \hat{F}_{\zeta\zeta} + \hat{\mathbf{F}}_{p\zeta}^T\mathbf{D} \\ \mathbf{D} = -(\hat{\mathbf{F}}_{pp})^{-1}\hat{\mathbf{F}}_{p\zeta} \\ \mathbf{S} = (\hat{\mathbf{F}}_{pp})^{-1}. \end{cases}$$

The constitutive law in terms of the quantities $\hat{\boldsymbol{\mathcal{N}}}$ and $\hat{\boldsymbol{\mathcal{M}}}$ is then obtained, integrating along ζ and imposing a constant with ζ stress $\hat{S}_{\zeta\zeta} = \hat{s}_{\zeta\zeta}$, as

$$\begin{aligned} \begin{bmatrix} \hat{\boldsymbol{\mathcal{N}}} \\ \hat{E}_{\zeta\zeta} \\ \hat{\boldsymbol{\mathcal{M}}} \end{bmatrix} &= \frac{1}{2}\int_{-1}^{1} \begin{bmatrix} \mathbf{S} & \mathbf{D} & \zeta\mathbf{S} \\ -\mathbf{D} & R & -\zeta\mathbf{D} \\ \zeta\mathbf{S} & \zeta\mathbf{D} & \zeta^2\mathbf{S} \end{bmatrix} d\zeta \begin{bmatrix} \hat{\mathbf{e}} \\ \hat{s}_{\zeta\zeta} \\ \hat{\boldsymbol{\chi}} \end{bmatrix} \\ &= \begin{bmatrix} \mathbf{S}_0 & \mathbf{D}_0 & \mathbf{S}_1 \\ -\mathbf{D}_0 & R_0 & \mathbf{D}_1 \\ \mathbf{S}_1 & \mathbf{D}_1 & \mathbf{S}_2 \end{bmatrix} \begin{bmatrix} \hat{\mathbf{e}} \\ \hat{s}_{\zeta\zeta} \\ \hat{\boldsymbol{\chi}} \end{bmatrix} \end{aligned}$$

which furnishes the thickness locking free generalized constitutive law

$$\hat{\boldsymbol{\sigma}}[\xi, \eta] = \hat{\mathbf{C}}_\epsilon \hat{\boldsymbol{\varepsilon}}[\xi, \eta] \tag{6.25}$$

where

$$\hat{\mathbf{C}}_\epsilon \equiv \begin{bmatrix} \mathbf{S}_0 + \mathbf{D}_0\mathbf{D}_0^T/R_0 & \mathbf{D}_0/R_0 & \mathbf{S}_1 + \mathbf{D}_0\mathbf{D}_1^T/R_0 & \mathbf{0} \\ \mathbf{D}_0^T/R_0 & 1/R_0 & \mathbf{D}_1^T/R_0 & \mathbf{0} \\ (\mathbf{S}_1 + \mathbf{D}_0\mathbf{D}_1^T/R_0)^T & \mathbf{D}_1/R_0 & \mathbf{S}_2 + \mathbf{D}_1\mathbf{D}_1^T/R_0 & \mathbf{0} \\ \mathbf{0} & \mathbf{0} & \mathbf{0} & \hat{\mathbf{C}}_{t0} \end{bmatrix}$$

and

$$\hat{\mathbf{C}}_{t0} = \int_{-1}^{1} \hat{\mathbf{C}}_t d\zeta.$$

The modified generalized constitutive matrix in the global system $\{X, Y, Z\}$ is obtained as $\mathbf{C}_\epsilon = \mathbf{R}_\epsilon^T \hat{\mathbf{C}}_\epsilon \mathbf{R}_\epsilon$ with $\mathbf{R}_\epsilon$ a suitable rotation matrix.

6.3 Integration and Mixed Integration Points

In this section, after a brief description of the nonlinear analysis framework, a numerical investigation on the use of patch-wise integration rules in large deformation problems is carried out. The Mixed Integration Point strategy is then introduced to improve the performance of the Newton method with the aim of reducing the iterative effort.

6.3.1 Nonlinear analysis framework

The equilibrium of slender hyperelastic structures subject to conservative loads $f[\lambda]$ proportionally increasing with the amplifier factor λ is expressed by the virtual work equation

$$\Phi[u]'\,\delta u - \lambda f\,\delta u = 0 \quad , \quad u \in \mathcal{U}\ ,\ \delta u \in \mathcal{T} \tag{6.26}$$

where $u \in \mathcal{U}$ is the field of configuration variables, $\Phi[u]$ denotes the strain energy, $\mathcal{T}$ is the tangent space of $\mathcal{U}$ at u and a prime is used to express the Fréchet derivative with respect to u. $\mathcal{U}$ is a linear manifold so that its tangent space $\mathcal{T}$ is independent of u. The discrete counterpart of Eq.(6.26) is

$$\mathbf{r}[\mathbf{u},\,\lambda] \equiv \mathbf{s}[\mathbf{u}] - \lambda\,\boldsymbol{f} = \mathbf{0}, \quad \text{with} \quad \begin{cases} \mathbf{s}^T\delta\mathbf{u} \equiv \Phi'[u]\delta u \\ \boldsymbol{f}^T\delta\mathbf{u} \equiv f\,\delta u \end{cases} \tag{6.27}$$

where $\mathbf{r} : \mathbb{R}^{N+1} \to \mathbb{R}^N$ is a nonlinear vectorial function of the vector $\mathbf{z} \equiv \{\mathbf{u}, \lambda\} \in \mathbb{R}^{N+1}$, collecting the configuration $\mathbf{u} \in \mathbb{R}^N$ and the load multiplier $\lambda \in \mathbb{R}$, $\mathbf{s}[\mathbf{u}]$ is the *internal force vector* and $\boldsymbol{f}$ the *reference load vector*. Eq.(6.27) represents a system of N-equations and $N+1$ unknowns and its solutions define the *equilibrium paths* as curves in $\mathbb{R}^{N+1}$ from a known initial configuration $\mathbf{u}_0$, corresponding to $\lambda = 0$. The tangent stiffness matrix is also defined as

$$\delta\mathbf{u}^T\mathbf{K}[\mathbf{u}]\tilde{\mathbf{u}} = \Phi''[u]\tilde{u}\delta u \ \ , \ \ \forall\,\delta\mathbf{u}, \tilde{\mathbf{u}} \tag{6.28}$$

where δu and $\tilde{u}$ are generic variations of the configuration field u and $\delta\mathbf{u}$ and $\tilde{\mathbf{u}}$ the corresponding discrete vectors.

The Riks approach [3] is the preferred strategy for solving Eq.(6.27) by adding a constraint of the shape $g[\mathbf{u},\lambda]-\xi=0$, which defines a surface in $\mathbb{R}^{N+1}$. Assigning successive values to the control parameter $\xi=\xi_{(k)}$ the solution of the nonlinear system

$$\mathbf{R}[\xi]\equiv\begin{bmatrix}\mathbf{r}[\mathbf{u},\lambda]\\ g[\mathbf{u},\lambda]-\xi\end{bmatrix}=\mathbf{0} \tag{6.29}$$

defines a sequence of points (steps) $\mathbf{z}_{(k)}\equiv\{\mathbf{u}_{(k)},\,\lambda_{(k)}\}$ belonging to the equilibrium path. Starting from a known equilibrium point $\mathbf{z}^0\equiv\mathbf{z}_{(k)}$, the new one $\mathbf{z}_{(k+1)}$ is evaluated correcting a first *extrapolation* $\mathbf{z}^1=\{\mathbf{u}^1,\,\lambda^1\}$ by a sequence of estimates $\mathbf{z}^j$ (loops) by a Newton iteration

$$\begin{cases}\bar{\mathbf{J}}\dot{\mathbf{z}}=-\mathbf{R}^j\\ \mathbf{z}^{j+1}=\mathbf{z}^j+\dot{\mathbf{z}}\end{cases} \tag{6.30a}$$

where $\mathbf{R}^j\equiv\mathbf{R}[\mathbf{z}^j]$ and $\bar{\mathbf{J}}$ is the Jacobian of the nonlinear system (6.29) at $\mathbf{z}^j$ or a suitable estimate. The simplest choice for $g[\mathbf{u},\lambda]$ is the linear constraint corresponding to the orthogonal hyperplane

$$\mathbf{n}_u^T(\mathbf{u}-\mathbf{u}^j)+n_\lambda\,(\lambda-\lambda^j)=\Delta\xi\quad\text{where}\quad\begin{cases}\mathbf{n}_u\equiv\mathbf{M}\,(\mathbf{u}^j-\mathbf{u}_{(k)})\\ \mathbf{n}_\lambda\equiv\mu\,(\lambda^j-\lambda_{(k)})\end{cases} \tag{6.30b}$$

$\mathbf{M}$ and μ being some suitable metric factors, $\Delta\xi$ an assigned increment of ξ and

$$\bar{\mathbf{J}}\approx\left[\frac{\partial\mathbf{R}[\mathbf{z}]}{\partial\mathbf{z}}\right]_{\mathbf{z}^j}=\begin{bmatrix}\bar{\mathbf{K}} & -\boldsymbol{f}\\ \mathbf{n}_u^T & n_\lambda\end{bmatrix}. \tag{6.30c}$$

The load-controlled scheme is obtained assuming $g[\mathbf{u},\lambda]=\lambda$ (see [32] for further details) while keeping $\bar{\mathbf{K}}=\mathbf{K}[\mathbf{u}^1]$ we have the modified Newton scheme. The solution of Eq.(6.30) is conveniently performed as follows

$$\begin{cases}\dot{\lambda}=\dfrac{\mathbf{n}_u^T\bar{\mathbf{K}}\mathbf{r}^j}{n_\lambda+\mathbf{n}_u^T\bar{\mathbf{K}}\boldsymbol{f}}\\ \bar{\mathbf{K}}\dot{\mathbf{u}}=\dot{\lambda}\boldsymbol{f}-\mathbf{r}^j.\end{cases} \tag{6.31}$$

6.3.2 Displacement-based isogeometric formulations

The strain energy can be expressed as a sum of element contributions $\Phi[u]\equiv\sum_e\Phi_e[u]$

$$\Phi_e[u]\equiv\int_{\Omega_e}\left(\frac{1}{2}\boldsymbol{\varepsilon}^T\mathbf{C}\boldsymbol{\varepsilon}\right)d\Omega_e \tag{6.32}$$

where Ω_e is the element domain. The first variation of the generalized strains in Eq.(6.22) can be written as

$$\delta\boldsymbol{\varepsilon} = \mathbf{B}[\mathbf{d}_e]\delta\mathbf{d}_e \quad \text{with} \quad \mathbf{B}[\mathbf{d}_e] = \mathbf{L} + \mathbf{Q}[\mathbf{d}_e]$$

and, then, the first variation of the strain energy is

$$\begin{aligned}\Phi_e[u]'\delta u &\equiv \int_{\Omega_e} \left(\delta\boldsymbol{\varepsilon}^T \mathbf{C}_\epsilon \boldsymbol{\varepsilon}\right) d\Omega_e \\ &= \int_{\Omega_e} \left(\delta\mathbf{d}_e^T \mathbf{B}[\mathbf{d}_e]^T \mathbf{C}_\epsilon \boldsymbol{\varepsilon}[\mathbf{d}_e]\right) d\Omega_e = \delta\mathbf{d}_e^T \mathbf{s}_e[\mathbf{d}_e]\end{aligned} \tag{6.33}$$

where $\mathbf{s}_e[\mathbf{d}_e]$ is the element internal force vector. The second variation of the strain measure is

$$\delta\tilde{\boldsymbol{\varepsilon}} = \mathbf{Q}[\tilde{\mathbf{d}}_e]\delta\mathbf{d}_e = \mathbf{Q}[\delta\mathbf{d}_e]\tilde{\mathbf{d}}_e$$

and its kth component can be evaluated as

$$\delta\tilde{\varepsilon}_k = \tilde{\mathbf{d}}_e^T \boldsymbol{\Psi}_k \delta\mathbf{d}_e.$$

Letting $\boldsymbol{\sigma}[\mathbf{d}_e] = \mathbf{C}_\epsilon\boldsymbol{\varepsilon}[\mathbf{d}_e]$, the following expression holds

$$\boldsymbol{\sigma}^T\delta\tilde{\boldsymbol{\varepsilon}} \equiv \sum_k \sigma_k \delta\tilde{\varepsilon}_k = \tilde{\mathbf{d}}_e^T \boldsymbol{\mathcal{G}}[\boldsymbol{\sigma}[\mathbf{d}_e]]\delta\mathbf{d}_e$$

with

$$\boldsymbol{\mathcal{G}}[\boldsymbol{\sigma}[\mathbf{d}_e]] = \sum_k \sigma_k[\mathbf{d}_e]\boldsymbol{\Psi}_k. \tag{6.34}$$

The second variation of the strain energy is

$$\Phi_e''[u]\delta u\tilde{u} \equiv \int_{\Omega_e} \left(\delta\boldsymbol{\varepsilon}^T \mathbf{C}_\epsilon \tilde{\boldsymbol{\varepsilon}} + \delta\tilde{\boldsymbol{\varepsilon}}^T \boldsymbol{\sigma}[\mathbf{d}_e]\right) d\Omega_e = \delta\mathbf{d}_e^T \mathbf{K}_e[\mathbf{d}_e]\tilde{\mathbf{d}}_e \tag{6.35}$$

with the element tangent stiffness matrix defined as

$$\mathbf{K}_e[\mathbf{d}_e] \equiv \int_{\Omega_e} \left(\mathbf{B}[\mathbf{d}_e]^T \mathbf{C}_\epsilon \mathbf{B}[\mathbf{d}_e] + \boldsymbol{\mathcal{G}}[\boldsymbol{\sigma}[\mathbf{d}_e]]\right) d\Omega_e. \tag{6.36}$$

6.3.3 Locking and patch-wise reduced integration in geometrically nonlinear analysis

The high continuity of the interpolation functions used for the approximation of the displacement field does not make the formulation immune to interpolation locking phenomena (shear and membrane locking) when low order NURBS, the most used in practical applications, are employed.

Many strategies for resolving locking phenomena in Lagrangian FEM have been proposed over the years. Among them, element-wise reduced integrations

[111, 112], ANS [113, 114] and mixed formulations [10] are widely employed. Unfortunately, all these element-wise approaches are not able to eliminate lockings in the context of IGA, because of the inter-element high continuity of the NURBS basis.

On the other hand, mixed formulations [115, 104] with continuous shape functions for the stresses have been successfully proposed, providing locking-free models. However, in this way, the total number of unknowns significantly increases due to the stress variables, which cannot be condensed at element level as is usual in the FEM context. A patch-wise condensation is still possible, but this does not seem a convenient choice, because it leads to a full condensed stiffness matrix with negative effects in terms of memory and computational efficiency.

Recently, patch-wise integration rules, which take into account the inter-element high continuity of the displacement interpolation have been proposed [102, 101] and applied to linear elastic problems. In our opinion, these works represent an important development in IGA. The d-dimensional target space of order p and regularity r, labelled as $\mathcal{S}_r^p$, is exactly integrated by a number of $\approx ((p-r)/2)^d$ integration points per element, distributed over the patch, significantly lower than in standard Gauss quadrature rules. Their positions and weights are not equal for each element, but are evaluated, once and for all, in a pre-processing phase and depend on r, p and patch mesh. The algorithms which provide these kinds of integration rules can be found in [102, 101] and are very efficient. Their computational burden is just a small fraction of the total cost of a linear analysis and negligible compared to a nonlinear analysis.

The patch-wise exact integration of a given space $\mathcal{S}_r^p$ also opens up new possibilities for patch-wise reduced integration schemes. In fact p and r can be selected by the user and are not required to be those for the exact integration of the problem space. If the integration space presents spurious modes a certain number of quadrature points are added near the boundary elements in order to remove them and the approximation space is said to be over-integrated and labeled as $\bar{\mathcal{S}}_r^p$ [102, 101]. With respect to the element-wise reduced integrations, an appropriate selection of the patch-wise reduced integration rules makes it possible to avoid spurious modes, alleviate or eliminate interpolation locking in the linear elastic range and further reduce the number of integration points.

This strategy, in our opinion, seems preferable to mixed formulations with continuous stress interpolation since it does not increase the number of unknowns, preserves the sparsity of the stiffness matrix and makes the integration efficient. The last one represents a significant part of the total cost of the analysis, in IGA much more than in FEM formulations, and the reduction of integration points drastically increases the computational efficiency.

In the following, a numerical investigation on different patch-wise integration rules for the proposed solid-shell formulation in large deformation problems is carried out to look for an optimal solution in terms of accuracy, efficiency and robustness. Remembering that in patch-wise rules the number of integration points

n can be different element-by-element, the strain energy can then be evaluated as

$$\Phi_e[\mathbf{d}_e] \equiv \frac{1}{2}\sum_{g=1}^{n} \boldsymbol{\varepsilon}_g[\mathbf{d}_e]^T \mathbf{C}_g \boldsymbol{\varepsilon}_g[\mathbf{d}_e]\; w_g \tag{6.37}$$

the internal force vector as

$$\mathbf{s}_e[\mathbf{d}_e] = \sum_{g}^{n} \Big(\mathbf{B}_g[\mathbf{d}_e]^T \mathbf{C}_g \boldsymbol{\varepsilon}_g[\mathbf{d}_e]\Big)\, w_g \tag{6.38}$$

while the tangent stiffness matrix is

$$\mathbf{K}_e[\boldsymbol{\sigma}_g[\mathbf{d}_e], \mathbf{d}_e] = \sum_{g}^{n} \Big(\mathbf{B}_g[\mathbf{d}_e]^T \mathbf{C}_g \mathbf{B}_g[\mathbf{d}_e] + \boldsymbol{\mathcal{G}}_g[\boldsymbol{\sigma}_g[\mathbf{d}_e]]\Big)\, w_g \tag{6.39}$$

where subscript g denotes quantities evaluated at the integration point $\boldsymbol{\zeta}_g$, w_g is the product of the corresponding weight and the determinant of the Jacobian matrix $\mathbf{J}$ evaluated at the integration point, $\mathbf{C}_g$ is $\mathbf{C}_\epsilon$ at the integration point.

Note that $\mathbf{K}_e[\mathbf{d}_e]$ is written as $\mathbf{K}_e[\boldsymbol{\sigma}_g[\mathbf{d}_e], \mathbf{d}_e]$ as a reminder of the way it is computed.

Interpolation locking tests

In the linear elastic range, low order NURBS interpolations usually exhibit shear and membrane locking. In the nonlinear range, when a Total Lagrangian formulation is adopted, other similar locking phenomena occur due to the different approximation of the linear and quadratic part of the Green-Lagrange strain components. This means that locking occurs in nonlinear analyses, even if the initial geometry is flat. In both linear and nonlinear cases, locking is related to the slenderness of the shell.

A series of patch-wise exact and reduced integration schemes for C^1 and C^2 NURBS basis are employed and compared. For the C^1 interpolation the comparison also includes element-wise reduced integration and the Assumed Natural Strain technique (ANS) [114], proposed for IGA in [107, 103].

Linear analysis The first test is a classical benchmark to address membrane locking in the linear elastic range. It regards the clamped curved beam in Fig.6.2, which is considered a severe test to assess discrete formulations [103]. The normalized displacement at point A is reported in Fig.6.3 for an increasing slenderness and for the different interpolations and integration schemes. The reference value $u_{A,ref}$, from Bernoulli beam theory, is 0.942. A mesh of 10×1 elements is employed.

Concerning the C^1 interpolation, the full S_0^4 integration presents a very strong locking and provides bad results also for $R/t = 100$ and completely wrong results

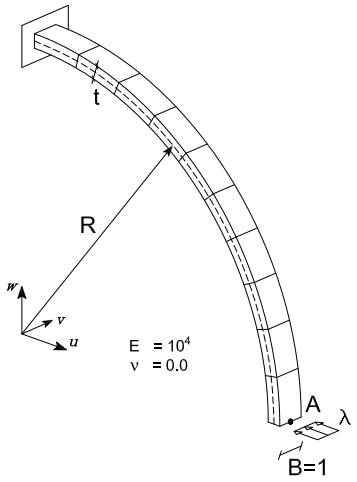

Figure 6.2: Curved bar: geometry and loads.

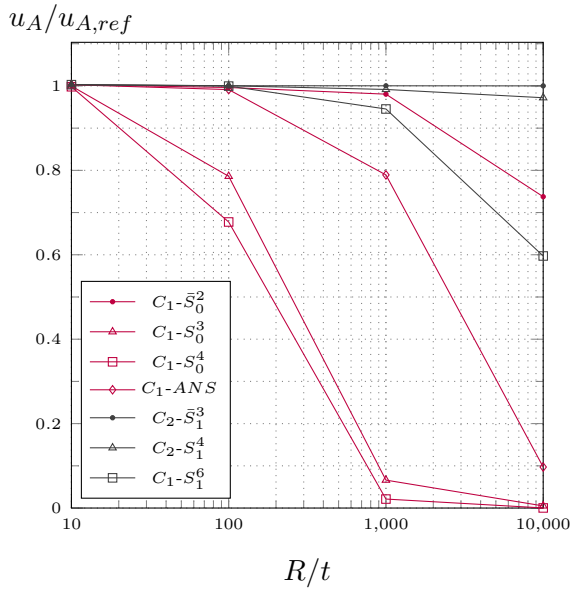

Figure 6.3: Curved bar: linear displacement for different slenderness ratio.

for $R/t = 1000$. The ANS technique gives good results for $R/t = 100$ slightly alleviating locking but it is not satisfactory for $R/t = 1000$. Furthermore the 2×2 Gauss element-wise reduced integration shows the identical results as ANS, which employs a grid of 3×3 Gauss points per element. The $\bar{S}_0^2$ reduced integration has the best performance and is almost insensitive to locking, a part from the extremely slender case $R/t = 10000$. From the computational point of view, it is worth noting that $\bar{S}_0^2$ uses about one integration point per element and is then more efficient than ANS and 2×2 reduced integration.

For the C^2 interpolation, the full integration S_1^6 is clearly affected by locking. On the contrary, both the integration schemes $\bar{S}_1^3$ and S_1^4 provide excellent results and are practically insensitive to locking. It is worth noting that $\bar{S}_1^3$ requires about one integration point per element, while S_1^4 about 2.25 integration points per element, so that both strategies are very efficient compared with Gauss rules.

Nonlinear analysis In order to show the performances of the different strategies in dealing with locking, the simple cantilever beam depicted in Fig.6.4 is analyses with the proposed solid-shell model, for different values of the slenderness parameters $k = L/t$ and under two different load conditions.

For the shear load case, Fig.6.5 shows the equilibrium paths, up to the maximum value of the load $\lambda_{max} = 4 \cdot 10^7/k^3$, obtained with the C^1 interpolation for two different values of $k = 100$ and $k = 1000$ and different meshes. The full

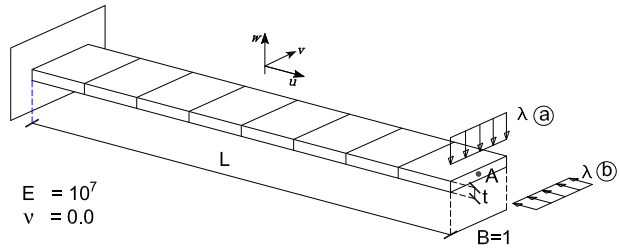

Figure 6.4: Cantilever beam under two load cases: geometry and loads.

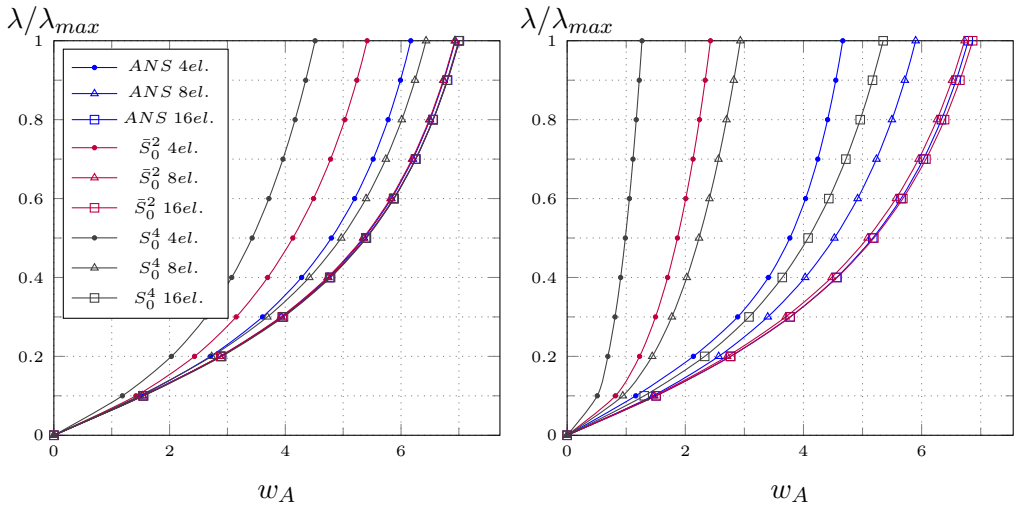

Figure 6.5: Cantilever beam under shear force: equilibrium path for C^1 and $L/h = 100$ (left) and $L/h = 1000$ (right).

S_0^4 integration scheme provides bad results also for the smallest value of k, unless a large number of elements is used, and completely wrong results for $k = 1000$. The ANS technique gives good results for $k = 100$ slightly alleviating locking but it is not satisfactory for $k = 1000$. Furthermore, the 2×2 Gauss element-wise reduced integration shows the identical results as ANS (3×3 Gauss points per element) also in nonlinear context. The $\bar{S}_0^2$ reduced integration seems the best choice being almost insensitive to locking effects, except for the coarsest mesh, which is penalized by the over-integration required to avoid singularities. The general recommendation is to use it with at least 5 elements. $\bar{S}_0^2$ is also far more efficient than ANS and 2×2 reduced integration.

For the C^2 interpolation, the equilibrium paths of the cantilever beam under shear load discretised with 4 and 8 elements are reported in Fig.6.6. Also in this case, the full integration S_1^6 exhibits locking. On the contrary, both the integration schemes $\bar{S}_1^3$ and S_1^4 provide very good results. S_1^4 is practically insensitive to locking effects for every mesh, while $\bar{S}_1^3$ is slightly penalized for the coarsest mesh

		4 elm.			8 elm.			16 elm.		
	L/h	$\bar{S}_0^2$	S_0^4	ANS	$\bar{S}_0^2$	S_0^4	ANS	$\bar{S}_0^2$	S_0^4	ANS
C^1	10^2	0,767	0,610	0,873	0,981	0,896	0,982	0,992	0,983	0,993
	10^3	0,343	0,164	0,661	0,952	0,385	0,835	0,972	0,722	0,961
	L/h	$\bar{S}_1^3$	S_1^4	S_1^6	$\bar{S}_1^3$	S_1^4	S_1^6	$\bar{S}_1^3$	S_1^4	S_1^6
C^2	10^2	0,977	0,992	0,961	0,999	1,000	0,998	1,000	1,000	1,000
	10^3	0,941	0,988	0,797	0,998	0,990	0,946	1,000	1,000	0,997

Table 6.1: Cantilever-beam: normalized end displacement at $\lambda/\lambda_{max} = 1$ for different interpolations and slenderness.

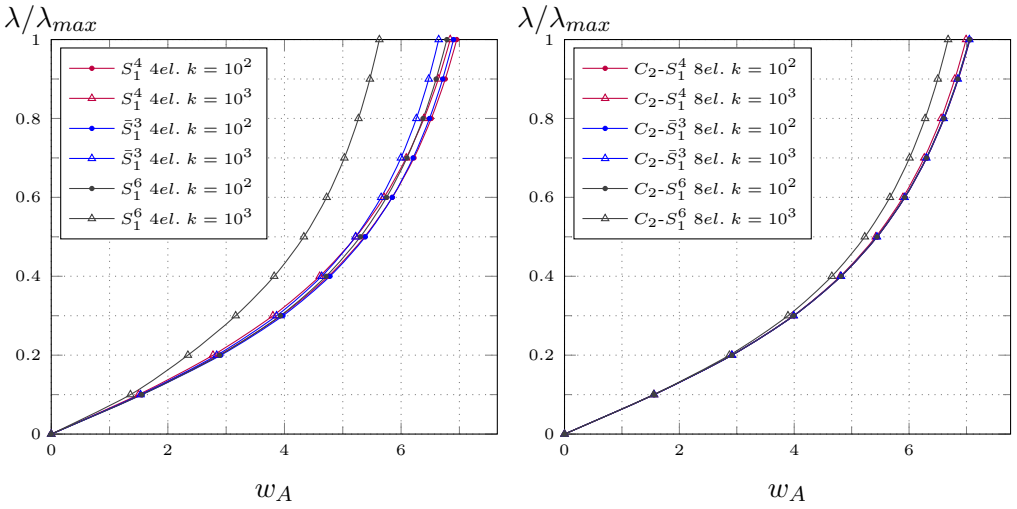

Figure 6.6: Cantilever beam under shear force: equilibrium path for C^2 and 4 e 8 elements.

due to the over integration required to avoid singularities.

In Tab.6.1 the results previously described are summarized reporting the value of the end beam displacement w_A corresponding to a unitary load normalized with respect to the reference values w_A^{ref} obtained with C^2 interpolation, 32 elements and a S_1^4 integration. The table makes the comparison of the different strategies easy and highlights the great accuracy and insensitivity to locking of the C^2 interpolation when integrated with $\bar{S}_1^3$ and S_1^4 schemes and the enormous qualitative leap when passing from C^1 to C^2. Since the number of DOFs of the C^1 and the C^2 interpolation as well as the number of integration points, using the same mesh, is almost the same, the cost of the C^2 interpolation is just slightly higher than the C^1 one.

The second test regards the same cantilever beam under compression, i.e. a standard Euler cantilever beam. A very small shear imperfection load is added

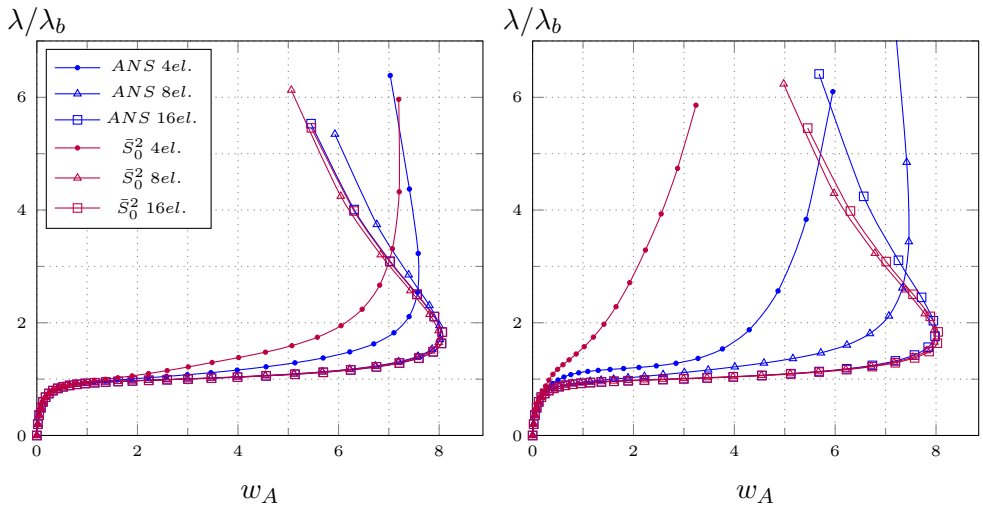

Figure 6.7: Euler beam under compression force: equilibrium path for C^1 and $L/h = 100$ (left) and $L/h = 1000$ (right).

to avoid the jump of the bifurcation. The equilibrium path for different discretisations, integration schemes and slenderness ratios are reported in Fig.6.7 for the C^1 interpolation and in Fig.6.8 for the C^2 one. The load factor is normalized with respect to analytical buckling load λ_b. Similar comments to the previous test hold. In particular, the reduced integration schemes $\bar{S}_0^2$ for C^1 and $\bar{S}_1^3$ and S_1^4 for C^2 provide good predictions. However, as in the previous load case only the C^2 interpolation with S_1^4 integration is practically insensitive to k even for a very coarse mesh, where, conversely, the over-integrated schemes are penalized. Finally, the C^2 interpolation outperforms the C^1 one again in terms of accuracy, using the same mesh, and then employing a similar number of DOFs and integration points.

Generally, the C^2 interpolation seems preferable to the C^1 due to the possibility of also using coarse meshes, especially when integrated with the S_1^4 scheme, which is insensitive to locking also for very slender structures and seems a more robust choice with respect to the $\bar{S}_1^3$ scheme. For these reasons, it is recommended among the strategies investigated. Other numerical tests will be presented in the next section to further validate this proposal.

6.3.4 The iterative scheme with mixed integration points

The isogeometric solid-shell model proposed in section 6.2 with the patch-wise reduced integration described in subsection 6.3.3 is very accurate and efficient and represents a reliable choice from the point of view of the discrete approximation and the efficiency of the integration. However, the efficiency and the robustness of a nonlinear analysis do not only depend on the number of unknowns and integration points, but also on the iterative effort, that is on the capability of the Newton

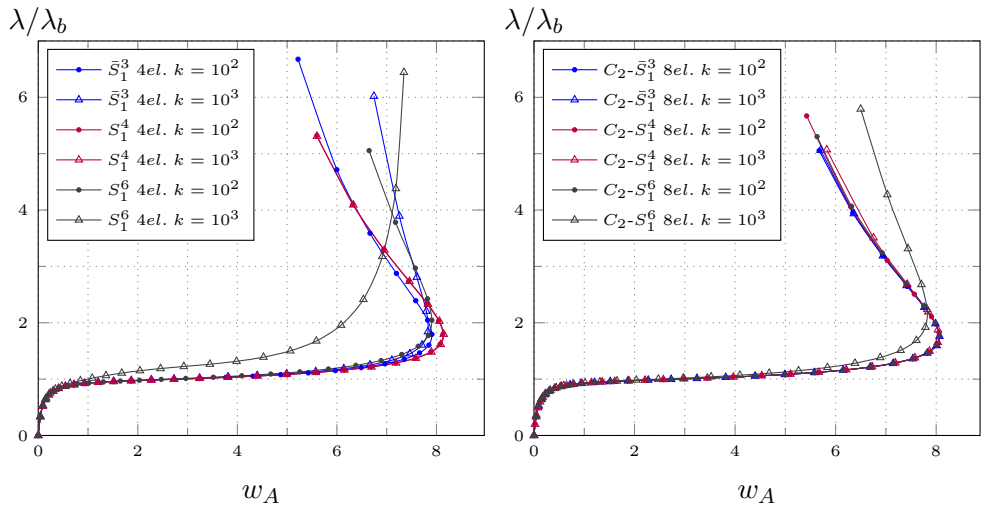

Figure 6.8: Euler beam under shear force: equilibrium path for C^2 and 4 e 8 elements.

method to converge using a low number of iterations and to withstand large step sizes (increments). In [32, 49], it is shown that the Newton method exhibits a slow convergence and requires a small step size for slender elastic structures undergoing large displacements when any purely displacement-based formulation is adopted. This could be considered as a sort of "locking" of the Newton method, since its performance gets worse when the slenderness of the structures increases. This fact is unrelated to the accuracy of the interpolation and always occurs in displacement formulations where the stresses $\boldsymbol{\sigma}_g[\mathbf{d}_e]$, used to evaluate the tangent matrix $\mathbf{K}_e[\boldsymbol{\sigma}_g[\mathbf{d}_e], \mathbf{d}_e]$, are forced to satisfy the constitutive equations at each iteration.

Conversely, mixed (stress-displacement) formulations are not affected by this phenomenon, because the stresses are directly extrapolated and corrected in the iterative process, allowing a faster convergence of the Newton method and very large steps, independently of the slenderness of the structure. Further details on this phenomenon can be found in [32, 49].

In [70], a strategy called Mixed Integration Point (MIP) has been proposed in order to overcome these limitations in standard displacement-based FE problems. The approach, however, seems general and it is now extended and tested in the proposed displacement-based isogeometric formulation.

The fundamental idea of the MIP Newton scheme is to relax the constitutive equations at the level of each integration point during the iterations. This is made

by rewriting the total energy in a pseudo Hellinger-Reissner form on the element

$$\Pi_e[\mathbf{u}_e] \equiv \Phi_e[\mathbf{u}_e] - \mathbf{d}_e^T \boldsymbol{f}_e \quad \text{with} \quad \mathbf{u}_e = \begin{bmatrix} \boldsymbol{\sigma}_1 \\ \vdots \\ \boldsymbol{\sigma}_n \\ \mathbf{d}_e \end{bmatrix} \tag{6.40}$$

where $\boldsymbol{f}_e$ is the element counterpart of the load vector $\boldsymbol{f}$ and the pseudo "mixed" strain energy $\Phi_e[\mathbf{u}_e]$ is obtained by rewriting Eq.(6.37) as

$$\Phi_e[\mathbf{u}_e] \equiv \sum_{g=1}^{n} \left(\boldsymbol{\sigma}_g^T \boldsymbol{\varepsilon}_g[\mathbf{d}_e] - \frac{1}{2} \boldsymbol{\sigma}_g^T \mathbf{C}_g^{-1} \boldsymbol{\sigma}_g \right) w_g \tag{6.41}$$

in which the stresses at each integration point $\boldsymbol{\sigma}_g$ are now independent variables.

The first variation of (6.41) is

$$\Phi'_e \delta u = \sum_{g=1}^{n} \begin{bmatrix} \delta\boldsymbol{\sigma}_g \\ \delta\mathbf{d}_e \end{bmatrix}^T \begin{bmatrix} \mathbf{s}_{g\sigma} \\ \mathbf{s}_{gd} \end{bmatrix} w_g \tag{6.42}$$

with

$$\begin{cases} \mathbf{s}_{g\sigma} \equiv \boldsymbol{\varepsilon}_g[\mathbf{d}_e] - \mathbf{C}_g^{-1} \boldsymbol{\sigma}_g \\ \mathbf{s}_{gd} \equiv \mathbf{B}_g[\mathbf{d}_e]^T \boldsymbol{\sigma}_g. \end{cases} \tag{6.43}$$

The second variation of (6.40) and (6.41) is

$$\Phi''_e \delta u \tilde{u} = \sum_{g=1}^{n} \begin{bmatrix} \delta\boldsymbol{\sigma}_g \\ \delta\mathbf{d}_e \end{bmatrix}^T \begin{bmatrix} -\mathbf{C}_g^{-1} & \mathbf{B}_g \\ \mathbf{B}_g^T & \boldsymbol{\mathcal{G}}_g \end{bmatrix} \begin{bmatrix} \tilde{\boldsymbol{\sigma}}_g \\ \tilde{\mathbf{d}}_e \end{bmatrix} w_g \tag{6.44}$$

where $\boldsymbol{\mathcal{G}}_g \equiv \boldsymbol{\mathcal{G}}_e[\boldsymbol{\sigma}_g]$ is the matrix $\boldsymbol{\mathcal{G}}_e$ evaluated at the integration point g, that is now a function of the independent stresses $\boldsymbol{\sigma}_g$ only.

The linear system in Eq.(6.31), to be solved at each Newton iteration, can then be rewritten at the element level as

$$\begin{bmatrix} -\mathbf{C}_1^{-1} w_1 & & & \mathbf{B}_1 w_1 \\ & \ddots & & \vdots \\ & & -\mathbf{C}_n^{-1} w_n & \mathbf{B}_n w_n \\ \mathbf{B}_1^T w_1 & \dots & \mathbf{B}_n^T w_n & \sum_g^n \boldsymbol{\mathcal{G}}_g w_g \end{bmatrix}^j \begin{bmatrix} \dot{\boldsymbol{\sigma}}_1 \\ \vdots \\ \dot{\boldsymbol{\sigma}}_n \\ \dot{\mathbf{d}}_e \end{bmatrix} = (\lambda^j + \dot{\lambda}) \begin{bmatrix} \mathbf{0} \\ \vdots \\ \mathbf{0} \\ \boldsymbol{f}_e \end{bmatrix} - \begin{bmatrix} \mathbf{s}_{1\sigma} w_1 \\ \vdots \\ \mathbf{s}_{n\sigma} w_n \\ \sum_g^n \left(\mathbf{B}_g^T \boldsymbol{\sigma}_g w_g \right) \end{bmatrix}^j \tag{6.45}$$

where the superscript on matrices denotes that they are evaluated during the iterative process at the current estimate $\mathbf{u}_e^j$.

By performing a static condensation of the stress correction $\dot{\boldsymbol{\sigma}}_g$, locally defined at the level of the integration point, we obtain

$$\dot{\boldsymbol{\sigma}}_g = \mathbf{C}_g \mathbf{B}_g^j \dot{\mathbf{d}}_e + \mathbf{C}_g \mathbf{s}_{g\sigma}^j = \mathbf{C}_g \mathbf{B}_g^j \dot{\mathbf{d}}_e + \mathbf{C}_g \boldsymbol{\varepsilon}_g^j - \boldsymbol{\sigma}_g^j \tag{6.46}$$

and, letting $\mathbf{r}_{ce}[\mathbf{d}_e^j] = \mathbf{s}_{ce}[\mathbf{d}_e^j] - \lambda^j \mathbf{p}_e$, the linear system in the condensed form becomes

$$\mathbf{K}_e[\mathbf{u}_e^j]\dot{\mathbf{d}}_e = -\mathbf{r}_{ce}[\mathbf{d}_e^j] + \dot{\lambda}\boldsymbol{f}_e \tag{6.47}$$

with

$$\mathbf{K}_e[\boldsymbol{\sigma}_g^j, \mathbf{d}_e^j] = \sum_{g=1}^{n} \left(\mathbf{B}_g[\mathbf{d}_e^j]^T \mathbf{C}_g \mathbf{B}_g[\mathbf{d}_e^j] + \boldsymbol{\mathcal{G}}_g[\boldsymbol{\sigma}_g^j] \right) w_g \tag{6.48}$$

the condensed tangent stiffness matrix, that has the same expression as the classical displacement based one (6.39). However, this time it also depends on the independent stresses at the integration points, which are now directly extrapolated and corrected during the iterations.

Conversely, note that the condensed internal forces $\mathbf{s}_{ce}[\mathbf{d}_e^j]$

$$\mathbf{s}_{ce}[\mathbf{d}_e^j] = \sum_{g}^{n} \left(\mathbf{B}_g^{j\,T} \mathbf{C}_g \boldsymbol{\varepsilon}_g^j \right) w_g$$

coincide exactly with the internal forces of the displacement-based formulation in Eq.(6.38) and then the equilibrium path reconstructed is exactly the same as the initial displacement formulation.

This iterative scheme is then very close to the standard Newton one for purely displacement models. The main difference consists of the different value of the stresses at the integration points used for the evaluation of the tangent stiffness matrix. This means that the computational cost of a MIP iteration is practically the same as a standard one and only a few changes are required to transform a standard displacement-based Newton iteration into a MIP one.

It is worth noting that the MIP strategy, compared to the mixed formulation, does not require the definition of shape functions for the stresses and does not modify the expression of the condensed internal force vector and tangent matrix, preserving the sparsity of the initial displacement formulation and making the static condensation inexpensive.

The MIP modified Newton

The modified Newton method evaluates and decomposes the iteration matrix at the first extrapolation (predictor) of each step and represents an attractive choice in IGA much more than in low order FE formulations for two reasons. The first one is that the number of stiffness matrix evaluations, which involve integration and assembly, is much lower and, in IGA, this represents a significant part of the cost of the analysis. The second reason is that the ratio between the cost of an iteration performed with a new matrix and its cost using an already decomposed one is directly proportional to the band. This means that the modified Newton gets more and more convenient as the order of the NURBS, and then the band of the matrix, increases.

	Newton			MIP Newton			MIP M. Newton		
		k			k			k	
N_{steps}	10^2	10^3	10^4	10^2	10^3	10^4	10^2	10^3	10^4
1	14	fails	fails	5	5	5	15	15	15
5	43	fails	fails	16	16	16	21	21	21
10	62	77	fails	30	30	30	32	32	32
20	103	121	fails	51	51	51	51	51	51

Table 6.2: Cantilever beam under shear force ($C^2-S_1^4$, $L/t = 10^2$, 10^3, 10^4): total number of iterations for the evaluation of the equilibrium path vs the number of load subdivisions.

MIP Newton convergence tests

To highlight the robustness and the efficiency of the proposed MIP strategy, the equilibrium path of the example in Fig.6.6 has been reconstructed using a load-controlled scheme. The maximum load value has been subdivided in $Nsteps$ equal load increments. The total number of iterations required to evaluate the equilibrium path with different strategies, but under the same convergence criteria, are reported in Tab.6.2.

The performances of the standard Newton method clearly depend on the slenderness of the beam. In particular, its robustness, in terms of increment size worsens when the ratio $k = L/t$ increases and the method is not able to converge for $k = 10^4$ and requires 10 increments to converge for $k = 10^3$. Conversely, the MIP Newton is able to evaluate the equilibrium point corresponding to $\lambda = \lambda_{max}$ with just a single load increment and only 5 iterations. When the number of load steps $Nsteps$ increases, the number of iterations per step gets smaller, but the total number of iterations increases. However, even for the smallest step size the MIP Newton is more than twice as efficient as the standard Newton. Finally, even the modified MIP Newton withstands the largest step size and requires a number of iterations tending towards that of the full MIP Newton when the step size decreases. In this way the modified method represents a very good choice, considering that its computational cost is dominated by the number of matrix decompositions and so of increments, not of iterations. Finally, it is interesting to note that the performances of both the full and the modified MIP Newton are unrelated to the slenderness k and, in our opinion, this represents the main advantage of the MIP strategy.

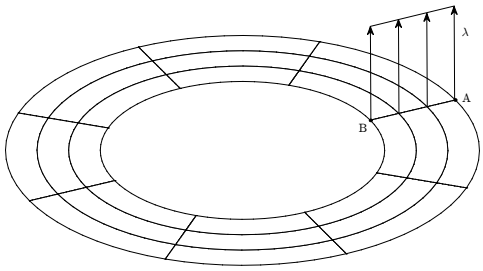

inner radius	6
external radius	10
thickness	0.03
E	$21 \cdot 10^6$
ν	0.0

Figure 6.9: Circular ring: geometry

6.4 Numerical results

In this section, the accuracy of the proposed isogeomentric solid-shell model with C^2 interpolation and S_1^4 patch-wise integration, labelled as C^2-S_1^4, is tested as well as the performances of the MIP strategy. Geometrically nonlinear problems are considered for shell structures in both isotropic and composite multi-layered materials. Some comparisons with FE results are reported. In particular we adopt the well-established hybrid stress linear FE of Sze [10] in the implementation proposed in [59], based on the Green-Lagrange strains, in order to avoid differences due to the strain measure. It is labelled as C^0-HS.

6.4.1 Slit annular plate subjected to line force

The first test is a circular ring undergoing large displacements, a very popular benchmark in geometrically nonlinear analysis [10, 103]. Geometry, load and boundary conditions are reported in Fig.6.9. Figure 6.11 shows the equilibrium path of the ring obtained using C^0-HS and C^2-S_1^4. Three meshes are considered for C^0-HS: 10×6 (420 DOFs), 20×6 (840 DOFs) and 30×6 (1260 DOFs) elements. The FE needs the finest mesh to obtain a converged curve, while C^2-S_1^4 provides the same curve with a mesh of 8×3 (576 DOFs). This is mainly due to an exact description of the circular geometry provided by the isogeometric formulation regardless of the mesh adopted. Conversely, the C^0-HS, in the case of curved shell, suffers when coarse meshes are employed, because of the linearised geometry. Observing the equilibrium path in Fig.6.11, obtained using a load-controlled scheme, as well as the evolution of the deformed configuration depicted in Fig.6.10, this nonlinear problem seems easy to solve. However, if we look at Tab.6.3, reporting the total number of iterations vs the number of equal load increments $Nsteps$ used to reach the maximum load value, it is clear that the standard full Newton method is unable to converge unless a large number of load subdivisions is employed. On the other hand, the MIP Newton easily converges even if the maximum load is reached using just one step. The MIP modified Newton fails for the largest step size, but is much more robust than the standard

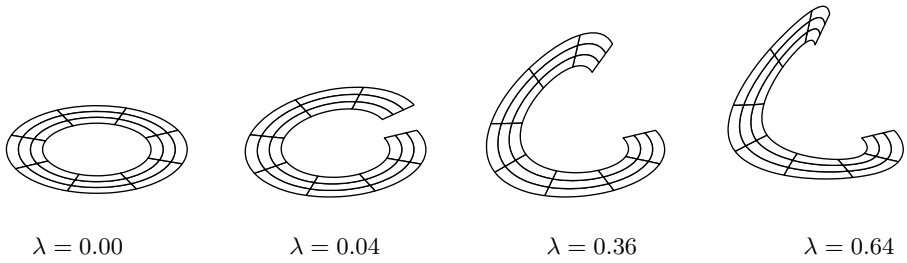

$\lambda = 0.00$ $\lambda = 0.04$ $\lambda = 0.36$ $\lambda = 0.64$

Figure 6.10: Circular ring: evolution of the deformed shape.

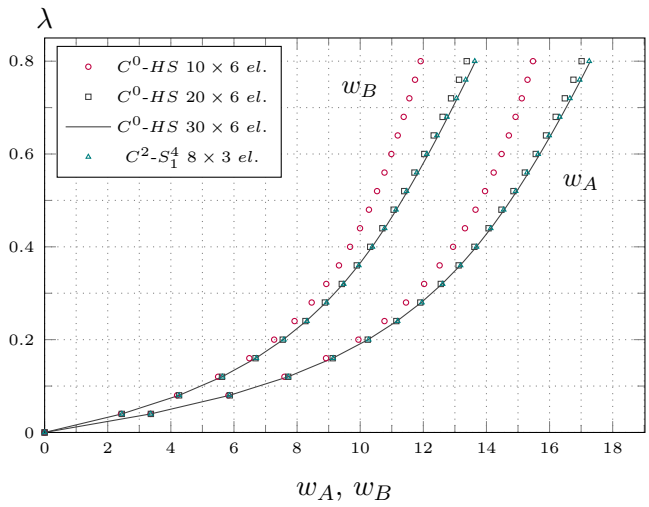

Figure 6.11: Circular ring: equilibrium path.

	Newton	MIP Newton	MIP M. Newton
Nsteps	iters	iters	iters
1	fails	8	fails
5	fails	19	47
10	fails	33	41
20	fails	55	60
30	202	73	74

Table 6.3: Slit annular plate: total number of iterations for the evaluation of the equilibrium path vs the number of load subdivisions.

full Newton. Furthermore, when *Nsteps* increases, the total number of iterations of the MIP modified Newton is practically the same as the standard Newton and, so, the modified version actually becomes the most convenient. Finally, even for the largest value of *Nsteps* the MIP Newton is about three times more efficient than the standard Newton.

6.4.2 The pinched cylinder

Another interesting test regarding large deformations is the pinched cylinder depicted in Fig.6.12, that has been studied by several authors [10, 106]. Exploiting the problem symmetries only an eighth of the cylinder is analysed using C^2-S_1^4 and C^0-HS. The equilibrium path of the cylinder is reported in Fig.6.13. Three uniform meshes are considered for C^2-S_1^4. The coarsest one 30×30 (6208 DOFs) already furnishes a good curve, which, however, is not smooth but exhibits fluctuations. This phenomenon is already known in literature in both the FE [116] and IGA [106] context when coarse meshes are employed. It is due to wrinkles developing and moving during the loading process, as can be noted looking at the evolution of the deformed configuration in Fig.6.14. The second mesh adopted for C^2-S_1^4 is 40×40 (10668 DOFs), which provides a smoother curve that is practically coincident with that provided by the 50×50 mesh (16328 DOFs). Finally the C^0-HS results obtained with two meshes is also reported. The 40×40 mesh (9680 DOFs) gives a good prediction but presents a clear discretisation error, which slowly decreases by refining the mesh. In fact, the curve given by the 75×75 mesh (33900 DOFs) tends towards the isogeometric curve. Again, as in the previous test, C^2-S_1^4 converges quickly to the most likely solution because of the exact geometry, while C^0-HS is probably penalized by the linearised representation of the curved geometry.

The equilibrium path is obtained using an arc-length path-following analysis with the Riks constraint and an adaptive step size. The total number of steps and iterations required by the different iterative strategies are illustrated in Tab.6.4. The elapsed time, normalized with respect to that required by the standard Newton strategy, is also reported. Even in this test, the MIP Newton outperforms

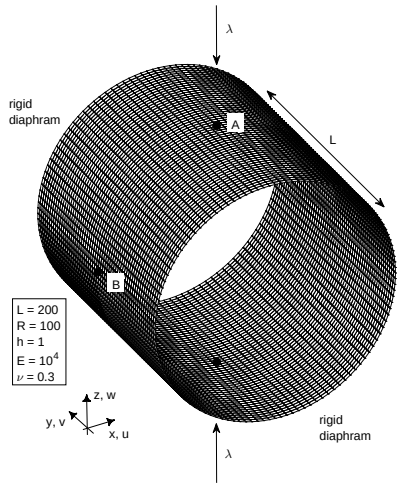

Figure 6.12: The pinched cylinder: geometry

	Newton		MIP Newton			MIP M. Newton		
mesh	steps	iters	steps	iters	elapsed time*	steps	iters	elapsed time*
50×50	127	507	61	235	0.47	89	352	0.24

∗ normalized with respect to Newton elapsed time.

Table 6.4: The pinched cylinder: total number of steps, iterations and normalized elapsed time for the evaluation of the equilibrium path with C^2-S_1^4.

the standard Newton, particularly in the modified version that is clearly the most efficient choice.

6.4.3 Clamped semi-cylinder

While the results presented so far regard isotropic materials, this benchmark tests the proposed solid-shell model and the MIP Newton in the case of a composite multi-layered shell. The structure is a semi-cylinder loaded by a concentrated force at the middle of one of the curved edges, while the other one is clamped. The vertical displacement of the straight edges is constrained. In Fig.6.16, the geometry and the boundary conditions are depicted. Due to its symmetry, only a half of the structure is analyzed. Two cases are considered: isotropic material, characterized by $E = 2068.50$ and $\nu = 0.3$, and a composite multi-layered material. The local reference system, used for defining the material proprieties, has the direction 1 aligned with the y of the global system and the direction 3 is the normal to the surface from inside out. The stacking sequences of the laminated material are [90/0/90] and [0/90/0], measured with respect to the direction 1 of the local ref-

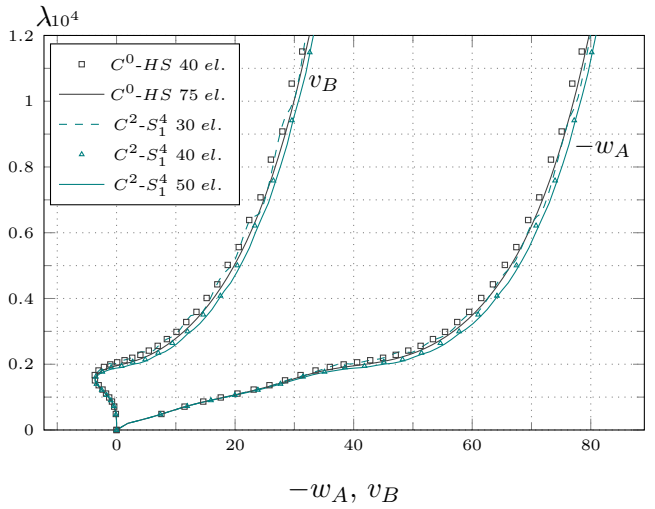

Figure 6.13: Pinched cylinder: equilibrium path.

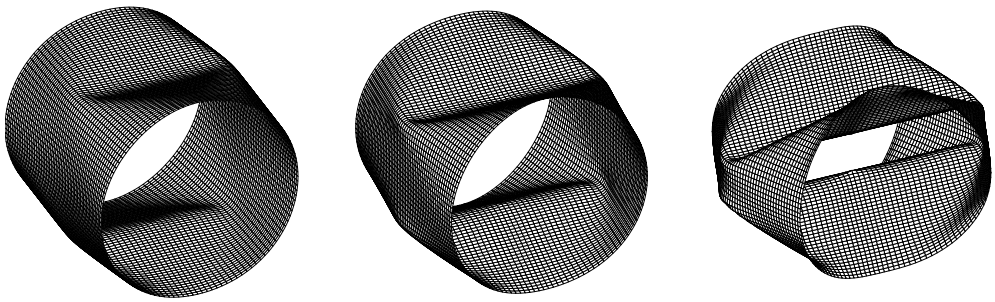

$\lambda = 1334$ $\lambda = 2243$ $\lambda = 12434$

Figure 6.14: Pinched cylinder: evolution of the deformed configuration.

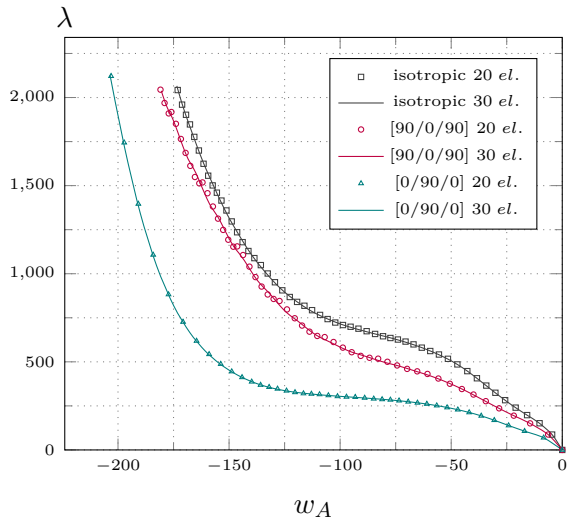

Figure 6.15: Clamped semi-cilinder: equilibrium paths with element C^2-S_1^4 for different meshes and layups.

erence system and the material properties are $E_1 = 2068.50$, $E_2 = E_3 = 517.125$, $\nu_{12} = \nu_{23} = \nu_{13} = 0.3$ and $G_{12} = G_{23} = G_{13} = 759.58$. Figure 6.15 shows the equilibrium paths obtained using the element C^2-S_1^4 and for the different material cases analysed. Two uniform meshes of 20×20 elements (2948 DOFs) and 30×30 elements (6208 DOFs) are used. The results of the coarse mesh are practically identical to those obtained with the finer one, except for the case [90/0/90] which exhibits small fluctuations, similar to the previously analysed pinched cylinder, which disappear when the finer mesh is employed. This behaviour is again related to the development of wrinkles as can be observed in the deformed shape at the last evaluated equilibrium point, pictured in Fig.6.16. The results, in both the isotropic and composite cases, can be compared with the solutions obtained by Abaqus, reported in [117], which are the same as the present ones. Also in this benchmark the robustness of the MIP strategy is evident. Table 6.5 shows how the MIP strategy drastically reduces the number of iterations required to trace the equilibrium path and how the MIP modified Newton is the most convenient choice in terms of computational time.

Lastly, Fig.6.17 shows two significant generalized stress components evaluated with a mesh of 30×30 C^2-S_1^4 elements (6208 DOFs) compared with a reference solution obtained with C^0-HS and a mesh of 60×60 elements (21720 DOFs). The concentrated force causes a singularity in the 3D continuum model. The maximum value of the colour map of $\mathcal{N}_1$ is then limited to make the comparison clearer over the structure by leaving the singular values just under the force out, which are also mesh-dependent.

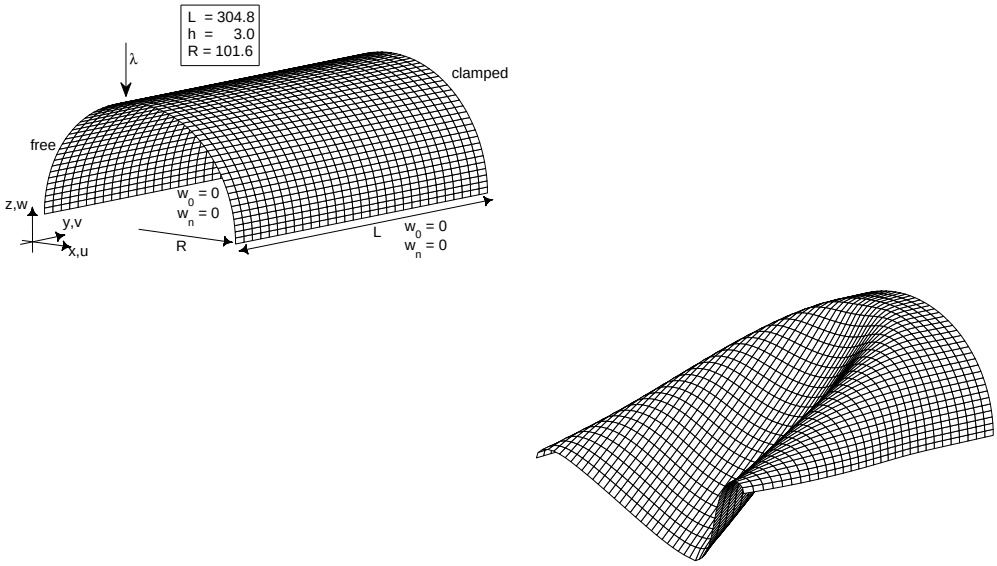

Figure 6.16: Clamped semi-cylinder: geometry and deformed configuration at the last evaluated equilibrium point for [90/0/90] .

	Newton		MIP Newton			MIP M. Newton		
layup	steps	iters	steps	iters	elapsed time*	steps	iters	elapsed time*
isotropic	95	382	37	138	0.36	55	216	0.20
[0/90/0]	64	253	32	113	0.44	51	195	0.27
[90/0/90]	92	380	36	142	0.37	62	255	0.23

$*$ normalized with respect to Newton elapsed time.

Table 6.5: Clamped semi-cylinder: total number of steps and iterations for the evaluation of the equilibrium path using 30×30 C^2-S_1^4 elements.

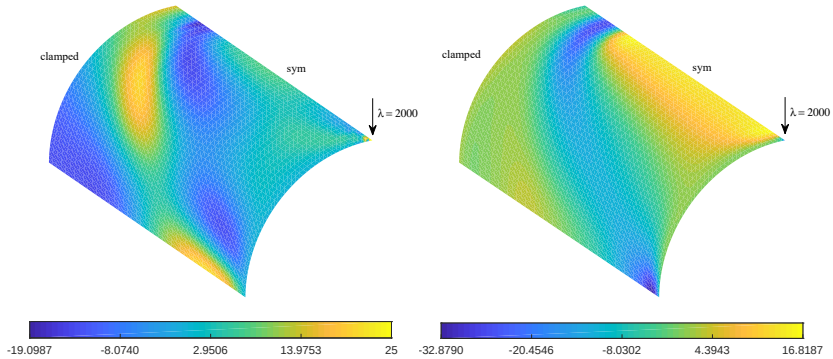

$\mathcal{N}_1$, C^2-S_1^4 30×30 elements $\mathcal{M}_1$, C^2-S_1^4 30×30 elements

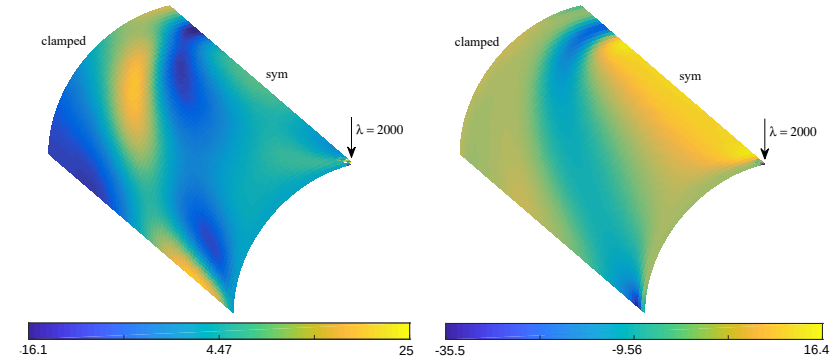

$\mathcal{N}_1$, C^0-HS 60×60 elements $\mathcal{M}_1$, C^0-HS 60×60 elements

Figure 6.17: Clamped semi-cylinder: generalized stresses at $\lambda = 2000$, layup [0/90/0].

6.5 Summary

In this chapter, an isogeometric solid-shell formulation for geometrically nonlinear analyses has been proposed. A linear through-the-thickness interpolation has been adopted for the geometry and the displacement field. This allows the solid model to be rewritten in a bidimensional way in terms of middle surface quantities, semi-sum and semi-difference of the top and bottom surface ones. These are interpolated using 2D NURBS shape functions with each control point equipped with six DOFs, as in standard shell models but without employing rotational DOFs. Multi-patch structures can be easily modeled because only C^0 continuity is required by the continuum model. A Total Lagrangian description is used exploiting the Green-Lagrange strain measure, which is linearized through the thickness of the shell in order to define the generalized quantities. This allows the use of a modified generalized constitutive matrix which prevents thickness locking and produces accurate results for multi-layered composites without introducing any additional DOF. A series of patch-wise integrations for C^1 and C^2 NURBS have been investigated in large deformation problems, in order to obtain an optimal solution in terms of accuracy, efficiency and robustness. The C^2-S_1^4 formulation has proved to be the best choice among those analyzed, being practically immune to locking and also accurate for very coarse meshes and thin shells. With respect to a mixed formulation with continuous stress shape functions, the proposal seems more attractive because it preserves the stiffness matrix sparsity, does not require any additional DOF, and just 2.25 integration points per element are needed. However the proposed displacement-based model, like any displacement formulation, is plagued, in geometrically nonlinear analyses, by a slow convergence of the Newton method used in reconstructing the equilibrium path. To avoid this drawback a Mixed Integration Point strategy has been adopted, which gives superior performances with respect to the standard Newton. In particular, MIP allows very large steps without any loss in convergence and makes it possible to reduce the iterative effort. It has been shown that the main feature of the MIP strategy is its insensitivity to the slenderness of the structure which, on the contrary, heavily affects the performance of the displacement formulation. This strategy is so robust that a modified version of the iterative method, which evaluates and decomposes the stiffness matrix only at the first iteration of each step, can be conveniently adopted. The proposed formulation is characterized by a high efficiency from the point of view of the discrete approximation, the numerical integration and the iterative effort, which are all crucial in geometrically nonlinear analyses. Interested readers can find further details in [118]. As future work, it would be interesting to extend the proposal to nonlinear dynamics, where the MIP strategy is expected to have the same impact on the efficiency as that demonstrated in the quasi-static case. In this context, an appropriate selection of the integration scheme for the mass matrix should be investigated.

Chapter 7

An isogeometric formulation of the Koiter's theory for buckling and initial post-buckling analysis of composite shells

Abstract

Numerical formulations of the Koiter theory allow the efficient prediction, through a reduced model, of the behaviour of shell structures when failure is dominated by buckling. In this work, an isogeometric version of the Koiter method is proposed, exploiting the NURBS-based solid-shell model derived in the previous chapter to accurately describe the geometry and the high continuity typical of the displacement field in buckling problems and to directly link the CAD model to the structural one. A linear interpolation is then adopted through the thickness together with a modified generalized constitutive matrix, which allows us to easily eliminate thickness locking and model multi-layered composites. Reduced integration schemes, which take into account the continuity of the shape functions, are used to avoid interpolation locking and make the integration faster. A Mixed Integration Point strategy makes it possible to transform the displacement model into a mixed (stress-displacement) one, required by the Koiter method to obtain accurate predictions, without introducing stress interpolation functions. The result is an efficient numerical tool for buckling and initial post-buckling analysis of composite shells, characterized by a low number of DOFs and integration points and by a simple and quick construction of the reduced model.

7.1 Introduction

Composite shells are nowadays employed as primary structural elements in a very wide range of applications. Their success is mainly due to the high strength/weight ratio that is crucial for lightweight structures. The failure of such elements often occurs because of buckling phenomena which make them sensitive to material, geometrical and load imperfections [5]. Thousands of equilibrium path evaluations can be required in order to detect the worst imperfection case in terms of failure load. Once discretisation techniques are applied to the continuum problem, the arc-length nonlinear analysis is the standard approach for solving the discrete nonlinear equations, where the unknowns are the discrete degrees of freedom (DOFs) and the load factor, and reconstructing the equilibrium path of such structures. Although this method easily provides the desired information for assigned data, it is too time consuming [57] and inappropriate for an imperfection sensitivity analysis with current CPUs when fine meshes are needed. Furthermore, the stacking sequence has proven to strongly affect the buckling and post-buckling response of the shells [4, 60, 1] and the design of an optimal layup can significantly increase the load-carrying capability. Consequently, the need for an optimization process leads to a further computational burden and requires more efficient tools of analysis and design.

For these reasons, a great amount of research has focused on developing reduced order models (ROMs) based on the finite element (FE) implementation [38, 58, 41, 42, 43, 44, 45, 59, 49, 62, 63, 64, 66] of the Koiter theory of elastic stability [7]. This numerical strategy, known as Koiter method and initially proposed in [67, 48], is capable of furnishing, with an acceptable computational cost, an accurate prediction of the limit load value and the initial post-critical behaviour for a very large number of imperfections. From this perspective it seems to be more effective in the design stage of slender structures.

The ROM consists in approximating the unknown fields using the initial path tangent and restricted number m of buckling modes associated to the first buckling loads and the corresponding quadratic correctives. In this way, the response of the structure is defined by a reduced system of nonlinear equations where the unknowns are the load factor and m modal amplitudes and the coefficients correspond to 2nd, 3rd and 4th order energy variations. The most convenient aspect of the method is that the effects of geometrical imperfections can be included a posteriori in the reduced system of the perfect structure. A very large number of imperfections can be considered in this way, since each of them only requires the solution of the reduced system, with a very low computational cost (usually fractions of seconds).

The global operations, which involve the total number of DOFs, are limited to the construction of the ROM of the perfect structure and are comparable to those required by a linearised buckling analysis. However, optimization processes of geometry and layup strongly modify the structural behaviour and require rep-

etition many times. In this case, the total computational cost is highly dependent on the discretisation. A solid-shell FE model [16, 11, 19, 12, 13] proves to be particularly convenient for the construction of the ROM, since it allows us to avoid the use of finite rotations, typical of other exact [14] or co-rotational [34] shell models, which make the evaluation of the high order strain energy variations complex and expensive. Although a large number of locking free linear solid-shell elements are available, their behaviour is not sufficiently accurate when modelling curved geometry and, as a consequence, a fine discretisation is required. On the other hand, increasing the interpolation order drastically reduces the computational convenience of the element because of the high number of DOFs and the time consuming integration and assembly of the quantities [30].

An interesting alternative is given by the isogeometric analysis (IGA) [9, 100] based on NURBS shape functions. In contrast to Lagrangian functions, their most attractive feature is the possibility of elevating the order of the interpolation with no practical change in the number of DOFs. The cost for the integration of the quantities is also kept quite low because the high continuity of the shape functions allows us to reduce the total number of integration points [101, 102]. Other important features are the exact reproduction of the geometry regardless of the mesh adopted and the possibility of a simple link between the CAD model and structural analysis. These aspects make IGA very attractive in particular in buckling problems, where a highly continuous solution is often expected.

Despite the many advantages, some difficulties have to be overcome. Although the use of very high order shape functions eliminates interpolation lockings, it increases the computational efforts for the integration and the assembly of the discrete quantities. Also the solution of the discrete problem becomes slower because the stiffness matrix sparsity decreases. For these reasons C^1 and C^2 NURBS interpolations are often preferred, even though they exhibit locking phenomena. The inter-element high continuity of the interpolation makes it no longer possible to employ element-wise reduced integrations and strategies like Assumed Natural Strain (ANS) [103] effectively; indeed, they only alleviate but do not completely eliminate locking and prove to be an unsuitable choice for very thin shells. This also happens when using mixed formulations with stress shape functions defined at element level.

Conversely, a satisfactory cure for locking is represented by mixed formulations where continuous stress shape functions [104, 105] are assumed. In this case, the total number of DOFs increases with respect to the initial displacement formulation and the static condensation of the stress variables, usually employed in finite element approaches and performed at element level, can only be carried out at patch level leading to a full condensed stiffness matrix. An effective alternative is the use of displacement formulations with patch-wise reduced integration rules [101] which have been shown to alleviate and, in same cases, eliminate lockings in linear elastic problems [102] and at the same time have the additional advantage of reducing the number of integration points. This strategy seems more attractive

than the mixed formulation since it preserves the stiffness matrix sparsity without introducing additional unknowns and allows a more efficient integration.

However, it has been shown in [48, 49] that the Koiter method requires a mixed formulation in order to avoid a locking phenomenon in the evaluation of the fourth-order coefficients of the reduced system of equations and to increase the range of validity of the ROM, which gets worse in displacement formulations when the slenderness of the structure increases [33, 49] and the pre-buckling path exhibits even small nonlinearities. This aspect can also be observed in path-following analyses [49, 10, 70] where displacement formulations lead to a slow convergence rate of the Newton scheme when slender structures are analysed. This is due to the bad estimate of the stresses when evaluated using extrapolated displacements. In Koiter analysis this phenomenon is much more evident because the equilibrium path is directly extrapolated using the ROM, and an equilibrium error is not corrected by an iterative scheme, so affecting the accuracy of the method. On the contrary mixed formulations avoid this drawback because the stresses are directly extrapolated. Furthermore, the joint use of a Green-Lagrange strain measure and of a mixed Hellinger-Reissner variational formulation [59, 49], leads to a $3rd$ order polynomial dependence of the strain energy on the discrete DOFs with the consequence of the zeroing of all the fourth order strain energy variations.

This chapter proposes an isogeometric numerical formulation of the Koiter theory for the analysis of composite shells which based on the solid-shell model described in the previus chapter. To obtain the mixed description of the problem, required by the Koiter formulation, the Mixed Integration Point (MIP) strategy is here extended to the proposed isogeometric Koiter analysis. It consists in relaxing the constitutive equations at each integration point, making it possible to rewrite the strain energy of the model in a pseudo Hellinger-Reissner form. It will be demonstrated that this approach pushes the efficiency of the Koiter analysis to the limit and, at the same time, preserves the accuracy of the ROM without the need for stress shape functions and the previously discussed drawback.

The chapter is organized as follows: Section 2 presents the isogeometric solid-shell model for composite shell structures; Section 3 discusses the buckling and initial post-buckling analysis based on the Koiter method focusing on the patch-wise reduced integration and reformulation of the analysis based on MIP strategy; numerical tests to validate the proposed isogeometric formulation of the Koiter theory for the analysis of common composite structural elements are presented in Section 4; finally the conclusions are reported.

7.2 Koiter IGA based on mixed integration points

When comparing FE formulations of the Koiter theory based on a purely displacement-based formulation and a mixed one, it has been shown in many works (see for

example [49, 59]) that the latter provides a superior performance. In particular, the use of stress and displacement DOFs as independent variables leads to a more efficient construction of the ROM and makes it accurate for a wider range. The improved accuracy is much more evident when the slenderness of the structure gets higher and the pre-critical path presents some nonlinearities. In the IGA context as opposed to FE analysis, however, the use of a mixed formulation is significant. In [115] it has been shown how the stress interpolation produces locking-free solutions only when the shape functions are continuous over the patch of elements. In this way, the total number of unknowns significantly increases due to the extra stress variables, which cannot be condensed at element level as is usual in the FEM context and it is not convenient. In this work, an isogeometric version of the Koiter method is proposed. Some conflicting aspects are evident. A mixed formulation would lead to an accurate Koiter analysis free from locking, but would compromise the overall efficiency because of the extra stress variables. On the other hand, the displacement formulation is plagued by locking and decreases the range of validity of the ROM. Recently, in [102, 101] patch-wise reduced integrations were successfully proposed for eliminating locking in linear analyses with displacement NURBS interpolations. The main idea of this work is to investigate the use of patch-wise reduced integrations to handle interpolation locking in constructing the ROM using the displacement solid-shell model derived in the previous section. The stresses at the integration points are then chosen as independent variables inspired by the mixed integration point (MIP) strategy proposed in [70] for path-following analyses. In this way the accuracy and efficiency of the ROM is preserved avoiding the use of a stress interpolation.

The steps of the Koiter algorithm, described in previous chapters, are now particularized to IGA using the MIP strategy and the patch-wise integration.

7.2.1 The nonlinear model and the numerical integration

We consider a slender hyperelastic structure subject to conservative loads $p[\lambda]$ proportionally increasing with the amplifier factor λ. The equilibrium is expressed by the virtual work equation

$$\Phi[u]'\,\delta u - \lambda \hat{p}\,\delta u = 0 \quad , \quad u \in \mathcal{U}\ ,\ \delta u \in \mathcal{T} \tag{7.1}$$

where $u \in \mathcal{U}$ is the field of configuration variables, $\Phi[u]$ denotes the strain energy, $\mathcal{T}$ is the tangent space of $\mathcal{U}$ at u and a prime is used to express the Frechèt derivative with respect to u. We assume that $\mathcal{U}$ will be a linear manifold so that its tangent space $\mathcal{T}$ will be independent of u. When a mixed format is adopted the configuration variables u collect both displacement and stress fields.

The displacement based IGA formulation previously presented allows us to express the strain energy of the element as a sum of element contributions $\Phi[u] \equiv \sum_e \Phi_e[\mathbf{d}_e]$

$$\Phi_e[\mathbf{d}_e] \equiv \int_{\Omega_e} \left(\frac{1}{2}\boldsymbol{\varepsilon}^T \mathbf{C}_\epsilon \boldsymbol{\varepsilon}\right) d\Omega_e \tag{7.2}$$

where Ω_e is the element domain and a numerical integration is usually adopted.

Locking and patch-wise reduced integrations

Note that the same NURBS interpolation is employed over the middle surface of the shell for all the displacement components. As is well known, this produces interpolation locking when low order interpolations are considered. The linear term in Eq.(6.22) can be plagued by standard shear and membrane locking, which then occurs even in small deformation problems. Furthermore, when a Total Lagrangian formulation is used to describe the nonlinear behaviour a more evident additional locking occurs as consequence of the different approximation of the linear and the quadratic Green-Lagrange strain contributions in Eq.(6.22).

Recently, patch-wise integration rules, which take into account the inter-element high continuity of the displacement interpolation have been proposed [102, 101] and applied to linear elastic problems. In our opinion, these works represent an important development in IGA. The d-dimensional target space of order p and regularity r, labelled as $\mathcal{S}_r^p$, is exactly integrated by a number of $\approx ((p-r)/2)^d$ integration points per element, distributed over the patch, significantly lower than in standard Gauss quadrature rules. Their positions and weights are not equal for each element, but are evaluated, once and for all, in a pre-processing phase and depend on r, p and patch mesh. The algorithms which provide these kinds of integration rules can be found in [102, 101] and are very efficient. Their computational burden is just a small fraction of the total cost of a linear analysis and negligible compared to a nonlinear analysis.

The patch-wise exact integration of a given space $\mathcal{S}_r^p$ also opens up new possibilities for patch-wise reduced integration schemes. In fact p and r can be selected by the user and are not required to be those for the exact integration of the problem space. If the integration space presents spurious modes, a certain number of quadrature points are added near the boundary elements in order to remove them and the approximation space is said to be over-integrated and labelled as $\bar{\mathcal{S}}_r^p$ [102, 101]. With respect to the element-wise reduced integrations, an appropriate selection of the patch-wise reduced integration rules makes it possible to avoid spurious modes, alleviate or eliminate interpolation locking in the linear elastic range and further reduce the number of integration points.

Being that in patch-wise rules the number of integration points n can be different element-by-element, the strain energy can then be evaluated as

$$\Phi_e[\mathbf{d}_e] \equiv \frac{1}{2}\sum_{g=1}^{n} \boldsymbol{\varepsilon}_g[\mathbf{d}_e]^T \mathbf{C}_g \boldsymbol{\varepsilon}_g[\mathbf{d}_e]\; w_g \tag{7.3}$$

where subscript g denotes quantities evaluated at the integration point $[\xi_g, \eta_g]$, w_g is the product of the corresponding weight and the determinant of the Jacobian matrix $\mathbf{J}$ evaluated at the integration point and $\mathbf{C}_g$ is $\mathbf{C}_\epsilon$ at the integration point.

The use of a displacement-based IGA model is then theoretically very accurate and efficient and represents, potentially, a reliable choice from the point of view of the discrete approximation and the efficiency of the integration with respect to standard FE interpolation of the same order if interpolation locking is avoided.

7.2.2 MIP strategy

In Koiter analysis, regardless of the quality of the discrete approximation, a mixed format in stress and displacement is required to achieve accuracy and efficiency.

The fundamental idea of the MIP strategy is to relax the constitutive equations at the level of each integration point. This is made by rewriting the strain energy in a pseudo Hellinger-Reissner form on the element

$$\Phi_e[\mathbf{u}_e] \equiv \sum_{g=1}^{n} \left(\boldsymbol{\sigma}_g^T \boldsymbol{\varepsilon}_g[\mathbf{d}_e] - \frac{1}{2} \boldsymbol{\sigma}_g^T \mathbf{C}_g^{-1} \boldsymbol{\sigma}_g \right) w_g \tag{7.4}$$

where the stresses at each integration point $\boldsymbol{\sigma}_g$ are now independent variables being

$$\mathbf{u}_e = \begin{bmatrix} \boldsymbol{\sigma}_1 \\ \vdots \\ \boldsymbol{\sigma}_n \\ \mathbf{d}_e \end{bmatrix} \tag{7.5}$$

From the stationary condition with respect to $\boldsymbol{\sigma}_g$ we obtain the constitutive law at the integration point g

$$\mathbf{s}_{g\sigma} \equiv \boldsymbol{\varepsilon}_g[\mathbf{d}_e] - \mathbf{C}_g^{-1} \boldsymbol{\sigma}_g \tag{7.6}$$

that, if substituted in Eq.(7.4), again furnishes the displacement formulation in Eq.(7.3). This means that we only change the format, from displacement to mixed, not the discrete approximation of the problem and the true equilibrium path obtained with the two formulations, when a path-following scheme is adopted, is exactly the same as the initial displacement formulation [70].

Another important consequence of the MIP rewriting of the problem equations is that, when a Green-Lagrange strain measure is used as in the present Total Lagrangian solid-shell model, the polynomial dependence of the strain energy on the discrete parameters $\mathbf{u}_e$ in the MIP format is of the 3rd order only, instead of the 4th order of the initial displacement formulation.

7.2.3 The implementation of the Koiter method using mixed integration points

The asymptotic approach is based on a third order Taylor expansion of Eq.(6.26), in terms of load factor λ and modal amplitudes ξ_i.

7.2.4 Strain energy variations using Mixed Integration Points

In the following $\mathbf{u}_{ig} = \{\boldsymbol{\sigma}_{ig}, \mathbf{d}_{ie}\}$ will denote the vector representation on the integration point g of u_i.

The first variation of (7.4) is

$$\Phi'_e u_1 = \sum_{g=1}^{n} \begin{bmatrix} \boldsymbol{\sigma}_{1g} \\ \mathbf{d}_{1e} \end{bmatrix}^T \begin{bmatrix} \mathbf{s}_{g\sigma} \\ \mathbf{s}_{gd} \end{bmatrix} w_g \tag{7.7a}$$

with

$$\begin{cases} \mathbf{s}_{g\sigma} \equiv \boldsymbol{\varepsilon}_g[\mathbf{d}_e] - \mathbf{C}_g^{-1}\boldsymbol{\sigma}_g \\ \mathbf{s}_{gd} \equiv \mathbf{B}_g[\mathbf{d}_e]^T \boldsymbol{\sigma}_g. \end{cases} \tag{7.7b}$$

and $\mathbf{B}_g[\mathbf{d}_e] = \mathbf{L}_g + \mathbf{Q}_g[\mathbf{d}_e]$.

The second variation of (7.4) is

$$\Phi''_e u_1 u_2 = \sum_{g=1}^{n} \left\{ \boldsymbol{\sigma}_{1g}^T \mathbf{B}_g[\mathbf{d}_e]\mathbf{d}_{2e} + \boldsymbol{\sigma}_{2g}^T \mathbf{B}_g[\mathbf{d}_e]\mathbf{d}_{1e} + \boldsymbol{\sigma}_g^T \mathbf{Q}_g[\mathbf{d}_{1e}]\mathbf{d}_{2e} \right\} w_g. \tag{7.7c}$$

Letting

$$\varepsilon_{gk}^Q = \mathbf{d}_{1e}^T \boldsymbol{\Psi}_{gk} \mathbf{d}_{2e}.$$

the kth component of vector $\mathbf{Q}_g[\mathbf{d}_{1e}]\mathbf{d}_{2e}$ the following expression holds

$$\boldsymbol{\sigma}_g^T \mathbf{Q}_g[\mathbf{d}_{1e}]\mathbf{d}_{2e} \equiv \sum_k \sigma_{gk}\, \varepsilon_{gk}^Q = \mathbf{d}_{1e}^T \boldsymbol{\mathcal{G}}[\boldsymbol{\sigma}_g]\mathbf{d}_{2e}$$

with

$$\boldsymbol{\mathcal{G}}[\boldsymbol{\sigma}_g] = \sum_k \sigma_{gk} \boldsymbol{\Psi}_{gk}. \tag{7.7d}$$

In matrix form the second variation of (7.4) then becomes

$$\begin{aligned} \Phi''_e u_1 u_2 &= \sum_{g=1}^{n} \begin{bmatrix} \boldsymbol{\sigma}_{1g} \\ \mathbf{d}_{1e} \end{bmatrix}^T \begin{bmatrix} -\mathbf{C}_g^{-1} & \mathbf{B}_g \\ \mathbf{B}_g^T & \boldsymbol{\mathcal{G}}_g \end{bmatrix} \begin{bmatrix} \boldsymbol{\sigma}_{2g} \\ \mathbf{d}_{2e} \end{bmatrix} w_g \\ &= \sum_g \mathbf{u}_{1g}^T \mathbf{K}_g \mathbf{u}_{2g} \end{aligned} \tag{7.7e}$$

where $\boldsymbol{\mathcal{G}}_g \equiv \boldsymbol{\mathcal{G}}_e[\boldsymbol{\sigma}_g]$.

The second variation can also be written in vector form introducing the *incremental force vector* so defined

$$\Phi''_e u_1 u_2 = \sum_g \mathbf{u}_{1g}^T \mathbf{s}'_g[\mathbf{u}_{2g}] \quad \text{with} \quad \mathbf{s}'_g[\mathbf{u}_{2g}] \equiv \begin{bmatrix} -\mathbf{C}_g^{-1}\boldsymbol{\sigma}_{2g} + \mathbf{B}_g \mathbf{d}_{2e} \\ \mathbf{B}_g^T \boldsymbol{\sigma}_{2g} + \boldsymbol{\mathcal{G}}_g \mathbf{d}_{2e} \end{bmatrix} \tag{7.7f}$$

The third variation of the strain energy is

$$\Phi''_e u_1 u_2 u_3 = \sum_{g=1}^{n} \left\{ \boldsymbol{\sigma}_{1g}^T \mathbf{Q}_g[\mathbf{d}_{3e}]\mathbf{d}_{2e} + \boldsymbol{\sigma}_{2g}^T \mathbf{Q}_g[\mathbf{d}_{3e}]\mathbf{d}_{1e} + \boldsymbol{\sigma}_{3g}^T \mathbf{Q}_g[\mathbf{d}_{1e}]\mathbf{d}_{2e} \right\} w_g \quad (7.7g)$$

that can also be written in vector form introducing the *secondary force vector* as

$$\Phi'''_e \delta u_1 \delta u_2 \delta u_3 = \sum_g \mathbf{u}_{1g}^T \mathbf{s}''_g[\mathbf{u}_{2g}, \mathbf{u}_{3g}] \quad \text{with} \quad \mathbf{s}''_g[\mathbf{u}_{2g}, \mathbf{u}_{3g}] \equiv \begin{bmatrix} \mathbf{Q}_g[\mathbf{d}_{3e}]\mathbf{d}_{2e} \\ \mathbf{Q}_g[\mathbf{d}_{3e}]^T \boldsymbol{\sigma}_{2g} + \boldsymbol{\mathcal{G}}_g[\boldsymbol{\sigma}_{3g}]\mathbf{d}_{2e} \end{bmatrix} \quad (7.7h)$$

Note that all fourth order strain energy variations of the initial displacement based formulation are identically zero due to the 3rd order polynomial dependence of the strain energy on the discrete parameters.

Finally, as usual, for each element vector $\mathbf{y}_e$ and matrix $\mathbf{Y}_e$ the global quantities are obtained using standard assemblage operations as

$$\mathbf{y} = \sum_e \boldsymbol{\mathcal{A}}_e^T \mathbf{y}_e, \quad \mathbf{Y} = \sum_e \boldsymbol{\mathcal{A}}_e^T \mathbf{Y}_e \boldsymbol{\mathcal{A}}_e. \quad (7.8)$$

while scalar quantities are simply sums of element contributions.

7.2.5 Solution of the Koiter linear systems and eigenvalue problem in condensed form

Koiter analysis requires the evaluation of a series of linear systems and an eigenvalue problem. Their solution can be obtained by static condensation of the stress variables. This is an important aspect of the proposed IGA MIP formulation which allows us to eliminate them at integration point level, maintaining the computational cost of the displacement one.

Fundamental path

Equation (2.36a) becomes at the element level

$$\begin{bmatrix} -\mathbf{C}_1^{-1} w_1 & & & \mathbf{L}_1 w_1 \\ & \ddots & & \vdots \\ & & -\mathbf{C}_n^{-1} w_n & \mathbf{L}_n w_n \\ \mathbf{L}_1^T w_1 & \dots & \mathbf{L}_n^T w_n & \mathbf{0} \end{bmatrix} \begin{bmatrix} \hat{\boldsymbol{\sigma}}_1 \\ \vdots \\ \hat{\boldsymbol{\sigma}}_n \\ \hat{\mathbf{d}}_e \end{bmatrix} = \begin{bmatrix} \mathbf{0} \\ \vdots \\ \mathbf{0} \\ \boldsymbol{f}_e \end{bmatrix} \quad (7.9)$$

By performing a static condensation of the stress correction $\dot{\boldsymbol{\sigma}}_g$, locally defined at the integration point, we obtain

$$\hat{\boldsymbol{\sigma}}_g = \mathbf{C}_g \mathbf{L}_g \hat{\mathbf{d}}_e \quad (7.10)$$

and then

$$\mathbf{K}_{0e}^c \hat{\mathbf{d}}_e = \boldsymbol{f}_e \quad \text{with} \quad \mathbf{K}_{0e}^c = \sum_{g=1}^{n} \left(\mathbf{L}_g^T \mathbf{C}_g \mathbf{L}_g \right) w_g \quad (7.11)$$

where the condensed element tangent stiffness matrix $\mathbf{K}^c_{0e}$ coincides with the classical displacement-based one

Buckling problem

The buckling problem can be written as

$$\begin{bmatrix} -\mathbf{C}_1^{-1}w_1 & & & (\mathbf{L}_1+\lambda\mathbf{Q}_1[\hat{\mathbf{d}}_e])w_1 \\ & \ddots & & \vdots \\ & & -\mathbf{C}_n^{-1}w_n & (\mathbf{L}_n+\lambda\mathbf{Q}_n[\hat{\mathbf{d}}_e])w_n \\ (\mathbf{L}_1+\lambda\mathbf{Q}_1[\hat{\mathbf{d}}_e])^T w_1 & \dots & (\mathbf{L}_n+\lambda\mathbf{Q}_n[\hat{\mathbf{d}}_e])^T w_n & \lambda\sum_g \boldsymbol{\mathcal{G}}_g[\hat{\boldsymbol{\sigma}}_g]w_g \end{bmatrix} \begin{bmatrix} \dot{\boldsymbol{\sigma}}_1 \\ \vdots \\ \dot{\boldsymbol{\sigma}}_n \\ \dot{\mathbf{d}}_e \end{bmatrix} = \begin{bmatrix} \mathbf{0} \\ \vdots \\ \mathbf{0} \\ \mathbf{0} \end{bmatrix} \tag{7.12}$$

and also in this case, eliminating the stresses of the integration points

$$\dot{\boldsymbol{\sigma}}_g = \mathbf{C}_g(\mathbf{L}_g+\lambda\mathbf{Q}_g[\hat{\mathbf{d}}_e])\dot{\mathbf{d}}_e$$

and substituting in Eq.(7.12)

$$\left\{\sum_g \left((\mathbf{L}_g+\lambda\mathbf{Q}_g)^T\mathbf{C}_g(\mathbf{L}_g+\lambda\mathbf{Q}_g)+\lambda\boldsymbol{\mathcal{G}}_g[\hat{\boldsymbol{\sigma}}_g]\right)w_g\right\}\dot{\mathbf{d}}_e=\mathbf{0},$$

we obtain the element contribution to the quadratic eigenvalue problem

$$\sum_g(\mathbf{K}^c_{0g}+\lambda\mathbf{K}^c_{1g}+\lambda^2\mathbf{K}^c_{2g})\dot{\mathbf{d}}_e=\mathbf{0}.$$

A linearized problem can also be obtained when the quadratic part of the strain along the fundamental path $\mathbf{Q}_g[\hat{\mathbf{d}}_e]$ is negligible and then

$$\left\{\sum_g \left(\mathbf{L}_g^T\mathbf{C}_g\mathbf{L}_g+\lambda\boldsymbol{\mathcal{G}}_g[\hat{\boldsymbol{\sigma}}_g]\right)w_g\right\}\dot{\mathbf{d}}_e=\mathbf{0}.$$

Quadratic correctives

Finally, the linear system in Eq.(2.36d) becomes

$$\begin{bmatrix} -\mathbf{C}_1^{-1}w_1 & & & \mathbf{B}_1w_1 \\ & \ddots & & \vdots \\ & & -\mathbf{C}_n^{-1}w_n & \mathbf{B}_nw_n \\ \mathbf{B}_1^Tw_1 & \dots & \mathbf{B}_n^Tw_n & \sum_g\boldsymbol{\mathcal{G}}_gw_g \end{bmatrix}_b \begin{bmatrix} \hat{\dot{\boldsymbol{\sigma}}}_1 \\ \vdots \\ \hat{\dot{\boldsymbol{\sigma}}}_n \\ \hat{\dot{\mathbf{d}}}_e \end{bmatrix} = -\begin{bmatrix} \mathbf{Q}_1[\hat{\mathbf{d}}_e]\hat{\mathbf{d}}_e \\ \vdots \\ \mathbf{Q}_n[\hat{\mathbf{d}}_e]\hat{\mathbf{d}}_e \\ \sum_g\left(\mathbf{Q}_g[\hat{\mathbf{d}}_e]^T\hat{\boldsymbol{\sigma}}_g+\boldsymbol{\mathcal{G}}_g[\hat{\boldsymbol{\sigma}}_g]\hat{\mathbf{d}}_e\right) \end{bmatrix} \tag{7.13}$$

where subscript b on matrices denotes that they are evaluated in $\mathbf{u}_{bg}=\lambda_b\{\hat{\boldsymbol{\sigma}}_g,\hat{\mathbf{d}}_e\}$.

E_{11}	$E_{22} = E_{33}$	$\nu_{12} = \nu_{13}$	ν_{23}	$G_{12} = G_{13}$	G_{23}
181e9	10.27e9	0.28	0	7.17e9	5.135e9

Table 7.1: Composite square plate: material properties.

By condensing out the stress correction at the integration points

$$\hat{\tilde{\boldsymbol{\sigma}}}_g = \mathbf{C}_g \mathbf{B}_g \hat{\tilde{\mathbf{d}}}_e + \mathbf{C}_g \mathbf{Q}_g[\hat{\mathbf{d}}_e]\hat{\mathbf{d}}_e \tag{7.14}$$

we obtain the linear system in the condensed form

$$\mathbf{K}_{be}\hat{\tilde{\mathbf{d}}}_e = -\hat{\tilde{\mathbf{s}}}_c \tag{7.15}$$

with

$$\begin{aligned} \mathbf{K}_e[\hat{\mathbf{u}}_e] &= \sum_g \left(\mathbf{B}_g^T \mathbf{C}_g \mathbf{B}_g + \boldsymbol{\mathcal{G}}_g[\boldsymbol{\sigma}_g] \right)_b w_g \\ \mathbf{s}_{ce}[\hat{\mathbf{u}}_e] &= \sum_g \left(\mathbf{Q}_g[\hat{\mathbf{d}}_e]^T \hat{\boldsymbol{\sigma}}_g + \boldsymbol{\mathcal{G}}_g[\hat{\boldsymbol{\sigma}}_g]\hat{\mathbf{d}}_e + \mathbf{B}_g^T \mathbf{C}_g \mathbf{Q}_g[\hat{\mathbf{d}}_e]\hat{\mathbf{d}}_e \right) w_g \end{aligned} \tag{7.16}$$

as the condensed tangent stiffness matrix, that has the same expression as the classical displacement based one but directly depends on the stresses, and the condensed secondary forces respectively.

7.3 Numerical results

The proposed numerical tool is now tested in common composite structures, such as plates, panels and cylinders. The first goal is to test the accuracy of the isogeometric solid-shell model in representing the buckling and post-buckling configuration. To this end, different meshes, interpolations and numerical integrations are considered. The second goal is to assess the accuracy of the ROM built with the proposed MIP isogeometric formulation of the Koiter method by comparing the results with reference solutions obtained by path-following analyses based on the full model.

7.3.1 Composite square plate under compression

The first test, depicted in Fig.7.1, is a simply supported laminated plate under compression. The material properties are reported in Tab.7.1. The layup adopted is $[0°/90°]_{4S}$. The test has been studied in [64] using shell elements and in [1] by a Ritz method. Firstly, the accuracy of the proposed isogeometric solid-shell model is tested in the evaluation of the four lowest buckling loads, which are reported in Tab.7.2 and Tab.7.3 for the C^1 and the C^2 interpolation respectively. The corresponding buckling modes are pictured in Fig.7.2. Different integration schemes

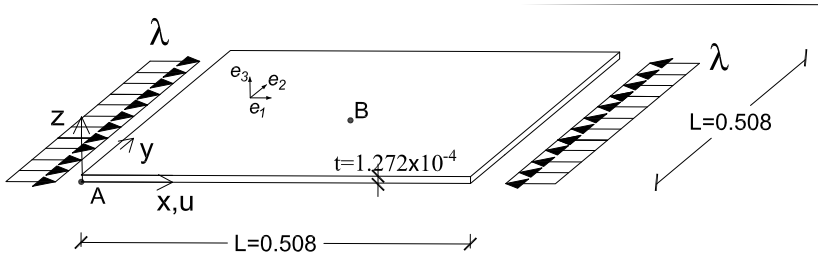

Figure 7.1: Composite square plate: geometry, load and boundary conditions.

4 elm.				8 elm.				16 elm.			
$\bar{S}_0^2$	S_0^3	S_0^4	ANS	$\bar{S}_0^2$	S_0^3	S_0^4	ANS	$\bar{S}_0^2$	S_0^3	S_0^4	ANS
1.010	1.004	1.185	1.184	1.000	1.002	1.179	1.121	1.000	1.000	1.113	1.006
1.367	*	*	1.483	1.007	1.073	*	1.439	1.000	1.006	1.561	1.064
1.348	*	*	1.457	1.006	1.071	*	1.422	1.000	1.006	1.648	1.076
1.328	*	*	1.636	1.022	1.015	*	1.591	1.000	1.007	*	1.188

$* > 2$

Table 7.2: Composite square plate: first 4 normalised buckling loads for C^1 interpolation.

are considered as well as the local ANS proposed in [103]. In particular, Tab.7.2 shows the good performance of $\bar{S}_0^2$, which turns out to be the best integration among those considered in terms of both accuracy and efficiency, providing good results for the 8×8 mesh and requiring just ≈ 1 integration point per element. Conversely, ANS and the full integration S_0^4, which require 9 and ≈ 4 integration points per element respectively, prove to be inaccurate because of the interpolation locking. It increases with the slenderness of the plate and slowly vanishes when the mesh is refined. Moreover, Tab.7.3 shows the advantages of a higher continuity in buckling problems, showing that the C^2 interpolation with $\bar{S}_1^3$ and, in particular, S_1^4 integration provides good results even using a 4×4 mesh. $\bar{S}_1^3$ requires ≈ 1 integration point per element but is slightly penalized for coarse meshes by the over-integration, while S_1^4 furnishes exact results for a 8×8 mesh and makes use of ≈ 2.25 integration points per element. The full integration S_1^6, making use of ≈ 6.25 integration points per element, is unusable due to locking phenomena that also hold for the finest mesh.

The equilibrium path in the pre-critical and initial post-critical range is reconstructed using the Koiter method and reported in Fig.7.3 for C^1 and Fig.7.4 for C^2. A small geometrical imperfection $\tilde{e}$ with the shape of the first buckling mode and $\|\tilde{e}\|_\infty = 0.01t$ is considered. In addition, a reference solution obtained using a very fine mesh and the standard Riks method which solves step-by-step the nonlinear equations of the full discrete model is reported. For this test, just one buckling mode is used in the ROM of the Koiter method which, then, requires

4 elm.			8 elm.			16 elm.		
$\bar{S}_1^3$	S_1^4	S_1^6	$\bar{S}_1^3$	S_1^4	S_1^6	$\bar{S}_1^3$	S_1^4	S_1^6
1.003	1.000	1.185	1.000	1.000	1.170	1.000	1.000	1.028
1.031	1.030	1.479	1.003	1.000	1.473	1.000	1.000	1.240
1.034	1.028	1.451	1.004	1.000	1.446	1.000	1.000	1.255
1.139	1.012	1.618	1.016	1.002	1.614	1.001	1.000	1.412

Table 7.3: Composite square plate: first 4 normalised buckling loads for C^2 interpolation.

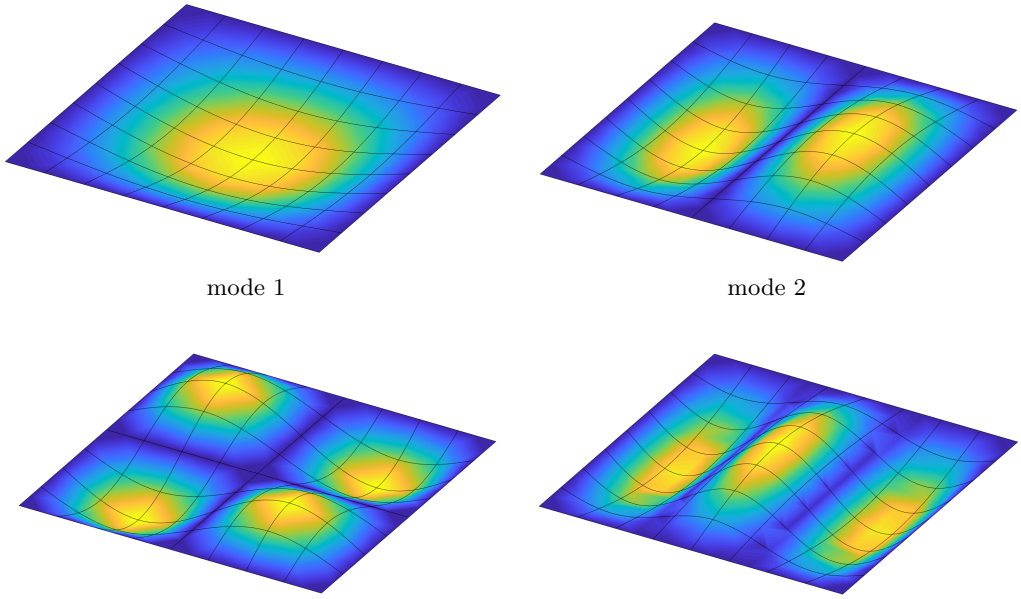

mode 1 mode 2

mode 3 mode 4

Figure 7.2: Composite square plate: first 4 buckling modes.

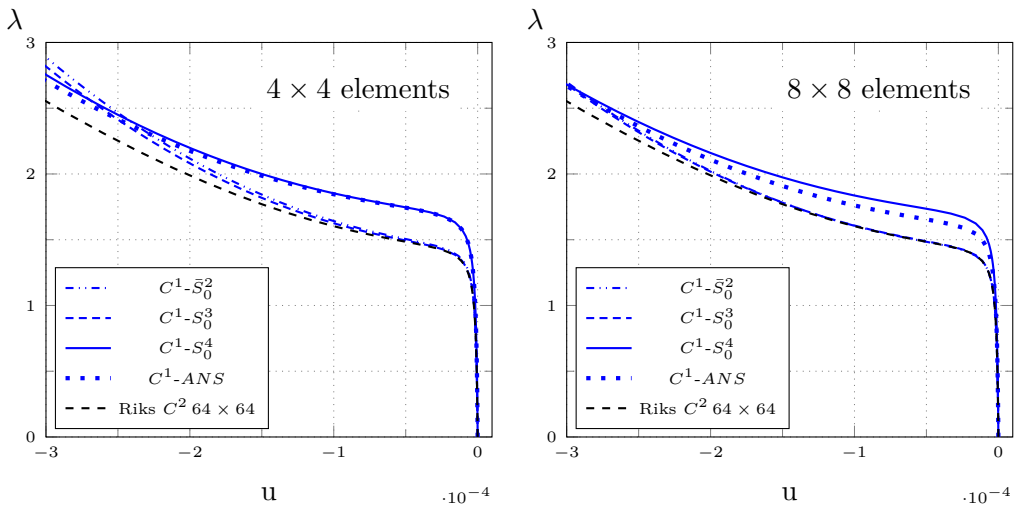

Figure 7.3: Composite square plate: equilibrium path using the C^1 interpolation

that only one nonlinear equation be solved. Looking at Fig.7.3 we can note that, although the bifurcation point is almost exact using C^1-$\bar{S}_0^2$, a 4×4 mesh exhibits a stiffer post-buckling response compared to the reference solution as consequence of interpolation locking of the linear and quadratic strains. However, the error becomes much lower by considering a 8×8 mesh. Figure 7.4, on the other hand, highlights the benefits of a higher continuity: C^2-$\bar{S}_1^3$ and C^2-S_1^4 agree very well with the reference path also for the coarsest mesh.

As a general comment, a drastic reduction in the number of DOFs is achieved with respect to the locking free linear shell elements used in [64] for the same test.

7.3.2 Composite curved panel under compression

The second test regards a curved panel under compression whose geometry, loads, and boundary conditions are represented in Fig.7.5. The material properties can be found in Tab.7.4. Two different layups are considered: $[0]_6$ and $[45, -45, 0]_s$. The lamination significantly influences the shape of the buckling modes as illustrated in Fig.7.6. The slenderness of the panel is much lower than that of the previous test. This means that the effects of the interpolation locking are less evident. This is confirmed by Tables 7.5, 7.6, 7.7 and 7.8 which show the convergence of the first 4 linearised buckling loads. The high continuity together with the exact representation of the geometry leads to very good results with all the integration strategies. Again, however, the $\bar{S}_0^2$ for C^1 and S_1^4 and $\bar{S}_1^3$ for C^2 represent the best choices in terms of accuracy and efficiency.

The study of the initial post-buckling behaviour of the panel is carried out considering the presence of a geometrical imperfection $\tilde{e}$ that is a combination of the first and the second buckling modes. In particular, it is the difference between

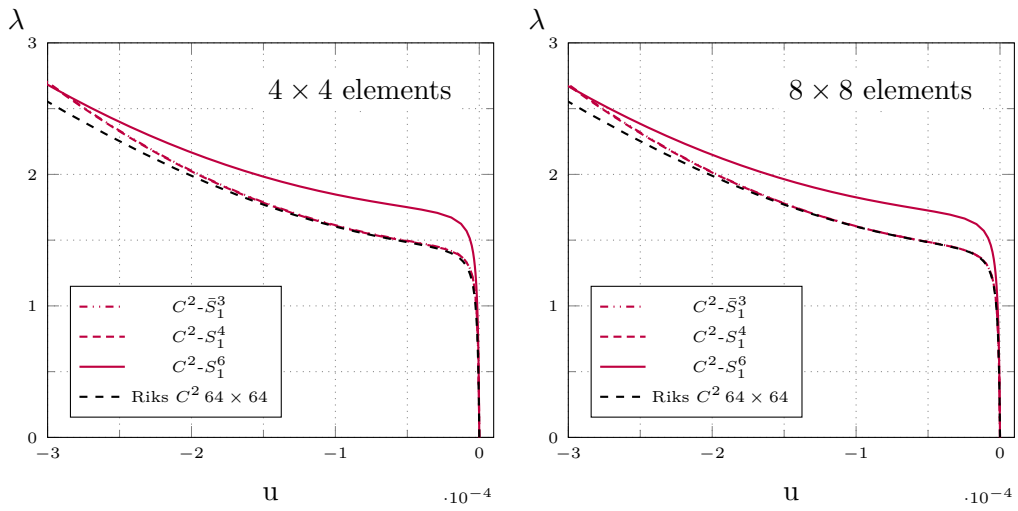

Figure 7.4: Composite square plate: equilibrium path using the C^2 interpolation

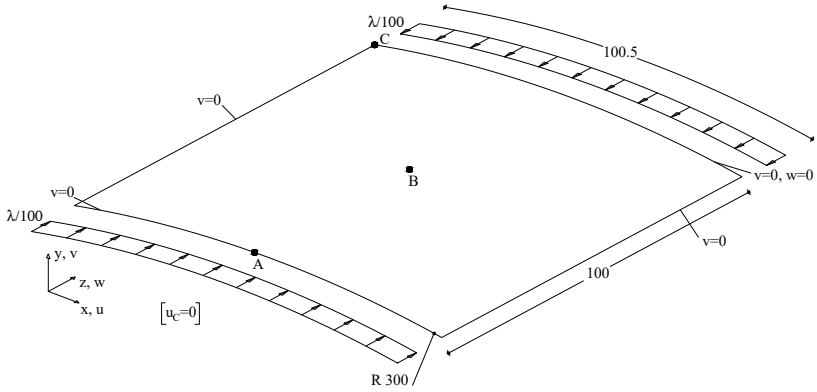

Figure 7.5: Composite curved panel: geometry and boundary conditions.

E_{11}	$E_{22} = E_{33}$	$\nu_{12} = \nu_{13}$	ν_{23}	$G_{12} = G_{13}$	G_{23}
30.6	8.7	0.29	0.5	3.24	2.9

Table 7.4: Composite curved panel: material properties.

4 elm.				8 elm.				16 elm.			
$\bar{S}_0^2$	S_0^3	S_0^4	ANS	$\bar{S}_0^2$	S_0^3	S_0^4	ANS	$\bar{S}_0^2$	S_0^3	S_0^4	ANS
1.053	1.055	1.078	1.042	1.002	0.998	1.020	1.008	0.995	0.995	0.998	0.996
1.158	1.424	1.694	1.177	1.005	1.008	1.069	1.018	0.996	0.998	1.003	0.997
1.259	1.609	$*$	1.299	1.009	1.035	1.124	1.039	1.003	1.004	1.012	1.003
1.408	1.746	$*$	1.396	1.007	1.061	1.213	1.067	1.003	1.005	1.020	1.004

$* > 2$

Table 7.5: Composite curved panel: first 4 normalised buckling loads for $[0]_6$ with C^1 interpolation.

4 elm.				8 elm.				16 elm.			
$\bar{S}_0^2$	S_0^3	S_0^4	ANS	$\bar{S}_0^2$	S_0^3	S_0^4	ANS	$\bar{S}_0^2$	S_0^3	S_0^4	ANS
1.096	1.144	1.263	1.165	1.016	1.018	1.095	1.054	1.001	1.002	1.015	1.004
1.082	1.201	1.656	1.106	1.013	1.010	1.078	1.036	0.998	0.999	1.011	1.001
1.080	1.346	$*$	1.333	1.007	1.010	1.157	1.061	0.998	0.999	1.010	0.999
1.235	1.456	$*$	1.848	1.035	1.073	1.228	1.119	1.003	1.012	1.049	1.011

$* > 2$

Table 7.6: Composite curved panel: first 4 normalised buckling loads for $[45, -45, 0]_s$ with C^1 interpolation.

4 elm.			8 elm.			16 elm.		
$\bar{S}_1^3$	S_1^4	S_1^6	$\bar{S}_1^3$	S_1^4	S_1^6	$\bar{S}_1^3$	S_1^4	S_1^6
0.995	1.034	1.031	1.001	1.005	1.004	1.001	1.002	1.001
1.000	1.013	1.073	1.001	1.004	1.003	1.001	1.001	1.001
1.008	1.063	1.132	1.003	1.008	1.007	1.002	1.003	1.003
1.014	1.104	1.210	1.004	1.009	1.010	1.002	1.003	1.003

Table 7.7: Composite curved panel: first 4 normalised buckling loads for $[0]_s$ with C^2 interpolation.

4 elm.			8 elm.			16 elm.		
$\bar{S}_1^3$	S_1^4	S_1^6	$\bar{S}_1^3$	S_1^4	S_1^6	$\bar{S}_1^3$	S_1^4	S_1^6
0.995	1.097	1.110	1.006	1.014	1.018	1.002	1.005	1.004
1.014	1.044	1.068	1.006	1.012	1.015	1.001	1.003	1.003
1.002	1.121	1.167	1.003	1.007	1.014	1.001	1.003	1.002
1.062	1.205	1.280	1.041	1.022	1.061	1.001	1.003	1.003

Table 7.8: Composite curved panel: first 4 normalised buckling loads $[45, -45, 0]_s$ with C^2 interpolation.

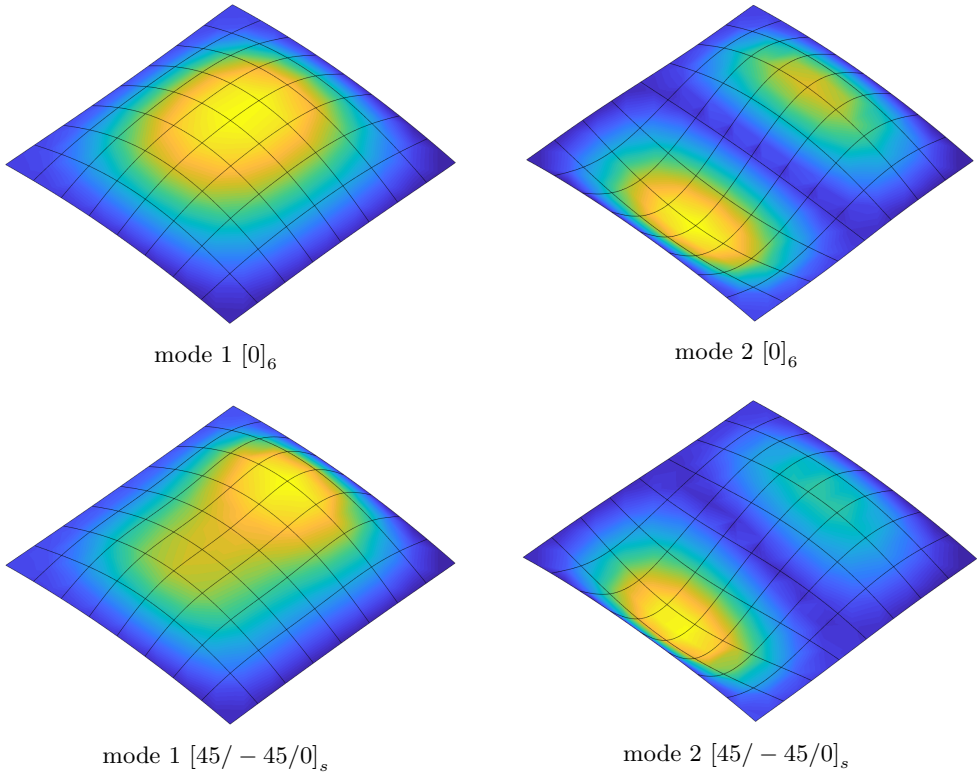

Figure 7.6: Composite curved panel: first and second buckling mode corresponding to two different layups

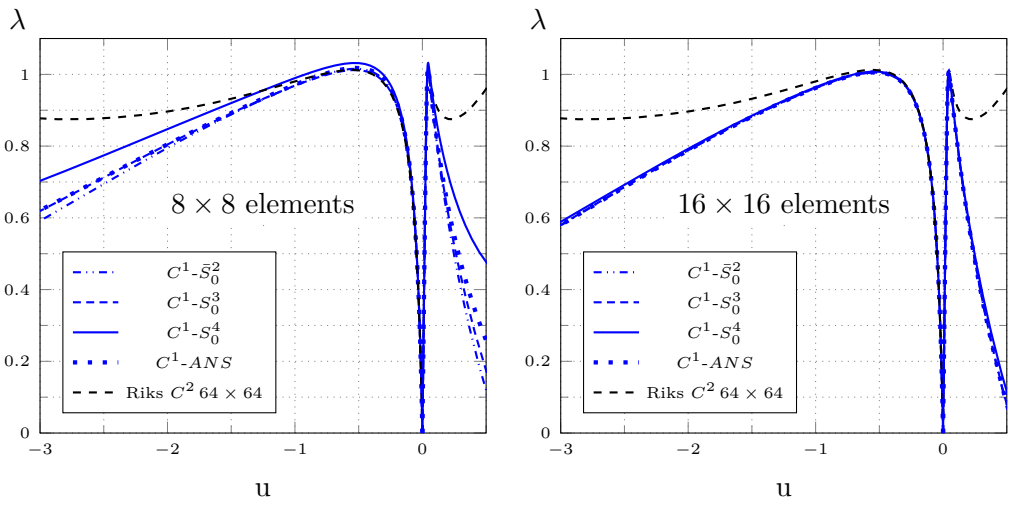

Figure 7.7: Composite curved panel: equilibrium path for $[0]_6$ and C^1 interpolation

E_{11}	$E_{22} = E_{33}$	ν_{12}	$\nu_{23} = \nu_{13}$	$G_{12} = G_{13} = G_{23}$
123.6	8.7	0.32	0	5.7

Table 7.9: Laminate composite cylinder: material properties.

them scaled in order to obtain $\|\tilde{e}\|_\infty = 0.1t$. The Koiter solution is evaluated using a ROM based on the first two buckling modes only, since the higher ones are far from the first two, and it is compared with reference paths. For both the layups, the initial post-buckling exhibits a limit load as shown in Fig.7.7 and Fig.7.8 for $[0]_6$ and in Fig.7.9 and 7.10 for $[45, -45, 0]_s$. C^1-$\bar{S}_0^2$, C^2-$\bar{S}_1^3$ and C^2-S_1^4 are the best performing strategies, providing a good estimate of the limit loads with a 8×8 mesh, which become practically exact using a 16×16 mesh.

7.3.3 Laminate composite cylinder subjected to axial compression

The cylinder considered in the following and labelled Z33 was manufactured and tested by DLR (German Aerospace Center) and commonly used as a validation model for numerical developments in the context of laminate composite shell design [98]. The stacking sequence is ${}_{in}[0/0/19/-19/37/-37/45/-45/51/-51]_{out}$ with the angles measured from the cylinder axis with respect to the outward normal. The cylinder has a height of 510, a radius of $R = 250$ and a wall-thickness of $t = 1.25$, cf Fig.7.11. The material properties are reported in Table 7.9

The cylinder is clamped at the bottom face and only the axial translation is allowed at the top surface. A uniformly distributed load along the top rim is

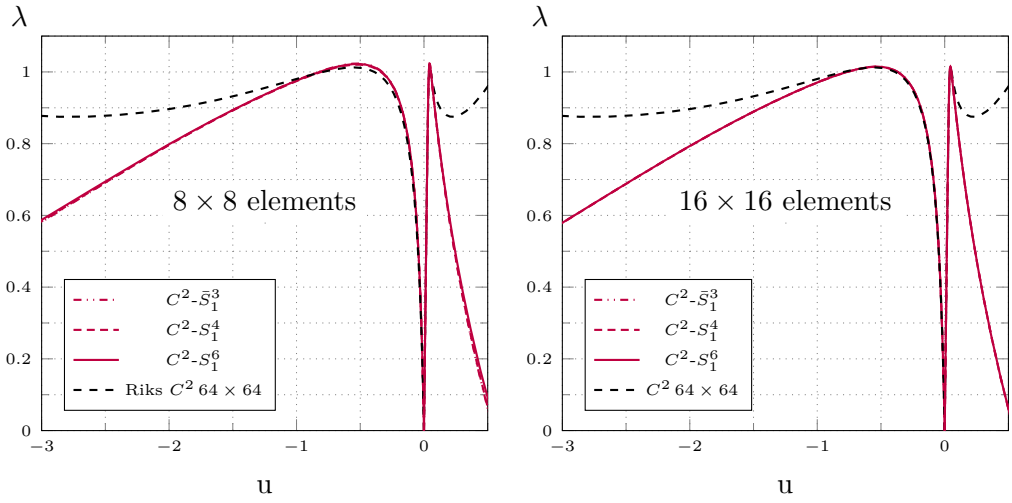

Figure 7.8: Composite curved panel: equilibrium path for $[0]_6$ and C^2 interpolation

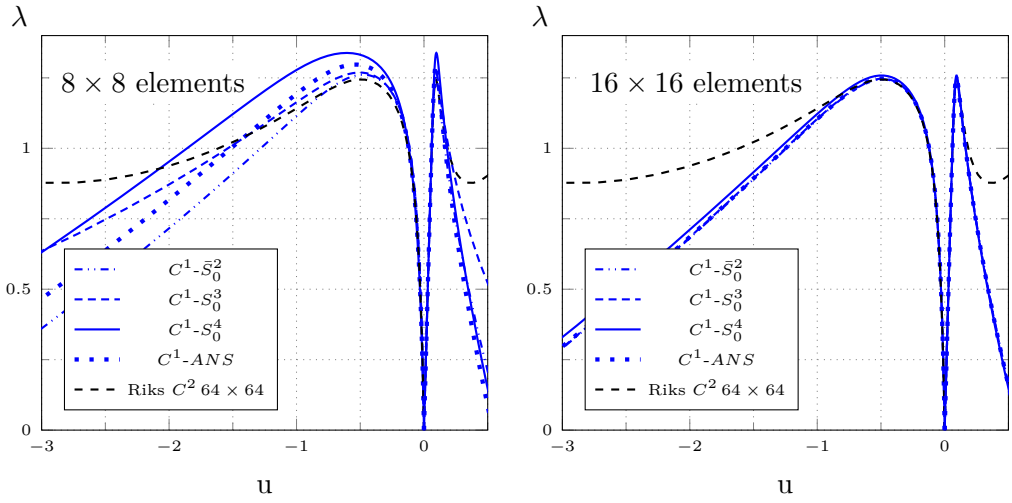

Figure 7.9: Composite curved panel: equilibrium path for $[45/-45/0]$ and C^1 interpolation

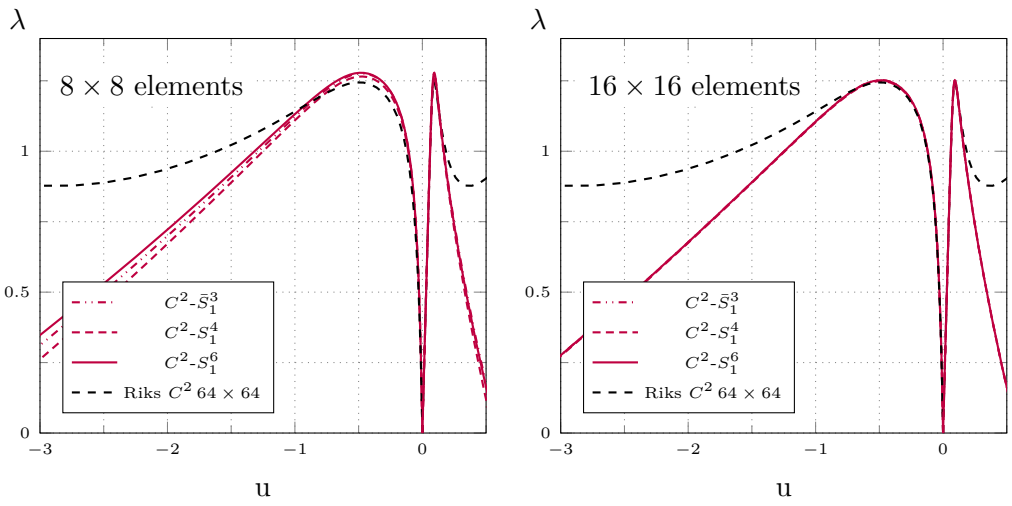

Figure 7.10: Composite curved panel: equilibrium path for $[45/-45/0]$ and C^2 interpolation

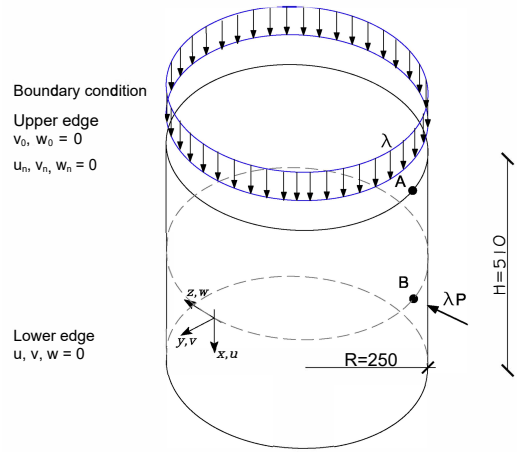

Figure 7.11: Laminate composite cylinder: model properties.

applied in axial direction. The lowest buckling loads of the perfect structure are reported in Tab.7.10 and Tab.7.11 for the C^1 and the C^2 interpolation respectively. The corresponding buckling modes are depicted in Fig.7.12. Due to problem symmetries they occur in couples. Also for this test, C^1-$\bar{S}_0^2$, C^2-$\bar{S}_1^3$ and C^2-S_1^4 turn out to be particularly accurate and provide good results with a relatively coarse mesh in comparison with those usually employed in the FE analysis, as in the previous chapters.

In evaluating the initial post-buckling behaviour a load imperfection is introduced by a concentrated force halfway up the cylinder axis. By including just one

12 elm.				24 elm.				48 elm.			
$\bar{S}_0^2$	S_0^3	S_0^4	ANS	$\bar{S}_0^2$	S_0^3	S_0^4	ANS	$\bar{S}_0^2$	S_0^3	S_0^4	ANS
0.957	1.594	$*$	1.658	1.003	1.041	1.200	1.056	1.000	1.002	1.015	1.001
0.960	1.596	$*$	1.664	1.006	1.046	1.200	1.059	1.000	1.002	1.015	1.001
0.959	1.618	$*$	1.661	1.005	1.044	1.200	1.060	1.000	1.002	1.014	1.001
0.962	1.618	$*$	1.719	1.007	1.048	1.208	1.060	1.000	1.002	1.014	1.001

$* > 2$

Table 7.10: Laminate composite cylinder: first 4 normalised buckling loads with C^1 interpolation.

12 elm.			24 elm.			48 elm.		
$\bar{S}_1^3$	S_1^4	S_1^6	$\bar{S}_1^3$	S_1^4	S_1^6	$\bar{S}_1^3$	S_1^4	S_1^6
1.156	1.120	1.245	1.003	1.011	1.007	1.000	1.001	1.000
1.176	1.127	1.245	1.003	1.011	1.007	1.000	1.001	1.000
1.175	1.150	1.266	1.002	1.012	1.006	1.000	1.001	1.000
1.183	1.150	1.278	1.002	1.012	1.006	1.000	1.001	1.000

Table 7.11: Laminate composite cylinder: first 4 normalised buckling loads with C^2 interpolation.

mode in the ROM, a good prediction of the limit load is obtained as shown in Fig.7.13 and Fig.7.11.

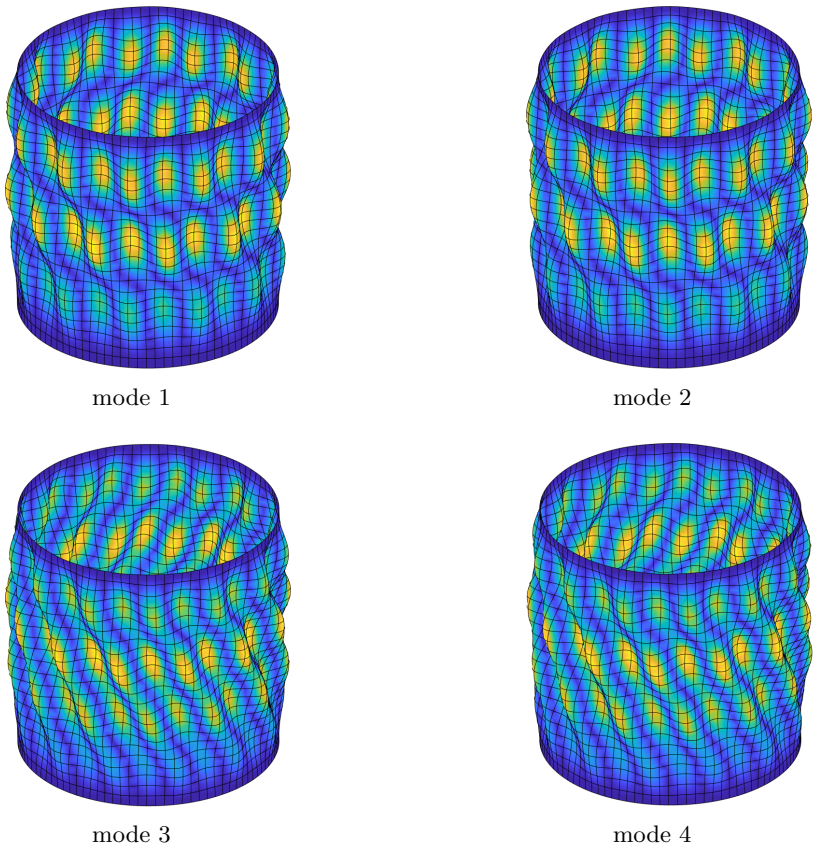

mode 1 mode 2

mode 3 mode 4

Figure 7.12: Laminate composite cylinder: first 4 buckling modes.

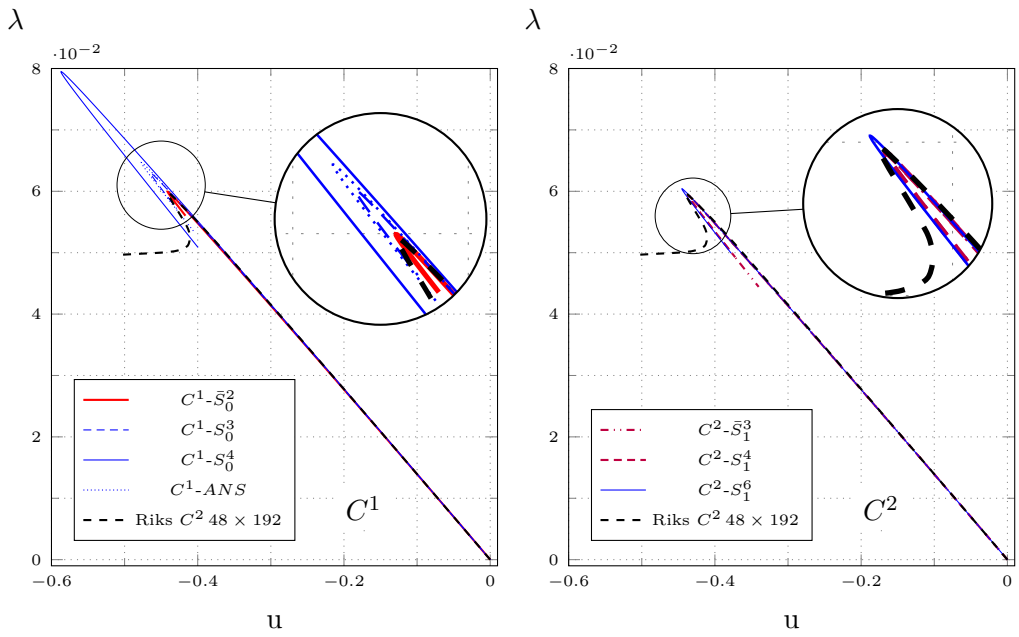

Figure 7.13: Laminate composite cylinder: equilibrium path using 24×96 mesh

7.4 Summary

The failure of slender composite shell structure is often dominated by buckling, while the material behavior is purely elastic. In this context, the Koiter method, which is a numerical formulation of Koiter's theory of elastic stability, represents a reliable and efficient tool of analysis. While standard path-following analyses solve the nonlinear equations of the discretized structure using all the discrete DOFs, the Koiter method uses a discretization technique just for the construction of a reduced model based on the first buckling modes, the corresponding corrective modes and the associated strain energy variations. Only the reduced nonlinear equations in a few unknowns, that is the modal amplitudes and the load factor, are then solved in order to obtain the equilibrium path.

This work explored the use of IGA for the evaluation of the reduced model ingredients. The continuum shell problem was formulated in a Total Lagrangian way following the solid-shell concept, which makes it possible to avoid the use of finite rotations employing a simple Green Lagrange strain measure. The same interpolation was used for the geometry and displacement field. In particular, NURBS functions were employed for the middle surface quantities, obtained by refining those provided directly by a CAD model. Apart from the exact geometry, these highly continuous functions seem very suitable in approximating the deformed configuration of buckling problems. To maintain a low number of DOFs, a linear interpolation was adopted through the thickness of the shells. A modified generalized constitutive matrix was defined to prevent thickness locking and to make it easy to consider multi-layered composites. Path-wise reduced integrations were investigated to handle interpolation locking and to reduce the number of integration points. The mixed integration point strategy was used to re-write the displacement-based model into a mixed (stress-displacement) one, which has been shown to be more accurate and efficient in Koiter analyses. In particular, this approach makes it possible to avoid the evaluation of the fourth order strain energy variations, usually required to build the reduced order model. The proposed numerical framework was tested in the analysis of common thin-walled composite structures under compression: plates, curved panels and cylinders. The results showed that the isogeometric model is able to furnish an excellent approximation of the buckling loads, the limit loads and the initial post-buckling behavior employing a very low number of DOFs coupled with the reduced number of integration points, which further increases the efficiency of the analysis. In particular the C^1-$\bar{S}_0^2$ and C^2-$\bar{S}_1^3$ approaches proves to be convenient because it requires just one integration point per element without spurious modes.

The resulting numerical tool is an efficient approach for the design of slender composite shells. Further details can be found in [119]. Future developments will investigate its use in structural optimization processes.

Conclusions

This work has considered different aspects in the numerical analysis and design of slender shell structures. The first chapter discussed the important advantages of using a mixed (stress-displacement) solid model for analysing slender shell structures over traditional shell models. Among them, it is worth mentioning the possibility of using a Total Lagrangian formulation with a simple strain measure, without dealing with finite rotations, and of modelling the connections of different components accurately, as for instance in the case of thin-walled beams and stiffened panels. The use of a mixed format of the equations improves the performances of the solution strategies significantly, compared to the displacement-based format usually adopted in commercial finite element codes. This is due to the different error of the linearisations used within the solution methods. In the Riks approach, the mixed format allows us to reduce the iterative effort, while in the Koiter method it leads to a more accurate and reliable reduced order model. The joint use of a mixed formulation and a solid model has an interesting feature: the strain energy becomes a third order function of the discrete degrees of freedom. This fact was exploited in the second chapter, where a new strategy to include, a-posteriori, geometrical imperfections in Koiter analysis was derived, overcoming the inaccuracies of previous proposals. The main idea is to correct the reduced model of the perfect structure in order to take account of the imperfections. As a consequence, the imperfection effects can then be considered accurately by simply adding some terms to the perfect structure reduced equations, which have been derived coherently with the reduced model correction. A robust and efficient mixed linear solid-shell finite element for multi-layered shells was introduced, allowing an efficient and accurate discrete approximation and maintaining the features of a mixed solid model. A large number of numerical tests were reported to validate the equilibrium path provided by the new imperfection account. The proposal made the Koiter method a reliable and efficient tool for analysing imperfection sensitive structures. In the third chapter, the great efficiency and improved accuracy of the Koiter method was used within a stochastic optimisation strategy for composite shells. The goal is to search for the best stacking sequence that maximises the structural performances, optimising the post-buckling behaviour. Its feasibility is due to the reduced order model built for each material setup, which allows us to: i) obtain optimal layups by a random scan of the fibre an-

gles domain; ii) take account of the geometrical imperfections in the evaluation of the structural response. This last point, crucial for a reliable design, was made possible by a Monte Carlo simulation aimed at detecting the worst shape of the imperfection, which proves to be extremely efficient because the imperfection effects are considered in the reduced order model of the perfect structure. The optimisation of composite panels was reported as an example of the great capabilities of this design tool. The study carried out in the first chapter explained that the advantages of the mixed formulation over the displacement-based one is not linked to the discrete approximation, but is due to the direct use of the stresses as independent variables in the solution algorithms. Starting from this consideration, the forth chapter extended the benefits of the mixed formulation to any displacement-based finite element model. The idea is to introduce stress variables in the solution process, even if the discrete approximation is governed by displacement variables only. The proposed strategy, called Mixed Integration Points, consists in relaxing the constitutive equations at each integration point, where the stresses become independent variables. The size of the global quantities is, however, preserved, because the stresses are defined locally at each integration point. The strategy was implemented within the Newton iterative scheme with just a few simple changes in the standard approach, but with a significant reduction in the iterative effort. The fifth chapter addressed the novel Koiter-Newton method and, in particular, an implementation of the algorithm based on the mixed solid-shell model. The resulting strategy is able to recover the equilibrium path of thin-walled structures undergoing buckling using just a few true equilibrium points. The mixed formulation plays the important role of reducing the iterative effort to a few iterations per step. This means that a very low number of total iterations are required by this Koiter-Newton approach for evaluating the equilibrium path, preserving the accuracy of the Riks method. Although the linear solid-shell finite element discretisation proved to be very robust and efficient, it requires a significant number of degrees of freedom for the analysis of curved shells and for approximating the buckling modes of compressed structures, usually characterised by highly continuous shapes. This leads to significant computational times for all the solution strategies. For this reason, the solid-shell discrete model was reformulated in the sixth chapter, following the isogeometric concept. NURBS functions were employed to interpolate geometry and displacement fields on the middle surface of the shell, in order to take advantage of their high continuity and of the exact geometry description. The extension was, however, significant, because the high continuity and displacement-based formulation lead to some issues concerning interpolation locking and iterative effort. An effective way of overcoming these drawbacks was presented by combining the Mixed Integration Point strategy with a suitable patch-wise reduced integration. The isogeometric solid-shell model proved to be much more convenient than low order finite elements, especially in the analysis of curved shells undergoing buckling. For this reason, it was used in the seventh chapter for constructing the reduced order model of the

Koiter method. The proposal pushes the efficiency of the method to the limit, because a very low number of discrete variables and integration points are needed. To summarise, this work derived a reliable and efficient numerical framework for the analysis and design of slender elastic shells, in particular when composite materials are adopted. Advances in the different aspects of this challenging topic were presented, which offer the engineering community effective tools for tackling the problem.

Bibliography

[1] S. Henrichsen, P. Weaver, E. Lindgaard, E. Lund, Post-buckling optimization of composite structures using Koiter's method, International Journal for Numerical Methods in Engineeringdoi:10.1002/nme.5239.

[2] T. H. H. Pian, C.-C. Wu, Hybrid and Incompatible Finite Element Methods, Chapman & All, CRC, New-York, 1969.

[3] E. Riks, An incremental approach to the solution of snapping and buckling problems, International Journal of Solids and Structures 15 (7) (1979) 529–551. doi:10.1016/0020-7683(79)90081-7.

[4] E. Lindgaard, E. Lund, K. Rasmussen, Nonlinear buckling optimization of composite structures considering "worst" shape imperfections, International Journal of Solids and Structures 47 (22–23) (2010) 3186 – 3202. doi:http://dx.doi.org/10.1016/j.ijsolstr.2010.07.020.

[5] E. Barbero, A. Madeo, G. Zagari, R. Zinno, G. Zucco, Imperfection sensitivity analysis of laminated folded plates, Thin-Walled Structures 90 (2015) 128 – 139. doi:http://dx.doi.org/10.1016/j.tws.2015.01.017.

[6] R. Casciaro, Computational Asymptotic Post-Buckling Analysis of Slender Elastic Structures, CISM Courses and Lectures NO. 470 (2005) .

[7] W. Koiter, On the stability of elastic equilibrium.

[8] K. Liang, M. Abdalla, Z. Gürdal, A Koiter-Newton approach for nonlinear structural analysis, International Journal for Numerical Methods in Engineering 96 (12) (2013) 763–786. doi:10.1002/nme.4581.

[9] J. A. Cottrell, T. J. R. Hughes, Y. Bazilevs, Isogeometric Analysis: Toward Integration of CAD and FEA, 2009. doi:978-0-470-74873-2.

[10] K. Sze, W. Chan, T. Pian, An eight-node hybrid-stress solid-shell element for geometric non-linear analysis of elastic shells, International Journal for Numerical Methods in Engineering 55 (7) (2002) 853–878. doi:10.1002/nme.535.

[11] S. Klinkel, F. Gruttmann, W. Wagner, A robust non-linear solid shell element based on a mixed variational formulation, Computer Methods in Applied Mechanics and Engineering 195 (1-3) (2006) 179–201. doi:10.1016/j.cma.2005.01.013.

[12] L. Vu-Quoc, X. G. Tan, Optimal solid shells for non-linear analyses of multilayer composites. I Statics, Computer Methods in Applied Mechanics and Engineering 192 (9-10) (2003) 975–1016. doi:10.1016/S0045-7825(02)00435-8.

[13] Q. Li, Y. Liu, Z. Zhang, W. Zhong, A new reduced integration solid-shell element based on EAS and ANS with hourglass stabilization, International Journal for Numerical Methods in Engineering (2015) 1885–1891arXiv:1010.1724, doi:10.1002/nme.

[14] G. Garcea, A. Madeo, R. Casciaro, The implicit corotational method and its use in the derivation of nonlinear structural models for beams and plates, J. Mech. Mater. Struct. 7 (6) (2012) 509–539. doi:10.2140/jomms.2012.7.509.

[15] G. Garcea, A. Madeo, R. Casciaro, Nonlinear FEM analysis for beams and plate assemblages based on the implicit corotational method, J. Mech. Mater. Struct. 7 (6) (2012) 539–574. doi:10.2140/jomms.2012.7.539.

[16] K. Sze, Three-dimensional continuum finite element models for plate/shell analysis, Prog. Struct. Engng. Mater 4 (2002) 400–407.

[17] S. Klinkel, F. Gruttmann, W. Wagner, Continuum based three-dimensional shell element for laminated structures, Computers and Structures 71 (1) (1999) 43–62. doi:10.1016/S0045-7949(98)00222-3.

[18] S. Reese, P. Wriggers, B. D. Reddy, New locking-free brick element technique for large deformation problems in elasticity, Computers and Structures 75 (3) (2000) 291–304. doi:10.1016/S0045-7949(99)00137-6.

[19] M. Schwarze, S. Reese, A reduced integration solid-shell finite element based on the EAS and the ANS concept—Geometrically linear problems, Computer Methods in Applied Mechanics and Engineering (80) (2009) 1322–1355. doi:10.1002/nme.

[20] M. Schwarze, S. Reese, A reduced integration solid-shell finite element based on EAS and the ANS concept: Large deformation problems, International Journal for Numerical Methods in Engineering (85) (2011) 289–329. doi:10.1002/nme.

[21] K. Sze, A. Ghali, Hybrid hexahedral element for solids, plates, shells and beams by selective scaling, International Journal for Numerical Methods in Engineering 36 (9) (1993) 1519–1540.

[22] L. Vu-Quoc, X. Tan, Efficient Hybrid-EAS solid element for accurate stress prediction in thick laminated beams, plates, and shells, Computer Methods in Applied Mechanics and Engineering 253 (2013) 337–355. doi:10.1016/j.cma.2012.07.025.
URL `http://dx.doi.org/10.1016/j.cma.2012.07.025`

[23] J. Frischkorn, S. Reese, A solid-beam finite element and non-linear constitutive modelling, Computer Methods in Applied Mechanics and Engineering 265 (2013) 195–212. doi:10.1016/j.cma.2013.06.009.

[24] K. Sze, X. Liu, S. Lo, Hybrid-stress six-node prismatic elements, International Journal for Numerical Methods in Engineering 61 (9) (2004) 1451–1470. doi:10.1002/nme.1118.

[25] K. Sze, S.-J. Zheng, A stabilized hybrid-stress solid element for geometrically nonlinear homogeneous and laminated shell analyses, Computer Methods in Applied Mechanics and Engineering 191 (17-18) (2002) 1945–1966. doi:10.1016/S0045-7825(01)00362-0.

[26] K. Sze, X. Liu, S. Lo, Hybrid-stress six-node prismatic elements, International Journal for Numerical Methods in Engineering 61 (9) (2004) 1451–1470. doi:10.1002/nme.1118.

[27] K. Sze, S. Lo, L.-Q. Yao, Hybrid-stress solid elements for shell structures based upon a modified variational functional, International Journal for Numerical Methods in Engineering 53 (12) (2002) 2617–2642. doi:10.1002/nme.402.

[28] K. Sze, L. Yao, A hybrid stress ANS solid-shell element and its generalization for smart structure modelling. Part I - Solid-shell element formulation, International Journal for Numerical Methods in Engineering 48 (4) (2000) 545–564.

[29] D. Wu, S. Lo, N. Sheng, K. Sze, Universal three-dimensional connection hexahedral elements based on hybrid-stress theory for solid structures, International Journal for Numerical Methods in Engineering 81 (3) (2010) 307–334. doi:10.1002/nme.2693.

[30] K. Sze, S.-J. Zheng, S. Lo, A stabilized eighteen-node solid element for hyperelastic analysis of shells, Finite Elements in Analysis and Design 40 (3) (2004) 319–340. doi:10.1016/S0168-874X(03)00050-7.

[31] K. Sze, L.-Q. Yao, T. Pian, An eighteen-node hybrid-stress solid-shell element for homogenous and laminated structures, Finite Elements in Analysis and Design 38 (4) (2002) 353–374. doi:10.1016/S0168-874X(01)00089-0.

[32] G. Garcea, G. Trunfio, R. Casciaro, Mixed formulation and locking in path-following nonlinear analysis, Computer Methods in Applied Mechanics and Engineering 165 (1-4) (1998) 247–272.

[33] G. Garcea, G. Salerno, R. Casciaro, Extrapolation locking and its sanitization in Koiter's asymptotic analysis, Computer Methods in Applied Mechanics and Engineering 180 (1-2) (1999) 137–167.

[34] G. Garcea, A. Madeo, G. Zagari, R. Casciaro, Asymptotic post-buckling FEM analysis using corotational formulation, International Journal of Solids and Structures 46 (2) (2009) 377–397.

[35] G. Garcea, A. Bilotta, A. Madeo, R. Casciaro, Direct evaluation of the post-buckling behavior of slender structures through a numerical asymptotic formulation, Springer Verlag, 2014. doi:10.1007/978-94-007-6827-7 10.

[36] W. Lacarbonara, Nonlinear Structural Mechanics, Spinger Verlag, New-York, 2013.

[37] R. Casciaro, G. Garcea, G. Attanasio, F. Giordano, Perturbation approach to elastic post-buckling analysis, Computers & Structures 66 (5) (1998) 585–595.

[38] T. Rahman, E. Jansen, Finite element based coupled mode initial post-buckling analysis of a composite cylindrical shell, Thin-Walled Structures 48 (1) (2010) 25–32. doi:10.1016/j.tws.2009.08.003.

[39] F. Flores, L. Godoy, Elastic post-buckling analysis via finite element and perturbation techniques. Part 1: Formulation, International Journal for Numerical Methods in Engineering 33 (9) (1992) 1775–1794.

[40] E. Barbero, I. Raftoyiannis, L. Godoy, Finite elements for post-buckling analysis. II-Application to composite plate assemblies, Computers and Structures 56 (6) (1995) 1019–1028.

[41] E. Boutyour, H. Zahrouni, M. Potier-Ferry, M. Boudi, Asymptotic-numerical method for buckling analysis of shell structures with large rotations, Journal of Computational and Applied Mathematics 168 (1-2) (2004) 77–85. doi:10.1016/j.cam.2003.05.010.

[42] N. Silvestre, D. Camotim, Asymptotic-numerical method to analyze the postbuckling behavior, imperfection-sensitivity, and mode interaction in frames, Journal of Engineering Mechanics 131 (6) (2005) 617–632. doi:10.1061/(ASCE)0733-9399(2005)131:6(617).

[43] B. Schafer, L. Graham-Brady, Stochastic post-buckling of frames using Koiter's method, International Journal of Structural Stability and Dynamics 6 (3) (2006) 333–358. doi:10.1142/S0219455406001976.

[44] H. Chen, L. Virgin, Finite element analysis of post-buckling dynamics in plates-Part I: An asymptotic approach, International Journal of Solids and Structures 43 (13) (2006) 3983–4007. doi:10.1016/j.ijsolstr.2005.04.036.

[45] N. L. Rizzi, V. Varano, S. Gabriele, Initial postbuckling behavior of thin-walled frames under mode interaction, Thin-Walled Structures 68 (2013) 124 – 134. doi:http://dx.doi.org/10.1016/j.tws.2013.03.004.

[46] W. Koiter, On the stability of elastic equilibrium, English transl. NASA TT-F10, 883 (1967) and AFFDL-TR70-25 (1970) Edition, Techische Hooge School at Delft, 1945.

[47] G. Zagari, A. Madeo, R. Casciaro, S. De Miranda, F. Ubertini, Koiter analysis of folded structures using a corotational approach, International Journal of Solids and Structures 50 (5) (2013) 755–765. doi:10.1016/j.ijsolstr.2012.11.007.

[48] G. Garcea, Mixed formulation in Koiter analysis of thin-walled beams, Computer Methods in Applied Mechanics and Engineering 190 (26-27) (2001) 3369–3399.

[49] D. Magisano, L. Leonetti, G. Garcea, Advantages of the mixed format in geometrically nonlinear analysis of beams and shells using solid finite elements, International Journal for Numerical Methods in Engineering 109 (9) (2017) 1237–1262. doi:10.1002/nme.5322.

[50] P. Dinis, D. Camotim, Post-buckling behaviour and strength of cold-formed steel lipped channel columns experiencing distortional/global interaction, Computers and Structures 89 (3-4) (2011) 422–434. doi:10.1016/j.compstruc.2010.11.015.

[51] P. B. Dinis, D. Camotim, Cold-formed steel columns undergoing local-distortional coupling: Behaviour and direct strength prediction against interactive failure, Computer & Structures 147 (SI) (2015) 181–208. doi:10.1016/j.compstruc.2014.09.012.

[52] R. Khakimova, C. J. Warren, R. Zimmermann, S. G. P. Castro, M. A. Arbelo, R. Degenhardt, The single perturbation load approach applied to imperfection sensitive conical composite structures, Thin-Walled Structures 84 (2014) 369–377. doi:10.1016/j.tws.2014.07.005.

[53] S. G. P. Castro, R. Zimmermann, M. A. Arbelo, R. Khakimova, M. W. Hilburger, R. Degenhardt, Geometric imperfections and lower-bound methods used to calculate knock-down factors for axially compressed composite cylindrical shells, Thin-Walled Structures 74 (2014) 118–132. doi:10.1016/j.tws.2013.08.011.

[54] M. A. Arbelo, R. Degenhardt, S. G. P. Castro, R. Zimmermann, Numerical characterization of imperfection sensitive composite structures, Composite Structures 108 (2014) 295–303. doi:10.1016/j.compstruct.2013.09.041.

[55] D. Dubina, V. Ungureanu, Instability mode interaction: From Van der Neut model to ECBL approach, Thin-Walled Structures 81 (2014) 39–49. doi:10.1016/j.tws.2013.10.014.

[56] G. Zagari, G. Zucco, A. Madeo, V. Ungureanu, R. Zinno, D. Dubina, Evaluation of the erosion of critical buckling load of cold-formed steel members in compression based on Koiter asymptotic analysis, Thin-Walled Structures 108 (2016) 193–204. doi:10.1016/j.tws.2016.08.011.

[57] V. Papadopoulos, G. Soimiris, M. Papadrakakis, Buckling analysis of I-section portal frames with stochastic imperfections, Engineering Structures 47 (SI) (2013) 54–66. doi:10.1016/j.engstruct.2012.09.009.

[58] E. Barbero, L. Godoy, I. Raftoyiannis, Finite elements for three-mode interaction in buckling analysis, International Journal for Numerical Methods in Engineering 39 (3) (1996) 469–488, cited By 14.

[59] D. Magisano, L. Leonetti, G. Garcea, Koiter asymptotic analysis of multilayered composite structures using mixed solid-shell finite elements, Composite Structures 154 (2016) 296–308. doi:10.1016/j.compstruct.2016.07.046.

[60] S. White, P. Weaver, Towards imperfection insensitive buckling response of shell structures-shells with plate-like post-buckled responses, Aeronautical Journal 120 (1224) (2016) 233–253. doi:10.1017/aer.2015.14.

[61] S. White, G. Raju, P. Weaver, Initial post-buckling of variable-stiffness curved panels, Journal of the Mechanics and Physics of Solids 71 (2014) 132 – 155. doi:http://dx.doi.org/10.1016/j.jmps.2014.07.003.

[62] K. Liang, M. Ruess, M. Abdalla, The Koiter-Newton approach using von Karman kinematics for buckling analyses of imperfection sensitive structures, Computer Methods in Applied Mechanics and Engineering 279 (2014) 440–468. doi:10.1016/j.cma.2014.07.008.

[63] A. Madeo, R. Groh, G. Zucco, P. Weaver, G. Zagari, R. Zinno, Post-buckling analysis of variable-angle tow composite plates using Koiter's approach and the finite element method, Thin-Walled Structures 110 (2017) 1–13. doi:10.1016/j.tws.2016.10.012.

[64] E. Barbero, A. Madeo, G. Zagari, R. Zinno, G. Zucco, Koiter asymptotic analysis of folded laminated composite plates, Composites Part B: Engineering 61 (2014) 267–274, cited By 6. doi:10.1016/j.compositesb.2014.01.045.

[65] T. Rahman, E. Jansen, Finite element based coupled mode initial post-buckling analysis of a composite cylindrical shell, Thin-Walled Structures 48 (1) (2010) 25–32. doi:10.1016/j.tws.2009.08.003.

[66] T. Rahman, S. Ijsselmuiden, M. Abdalla, E. Jansen, Postbuckling analysis of variable stiffness composite plates using a finite element-based perturbation method, International Journal of Structural Stability and Dynamics 11 (4) (2011) 735–753. doi:10.1142/S0219455411004324.

[67] R. Casciaro, G. Salerno, A. Lanzo, Finite element asymptotic analysis of slender elastic structures: A simple approach, International Journal for Numerical Methods in Engineering 35 (7) (1992) 1397–1426. doi:10.1002/nme.1620350703.

[68] G. Garcea, L. Leonetti, D. Magisano, R. Gonçalves, D. Camotim, Deformation modes for the post-critical analysis of thin-walled compressed members by a Koiter semi-analytic approach, International Journal of Solids and Structures 110-111 (2017) 367–384. doi:10.1016/j.ijsolstr.2016.09.010.

[69] R. Peek, M. Kheyrkhahan, Postbuckling behavior and imperfection sensitivity of elastic structures by the Lyapunov-Schmidt-Koiter approach, Computer Methods in Applied Mechanics and Engineering 108 (3-4) (1993) 261–279. doi:10.1016/0045-7825(93)90005-I.

[70] D. Magisano, L. Leonetti, G. Garcea, How to improve efficiency and robustness of the Newton method in geometrically non-linear structural problem discretized via displacement-based finite elements, Computer Methods in Applied Mechanics and Engineering 313 (2017) 986 – 1005. doi:http://dx.doi.org/10.1016/j.cma.2016.10.023.

[71] G. Garcea, F. S. Liguori, L. Leonetti, D. Magisano, A. Madeo, Accurate and efficient a posteriori account of geometrical imperfections in Koiter finite element analysis, International Journal for Numerical Methods in Engineering 112 (9) (2017) 1154–1174, nme.5550. doi:10.1002/nme.5550.

[72] Z. Wu, G. Raju, P. M. Weaver, Optimization of postbuckling behaviour of variable thickness composite panels with variable angle tows: Towards "buckle-free" design concept, International Journal of Solids and Structures-doi:https://doi.org/10.1016/j.ijsolstr.2017.08.037.

[73] G. Zucco, R. Groh, A. Madeo, P. Weaver, Mixed shell element for static and buckling analysis of variable angle tow composite plates, Composite Structures 152 (Supplement C) (2016) 324 – 338. doi:https://doi.org/10.1016/j.compstruct.2016.05.030.

[74] B. Wang, K. Tian, C. Zhou, P. Hao, Y. Zheng, Y. Ma, J. Wang, Grid-pattern optimization framework of novel hierarchical stiffened shells allowing for imperfection sensitivity, Aerospace Science and Technology 62 (Supplement C) (2017) 114 – 121. doi:https://doi.org/10.1016/j.ast.2016.12.002.

[75] S. B. Biggers, S. Srinivasan, Compression buckling response of tailored rectangular composite plates, AIAA Journal 31 (3) (1993) 590–596. doi:https://doi.org/10.2514/3.61543.

[76] S. Nagendra, D. Jestin, Z. Gürdal, R. Haftka, L. Watson, Improved genetic algorithm for the design of stiffened composite panels, Computers & Structures 58 (3) (1996) 543 – 555. doi:https://doi.org/10.1016/0045-7949(95)00160-I.

[77] Z. Wu, P. M. Weaver, G. Raju, B. C. Kim, Buckling analysis and optimisation of variable angle tow composite plates, Thin-Walled Structures 60 (Supplement C) (2012) 163 – 172. doi:https://doi.org/10.1016/j.tws.2012.07.008.

[78] B. H. Coburn, P. M. Weaver, Buckling analysis, design and optimisation of variable-stiffness sandwich panels, International Journal of Solids and Structures 96 (Supplement C) (2016) 217 – 228. doi:https://doi.org/10.1016/j.ijsolstr.2016.06.007.

[79] E.Barkanov, O.Ozolins, E.Eglitis, F.Almeida, M.C.Bowering, G.Watson, Optimal design of composite lateral wing upper covers. Part I: Linear buckling analysis, Aerospace Science and Technology 38 (Supplement C) (2014) 1 – 8. doi:https://doi.org/10.1016/j.ast.2014.07.010.

[80] J. Thompson, Optimization as a generator of structural instability, International Journal of Mechanical Sciences 14 (9) (1972) 627–629.

[81] D. K. Shin, Z. Gurdal, O. H. Griffin, Jr., Minimum weight design of laminated composite plates for postbuckling performance, Applied Mechanics Reviews (1991) S219–S231doi:http://dx.doi.org/10.1115/1.3121359.

[82] E. Lindgaard, E. Lund, Nonlinear buckling optimization of composite structures, Computer Methods in Applied Mechanics and Engineering 199 (37) (2010) 2319 – 2330. doi:https://doi.org/10.1016/j.cma.2010.02.005.

[83] E. Lindgaard, E. Lund, K. Rasmussen, Nonlinear buckling optimization of composite structures considering "worst" shape imperfections, International Journal of Solids and Structures 47 (22) (2010) 3186 – 3202. doi:https://doi.org/10.1016/j.ijsolstr.2010.07.020.

[84] S. R. Henrichsen, E. Lindgaard, E. Lund, Robust buckling optimization of laminated composite structures using discrete material optimization consid-

ering "worst" shape imperfections, Thin-Walled Structures 94 (Supplement C) (2015) 624 – 635. doi:https://doi.org/10.1016/j.tws.2015.05.004.

[85] R. Degenhardt, A. Kling, K. Rohwer, A. Orifici, R. Thomson, Design and analysis of stiffened composite panels including post-buckling and collapse, Computers & Structures 86 (9) (2008) 919 – 929, composites. doi:https://doi.org/10.1016/j.compstruc.2007.04.022.

[86] Z. Wu, P. M. Weaver, G. Raju, Postbuckling optimisation of variable angle tow composite plates, Composite Structures 103 (Supplement C) (2013) 34 – 42. doi:https://doi.org/10.1016/j.compstruct.2013.03.004.

[87] D. Wang, M. M. Abdalla, W. Zhang, Buckling optimization design of curved stiffeners for grid-stiffened composite structures, Composite Structures 159 (Supplement C) (2017) 656 – 666. doi:https://doi.org/10.1016/j.compstruct.2016.10.013.

[88] S. R. Henrichsen, P. M. Weaver, E. Lindgaard, E. Lund, Post-buckling optimization of composite structures using Koiter's method, International Journal for Numerical Methods in Engineering 108 (8) (2016) 902–940, nme.5239. doi:10.1002/nme.5239.

[89] D. Bushnell, Optimization of composite, stiffened, imperfect panels under combined loads for service in the postbuckling regime, Computer Methods in Applied Mechanics and Engineering 103 (1) (1993) 43 – 114. doi:https://doi.org/10.1016/0045-7825(93)90041-U.

[90] S. C. White, P. M. Weaver, Towards imperfection insensitive buckling response of shell structures-shells with plate-like post-buckled responses, The Aeronautical Journal 120 (1224) (2016) 233–253. doi:10.1017/aer.2015.14.

[91] R. L. Riche, R. T. Haftka, Optimization of laminate stacking sequence for buckling load maximization by genetic algorithm, AIAA Journaldoi:doi:10.2514/3.11710.

[92] K. Svanberg, The method of moving asymptotes—a new method for structural optimization, International Journal for Numerical Methods in Engineering 24 (2) (1987) 359–373. doi:10.1002/nme.1620240207.
URL `http://dx.doi.org/10.1002/nme.1620240207`

[93] L. S. Johansen, E. Lund, J. Kleist, Failure optimization of geometrically linear/nonlinear laminated composite structures using a two-step hierarchical model adaptivity, Computer Methods in Applied Mechanics and Engineering 198 (30) (2009) 2421 – 2438. doi:https://doi.org/10.1016/j.cma.2009.02.033.

[94] Z. B. Zabinsky, Random Search Algorithms, John Wiley & Sons, Inc., 2010. doi:10.1002/9780470400531.eorms0704.

[95] R. Degenhardt, A. Kling, A. Bethge, J. Orf, L. Kärger, R. Zimmermann, K. Rohwer, A. Calvi, Investigations on imperfection sensitivity and deduction of improved knock-down factors for unstiffened cfrp cylindrical shells, Composite Structures 92 (8) (2010) 1939 – 1946. doi:https://doi.org/10.1016/j.compstruct.2009.12.014.

[96] F. S. Liguori, A. Madeo, D. Magisano, L. Leonetti, G. Garcea, Post-buckling optimisation strategy of imperfection sensitive composite shells using Koiter method and Monte Carlo simulation, Computer Methods in Applied Mechanics and Engineering (Submitted for publication).

[97] K. Liang, M. Ruess, M. Abdalla, An eigenanalysis-based bifurcation indicator proposed in the framework of a reduced-order modeling technique for non-linear structural analysis, International Journal of Non-Linear Mechanics 81 (2016) 129–138. doi:10.1016/j.ijnonlinmec.2016.01.013.

[98] S. G. Castro, R. Zimmermann, M. A. Arbelo, R. Degenhardt, Exploring the constancy of the global buckling load after a critical geometric imperfection level in thin-walled cylindrical shells for less conservative knock-down factors, Thin-Walled Structures 72 (2013) 76 – 87. doi:http://dx.doi.org/10.1016/j.tws.2013.06.016.

[99] D. Magisano, K. Liang, G. Garcea, L. Leonetti, M. Ruess, An efficient mixed variational reduced-order model formulation for nonlinear analyses of elastic shells, International Journal for Numerical Methods in Engineeringdoi:10.1002/nme.5629.

[100] V. P. Nguyen, C. Anitescu, S. P. Bordas, T. Rabczuk, Isogeometric analysis: An overview and computer implementation aspects, Mathematics and Computers in Simulation 117 (2015) 89 – 116. doi:https://doi.org/10.1016/j.matcom.2015.05.008.

[101] K. A. Johannessen, Optimal quadrature for univariate and tensor product splines, Computer Methods in Applied Mechanics and Engineering 316 (2017) 84 – 99, special Issue on Isogeometric Analysis: Progress and Challenges. doi:http://doi.org/10.1016/j.cma.2016.04.030.

[102] C. Adam, T. Hughes, S. Bouabdallah, M. Zarroug, H. Maitournam, Selective and reduced numerical integrations for NURBS-based isogeometric analysis, Computer Methods in Applied Mechanics and Engineering 284 (2015) 732–761. doi:10.1016/j.cma.2014.11.001.

[103] J. Caseiro, R. Valente, A. Reali, J. Kiendl, F. Auricchio, R. Alves de Sousa, Assumed natural strain NURBS-based solid-shell element for the analysis of large deformation elasto-plastic thin-shell structures, Computer Methods in Applied Mechanics and Engineering 284 (2015) 861–880. doi:10.1016/j.cma.2014.10.037.

[104] R. Echter, B. Oesterle, M. Bischoff, A hierarchic family of isogeometric shell finite elements, Computer Methods in Applied Mechanics and Engineering 254 (2013) 170–180, cited By 61. doi:10.1016/j.cma.2012.10.018.

[105] R. Bouclier, T. Elguedj, A. Combescure, Efficient isogeometric NURBS-based solid-shell elements: Mixed formulation and B-method, Computer Methods in Applied Mechanics and Engineering 267 (2013) 86–110, cited By 20. doi:10.1016/j.cma.2013.08.002.

[106] S. Hosseini, J. J. C. Remmers, C. V. Verhoosel, R. de Borst, An isogeometric solid-like shell element for nonlinear analysis, International Journal for Numerical Methods in Engineering 95 (3) (2013) 238–256. doi:10.1002/nme.4505.

[107] J. F. Caseiro, R. A. F. Valente, A. Reali, J. Kiendl, F. Auricchio, R. J. Alves de Sousa, On the Assumed Natural Strain method to alleviate locking in solid-shell NURBS-based finite elements, Computational Mechanics 53 (6) (2014) 1341–1353. doi:10.1007/s00466-014-0978-4.

[108] W. T. Les Piegl, The NURBS book, 1997. doi:10.1007/978-3-642-59223-2.

[109] C. H. Thai, H. Nguyen-Xuan, S. P. A. Bordas, N. Nguyen-Thanh, T. Rabczuk, Isogeometric Analysis of Laminated Composite Plates Using the Higher-Order Shear Deformation Theory, Mechanics of Advanced Materials and Structures 22 (6) (2015) 451–469. doi:10.1080/15376494.2013.779050.

[110] Y. Guo, M. Ruess, A layerwise isogeometric approach for NURBS-derived laminate composite shells, Composite Structures 124 (2015) 300 – 309. doi:https://doi.org/10.1016/j.compstruct.2015.01.012.

[111] O. C. Zienkiewicz, R. L. Taylor, J. M. Too, Reduced integration technique in general analysis of plates and shells, International Journal for Numerical Methods in Engineering 3 (2) (1971) 275–290. doi:10.1002/nme.1620030211.

[112] T. Belytschko, B. L. Wong, H.-Y. Chiang, Advances in one-point quadrature shell elements, Computer Methods in Applied Mechanics and Engineering 96 (1) (1992) 93 – 107. doi:http://dx.doi.org/10.1016/0045-7825(92)90100-X.

[113] T. Hughes, T. Tezduyar, Finite elements based upon mindlin plate theory with particular reference to the four-node bilinear isoparametric element., Journal of Applied Mechanics, Transactions ASME 48 (3) (1981) 587–596.

[114] M. L. Bucalem, K.-J. Bathe, Higher-order MITC general shell elements, International Journal for Numerical Methods in Engineering 36 (21) (1993) 3729–3754. doi:10.1002/nme.1620362109.

[115] R. Bouclier, T. Elguedj, A. Combescure, Efficient isogeometric nurbs-based solid-shell elements: Mixed formulation and -method, Computer Methods in Applied Mechanics and Engineering 267 (2013) 86 – 110. doi:https://doi.org/10.1016/j.cma.2013.08.002.

[116] R. Hauptmann, K. Schweizerhof, A systematic development of 'solid-shell' element formulations for linear and non-linear analyses employing only displacement degrees of freedom, International Journal for Numerical Methods in Engineering 42 (1) (1998) 49–69. doi:10.1002/(SICI)1097-0207(19980515)42:1<49::AID-NME349>3.0.CO;2-2.

[117] K. Sze, X. Liu, S. Lo, Popular benchmark problems for geometric nonlinear analysis of shells, Finite Elements in Analysis and Design 40 (11) (2004) 1551 – 1569. doi:http://dx.doi.org/10.1016/j.finel.2003.11.001.

[118] L. Leonetti, F. Liguori, D. Magisano, G. Garcea, An efficient isogeometric solid-shell formulation for geometrically nonlinear analysis of elastic shells, Computer Methods in Applied Mechanics and Engineering (Accepted for publication).

[119] L. Leonetti, F. Liguori, D. Magisano, G. Garcea, An isogeometric formulation of the Koiter's theory for buckling and initial post-buckling analysis of composite shells (Submitted for publication).